Biomolecule encapsulation in biocompatible metal-organic frameworks

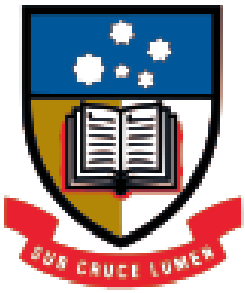

The University of Adelaide

School of Physical Sciences

Department of Chemistry

Submitted in fulfilment of the degree

Master of Philosophy (Chemical Science)

Presented by

Tania Pullin B. Sc. (Advanced)

Supervisors: Professor Christopher Sumby, Professor Christian Doonan and Dr. Kenji Sumida

November 2019

Table of Contents

Abstract

Metal-organic frameworks (MOFs) are a class of crystalline materials defined by high surface area and porosity. MOFs are constructed from organic linkers and metal nodes, resulting in a structure that extends in two or three dimensions. Owing to their porosity and surface areas, MOFs have been used extensively for gas storage, catalysis and biological applications such as drug delivery.

Biomolecules are molecules of biological origin, including proteins, enzymes and DNA which, due to their unique properties, are of interest in numerous fields including as therapeutics or biocatalysts. However, their use can be limited by their low stability in non-biological conditions. Thus, a means of protecting biomolecules from challenge conditions (high or low pH, organic solvents or elevated temperatures) could expand the opportunities for their application. One such method of protection is biomimetic mineralisation wherein a MOF coating is grown around the biomolecule. This protective strategy is also applicable to larger biological assemblies such as cells.

The primary aim of this thesis was to investigate a number of MOFs, for example those possessing biocompatible building blocks, and determine whether these materials were able to encapsulate proteins via biomimetic mineralisation and offer protection against harsh conditions. By extension, this allowed investigation of the MOF features necessary to facilitate biomimetic mineralisation. Initially zinc-based MOFs with amino-acid linkers, L-glutamic acid and L-carnosine (β-Alanine-L-Histidine), were investigated. However, zinc glutamate (BioMOF-1) was unable to encapsulate proteins, while zinc carnosine (BioMOF-2) was unable to stabilise encapsulated proteins against test challenge conditions.

The focus was then shifted to zinc-based MOFs with N-donor containing ligands; 3,3’,5,5’-tetramethyl-4,4’-bipyrazole (H_2Me_4bpz) and 4,5-di(1H-tetrazol-5-yl)-2H-1,2,3-triazole (H_3TDT). Both MOFs are formed from azole donors, like zeolitic imidazole frameworks (ZIFs) which are most widely employed for biomolecule encapsulation and protection. While enzyme was potentially encapsulated within $Zn(Me_4bpz)$, the majority of activity observed was due to enzyme leaching resulting from MOF decomposition. For Zn(TDT), the sodalite topology was unable to be synthesised in aqueous conditions, instead a highly unstable material with unknown structure was formed. Due to the low stability, no further analysis was performed.

While none of the studied MOFs successfully encapsulated and protected enzymes, key conclusions were still made from this work. The zinc glutamate and zinc carnosine studies

highlighted that increased MOF biocompatibility does not necessarily lead to successful biomimetic mineralisation. Further, the results for Zn(Me_4bpz) and Zn(TDT) showed that the sole presence of azole donors does not guarantee successful biomimetic mineralisation. Instead, this is likely more dependent on the mechanism of MOF formation rather than the donor type. To further increase the understanding of biomimetic mineralisation and the required MOF chemistry, future work is needed. This future work may include a greater diversity of MOFs with biologically derived linkers and linkers containing solely azole donors. Further, the ligands used in this thesis could be altered to understand the effect of varying donor sets on the ability of the MOF to undergo biomimetic mineralisation.

.

Declaration

I certify that this work contains no material which has been accepted for the award of any other degree or diploma in my name, in any university or other tertiary institution and, to the best of my knowledge and belief, contains no material previously published or written by another person, except where due reference has been made in the text. In addition, I certify that no part of this work will, in the future, be used in a submission in my name, for any other degree or diploma in any university or other tertiary institution without the prior approval of the University of Adelaide and where applicable, any partner institution responsible for the joint-award of this degree.

I give permission for the digital version of my thesis to be made available on the web, via the University's digital research repository, the Library Search and also through web search engines, unless permission has been granted by the University to restrict access for a period of time.

I acknowledge the support I have received for my research through the provision of an Australian Government Research Training Program Scholarship.

Tania Pullin

21/11/2019

Acknowledgments

Firstly, I wish to thank my supervisors, Chris Sumby and Christian Doonan for their continual support and guidance over these past years. Special thanks go to Chris for the countless amount time he spent helping me with experimental problems and crystallography, in addition to providing many new ideas when things did not work as planned and reading many drafts of this thesis. The help Chris has given me along the way has taught me so much, and without his assistance I would not been able to produce the work that I did.

Many thanks also go to the members of the Sumby-Doonan group over the past two years who been there to help me with various issues and listen to my practice presentations. Special mentions go to Weibin Liang for helping me with all of the characterisation techniques for this project and Natasha Maddigan for helping me with a lot of the background knowledge for this project. Thanks also go to Oliver Linder-Patton for his help collecting SEM images and coming up with helpful solutions to experimental issues. To all of the members of Lab 10 – Rosemary, Chris, Marcello, Thomas and Drew, thanks for helping me around the lab, answer my questions and always being there for chat. To the members of Lab 9 – Michael, Ricardo and Natasha, thanks for being great lab mates.

Thanks are also due to family and friends who have encouraged me and kept me sane over these past two years. Special mention to my parents who have supported me throughout my whole life and helped me get to where I am today.

Lastly, to my partner Aiden, words cannot express how grateful I am to have had you by my side over these past years. Your constant support is what helped me make it through these two years.

Abbreviations

2-D: Two dimensional

3-D: Three dimensional

bioMOF: Biomolecule-derived metal-organic framework

BSA: Bovine serum albumin

CAT: Catalase

CFA: Coordination-framework Augsburg

CLSM: Confocal laser scanning microscopy

DMA: Dimethylacetamide

DMF: Dimethylformamide

DMSO: Dimethyl sulfoxide

DNA: Deoxyribonucleic acid

EDTA: Ethylenediaminetetraacetic acid

FBSA: FTC-tagged BSA

FCAT: FITC-tagged catalase

FHRP: FITC-tagged HRP

FITC: Fluorescein isothiocyanate

FMb: FITC-tagged myoglobin

FOX: Ferrous oxidation of xylenol orange

HOF: Hydrogen-bonded framework

HRP: Horseradish peroxidase

MAF: Metal-azolate framework

MAF-7: Metal-azolate framework-7[1]

Mb: Myoglobin

MFU: Metal-organic framework Ulm University

MOF: Metal-organic framework

NMR: Nuclear magnetic resonance

NU: North-western University

PBS: Phosphate buffered saline

PXRD: Powder X-ray diffraction

PZ: Polaprezinc (TGA-approved form of zinc carnosine)

RbCAT: RbITC-tagged catalase

RbITC: Rhodamine b isothiocyanate

RbMb: RbITC-tagged myoglobin

SAXS: Small angle X-ray scattering

SDS: Sodium dodecyl sulphate

SEM: Scanning electron microscopy

TBA: Tetrabutylammonium

TEA: Triethylamine

TGA: Therapeutic goods administration

THF: Tetrahydrofuran

UiO: University of Oslo

UV-Vis: Light emitted in the ultraviolet and visible regions of the electromagnetic spectrum

ZIF: Zeolitic imidazolate framework

ZIF-8: Zeolitic imidazolate framework 8 [2]

ZIF-90: Zeolitic imidazole framework 90 [3]

ZnCarn: Zn Carnosine MOF [4]

ZnGLUT: Zn Glutamate MOF [5]

CHAPTER 1: Introduction

1.1 Biomolecules

Biomolecules are molecules of biological origin, including proteins and DNA. Of particular interest to this project are enzymatic proteins which act as catalysts in biological systems. Proteins are comprised of amino-acids joined by amide bonds to form a linear chain, known as the primary structure. Hydrogen bonding between these amino-acid residues leads to the formation of helices or sheets, which make up the secondary structure. Further secondary interactions lead to the formation of the 3-D (tertiary) structure and multiple amino-acid chains may interact to form a larger (quaternary) structure (**Figure 1**). Each of these levels of protein structure influence the resultant physical and chemical properties, which lead to unique functionalities. Thus, the structure of a protein is vital for its function.

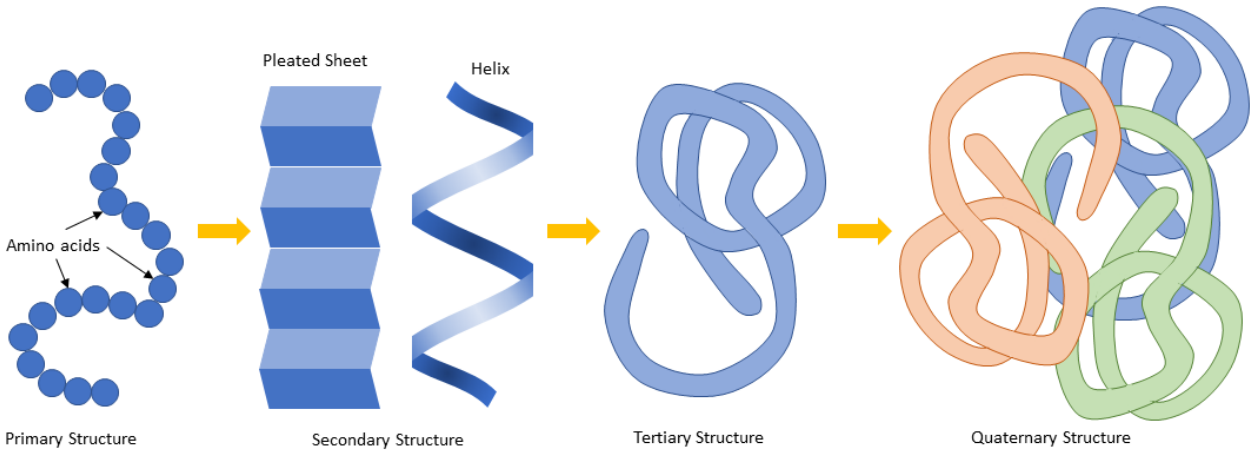

Figure 1: *The four levels of the structure of a protein.*

Proteins have shown importance in medicine as therapeutics, and in food technologies due to their structural properties.[6-9] Due to their catalytic activity under benign conditions and excellent chemo-, regio- and enantioselectivity, enzymes are widely investigated as catalysts for fine chemical synthesis. For example, cytochrome P450s could be used to catalyse the hydroxylation of various hydrophobic compounds,[10] alcohol dehydrogenases could catalyse oxidoreduction reactions,[11] and aldolases can be used for aldol addition reactions.[11] As a consequence of their biological origins and lack of by-products, they are viewed as a greener and more biocompatible alternative to synthetic catalysts.

A major limitation of enzymes in chemical synthesis is their limited stability in non-native environments. Typically, functional structures are only retained at low or room temperatures, in

aqueous solutions, and biological pH. However, the exact conditions required for stability vary between enzymes, as do the optimal conditions in which they operate (**Figure 2**).

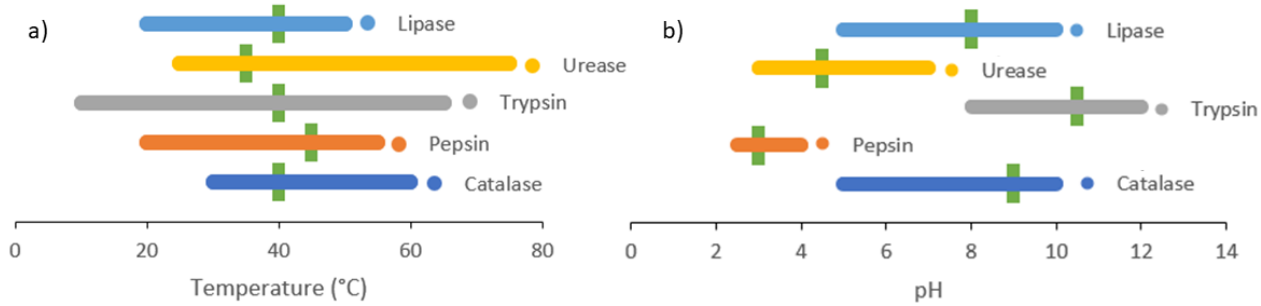

Figure 2: *a) pH and b) temperature stability ranges for lipase (Geotrichum marinum) (light blue),*[12] *urease (Enterobacter sp.) (yellow),*[13] *trypsin (Balistes capriscus) (grey),*[14] *pepsin (albatrossia pectoralis) (orange)*[15] *and catalase (Oceanobacillus oncorhynchi subsp. incaldanensis) (dark blue).*[16] *The green bar represents the pH or temperature at which the protein is most stable.*

If these native conditions are not maintained, denaturation of the enzyme can occur by disruption of the secondary interactions, leading to a break down in the secondary, tertiary or quaternary protein structure. As the structure of an enzyme is vital for its function, this denaturation leads to a loss of enzymatic ability. Given that a majority of industrial chemical syntheses utilise elevated temperature, organic solvents or other denaturing conditions, this introduces significant limitations and makes the use of enzymes challenging.

1.2 Biomolecule protection

In order to expand the conditions in which enzymes are stable, some form of protection needs to be implemented. This could potentially allow them to be used, for example, at elevated temperatures or in organic solvents, thereby making them applicable for industrial chemical processes. Due to the high demand to achieve this, it has been a widely investigated area with a number of strategies being reported in the literature which include cross-linking,[17] binding to a surface,[18] and encapsulation in a gel or mesoporous silica (**Figure 3**).[19]

While in all three cases, these methods were able to effectively protect or stabilise proteins, they each come with notable limitations. Cross-linking proteins relies on the presence and suitable concentrations of specific amino-acid residues within the protein structure. Further, the location of the cross links needs to be considered as they may block the active site. Thus, the cross-linking process needs to be tailored specifically to the target protein, but still may not be viable for some

biomolecules. For the surface-binding strategy, similar limitations are faced as the surface to needs to be tailored to the size, chemistry and structure of the target protein. Conversely, the gel encapsulation method is a general approach that does not require significant tailoring for each target biomolecule. However, the gels can have high density which may restrict the diffusion of substrate through to the encapsulated enzymes or lack the stability for use in fine chemical synthesis. Similarly, mesoporous silica can be used to encapsulate and protect enzymes.[20, 21] However, it has been reported that encapsulated biomolecules can leach from the silica relatively quickly, making it unsuitable for many applications.[22] Instead it would be highly desirable to have a generally applicable, highly porous coating that could allow facile substrate diffusion without enzyme leaching.

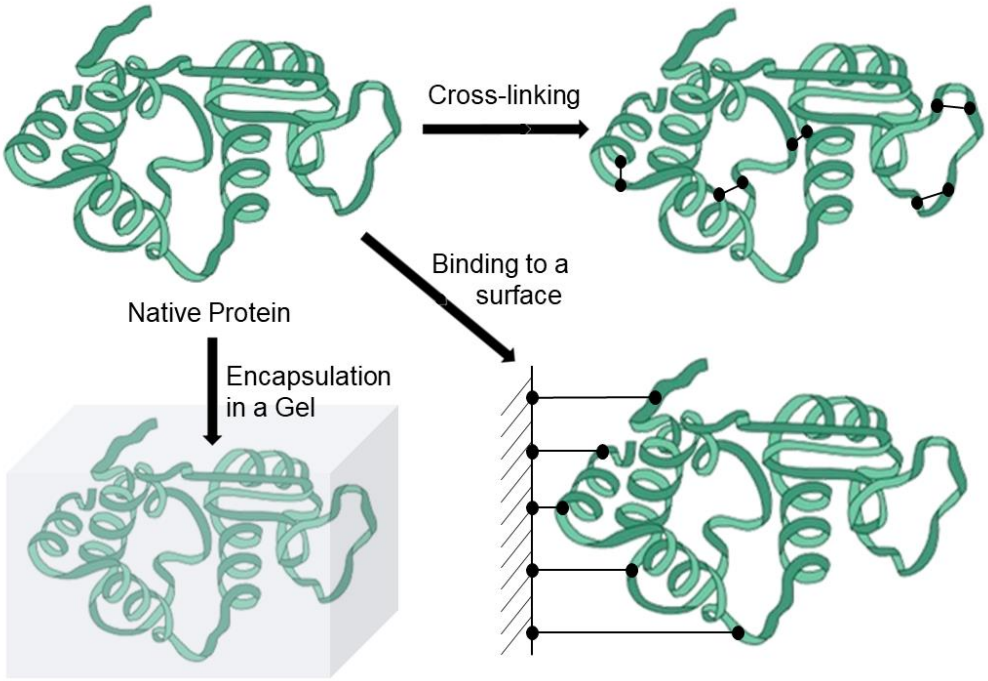

Figure 3: *Schematic of enzyme protection via cross-linking, binding to a surface and encapsulation in a gel (or mesoporous silica).*

1.3 MOFs for biomolecule protection

Metal-organic frameworks (MOFs) are a class of crystalline materials defined by high porosity and surface areas.[23] They are composed of metal nodes connected via organic linkers to form a framework structure (**Figure 4**).[24, 25] One key feature of MOFs that lend them to an extremely diverse array of applications is the ability to customise the structure and chemistry. The metal node, organic linkers and synthetic conditions can all be altered to impact their physical and chemical properties.

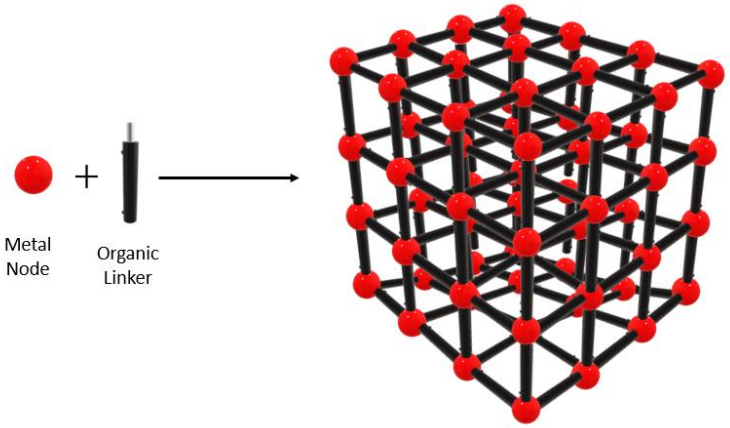

Figure 4: *Schematic representation showing the components and structure of a metal-organic framework (MOF).*

For example, varying the linker length while keeping the metal node constant can lead to the formation of isoreticular MOF families which are comprised of materials with identical topology but varying pore sizes.[26] A well-known example of this is the University of Oslo (UiO) family of MOFs, comprising of UiO-66, UiO-67 and UiO-68 which contain linkers with increasing numbers of phenyl groups such that the pore size varies but the topology remains identical (**Figure 5**).

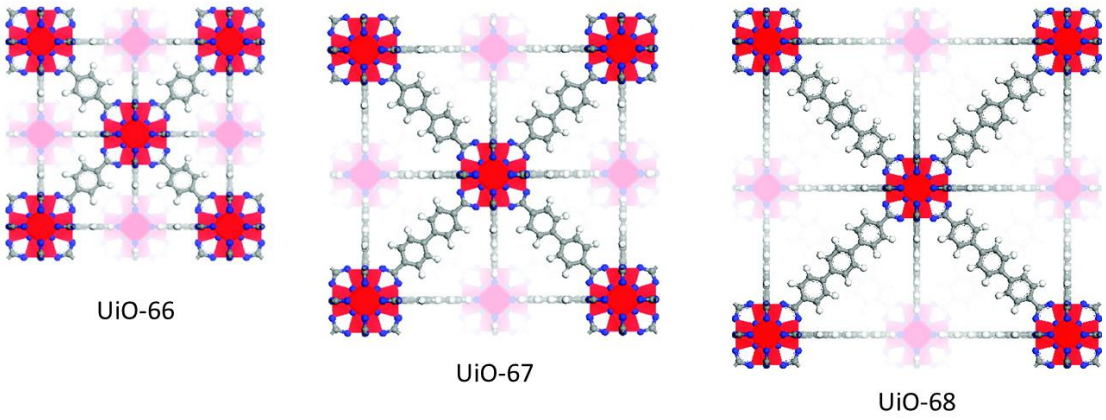

Figure 5: *Representations of the structures of UiO-66, UiO-67 and UiO-68 highlighting the increasing pore size as a result of ligand extension from 1,4-benzene dicarboxylate to 4,4'-biphenyl dicarboxylate and 4,4"-terphenyl dicarboxylate respectively. Zr = red, O = blue, C = grey, H = white.*[27]

The geometry and connectivity of the ligand can vary the structure of MOFs. For example, comparison of linear ligands such as the benzene dicarboxylate used in MOF-5[25] and tritopic ligands such as 1,3,5-benzenetribenzoate used in MOF-177[28] shows that this leads to the formation of MOFs with significantly different topologies, pore sizes and surface areas (**Figure 6**). Furthermore, the pore chemistry can be altered by addition of functional groups, which, for example, can be used to change pore hydrophobicity or serve as binding sites.[29, 30]

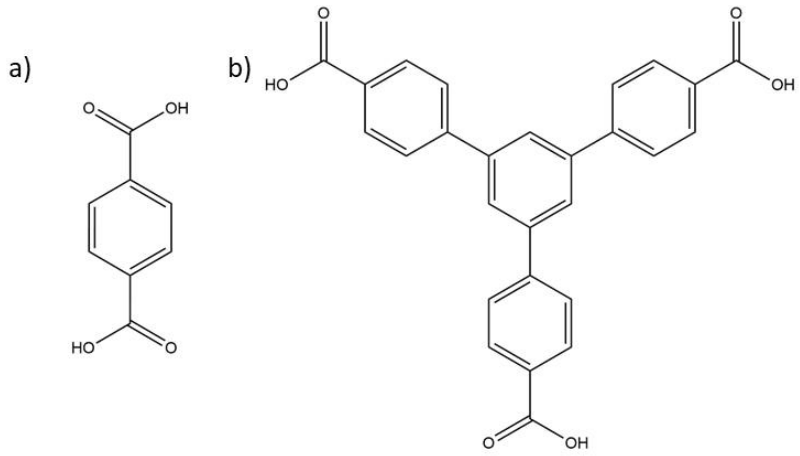

Figure 6: *a) The benzene dicarboxylate ligand from MOF-5,[25] and b) the 1,3,5-benzenetribenzoate linker used in MOF-177.[28]*

The binding sites present in the ligand can also be varied from carboxylate or azolate moieties which may impact the strength of the metal-ligand bond and the stability of the MOF. Typically, the metal-ligand bond is the source of MOF decomposition by either ligand protonation for chemical degradation or by bond breaking in thermal degradation. Thus, the MOF stability is typically improved by increasing the strength of this metal-ligand bond, which can be done using high-valent metal salts.[31]

The metal nodes can also be used to alter the MOF structure, while keeping the ligand constant. For example, Zr(IV) and Ti(IV) have been used to synthesise two MOFs with distinct structures that incorporate the benzene dicarboxylate linker (UiO-66 and MIL-125) (**Figure 7**).[32] Variation of metal nodes can also be used to alter the biocompatibility of the resultant MOFs.

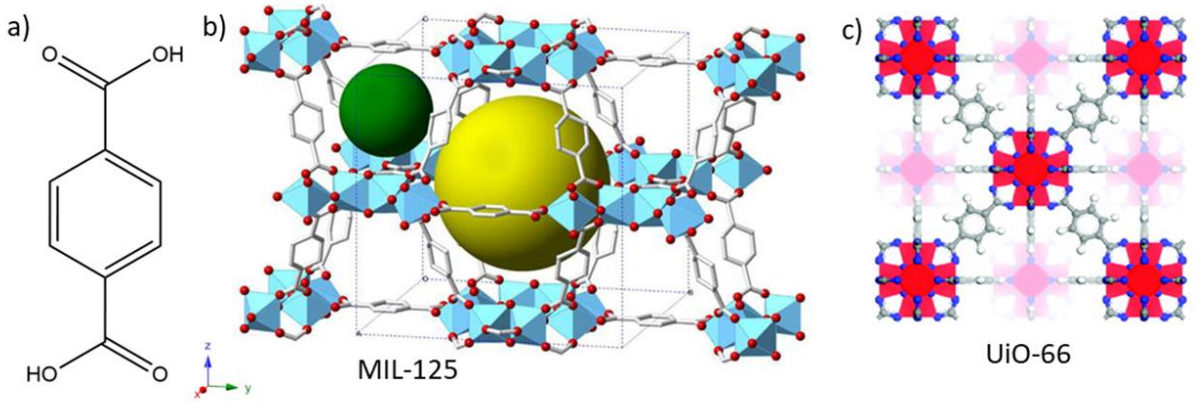

Figure 7: *a) the benzene dicarboxylate linker, b) the crystal structure of MIL-125 (Ti = blue, O = red, C =white),[33] and c) the crystal structure of UiO-66 (Zr = red, O = blue, C = grey, H = white).[27]*

As a consequence of these structural variations, MOFs are highly mutable materials whereby their properties can be varied to suit specific applications; this has been extensively documented in the literature. For example, the use of transition metals, either as the node or incorporated via post-synthetic metalation, in combination with the high surface areas make MOFs advantageous as heterogenous catalysts.[34-37] Moreover, the ability to alter the pore and aperture sizes within MOFs leads to applications in size-selective separation (gas and liquid phases).[38-40] The high porosity of MOFs and their ability to retain small molecules leads to potential use in gas storage.[39, 41, 42] Other applications for MOFs include luminescence,[43] lasing,[44] drug delivery,[45] non-linear optics[46] and biological protection.[6]

Very recently, MOFs have been used to encapsulate proteins and provide protection against harsh conditions.[47] Due to the porous nature of MOFs, which allows transport of small molecule substrates and escape of products, the enzymatic activity is retained. Early approaches explored the use of MOFs for biomolecule protection by infiltrating the protein into a pre-made mesoporous MOF structure, immobilizing microperozidase-11, horseradish peroxidase (HRP) and cytochrome c.[48, 49] In all cases, this method yielded high enzyme loading, and the encapsulated enzyme was more durable, and more recyclable compared to the free enzyme or enzyme loaded into a mesoporous silica support. Strong interactions between the framework and the enzymes ensured no leaching occurred. However, if the enzymes or framework are varied these interactions may not be strong enough to prevent leaching. Further, this method is limited by the pore aperture size of the MOF wherein only biomolecules with sizes smaller than the pores can be used. Finally, synthesis of mesoporous MOFs presents challenges regarding stability, in addition to the high chance of interpenetrated MOF growth as the linker size increases, which leads to a subsequent reduction in porosity.

As a result of these challenges, this method of biomolecule encapsulation is different to the process used herein.

1.4 Biomimetic mineralisation of MOFs for biomolecule encapsulation/protection

Biomimetic mineralisation is a process wherein a MOF coating is formed around a biomolecule, offering protection from external conditions (**Figure 8**). This occurs in much the same way as biomineralisation in Nature, where the growth of shells of calcium carbonate around sea urchins or crustaceans (**Figure 8**).[47] In this process, the biomolecule promotes the formation of the MOF such that it forms around the biomolecule, completely enshrouding it within a growing MOF particle (these may aggregate to form a more complex biocomposite).

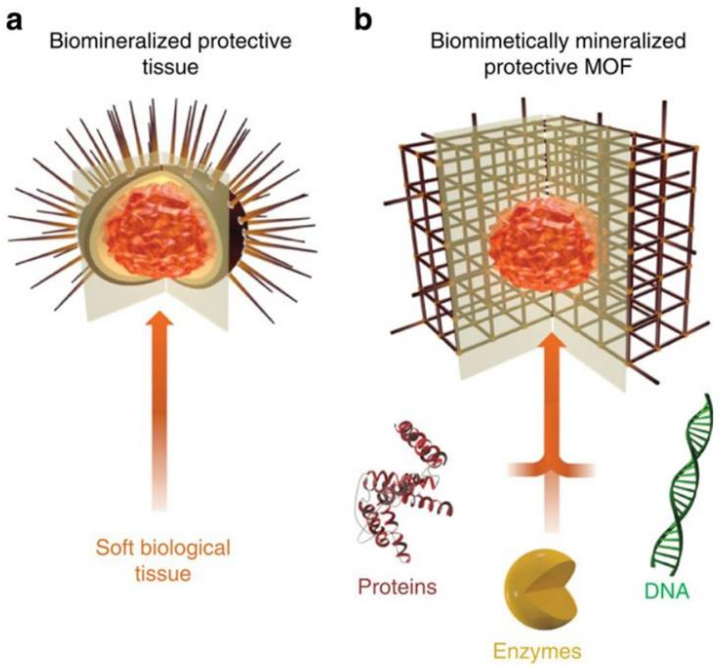

***Figure 8**: A schematic comparing biomimetic mineralisation to encapsulate biomolecules within a crystalline MOF to biomineralisation in Nature.*[47]

A more general approach to enzyme encapsulation within MOFs is via a co-precipitation mechanism. The key difference between this and biomimetic mineralisation is that the enzyme does not accelerate MOF growth during co-precipitation.[50] There have been numerous studies showing that co-precipitation leads to protection of encapsulated enzyme against harsh conditions.[50-52] Yet there have also been findings indicating that the protective capacity of an identical MOF biocomposite formed via the co-precipitation mechanism is lower than that obtained from biomimetic mineralisation.[6]

The original, and most commonly studied, MOF reported to successfully encapsulate and protect enzymes by both co-precipitation and biomimetic mineralisation is ZIF-8 (**Figure 9**).[47, 52] ZIF-8 can be formed at room temperature in aqueous conditions, making the synthesis compatible with proteins. Moreover, ZIF-8 has been documented to have low cytotoxicity, making it suitable for biological applications.[6]

The initial studies of biomimetic mineralisation by ZIF-8 were reported by Liang.[47] In this study, a number of proteins and enzymes were encapsulated within ZIF-8 crystals, as confirmed by Fourier-transform infrared (FTIR) spectroscopy and confocal laser scanning microscopy (CLSM). Following this, the enzymatic activity of the ZIF-8 biocomposite of horseradish peroxidase (HRP@ZIF-8) was then analysed using a pyrogallol assay. The results of these assays showed that the activity loss of HRP@ZIF-8 following exposure to proteolytic agents (trypsin), boiling water

and boiling DMF was significantly less than that of free HRP, HRP protected by calcium carbonate and HRP protected by mesoporous silica. This study also showed that pH modification could be used to remove the ZIF-8 coating and release the encapsulated biomolecule with retained activity. Following this initial report of ZIF-8 encapsulation of biomolecules, an extremely large number of additional ZIF-8 studies have been presented. These further confirmed the ability of ZIF-8 to successfully encapsulate and protect a wide range of biomolecules.[53-58]

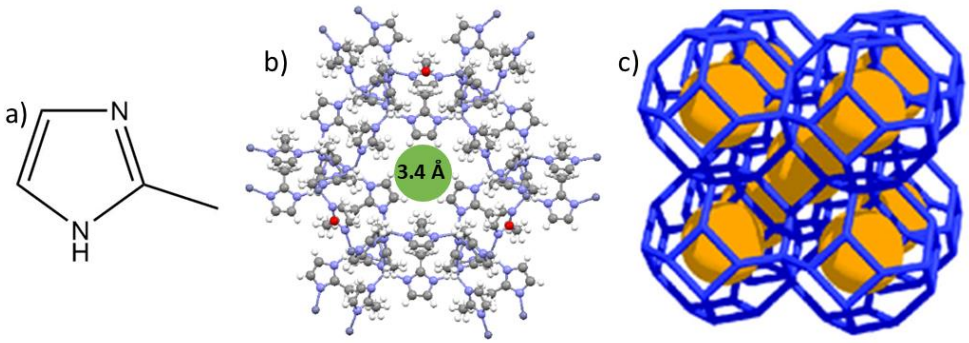

Figure 9: *a) The ligand used to form ZIF-8, b) crystal structure of ZIF-8, showing the 3.4 Å pore aperture (green) (C = grey, N = purple, H = white, Zn = red)[59] and c) the topology of sodalite ZIF-8, the orange balls represent the largest sphere able to fit inside the pores without touching the van der Waals radii.[60]*

Maddigan and co-workers investigated the effect of protein surface chemistry on successful encapsulation of the proteins within a ZIF-8 framework for a variety of proteins including BSA and haemoglobin (Hb).[61] Their results indicated that encapsulation within ZIF-8 was favoured by proteins with a isoelectric point (pI) less than approximately 7 such that they possessed negatively charged surfaces in the reaction conditions. This was proposed to allow for zinc aggregation at the charged protein surface, which then seeded the growth of ZIF-8 around the protein. The growth of ZIF-8 occurs via a stepwise deprotonation mechanism outlined in **Scheme 1**, which is thought to be one of the key reasons for its ability to successfully undergo biomimetic mineralisation.

Despite the well-documented success of ZIF-8, a primary limitation of ZIF-8 is the relatively small aperture size (3.4 Å) (**Figure 9**), which restricts the size of molecule able to diffuse through the MOF to the enzymatic site.[59] While some flexibility within the ZIF-8 structure has been reported,[62] this is minimal and so only molecules of a similar size to the aperture size will readily diffuse throughout the framework; molecules notably larger than the pore aperture will be retained on the surface of the ZIF.[59] This has been well characterised by Eum and co-workers, finding that there were competing effects between the size of the molecule and the

hydrophobicity of the MOF which impacted the diffusion ability of select molecules.[63] Furthermore, despite the relatively low toxicity of ZIF-8, the significant quantities of imidazole resulting from ZIF decomposition may pose risks. Imidazole has been shown to have serious effects on the platelet metabolism; it inhibits platelet aggregation which in turn hinders clotting.[64]

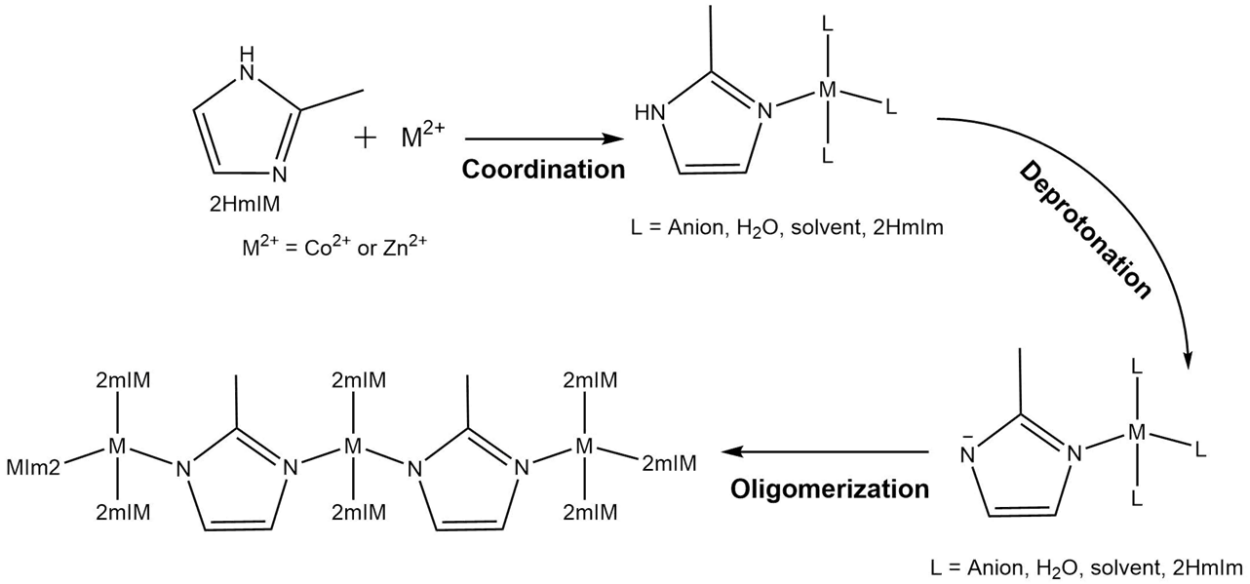

Scheme 1: *The proposed mechanism of ZIF-8 formation.*

Recent work by Liang and co-workers showed that the hydrophobicity of ZIF-8 caused encapsulated catalase to become inactive.[65] This was proposed to be due to the greater affinity that proteins have for hydrophobic surfaces, which led to conformational changes and subsequent activity loss. In comparison, hydrophilic MOFs, such as ZIF-90 and MAF-7 (**Figure 10** and **Figure 11** respectively), could successfully encapsulate and protect enzymes without appreciable activity loss.[50, 65] The data is still ambiguous in regard to whether these two MOF biocomposites form via biomimetic mineralisation or co-precipitation.

Similar to ZIF-8, ZIF-90 forms with a sodalite topology containing pores of 11.2 Å and pore apertures of 3.5 Å.[3] Similarly, MAF-7 which, although not labelled as a ZIF, is formed from a very similar ligand to the ZIF materials, using a triazole instead of imidazole-based ligands, and possesses an identical sodalite topology (**Figure 11**).[1, 65] While the ZIF-90 and MAF-7 coatings did not cause encapsulated enzymes to lose activity, their use is still hindered by relatively small pore apertures of 3.5 Å and 3.2 Å respectively.[1, 3] As such, it would be of interest to investigate alternative MOFs that do not face these limitations.

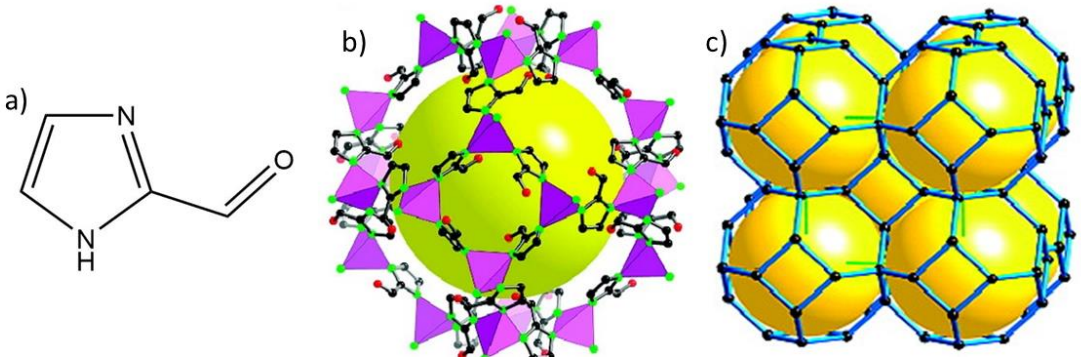

Figure 10: *a) The ZIF-90 ligand, b) the structure of a single ZIF-90 cage with ZnN_4 tetrahedra shown in pink (C = blank, N = green, O = red), the yellow ball represents the largest sphere able to fit in the cage without touching the van der Waals sphere, and c) the extended ZIF-90 network showing the sodalite topology.*[3]

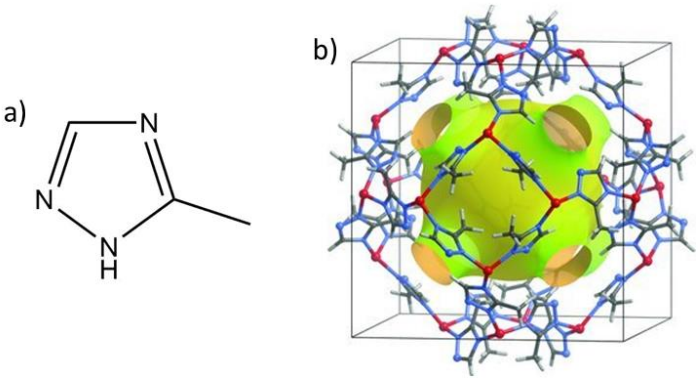

Figure 11: *a) The MAF-7 ligand and b) crystal structure of MAF-7 cage, green ball shows the largest sphere able to fit in the pore without touching the van der Waals spheres.*[1]

Despite the growing quantity of studies on biomimetic mineralisation with MOFs, it is still a relatively new field. As such, there remains a lack of understanding regarding the specific features of the MOFs that are key to ensuring successful biomimetic mineralisation. Thus, investigation into MOF chemistry and how specific features impact the ability of the MOF to undergo biomimetic mineralisation is important. This may allow for the production of general screening procedures to make it quicker and easier to select a MOF suitable for protecting a biomolecule in specific environments.

1.5 Thesis Aims and Overview

Protection and stabilisation of biomolecules is necessary to expand the conditions where they are stable, thus increasing the viability of their use across a range of applications. In particular, this thesis focuses on enzymes due to their vast array of promising applications, including in fine chemical synthesis, as a result of their enzymatic activity and high selectivity. The use of a

biomimetic mineralisation process allows the encapsulation of biomolecules within a protective, highly porous MOF shell, which allows excellent diffusion of substrate through to the enzymatic site. Further, the high stability of MOFs across a wide range of conditions such as heating, pH and organic solvents make them well suited to this application. However, despite significant research into the use of MOFs for biomimetic mineralisation, there are still a large number of factors that impact this process that are not well understood. One such key factor is the features of the MOFs that ensure successful biomimetic mineralisation. In addition, MOFs commonly used for this process, for example ZIF-8, have significant limitations in regard to pore size and potential toxicity.

This thesis describes research undertaken to add to current knowledge of biomimetic mineralisation by investigating different MOFs. The ability of these materials to encapsulate and protect enzymes was explored to examine whether they provide valid alternatives to ZIF-8 and related materials. Further, the mechanism by which these MOFs encapsulate biomolecules will be examined, to assess whether encapsulation occurs via biomimetic mineralisation or co-precipitation. Specifically, key focuses include the use of MOFs with biologically-derived linkers (Chapter 2), and MOFs with linkers possessing solely N-donor binding sites (Chapter 3), like the ZIF and MAF materials previously explored. Combined, these studies will provide a better understanding of enzyme encapsulation via biomimetic mineralisation.

CHAPTER 2: BioMOFs for enzyme encapsulation

2.1 Introduction and scope of the chapter

The term BioMOF refers to MOFs with biologically derived components.[66-68] For this thesis, bioMOF refers to MOFs comprised of linkers of biological origin. There have been a wide variety of different bioMOFs reported in literature, including examples where amino-acids and peptides have been used as the ligands.[69-72] Amino-acids are organic molecules with carboxylic acid and amine functional groups connected via an alpha carbon; the third group attached to the alpha carbon varies between amino-acid and, thus, modifies the chemistry. Peptides are formed by connecting amino-acids via amide bonds. There are twenty-one commonly occurring natural amino-acids, which allows for a vast library of peptides. Thus, amino-acid derived MOFs can have a wide range of chemical and physical properties. MOFs using cyclodextrin linkers (CD-MOFs) have also been extensively reported.[73] Due to the different types of cyclodextrins available; α-, β- and γ-CD, different MOF structures are able to be obtained. As such, a very wide variety of applications have been proposed for CD-MOFs including drug delivery,[74-76] removal of insecticides,[77] sensors,[78] food packaging,[79] electrical conductors[80] and photocatalysis.[81] Other sugars such as lactate have also been used as MOF linkers.[82] In particular, calcium lactate MOFs have been reported for use as agricultural fumigant encapsulants which are non-harmful due to the biocompatibility of both the linker and the metal used. Porphyrin-based MOFs have also been synthesised.[83] Porphyrins are heterocyclic macrocycle organic compounds which contains four modified pyrrole groups connected via alpha carbons. One particular porphyrin based MOF, PCN-221,[83] was used for drug delivery due to the high potential drug loading and high biocompatibility. The Rosi group has also shown that nucleobases, specifically adenine, can be used to form clusters with zinc, which were subsequently linked by an organic linker to form an extended porous and crystalline structure.[84]

Given this extremely diverse range of applications for bioMOFs, work presented herein examines their effectiveness for encapsulating biomolecules. It was proposed that the biological origin of both the linkers used and the biomolecules to be encapsulated could increase compatibility between the framework structure and the biomolecule, while also increasing the overall biocompatibility of the material. This project direction will utilise an extensive body of research on bioMOFs.

2.1.1 Review of bioMOFs for biomolecule encapsulation

A brief survey of reported amino-acid derived MOF structures is presented below to highlight the diversity of the field and to identify desirable MOFs for protein encapsulation. Several key criteria were established for the bioMOFs to enable them to be considered for use in the biomimetic mineralisation of biomolecules. These included:

- A 2-D or 3-D connected structure with > 3.4 Å pore openings;
- Binary (or two component) MOFs;
- Chemically and thermally stable materials demonstrating permanent porosity;
- Commercially available or synthetically accessible linkers;
- Use of a non-toxic metal ion;
- Aqueous (or predominantly aqueous solvent mixtures) used for synthesis;
- Room temperature synthesis conditions

Pore apertures greater than 3.4 Å represent an advance over ZIF-8, allowing for less hindered diffusion of larger substrates and products. The use of binary MOFs is desirable for two key reasons; MOFs which are able to successfully undergo biomimetic mineralisation are typically binary MOFs and it significantly reduces the complexity of the synthesis and characterisation. In particular, the use of additional components can lead to the formation of competing phases. Permanent porosity is required to ensure substrate diffusion can occur at all times without dependence on the reaction medium. By extension, the MOF must be stable in the thermal or chemical conditions where the composite will be used. One of the key advantages of using biologically derived linkers is the potentially higher biocompatibility and so the metal used should not compromise those advantages. Aqueous and room temperature synthesis conditions are needed to ensure the MOF synthesis is compatible with biomolecule encapsulation; otherwise denaturation may occur before encapsulation within the MOF. While the majority of MOF syntheses are performed solvothermally (in solution at high temperatures) in organic solvents, variations can be made to facilitate formation in water at room temperature.

The use of a non-toxic metal ion would allow for potential applications in biological systems, for example as therapeutics. Endogenous elements such as magnesium, iron, zinc, calcium and potassium are of particular interest for use in bioMOFs to be used in biological systems as higher quantities of MOF can be used before reaching a toxic concentration.[85] In addition, each of these elements perform vital roles in biological systems, such that both the metal and ligand and/or encapsulated material can be utilised. For these reasons, bioMOFs synthesised using these

elements as the metal source are most common. Further, exogenous elements such as copper or silver could also be considered for use in bioMOFs owing to their antimicrobial and imaging activities.[85]

Numerous MOFs have been synthesised with single amino-acid,[69, 86] di- and tri-peptide linkers,[72, 87] or other ligands onto which these molecules have been appended.[88] MOFs have also been formed with a combination of both organic and biologically derived linkers (mixed-linker MOFs), yet this adds synthetic complexity.[84, 89]

A selection of permanently porous materials with high thermal and chemical stability were examined, with many not meeting key criteria mentioned above. However, a small sample of known MOFs met most or all of the aforementioned requirements. A summary of these MOFs is outlined in **Table 1** followed by a more in-depth discussion.

Table 1: *Analysis of suitability of a selection of reported amino-acid derived bioMOFs*

	Cu (Gly-L-His-Gly)	Cu (Gly-L-His-Lys)	Zn (Gly-Thr)	Zn (Gly-Ala)	Zn (β-Ala-L-His)	Zn (L-Glutamate)
Reference	[90]	[90]	[91]	[71]	[4]	[5, 70]
2-D/3-D	✓	✓	✓	✓	✓	✓
>3.4 Å pore apertures	×	×	×	✓	✓	✓
Binary MOF	✓	✓	✓	✓	✓	✓
Chemically/thermally stable	×	×	✓	✓	✓	✓
Permanent porosity	×	×	✓	✓	✓	✓
Easily accessible components	×	×	✓	✓	✓	✓
Non-toxic metal ion	✓	✓	✓	✓	✓	✓
Aqueous/room temp. synthesis	✓	✓	×	×	×	✓

Of these six amino-acid based MOFs, the two most complex and also least suitable MOFs were two copper-based MOFs using tripeptide linkers of the form Gly-L-His-X (X = Gly or Lys).[90] Both materials were synthesised in aqueous conditions at room temperature, making the synthesis suitable for use with biomolecules, and both had a similar 3-D structure with 1-D channels (**Figure 12**). However, the relative synthetic complexity and availability of the tripeptide linkers used in the MOF presented a challenge as it would limit availability for MOF synthesis. Further, both MOFs have relatively small pore apertures of 2.4 Å which would hinder substrate diffusion. Thus, these issues deem the MOFs to be unsuitable.

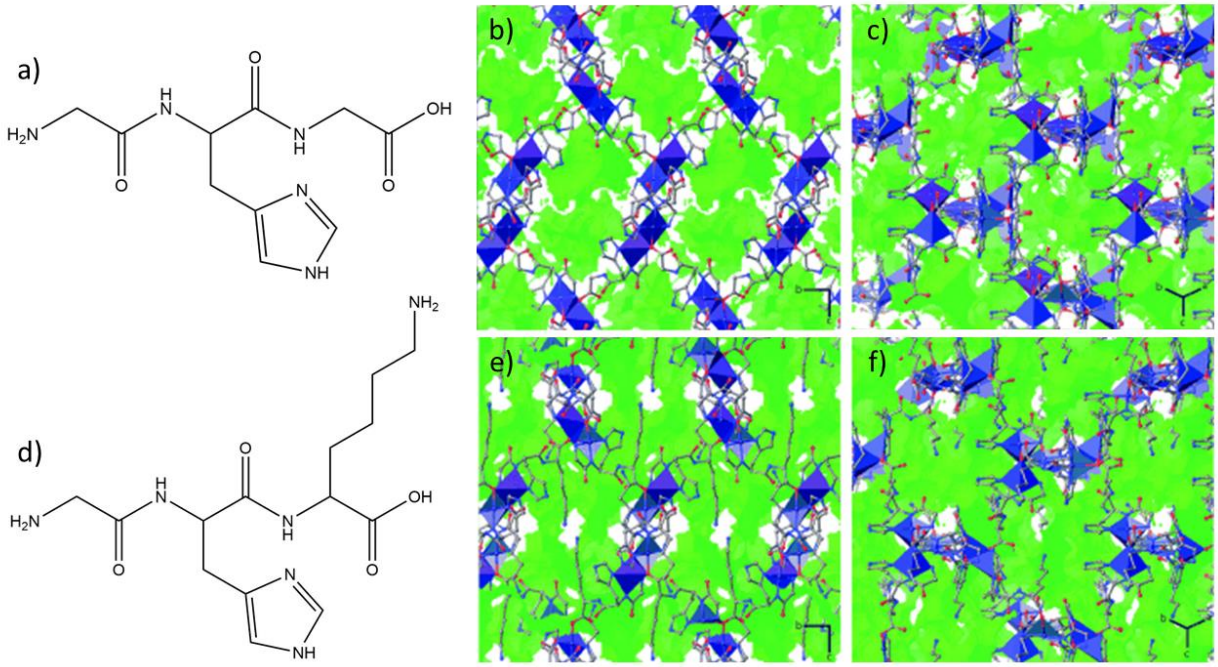

Figure 12: *a) Gly-L-His-Gly ligand and Cu(Gly-L-His-Gly) MOF single crystal structures viewed along the b) [100] and c) [111] directions. d) Gly-L-His-Lys ligand and Cu(Gly-L-His-Lys) MOF viewed along the e) [100] and f) [111] directions.*[90]

To reduce synthetic complexity, bioMOFs containing di-peptide linkers were subsequently investigated. All of the suitable dipeptide MOFs found contained zinc metal nodes, likely to due to its biological compatibility and low toxicity.

A zinc bioMOF with a Gly-Thr dipeptide linker was reported to form in methanol as a 2-D layered framework with 2.8 Å pore apertures opening into 1-D channels (**Figure 13**).[91] This small pore size is unfavourable and therefore made this MOF unsuitable.

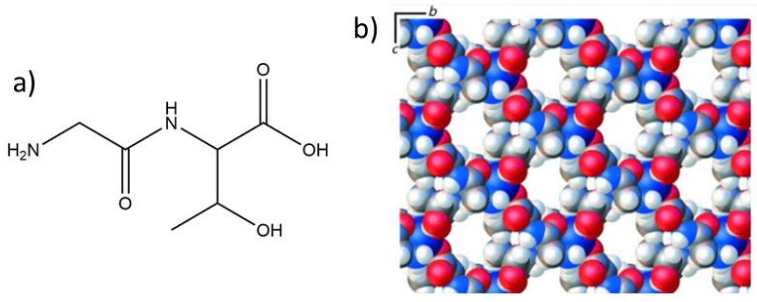

Figure 13: *a) Gly-Thr ligand and b) Zn(Gly-Thr)$_2$ MOF structure viewed along the a axis.*[91]

The threonine group can be replaced by alanine in the peptide to form a Gly-Ala dipeptide based bioMOF.[71] Unlike the Gly-Thr bioMOF, this material has a 3-D grid-like structure consisting of 1-D, square-shaped pores that were 4.8 Å at their widest dimension (**Figure 14**).While this pore

aperture size meets the criteria, the methyl groups of the dipeptide linker protrude into the pores, which would likely hinder substrate diffusion. Further, the literature synthesis conditions required extensive heating. As noted above, while such synthetic conditions could be modified, the ”hour-glass” shaped pores were undesirable and this material was not investigated.

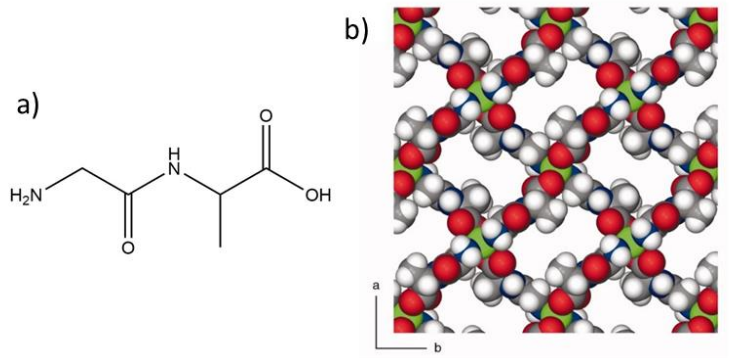

Figure 14: *a) Gly-Ala dipeptide ligand and b) Zn(Gly-Ala)$_2$ MOF structure viewed along the c axis.*[71]

One additional bioMOF comprised of dipeptide linkers was considered, namely, a zinc MOF with L-carnosine linkers (β-Ala-L-His) (**Figure 15**).[4] As a result of the imidazole functionality present in the linker, it is postulated that this may have similarities to the chemistry of ZIF-8 (although it was noted that both the amine and carboxylic acid groups are also involved in bonding). Zinc carnosine forms a 3-D framework with 1-D channels possessing *ca.* 5.2 Å pore apertures, which are larger than that of ZIF-8 (3.4 Å), making this bioMOF very promising from a substrate diffusion regard.

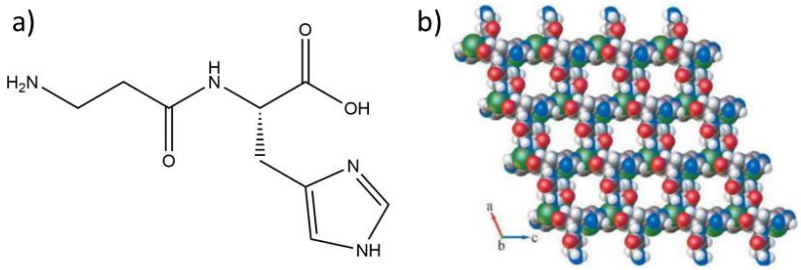

Figure 15: *a) Carnosine (β-Ala-L-His dipeptide) ligand and b) zinc carnosine MOF structure viewed along the b axis.*[4]

Zinc carnosine has also been reported to have numerous biological applications due to its low toxicity and has been approved by the therapeutic goods administration (TGA) under the name *polaprezinc* (PZ) as a commercially available drug.[92] Both zinc and carnosine are postulated to provide many benefits regarding brain health and immunity, leading to use as health supplements. There have been many published reports detailing potential clinical uses of zinc

carnosine including zinc supplementation, treatment of ulcers[93] and ulcerative colitis,[94] reducing risk of heat stroke,[95] improving gut repair processes,[96] and prevention of some neurodegenerative diseases.[97] As such, it is feasible to consider biological applications for zinc carnosine when used for biomolecule encapsulation. While the reported synthesis required the use of both organic solvents (dimethylformamide (DMF)) and extensive heating, the many promising aspects of this MOF discussed above outweigh this negative. Thus, developing a method to synthesise Zn carnosine in aqueous conditions at room temperature was deemed necessary.

MOFs with single amino-acid ligands were also investigated to further reduce synthetic complexity. A zinc-based MOF using L-glutamic acid linkers has been reported (**Figure 16**).[5, 70] As the linker is a single amino-acid, it is readily available and economically viable. The exact size of the pore apertures was not specified in the literature data, however, calculations from single crystal data suggest that the apertures would be approximately 5 by 10 Å, suggesting improved substrate diffusion compared to ZIF-8. The literature synthesis of zinc glutamate bioMOF was performed in an aqueous solution at room temperature (although with added sodium hydroxide), meaning that limited modifications were needed. Therefore, this bioMOF was also used in this project.

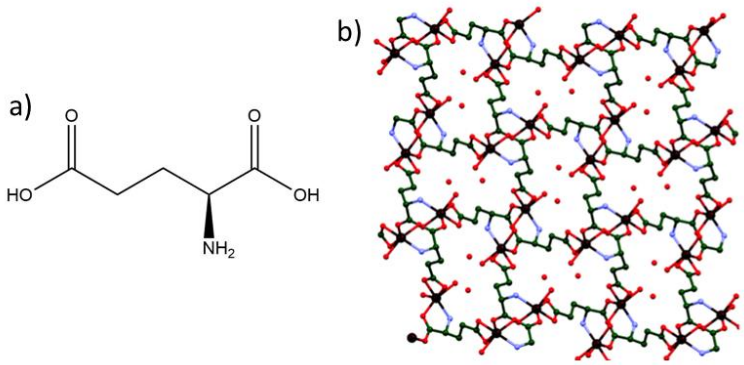

Figure 16: *a) L-Glutamic acid amino-acid ligand and b) zinc glutamate MOF structure viewed along the c axis, H atoms removed for clarity.*[5]

This chapter will outline the investigation of the two latter bioMOFs; zinc glutamate (ZnGlut) (**bioMOF-1**) and zinc carnosine (ZnCar) (**bioMOF-2**). Specifically, to investigate whether these MOFs afford protective coatings around enzymes and to determine whether these coatings form via biomimetic mineralisation.

2.2 Results and discussion

2.2.1 Zinc Glutamate (BioMOF-1)

2.2.1.1 Biocompatible synthesis and characterisation of bioMOF-1

To synthesise **bioMOF-1**, the literature conditions were initially trialled. This procedure involved direct mixing of a 1:2.5:1 molar ratio of L-glutamic acid, zinc sulphate and sodium hydroxide. To promote the formation of the correct crystalline zinc glutamate material, the metal salt and linker/base were dissolved separately in water, followed by dropwise addition of the zinc solution to the linker solution with stirring. Powder X-ray diffraction (PXRD) indicated that the precipitate formed via this method was crystalline and matched with the simulated PXRD pattern for zinc glutamate (**Figure 17**).

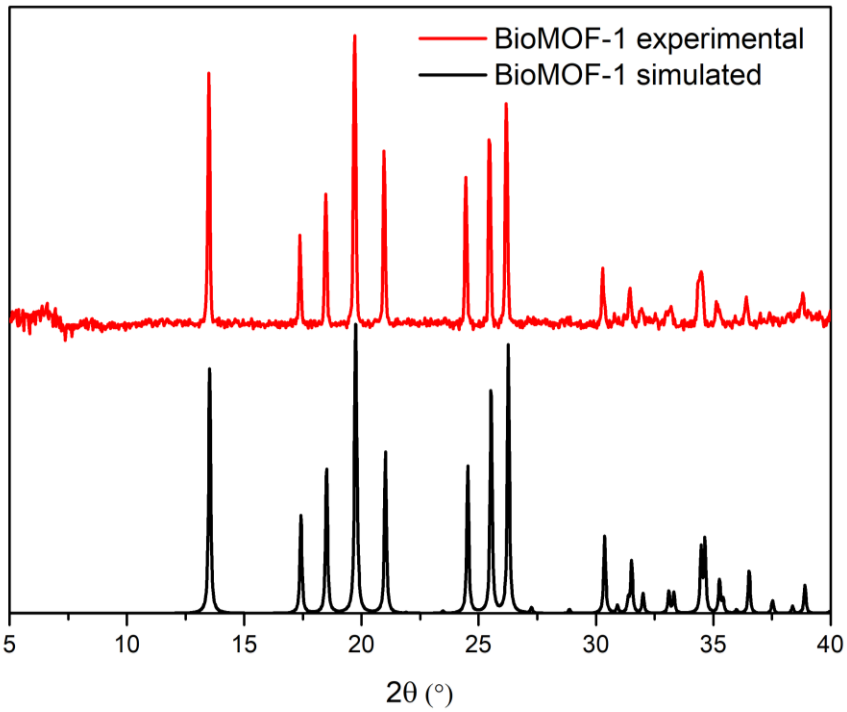

Figure 17: *PXRD pattern of synthesised* ***bioMOF-1*** *(red, baseline corrected) compared to the pattern (black) simulated from single crystal data.*

Despite the synthesis method for **bioMOF-1** being biocompatible, using these conditions caused immediate formation of the MOF upon mixing. Ideally, delayed MOF formation in the absence of enzyme is beneficial when attempting biomimetic mineralisation for two key reasons. The first reason being that if a MOF was synthesised very rapidly, the growth may be seeded independently of the protein/biomolecule via co-precipitation instead of biomimetic mineralisation. The second reason is to make detection of biomimetic mineralisation easier by

making it clearer whether the presence of enzyme led to accelerated MOF growth. More precise and quantitative measurements could then be carried using turbidity tests or *in situ* small angle X-ray scattering (SAXS) as required.

Attempts to delay the formation of **bioMOF-1** were performed by varying the type and amount of base, metal salt, and the concentration of other reagents. It was postulated that weaker bases could slow bioMOF formation, as could the use of metal salts with weaker conjugate bases. The weaker bases should give less rapid ligand deprotonation and, thus, slower MOF formation. The general method for these tests was to dissolve the ligand and base in water (5 mL), dissolve the zinc salt in water (5 mL) and add the zinc solution dropwise to the ligand solution with stirring. The conditions tested and results are summarised in **Table 15** in the appendix, with PXRD data shown in **Figure 18** and **Figure 19** for select groups of data.

The shaded conditions in **Table 15** (appendix) consistently produced the correct crystalline structure of **bioMOF-1**, as indicated by the PXRD data (**Figure 18** and **Figure 19**) and so these appeared to have the greatest potential. Within these groups, the rate of precipitation could be easily controlled through variation of the base concentration. The use of zinc nitrate was due to the longer overall delay in precipitation able to be achieved.

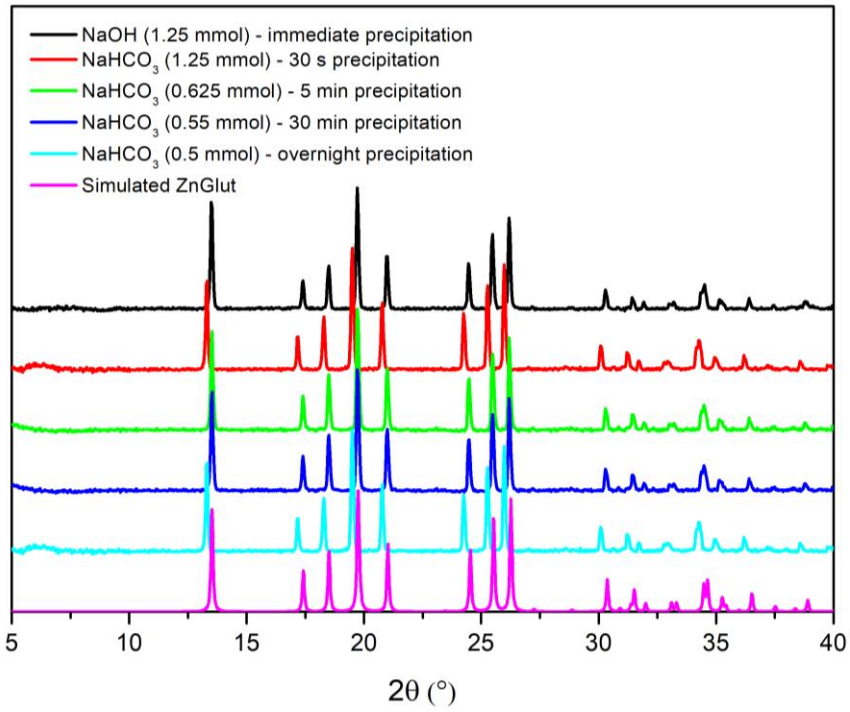

Figure 18: *PXRD data for* ***bioMOF-1*** *formed with varying amounts of base ($NaHCO_3$) using zinc nitrate hexahydrate as the metal source, compared to the simulated pattern for* ***bioMOF-1****.*

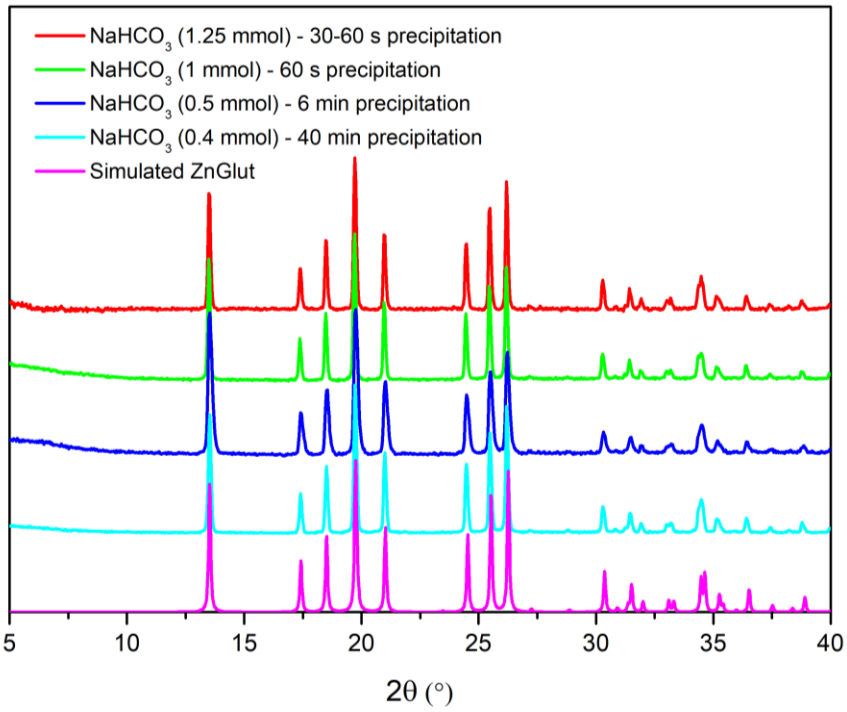

Figure 19: *PXRD data for* ***bioMOF-1*** *formed with varying amounts of base ($NaHCO_3$) using zinc acetate dihydrate as the metal source, compared to the simulated pattern for* ***bioMOF-1*** *constructed from single crystal data.*

2.2.1.2 Synthesis of protein@bioMOF-1 biocomposites

To ensure that biomolecule addition did not alter the structure of the MOF formed, MOF syntheses were conducted with a suite of proteins. The biomolecule encapsulation procedure involved the addition of enzyme into the ligand solution, followed by dropwise addition of the zinc solution. PXRD patterns for **bioMOF-1** composites formed in the presence of various proteins displayed some slight peak shifts, but overall indicated no significant structural changes (**Figure 20**). The original literature data for zinc glutamate also showed small shifts in the PXRD patterns for samples that were dried versus those treated with water.[70] Thus, the small shifts observed in the experimental PXRD patterns were likely due to slight solvation changes.

The rates of precipitation of **bioMOF-1** formed in the presence of each protein were observed and compared to **bioMOF-1** without protein (**Table 2**) to probe whether biomimetic mineralisation might be occurring.

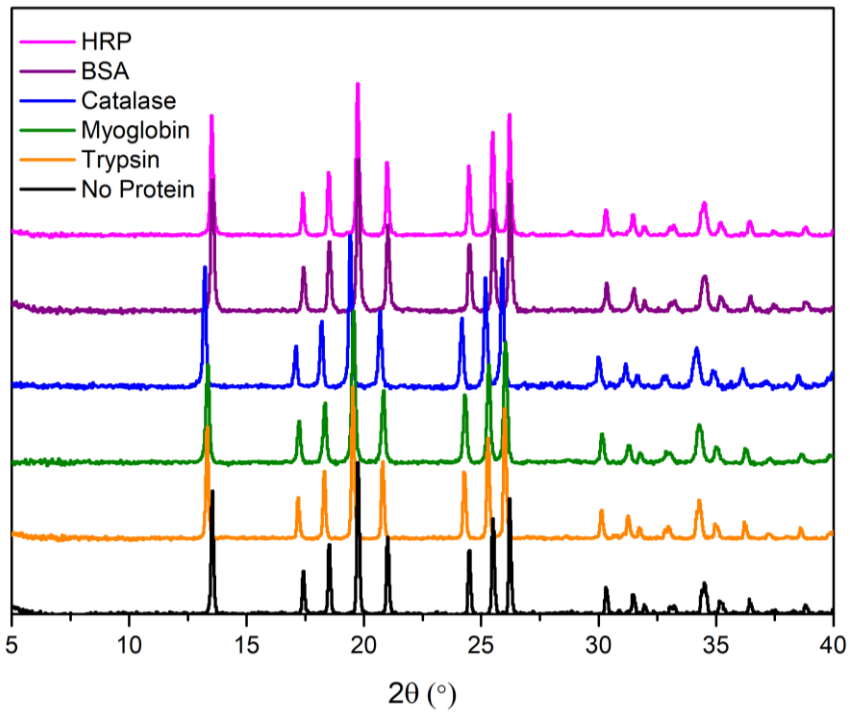

Figure 20: *PXRD for a) bioMOF-1 after addition of various enzymes during MOF synthesis compared to the simulated PXRD pattern from single crystal data.*

Table 2: *Resultant precipitation times after addition of various proteins to* ***bioMOF-1.*** *[a] coloured enzyme, [b] pI refers to the pH at which the protein carries no charge, [c] range of pIs resulting from mixture of isozymes.*

Protein (2 mg)	pI[b]	MW (kDA)	Time for Initial Precipitation
No protein	-	-	5 min
HRP[a]	3-9[c]	44	3 min
BSA	5.3	66	20-30 min
Aminated BSA	>5.3		5 min
Catalase[a]	5.4	250	5-10 min
Myoglobin[a]	7.6	17	11 min
Trypsin	10.7	23.3	4 min
Lysozyme	11, 11.3	14.4	-

The results in **Table 2** suggested that some slight acceleration of the MOF precipitation was occurring upon addition of select enzymes. For ZIF-8, it has been reported that proteins with lower pIs underwent facile biomimetic mineralisation.[61] At the pH in which ZIF-8 is synthesised the proteins with lower pIs carry greater negative charge, causing them to aggregate zinc ions and promote the formation of the MOF around the protein. However, for **bioMOF-1** there did not appear to be a relationship between pI and MOF growth rate. Amination (**Scheme 2**) of BSA was used to increase the pI of the protein to cause a reduced precipitation time compared to the unmodified enzyme, which could suggest that higher pIs may be more favourable in this system.

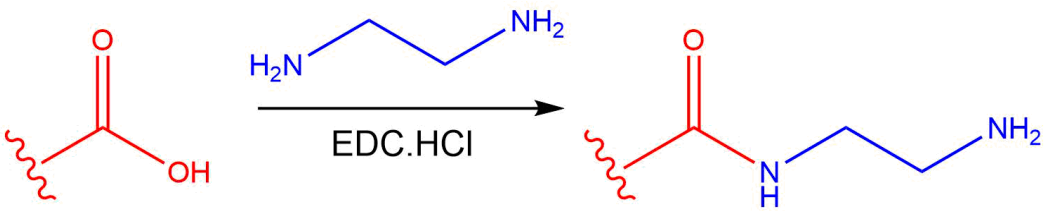

Scheme 2: *A reaction scheme showing the amination of carboxylic acid sites on a protein.*

To confirm these precipitation times with higher accuracy, turbidity testing was performed for **bioMOF-1** formed in the presence of BSA, HRP and catalase to represent proteins that either accelerated or delayed MOF formation (**Figure 21**). Turbidity testing involved collecting solution-state UV-Vis data during the precipitation event at a wavelength that was not absorbed by the material forming. Thus, increases in absorbance are due to greater interference with incident light due to precipitation. Higher absorbances are due to greater light scattering due to a larger quantity of material being formed and were not necessarily indicative of larger particle size.

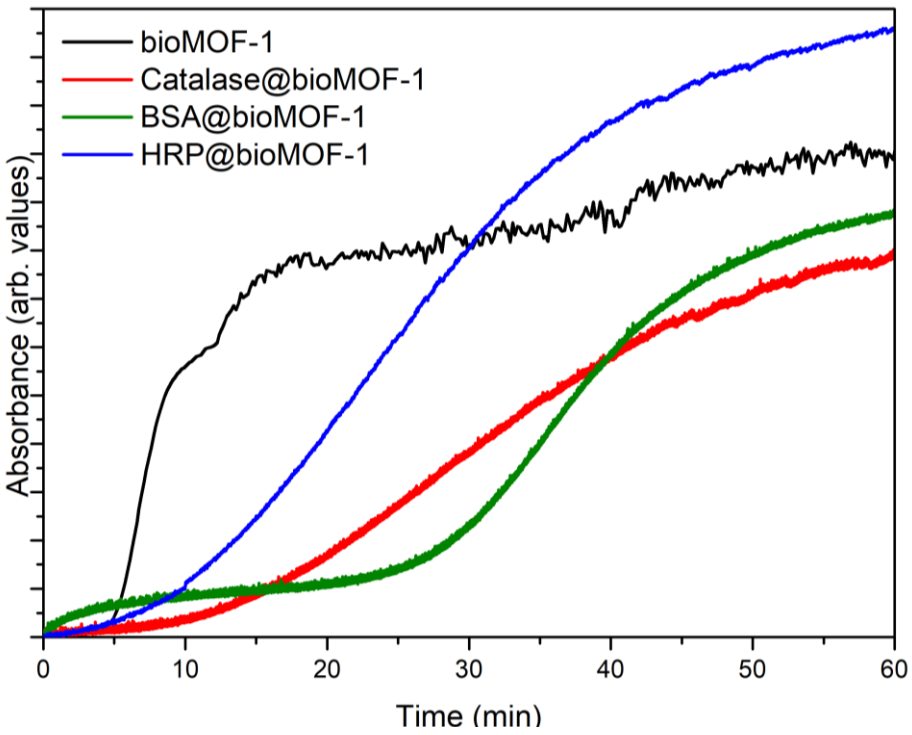

Figure 21: *Solution-state UV-Vis turbidity data for comparison of* ***bioMOF-1*** *formation without protein (black) and with protein added initially (BSA (red), HRP (blue) and catalase (green)). Time refers to the time after addition of zinc to ligand solution.*

The turbidity data confirmed the previously observed precipitation times for **bioMOF-1** formed in the presence of HRP, BSA and catalase and in the absence of enzyme. However, in the presence of each enzyme, the rate of MOF growth was reduced, as could be seen by the slower increase in absorbance once precipitation began. To further confirm this, catalase was added after

bioMOF-1 had begun to form (**Figure 22**). The addition of catalase caused the rate of MOF growth to reduce, further suggesting that the presence of proteins hindered or obstructed MOF growth.

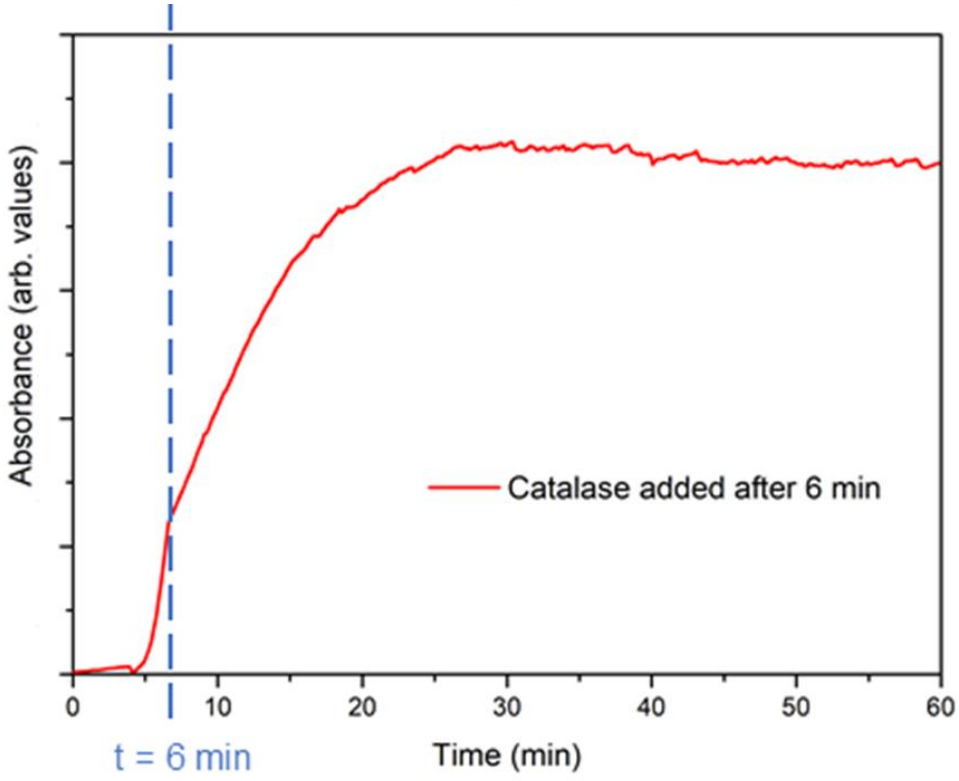

Figure 22: *Turbidity data for* ***bioMOF-1*** *with catalase added after 6 minutes. Time refers to time after addition of zinc to ligand solution.*

It was noted that the original precipitation time of **bioMOF-1** in the absence of enzyme was relatively short for the conditions tested above, being only 5 minutes. This may have been too short to show good distinction between enzymes that accelerated precipitation, and those that did not. The experiments were thus repeated with a reduced amount of base, so that **bioMOF-1** formed overnight in the absence of enzyme (**Table 3**). This was then performed in the presence of a selection of proteins, including examples that both accelerated and delayed MOF formation in the previous attempts.

Table 3: *Resultant precipitation times after addition of various proteins to* ***bioMOF-1*** *with varying amounts of* $NaHCO_3$ *added.*

Protein (2 mg)	Precipitation Time (0.0625 M $NaHCO_3$)	Precipitation Time (0.05 M $NaHCO_3$)
No protein	5 min	Overnight
HRP	3 min	2.5 hours
Trypsin	4 min	Overnight
Catalase	5-10 min	2.5 hours
Myoglobin	11 min	2.5 hours

From these results it can be seen that trends are not consistent between trials, with enzymes appearing to accelerate the formation of **bioMOF-1** in one trial, not accelerating it in the other and vice versa. As such, this implied significant discrepancies in precipitation between runs and so it is possible that there are additional factors influencing MOF formation.

To determine whether the proteins were present within the MOF composite, visual inspection was used as a preliminary test. Proteins that contain an iron-heme group within their structure, such as catalase, HRP and myoglobin, appear coloured due to the Soret bands of the heme group allowing it to absorb visible light. The colour of the **bioMOF-1** composite formed in the presence of catalase, myoglobin and HRP was noted, as was the colour of pure **bioMOF-1** and **bioMOF-**1 composites formed with non-heme containing proteins (**Table 4**).

Table 4: *Resultant product colourings after addition of various proteins to* ***bioMOF-1.*** *[a] coloured enzyme, [b] pI refers to the pH at which the protein carries no charge, [c] range of pIs resulting from mixture of isozymes.*

Protein (2 mg)	pI[b]	MW (kDA)	Colour of solid
No protein	-	-	White
HRP[a] (red)	3-9[c]	44	Off white
BSA (white)	5.3	66	White
Aminated BSA	>5.3		White
Catalase[a] (green)	5.4	250	Green
Myoglobin[a] (green)	7.6	17	Green/brown
Trypsin (white)	10.7	23.3	White

When formed in the absence of protein, **bioMOF-1** is a white powder, therefore, any colouration present in **bioMOF-1** composites formed with protein was likely to be a result of the biomolecule. In the presence of non-heme containing, non-coloured proteins, **bioMOF-1** also formed as a white powder, indicating the general presence of protein did not impact the colour of the material. **BioMOF-1** formed with heme-containing proteins consistently possessed similar colouring to the pure enzymes, indicating that enzyme was likely present in these samples.

To confirm these observations, solid-state UV-Vis spectroscopy was used to analyse samples of **bioMOF-1** synthesised in the presence of the heme-containing enzymes. Each of these enzymes exhibits a Soret peak at *ca.* 400 nm due to the heme group which was used to confirm the presence of the enzyme within the MOF samples. Solid-state UV-Vis data confirmed that pure **bioMOF-1** shows no absorbance in this wavelength region.

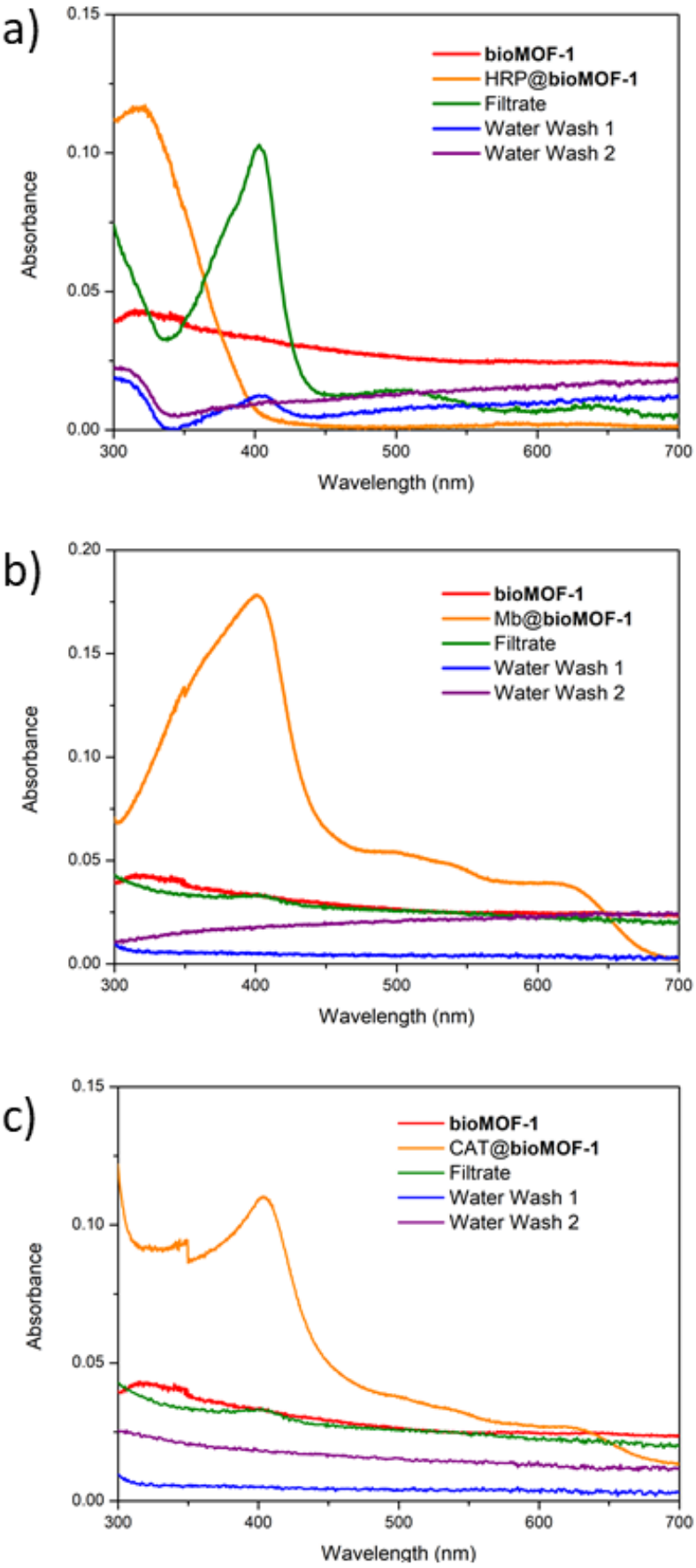

Figure 23: *Solid-state UV-Vis data for a) HRP@**bioMOF-1,** b) myoglobin@**bioMOF-1** and c) catalase@**bioMOF-1** in addition to solution-state UV-Vis data for the supernatants and water washes from the enzyme@**bioMOF-1** syntheses.*

The UV-Vis data for **bioMOF-1** formed in the presence of HRP (**Figure 23**) showed no Soret peak at 400 nm, indicating that no HRP was present within the MOF sample, or it was below the detection limit. Solution-state UV-Vis analysis was performed on the filtrate of the HRP@**bioMOF-1** synthesis which exhibited a strong Soret peak at 400 nm, as did the initial water washing solution. This indicated that the enzyme preferentially remained in solution, and any enzyme present in the solid was easily removed by washing. Conversely, for **bioMOF-1** formed in the presence of myoglobin and catalase, the UV-Vis data contained Soret peaks at 400 nm, indicating that enzyme was present in both of the MOF samples (**Figure 23b**/**c**). The UV-Vis data for neither the filtrate nor the water washes contained Soret peaks at 400 nm. This indicated that minimal concentrations of catalase and myoglobin remained in solution and that washing the samples with water was unable to remove the enzyme from the MOF.

Interestingly, previous observations indicated that both catalase and myoglobin delayed MOF growth, while HRP accelerated it. In turn, UV-Vis data showed that catalase and myoglobin were present in the enzyme@**bioMOF-1** sample, while HRP was not. This suggested that enzymes which were attracted to the MOF, hindered MOF formation, which is very different to the mechanism by which ZIF-8 biocomposites form. This strongly indicated that the precipitation of **bioMOF-1** occurred either independently of the enzyme, or as a co-precipitation event wherein the presence of protein inhibited MOF formation. Alternatively, it was possible that the protein complexed with one of the MOF components to prevent it from being involved in the MOF formation. This latter theory was supported by the understanding that the biomimetic mineralisation method for ZIF-8 involves the aggregation of zinc ions around the protein. While this is one of the key reasons for the success of ZIF-8 for biomolecule encapsulation, it may be a downfall for **bioMOF-1** if these complexes are hindering MOF formation.

2.2.1.3 Analysis of protein encapsulation/protection within bioMOF-1

Despite the previous results suggesting that it was unlikely that **bioMOF-1** forms composites via biomimetic mineralisation with the enzymes used, the ability of the MOF to protect proteins was still investigated. It was possible that **bioMOF-1** may be undergoing co-precipitation with the protein, which has been reported to lead to effective biomolecule encapsulation and protection.[6]

To provide a preliminary insight into the likelihood of protein encapsulation, confocal laser scanning microscopy (CLSM) was used. CLSM records images of fluorescent materials with high resolution. Fluorescently tagged enzymes were added to the synthesis of **bioMOF-1** to allow for confocal imaging of the resultant enzyme@MOF materials. The CLSM images gave an indication

of the location of the fluorescent enzyme in relation to the MOF crystals.[65, 98] Thus, it could be inferred whether the enzyme was likely to be encapsulated within the crystal or surface bound.

However, it must be acknowledged that this technique assumes that the fluorescently tagged enzyme behaves like the native enzyme and that the presence of the fluorescent tag did not alter the enzyme-MOF interactions. Fluorescein isothiocyanate (FITC) was chosen as the fluorescent tag to be used as it has been frequently used for biomimetic mineralisation for other MOFs.[47, 99]

For these studies, FITC-tagged catalase (FCAT) and FITC-tagged myoglobin (FMb) were used as UV-Vis data indicated that native catalase and myoglobin were both present in enzyme@**bioMOF-1** composites. CLSM images were taken for FCAT@**bioMOF-1** and FMb@**bioMOF-1** (**Figure 24**) formed using the two different syntheses that have been previously explored (pure MOF precipitation after 5 minutes or overnight due to varying base concentration). It was postulated that the crystals formed with a reduced base concentration would be larger due to the slower growth. In all cases, the precipitation times agreed with that for the native enzymes, indicating that the tagged enzymes were likely behaving comparatively.

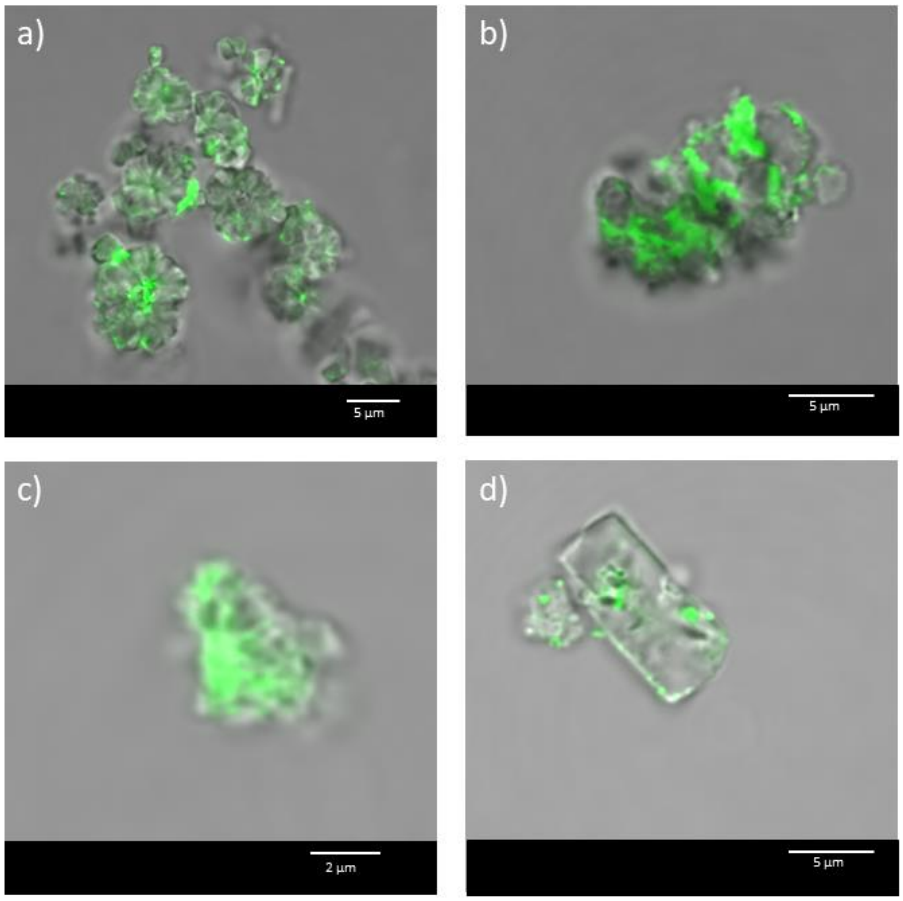

Figure 24: *Confocal images (overlay of bright field and fluorescence) for FCAT@**bioMOF-1** formed with a) 0.0625 M $NaHCO_3$ and b) 0.05 M $NaHCO_3$ and FMb@**bioMOF-1** formed with c) 0.0625 M $NaHCO_3$ and d) 0.05 M $NaHCO_3$. Tagged protein shown in green.*

The confocal images for both FCAT@**bioMOF-1** and FMb@**bioMOF-1** showed non-homogenous distribution of the enzyme across the MOF crystals. This indicated that the enzyme was most likely surface bound or at defects of the crystals, and so was unlikely to be encapsulated within the MOF. These results were not altered by the rate at which the crystals formed.

To test this hypothesis, a method of removing surface-bound enzyme was developed. This would ensure that any enzyme remaining in the MOF sample after this procedure must be encapsulated. To identify washing conditions, FITC-tagged catalase and myoglobin were adsorbed to **bioMOF-1** crystals by soaking crystals in an enzyme solution for 3 minutes, before isolation via centrifugation. This analysis was performed for FMb and FCAT. The enzyme-on-**bioMOF-1** samples were then washed with various mixtures of SDS and EDTA followed by CLSM analysis (**Table 16**). If any fluorescence remained after the washing procedure it was deemed to be unsuccessful.

One notable observation was the similarity in appearance for the enzyme@**bioMOF-1** (**Figure 24**) and enzyme-on-**bioMOF-1** (**Table 16**) crystalline composites for both FCAT and FMb prior to washing, suggesting that the enzyme was predominantly surface-adsorbed in the former.

In regard to the success of the washing procedures for surface-bound FMb, the only washing procedure that appeared to remove all protein was a 1:1 mixture of 10% SDS and 10% EDTA. However, it was extremely difficult to find crystals within the confocal sample which indicated that a significant proportion of the sample has dissolved. Thus, no washing procedure was found to be effective for removing surface-bound myoglobin without decomposing the MOF, and no further analysis was performed with myoglobin@**bioMOF-1**.

Surface-bound FCAT was removed with a 1:1 mixture of 10% SDS and 1% EDTA solutions. This difference between the behaviour of FCAT and FMb may have been due to the different pI of the enzymes, which would in turn cause differences in the overall surface charge and, thus, interactions with the MOF. Alternatively, it may be due to the significantly smaller size of Mb compared to catalase, which might have allowed it to get closer to the MOF or fit into defects on the crystal surface thereby conferring stronger binding or protection from the washing solutions. It was noted that while the aqueous 1:1 mixture of 10% SDS and 1% EDTA was effective at removing FCAT from the surface of the crystal, there were still signs of tagged enzyme left in solution in the confocal images. Hence, further water washes were performed to ensure this was removed effectively. It was also noted that the washing solutions may have slightly different effects on untagged proteins compared to those with FITC groups.

CAT@**bioMOF-1** was washed with a 1:1 mixture of 10% SDS and 1% EDTA to indicate what proportion of the enzyme was encapsulated within the MOF (**Figure 82** in the appendix), However, as a result of errors present in solid-state UV-Vis spectroscopy, this data was deemed to be unreliable.

Instead, CLSM was performed on a sample of FCAT@**bioMOF-1** before and after washing with the 1:1 mixture of 10% SDS and 1% EDTA (**Figure 25**).

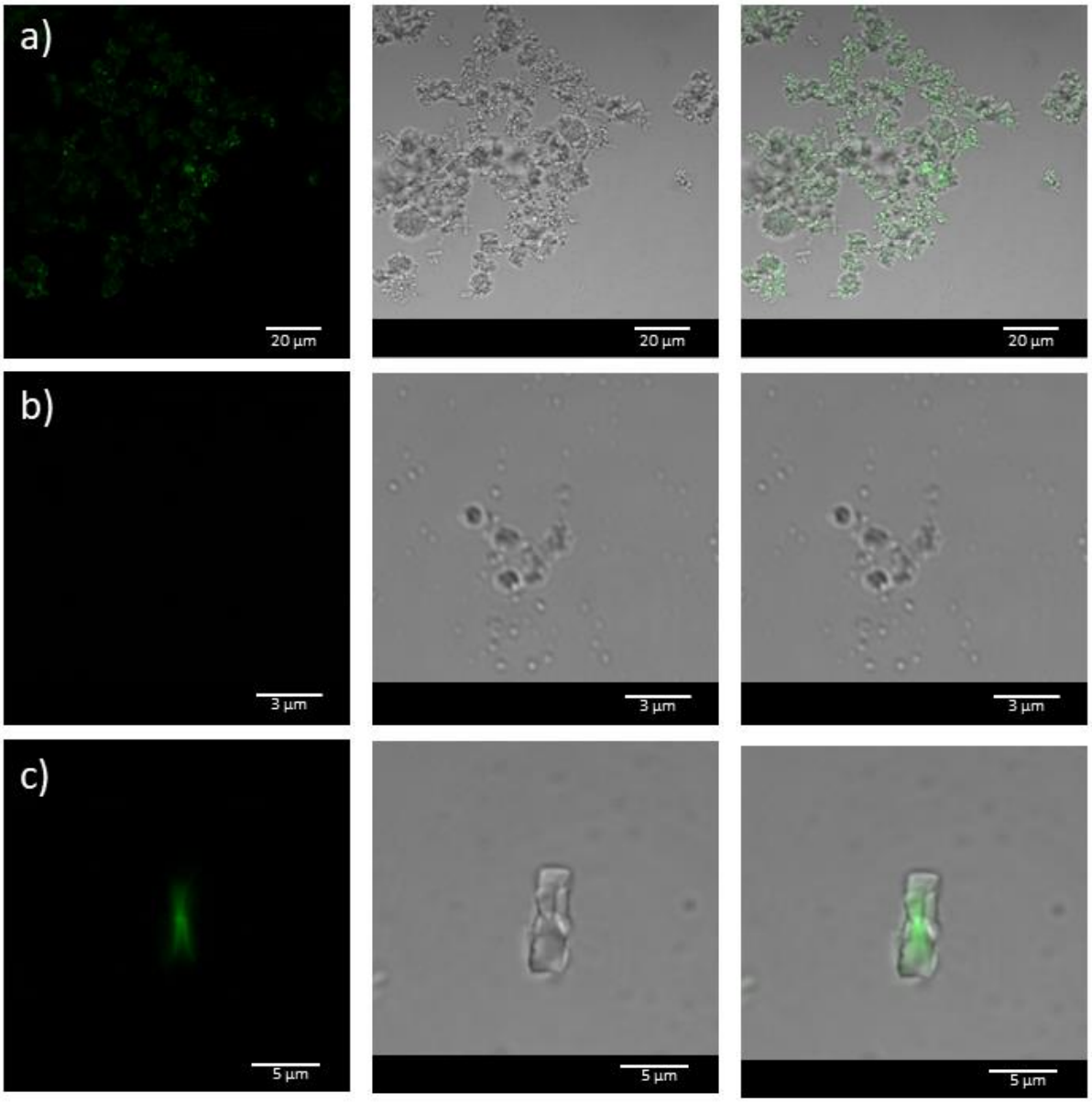

Figure 25: *CLSM images (fluorescence, bright field and overlay) of FCAT@**bioMOF-1** a) before and b/c) after washing with a 1:1 mixture of 10% SDS and 1% EDTA (x3). Tagged enzyme is shown in green.*

As seen in previous CLSM images of FCAT@**bioMOF-1**, there was a clear presence of fluorescent enzyme which was co-located with the crystals (**Figure 25a**). However, upon washing with the 1:1 mixture of 10% SDS and 1% EDTA the fluorescent enzyme was either removed completely (**Figure 25b**) or was reduced in quantity (**Figure 25c**). This further suggested that a large proportion of enzyme present in the **bioMOF-1** samples was surface bound. It also justified why there was still a Soret peak at 400 nm in the solid-state UV-Vis data for FCAT@**bioMOF-1** after washing with the 1:1 10% SDS and 1% EDTA mixture (see appendix data **Figure 82**).

To quantify the total enzyme removal, solution-state fluorescence data was collected for FCAT@**bioMOF-1** before and after washing with the 1:1 mixture of 10% SDS and 1% EDTA. This analysis was performed by dissolving the washed and unwashed samples in 10% EDTA (any remaining solid was removed via centrifugation) and the supernatant was analysed by fluorescence spectroscopy. This fluorescence intensity was then converted to an FCAT concentration using a calibration curve (**Figure 88** in the appendix). The fluorescence data for FCAT@**bioMOF-1** before and after the washing procedure (**Table 5**) revealed that there was more than a 70% reduction in FCAT concentration upon removing surface-bound enzyme, further indicating that the enzyme was predominantly surface bound.

Table 5: *Fluorescence data and FCAT concentration calculations for FCAT@ZnGlut before and after washing with a 1:1 mixture of 10% SDS and 1% EDTA*

	Fluorescence Intensity (518 nm)	Calculated FCAT Concentration (nM)	Volume (mL)	FCAT present (mol)	Mass Sample (mg)	**FCAT in sample (mol/g)**
FCAT@ZnGlut (No Wash)	344.61	404.78	1.0	0.40	4.1	**24.2 (100%)**
FCAT@ZnGLUT (1:1 10% SDS 1% EDTA Wash)	40.68	29.43	1.0	0.029	16.7	**7.18 (29.6%)**

Due to these combined observations, no further work was carried out for any enzyme@**bioMOF-1** material due to the inability to consistently encapsulate the enzyme within the MOF crystals. Furthermore, it was noted that any encapsulation was not likely to be occurring via the biomimetic mineralisation mechanism and therefore may not afford the protections needed.

2.2.2 Zinc Carnosine (BioMOF-2)

2.2.2.1 Biocompatible synthesis and characterisation of bioMOF-2

The second bioMOF of interest, zinc carnosine (**bioMOF-2**), was also initially synthesised via the literature conditions wherein a solution of L-Carnosine (0.03 M) and zinc nitrate hexahydrate (0.06 M) in water and DMF was heated overnight at 100°C.[4] The only deviation from the literature synthesis was that temperature ramping was not used, primarily because large crystals were not needed. PXRD data for the synthesised MOF crystals matched the PXRD pattern simulated from single crystal data for zinc carnosine (**Figure 26**). It was noted that there were discrepancies in relative peak intensities, however, this was attributed to preferred orientation effects.

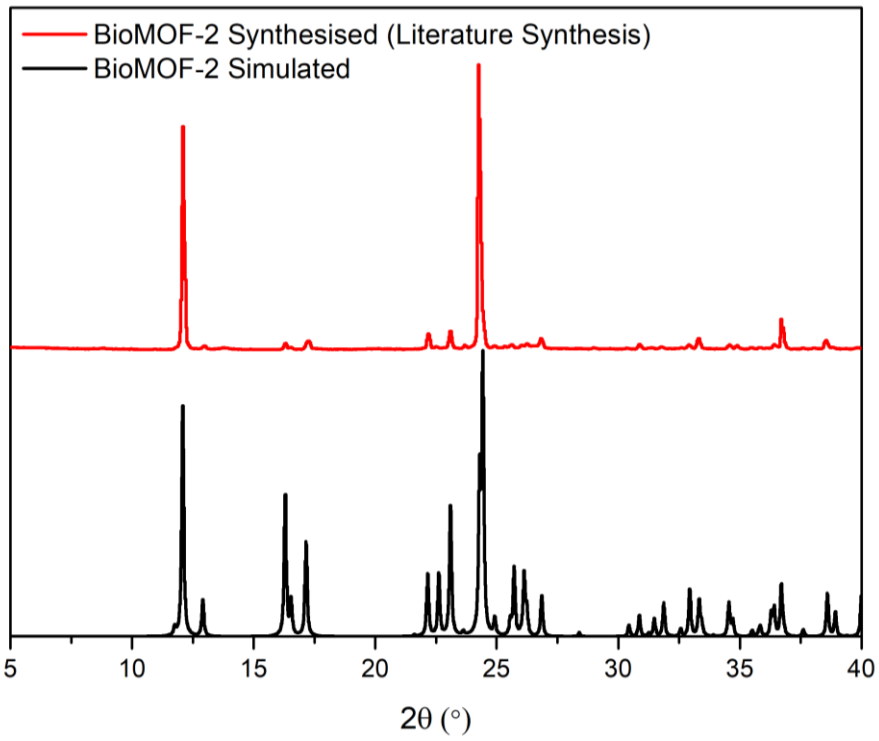

Figure 26: *PXRD data for experimental* ***bioMOF-2*** *(red) compared to simulated pattern (black) constructed from single crystal data.*

As the reported synthesis for **bioMOF-2** required the use of both organic solvents (DMF) and extensive heating, which are incompatible with protein protection, the procedure was altered to ensure the MOF could be synthesised in the presence of biomolecules.

Specifically, a procedure needed to be designed using only aqueous, or predominantly aqueous, conditions at room temperature and near biological pH. Initial attempts to do this were based around the method used for the synthesis of **bioMOF-1**. This involved addition of base, replacing solvents with water and removal of heating. The attempted conditions are shown in **Table 6**. The

general procedure for these trials was to dissolve the linker and base in water (5 mL) and dissolve the zinc salt in water (5 mL) separately, followed by dropwise addition of the zinc solution to the ligand solution.

Table 6: *Synthetic conditions in purely aqueous solutions attempted for* ***bioMOF-2.*** *All trials were performed in water (10 mL).*

Carnosine (mmol)	Base (mmol)	Zn Salt (mmol)	Time taken for initial precipitation	Washing procedure	PXRD
0.442 mmol	$NaHCO_3$ (0.625 mmol)	$Zn(NO_3)_2{\cdot}6H_2O$ (0.88 mmol)	immediate	water	Amorphous
	NaOH (0.625 mmol)	$Zn(NO_3)_2{\cdot}6H_2O$ (0.88 mmol)	immediate	water	Amorphous
	No base	$Zn(NO_3)_2{\cdot}6H_2O$ (0.88 mmol)	No precipitate overnight	N/A	N/A
	$NaHCO_3$ (0.625 mmol)	$Zn(NO_3)_2{\cdot}6H_2O$ (0.88 mmol)	immediate	methanol	Amorphous
0.221 mmol	$NaHCO_3$ (0.3125 mmol)	Zn Acetate$\cdot 2H_2O$ (0.44 mmol)	5 seconds	water	Amorphous
	$NaHCO_3$ (0.156 mmol)	Zn Acetate$\cdot 2H_2O$ (0.44 mmol)	60 seconds	water	Amorphous
	$NaHCO_3$ (0.078 mmol)	Zn Acetate$\cdot 2H_2O$ (0.44 mmol)	40 min	water	Amorphous
	NaOH (0.3125 mmol)	Zn Acetate$\cdot 2H_2O$ (0.44 mmol)	5 seconds	water	Amorphous
0.5 mmol	$NaHCO_3$ (0.625 mmol)	$ZnSO_4{\cdot}7H_2O$ (0.5 mmol)	30 seconds	water	Amorphous
	No base	$ZnSO_4{\cdot}7H_2O$ (0.5 mmol)	40 min	water	Amorphous

However, PXRD data indicated that all materials formed were amorphous and so, unlike **bioMOF-1**, **bioMOF-2** could not be formed in aqueous conditions purely by the addition of base. From the literature synthesis of zinc carnosine, it was noted that a methanol wash was used prior to isolation of the material. Further, for the ZIF-8 synthesis under biomimetic mineralisation conditions, alcohol washes are also performed.[2, 61, 100] Thus, additions of, and/or washes with varying volumes of either methanol or ethanol during the synthesis of **bioMOF-2** were attempted (**Table 7**). These attempts were conducted with the same general method as above, with all solvents other than water added to the ligand solution prior to the addition of zinc.

Table 7: *Synthetic conditions from* ***bioMOF-2*** *with added alcohol. All contained 0.22 mmol L-Carnosine and 0.44 mmol* $Zn(NO_3)_2 \cdot 6H_2O$.

Condition to be investigated	Base (mmol)	Solvents used (mL)		Time taken for initial precipitation	PXRD (Figure 27)
Effect of MeOH during synthesis	$NaHCO_3$ (0.3125 mmol)	H_2O (10 mL) MeOH (5 mL)	(2:1)	immediate	Amorphous
	$NaHCO_3$ (0.3125 mmol)	H_2O (10 mL) MeOH WASH		immediate	Amorphous
	No base	H_2O (10 mL) MeOH WASH		No precipitate formed overnight	N/A
Use of EtOH in synthesis; amount of base (2:1 H_2O : EtOH)	$NaHCO_3$ (0.3125 mmol)	H_2O (10 mL) EtOH (5 mL)	(2:1)	immediate	ZnCar
	$NaHCO_3$ (0.1560 mmol)	H_2O (10 mL) EtOH (5 mL)	(2:1)	Immediate	ZnCar
	$NaHCO_3$ (0.0786 mmol)	H_2O (10 mL) EtOH (5 mL)	(2:1)	Immediate	ZnCar
	No base	H_2O (10 mL) EtOH (5 mL)	(2:1)	35 min	ZnCar
Use of EtOH is synthesis; amount of base (9:1 H_2O : EtOH)	$NaHCO_3$ (0.0786 mmol)	H_2O (9 mL) EtOH (1 mL)	(9:1)	10 seconds	ZnCar
	No base	H_2O (9 mL) EtOH (1 mL)	(9:1)	overnight	ZnCar
Use of an EtOH wash; amount of base	$NaHCO_3$ (0.0786 mmol)	H_2O (10 mL) EtOH WASH		5 min	Amorphous
	No base	H_2O (10 mL) EtOH WASH		No precipitate formed overnight	N/A

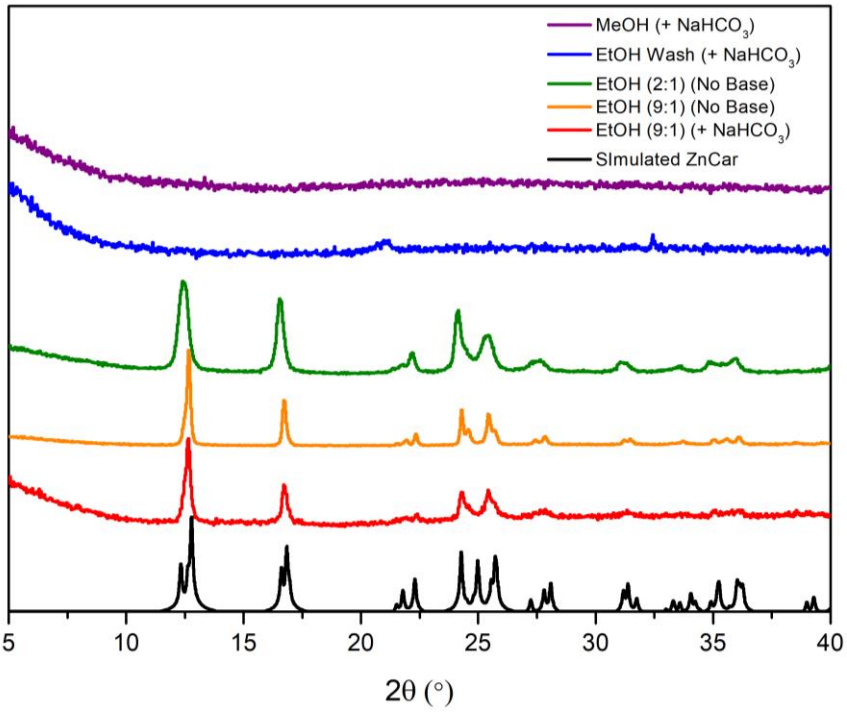

Figure 27: *PXRD data for* ***bioMOF-2*** *formed with 2:1* H_2O *: MeOH +* $NaHCO_3$ *(purple), pure water +* $NaHCO_3$ *with an EtOH wash (blue), 2:1* H_2O *: EtOH with no base (green), 9:1* H_2O *: EtOH with no base (orange) and with* $NaHCO_3$ *(red) compared to the pattern of* ***bioMOF-2*** *simulated from the single crystal data.*

Despite the original literature synthesis of zinc carnosine using methanol to wash the solid obtained from the reaction, the addition of methanol to the synthesis of **bioMOF-2** did not yield the desired crystalline product. Further, washing the amorphous product with methanol did not form the crystalline product.

However, the addition of ethanol promoted the formation of crystalline **bioMOF-2**, with higher ethanol concentrations promoting more rapid MOF growth, such that no base was needed, unlike for **bioMOF-1** formation which required base. It was also confirmed that purely washing the final product with ethanol was not sufficient to convert the amorphous precipitate into crystalline **bioMOF-2**, indicating that the ethanol needed to be present during the synthesis. PXRD data also indicated that lower concentrations of ethanol formed more crystalline material (**Figure 27**), possibly due to slower precipitation. This is supported by the comparison between **bioMOF-2** samples formed with or without the addition of sodium bicarbonate; with base present the material forms much more quickly and is consequently less crystalline.

Time lapse photos were taken of **bioMOF-2** formed using 0.005 M and 0 M $NaHCO_3$ in 2:1 mixture of water to ethanol to show the rate and quantity of precipitate formed over time (**Figure 28**).

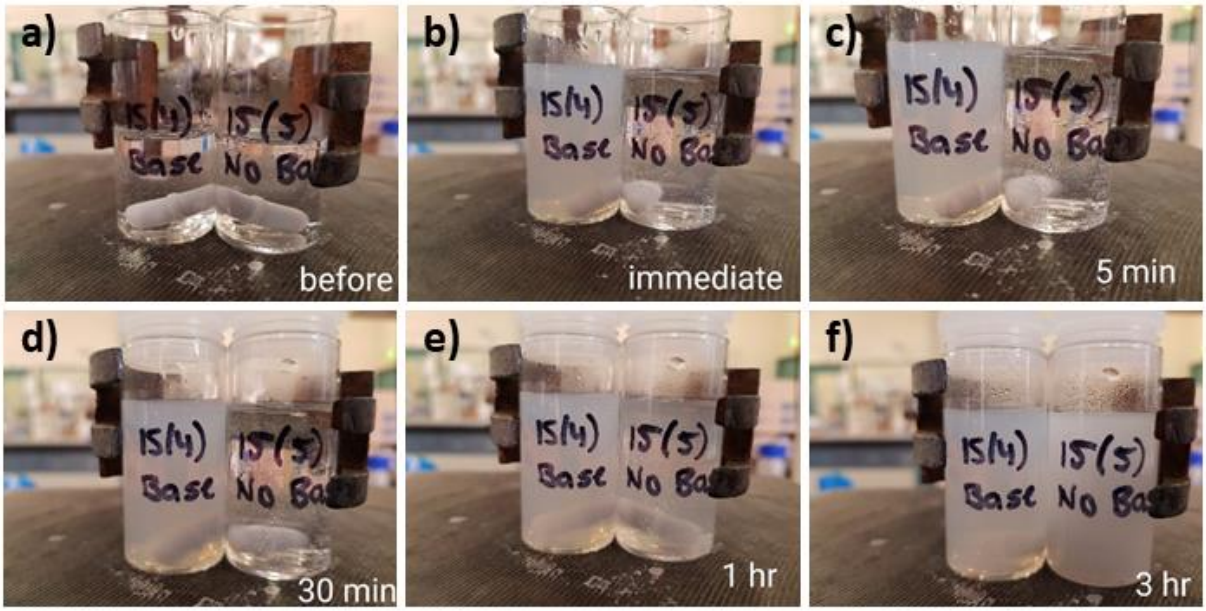

Figure 28: *Time-lapse photos of* ***bioMOF-2*** *formed in the presence of base (15(4)) and no base (15(5)) in a 2:1 water to ethanol solution a) before addition of zinc solution and b) immediately, c) 5 minutes, d) 30 minutes, e) 1 hour and f) 3 hours after addition of zinc to ligand solution.*

To ensure the material studied was highly crystalline, all further work with **bioMOF-2** utilised the synthesis in a 9:1 water and ethanol mixture with no added base. This synthesis also afforded the

longest delay in precipitation time, making it well suited to biomimetic mineralisation for reasons mentioned previously. Further, the reduced concentration of ethanol increased the biocompatibility of the MOF synthesis.

To characterise the morphology of **bioMOF-2** crystals, scanning electron microscopy (SEM) was utilised (**Figure 29**). The SEM images showed that **bioMOF-2** formed as homogenous plate-like crystals (≈ 1 µm), with sharp edges indicating high crystallinity. As is shown in **Figure 29d**, aggregates also formed, however, as no compositional information was obtained, no comment can be made on their origin.

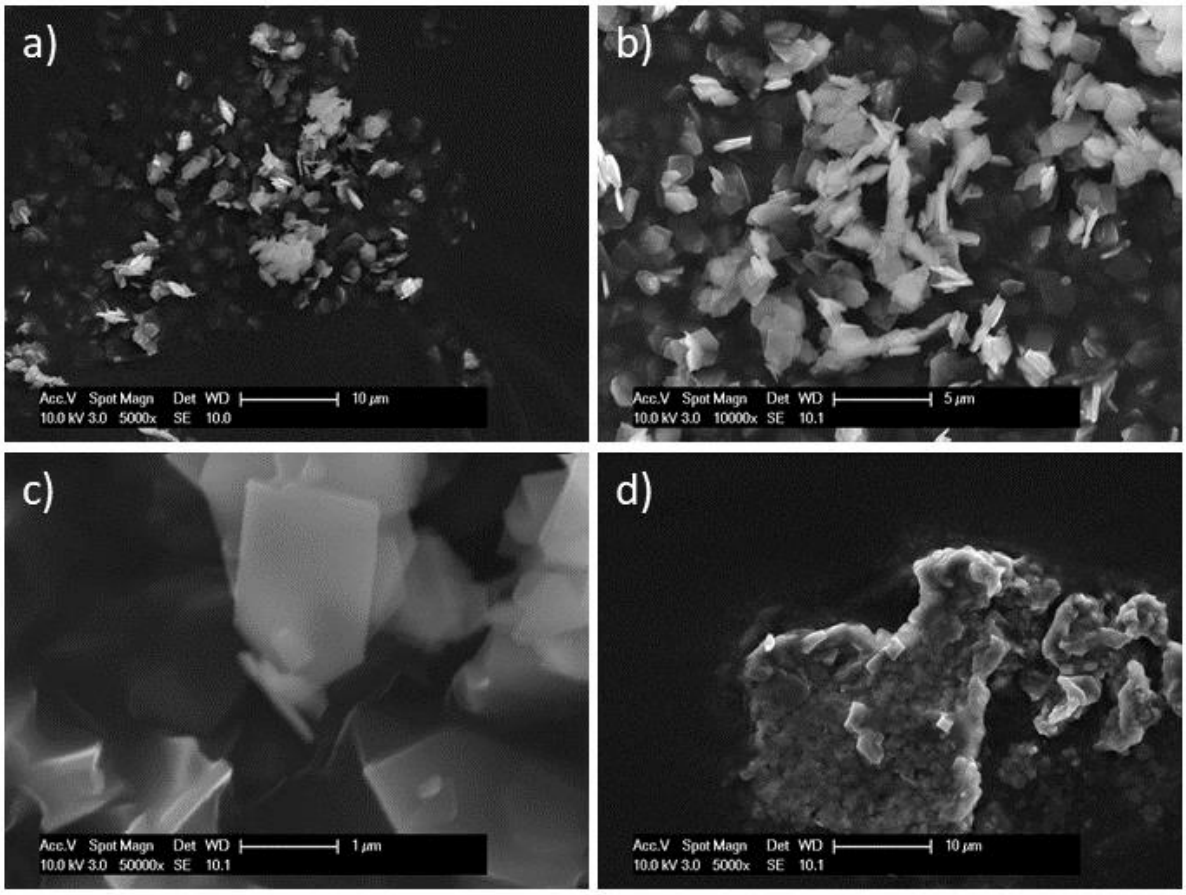

Figure 29: *SEM images for bioMOF-2 crystals at a) 5,000 x, b) 10,000 and c) 50,000 x magnification, and d) an unknown aggregate at 5,000 x magnification.*

The thermal and chemical stability of **bioMOF-2** was analysed to understand which environments the MOF could tolerate which, unlike for **bioMOF-1**, had not been reported extensively in literature.

To test the stability of **bioMOF-2** across a range of acidic and basic pHs (**Table 17** in the appendix), the MOF was stirred in a solution of known pH for 1 hour, after which time the solid was isolated

by centrifugation and dried. PXRD analysis (**Figure 83** in the appendix) revealed that **bioMOF-2** was stable over a pH range of 3 to 9, with good stability in mildly acidic conditions.

This pH stability contrasts with other MOFs that have been used for biomolecule encapsulation, including ZIFs and MAF-7. To provide some context, the pH stability range for **bioMOF-2** was compared to a range of other MOFs (**Table 8**).

Table 8: *Comparison of pH stability ranges for* ***bioMOF-2*** *to a variety of other MOFs.*

MOF	Linking groups	Metal	pH stability range
BioMOF-2	-COOH -NH_3 -NH (imidazole)	Zn	3-9
ZIF-8[101]	-NH (imidazole)	Zn	5-12
ZIF-90[102]	-NH (imidazole)	Zn	>6
MAF-7[65]	-NH (triazole)	Zn	>5
UiO-66[103]	-COOH	Zr	1-7
NU-1000[103]	-COOH	Zr	1-11
MOF-808[103]	-COOH	Zr	1-7
MOF-545[103]	-COOH	Zr	<0-7

From this small sample of MOFs, those containing carboxylate binding sites were generally more stable in acidic conditions, while those containing solely N-donor sites are stable at higher pHs. Thus, as **bioMOF-2** contains both of these binding sites, it is sensible that the stability range included a moderate range of both acidic and basic pHs.

To test the thermal and chemical stability of **bioMOF-2**, MOF samples were placed in either water or DMF and exposed to elevated temperatures for one hour (**Table 9**). In all cases, PXRD data revealed no decomposition (**Figure 83** in the appendix), showing that **bioMOF-2** possessed very high thermal stability and excellent chemical stability.

Table 9: *Thermal and DMF stability tests for* ***bioMOF-2.***

Solvent	Temperature	After 1 hour	PXRD	Conclusion
Water	r.t.	No decomposition	Correct	Stable
	50°C			
	80°C			
	120°C			
	Heat gun (10 s)			
DMF	r.t.			
	Heat gun (30 s)			

2.2.2.2 Synthesis of protein@bioMOF-2 biocomposites

To add protein to **bioMOF-2** for attempted encapsulation, the enzyme was added to the ligand solution, followed by dropwise addition of the aqueous zinc solution. As both **bioMOF-2** and ZIF-8 contain imidazole groups, the proteins chosen for **bioMOF-2** included ones that underwent successful biomimetic mineralisation with ZIF-8, as well as ones that did not.[61] Namely, BSA, catalase and HRP underwent biomimetic mineralisation with ZIF-8, whereas myoglobin, trypsin and lysozyme did not.

To ensure that the addition of enzyme did not alter the structure of the MOF, PXRD data for protein@**bioMOF-2** composites were collected. PXRD analysis of **bioMOF-2** formed with protein showed no peak shifts or changes in relative peak intensities compared to the pure **bioMOF-2,** indicating that no significant structural changes occurred upon enzyme inclusion in the reaction mixture (**Figure 30**).

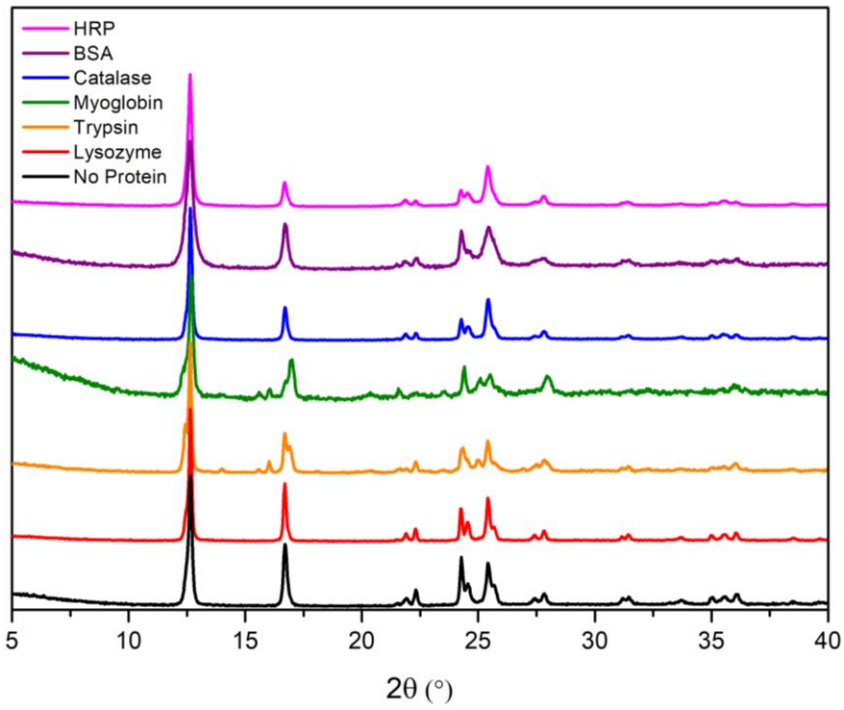

Figure 30: *PXRD for bioMOF-2 after addition of various enzymes during MOF synthesis compared to pure bioMOF-2.*

To determine whether the addition of protein impacted crystal morphology, SEM images of pure **bioMOF-2** and catalase@**bioMOF-2** were compared (**Figure 31**).

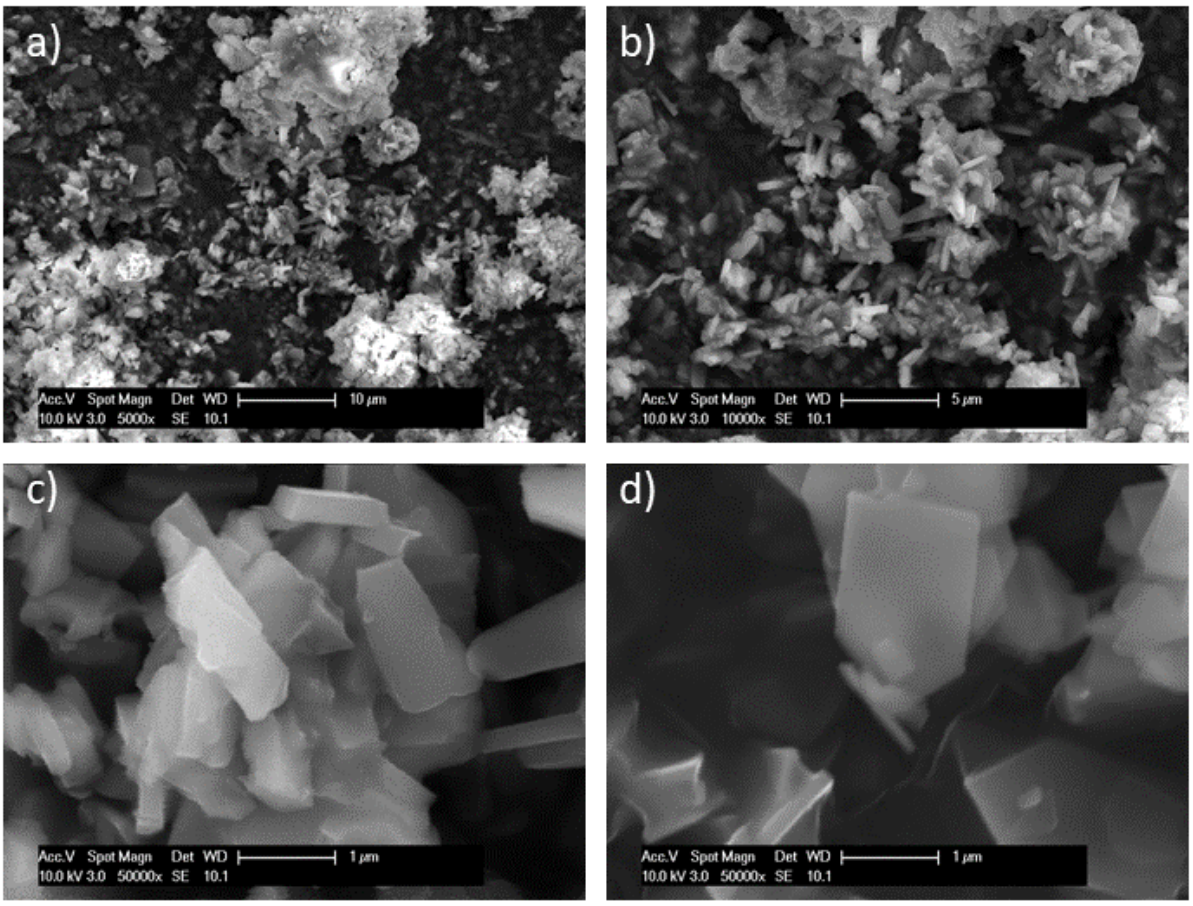

Figure 31: *Comparison of SEM images of catalase@bioMOF-2 (a-c) and bioMOF-2 (d) at 5,000 x, 10,000 x, and 50,000 x magnification.*

The crystals of CAT@**bioMOF-2** have very sharp and well-defined faces and edges, explaining the high crystallinity observed in the PXRD pattern. Further, there are some larger aggregates of unknown origin in the CAT@**bioMOF-2** sample (**Figure 31a**) which look similar to the aggregates seen for pure **bioMOF-2** (**Figure 29**). Interestingly the SEM images show that CAT@**bioMOF-2** forms as block-shaped crystals, compared to pure **bioMOF-2** which formed as plate-like crystals, of similar size. The exact reasoning is difficult to confirm, it may have been due to encapsulated enzymes promoting the formation of a different crystal morphology or the enzyme may promote aggregation of the plate-shaped crystals. Nevertheless, the SEM data indicated that the presence of enzyme impacted the crystal growth of **bioMOF-2** composites.

To determine whether biomimetic mineralisation was occurring for **bioMOF-2** biocomposite formation, the precipitation rates of the MOF with and without added enzyme were compared (**Table 10**). As previously mentioned, a key indicator of biomimetic mineralisation is accelerated MOF growth in the presence of enzyme.

Table 10: *Resultant precipitation times after addition of various proteins to* ***bioMOF-2.*** *[a] coloured enzyme, [b] pI refers to the pH at which the protein carries no charge, [c] range of pIs resulting from mixture of isozymes.*

Protein (2 mg)	pI[b]	MW (kDA)	Time for Initial Precipitation
No protein	-	-	Overnight
HRP[a]	3-9[c]	44	Immediate
BSA	5.3	66	5-10 seconds
Catalase[a]	5.4	250	Immediate
Myoglobin[a]	7.6	17	2 hours
Trypsin	10.7	23.3	3 days
Lysozyme	11, 11.3	14.4	2.5 hours

The precipitation times showed that significant acceleration of the MOF precipitation occurred upon addition of lower pI proteins, suggesting that both **bioMOF-2** and ZIF-8 follow similar trends wherein proteins of lower pI accelerate MOF formation. MOF precipitation was also accelerated, to a lesser degree, by higher pI proteins (myoglobin, lyzozyme), suggesting that pI was not necessarily the only factor governing biocomposite formation for **bioMOF-2**.

While the precipitation times recorded in **Table 10** are representative of the time taken for the initial precipitate to begin to form, it was also noted that the precipitation occurred very slowly, such that samples were collected after stirring overnight. This suggested that MOF growth occurred gradually as opposed to an instantaneous precipitation event.

To confirm the accuracy of these precipitation times and to determine whether MOF growth occurred gradually, turbidity testing was subsequently performed for the formation of **bioMOF-2** in the presence of select enzymes (**Figure 32**). BSA, HRP and catalase were chosen to represent the enzymes that rapidly increased the precipitation time, while myoglobin represented those that only slightly accelerated **bioMOF-2** formation.

For **bioMOF-2** formed in the presence of myoglobin, previous observations suggested that precipitation did not begin until 2.5 hours after combining the ligand and zinc solutions. Yet, turbidity data showed that precipitation commenced immediately after adding zinc to the ligand and myoglobin solution, but at a very slow rate ceasing after approximately 75 minutes. Thus, there are slight variations in the precipitation times between repeats of the experiment; however, the turbidity data still supported the general trend in observed precipitation times wherein select proteins significantly accelerate MOF formation (within seconds), while others accelerate it to a lesser extent.

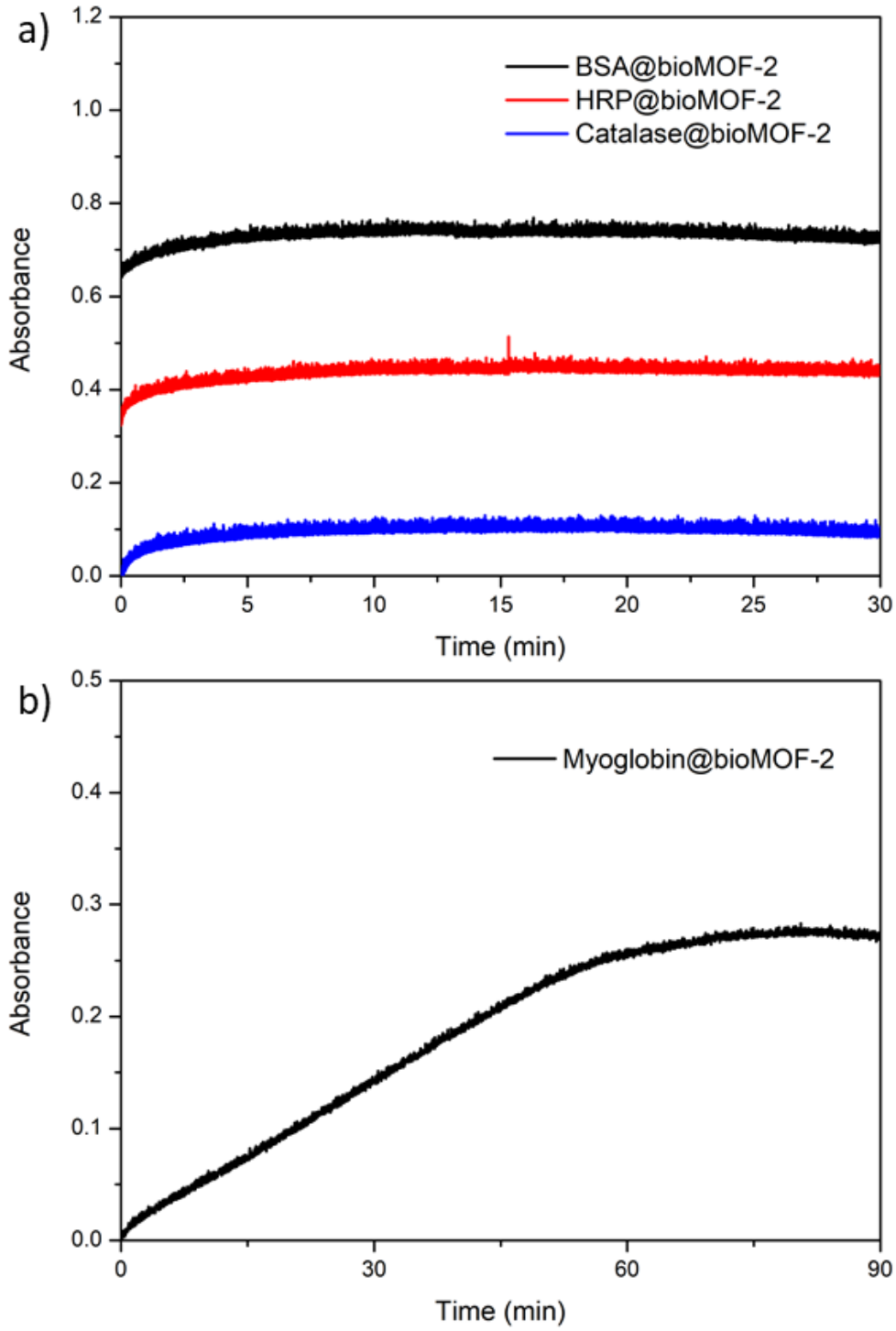

Figure 32: *Solution-state UV-Vis turbidity data for* ***bioMOF-2*** *formed in the presence of a) BSA (black), HRP (red) and CAT (blue) and b) Myoglobin. Time refers to the time after addition of zinc to ligand solution. The rate of the change of absorbance is indicative of the rate of precipitation, while absolute absorbance values do not necessarily indicate a greater volume of precipitation, or greater particle size.*

The turbidity data showed that **bioMOF-2** formed very rapidly in the presence of BSA, HRP and catalase upon addition of the zinc solution such that precipitation had begun before the collection of UV-Vis data had commenced. As a result, the turbidity data does not effectively depict the rapid formation. The turbidity data also showed that the maximum absorbances recorded for **bioMOF-2** formed in the presence of each of these proteins varied significantly. To investigate the cause of this variation, multiple turbidity testing runs were performed for each protein. The turbidity data revealed that the maximum absorbance reached for separate runs using the same protein also varied significantly. Thus, changes in the maximum absorbance reached per run were likely due to natural variations in the quantity of product produced and was not related to the specific protein used.

Interestingly, for **bioMOF-2** formed with catalase, BSA and HRP, there was no gradual MOF formation after the initial precipitation event as was previously theorised. The alternate explanation for the formation of a large quantity of MOF when left overnight was that a second precipitation event occurred during this time. To investigate this further, the **bioMOF-2** precipitate formed immediately in the presence of catalase, HRP and BSA was isolated and the supernatant was left to stir overnight, after which time additional material formed. This supported the hypothesis that at least two distinct precipitation events were occurring in the presence of these enzymes; one immediately after combining the ligand, enzyme and metal solutions, and one overnight. No such two-step precipitation was observed for enzymes that did not induce immediate precipitation (**Table 11**), suggesting that proteins with lower pIs promoted the formation of two distinct precipitates, while those with higher pIs did not.

Table 11: *Proteins used in the synthesis of* ***bioMOF-2*** *and whether they resulted in the formation of one or two distinct precipitates.*

Protein (2 mg)	pI	MW (kDA)	Number of Precipitates	
			One	Two
No protein	-	-	✓	
HRP	3-9	44		✓
BSA	5.3	66		✓
Catalase	5.4	250		✓
Myoglobin	7.6	17	✓	
Trypsin	10.7	23.3	✓	
Lysozyme	11, 11.3	14.4	✓	

To determine the compositions of each precipitate and to potentially determine the cause of the two precipitation events, both were isolated and analysed separately. Henceforth the first and second precipitates are referred to as **bioMOF-2-1** and **bioMOF-2-2**, respectively. **BioMOF-2-1**

formed in the presence of heme-containing enzymes possessed strong colouration similar to that of the pure enzyme, while **bioMOF-2-2** possessed only very slight colouration. The initial precipitation event likely removed a large quantity of protein from the reaction mixture, leaving minimal protein available for potential encapsulation within the crystalline precipitate that formed subsequently. To assist in the identification of the two precipitates, PXRD data was collected for each. PXRD data showed that only **bioMOF-2-2** was the correct crystalline zinc carnosine material, while **bioMOF-2-1** was amorphous (**Figure 33**).

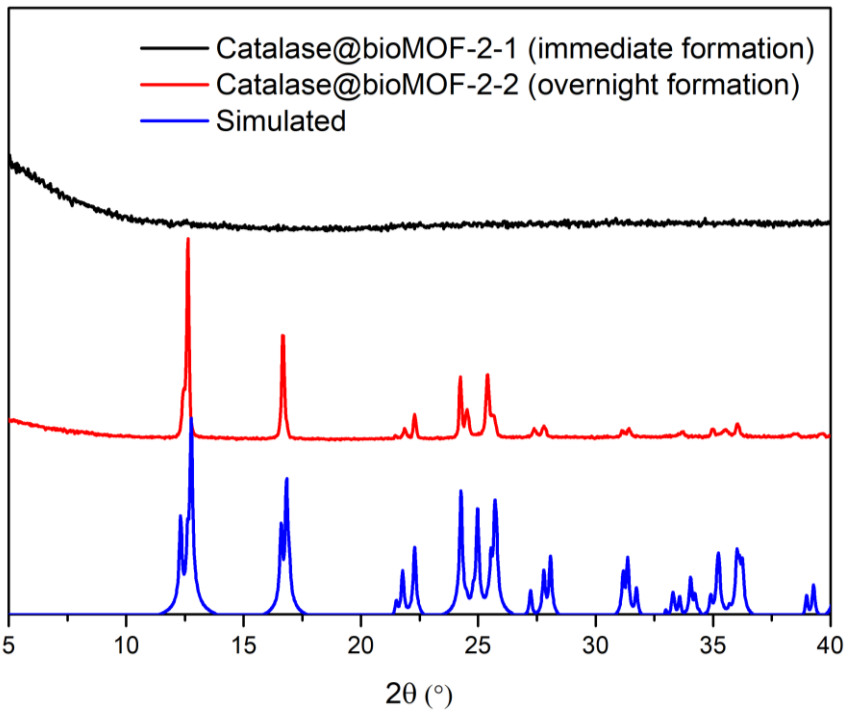

Figure 33: *PXRD data for* ***bioMOF-2-1*** *(black) and* ***bioMOF-2-2*** *(red) formed in the presence of catalase compared to the simulated pattern constructed from single crystal data (blue).*

Thus, what was initially thought to be acceleration of MOF formation caused by protein present in solution, was instead the precipitation of an amorphous material. The MOF did not form until the solution was left to stir overnight, and so this formation was no more rapid than when enzyme was not present. Thus, it was improbable that biomimetic mineralisation was occurring in this system via the same mechanism observed for ZIF-8.

To characterise the initial amorphous precipitate, ^{1}H NMR spectroscopy was used, which produced a spectrum consisting solely of solvent peaks, confirming that no carnosine was present. As such, it was postulated that this initial precipitate was either excess enzyme precipitating out of solution, or a zinc salt-enzyme composite. The latter proposal is supported by the ZIF-8 mechanism wherein the zinc ions are thought to aggregate around the protein.[61] In

either case, the presence of zinc and protein were vital to its formation. It was postulated that the concentration of zinc ions used was too high, causing the initial precipitation event; however, testing biocomposite preparation conditions with reduced zinc concentrations could not prevent the formation of this initial precipitate.

For all further testing, only crystalline **bioMOF-2-2** was used unless otherwise stated.

Select proteins containing a highly conjugated heme group, such as catalase, HRP and myoglobin, absorb in the visible range, making them appear coloured. Preliminary observation of the colour of **bioMOF-2-2** formed in the presence of these heme-containing proteins was conducted. This was also performed for **bioMOF-2-2** formed in the presence of non-heme containing proteins. The colours of these materials were compared to **bioMOF-2-2** (**Table 12**).

Table 12: *Colours of **bioMOF-2-2** biocomposites formed with various proteins.* [a] *coloured enzyme,* [b] *pI refers to the pH at which the protein carries no charge,* [c] *range of pIs resulting from mixture of isozymes.*

Protein (2 mg)	pI[b]	MW (kDA)	Colour of solid
No protein	-	-	White
HRP[a]	3-9[c]	44	White
BSA	5.3	66	White
Catalase[a]	5.4	250	Pale Brown
Myoglobin[a]	7.6	17	Pale Green
Trypsin	10.7	23.3	White
Lysozyme	11, 11.3	14.4	White

Samples of **bioMOF-2-2** formed with or without the addition of non-heme containing proteins were both white, whereas **bioMOF-2-2** formed with catalase and myoglobin possessed colouring similar to that of the enzymes, indicating the presence of these enzymes in the biocomposites. However, this was not observed for HRP, either because the concentration was below the eye's detection limit, or because HRP was not present in the **bioMOF-2-2** sample.

Solid-state UV-Vis spectroscopy was used to further confirm the presence of heme-containing enzymes in the **bioMOF-2-2** samples (**Figure 34**). The presence of a Soret band at 400 nm indicates the presence of a heme group. **BioMOF-2-2** showed no absorbance around 400 nm, and therefore any recorded absorbance in this region was attributed to the protein present.

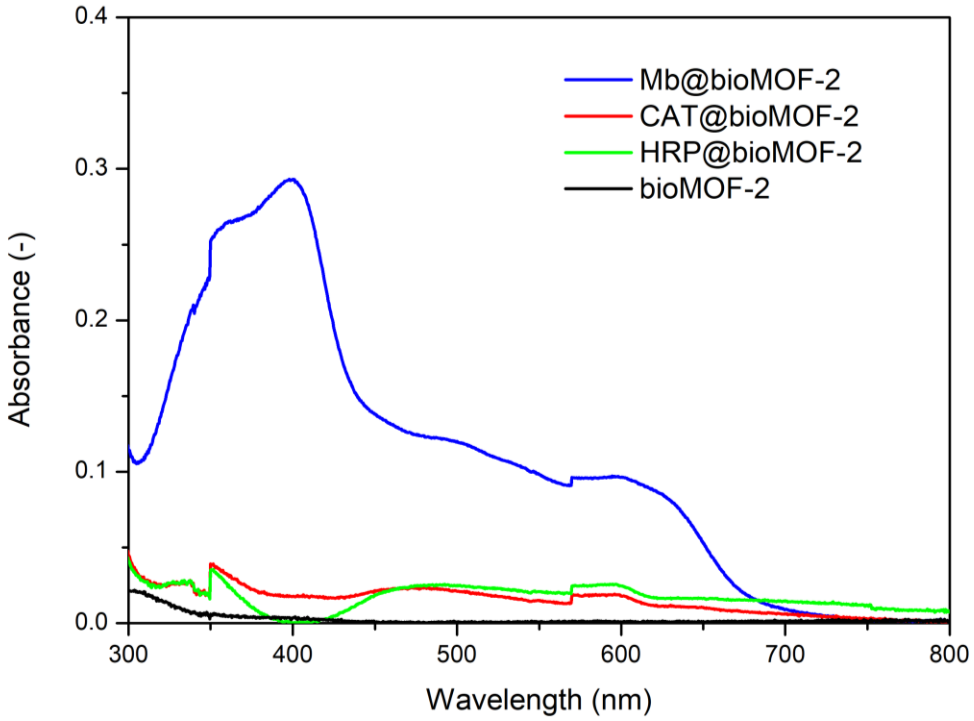

Figure 34: *Solid-state UV-Vis data for bare* ***bioMOF-2-2*** *(black) compared to catalase@****bioMOF-2*** *(red), myoglobin@****bioMOF-2-2*** *(blue) and HRP@****bioMOF-2*** *(green).*

Only the UV-Vis data for myoglobin@**bioMOF-2-2** contained a Soret peak at 400 nm, while no such peak was observed for catalase@**bioMOF-2-2** and HRP@**bioMOF-2-2**. This indicated that neither catalase nor HRP were located in the composites at detectable concentrations, which contrasted with the visual inspection suggesting the former was likely to be present. The absence of catalase and HRP was most likely due to the initial protein-rich amorphous precipitate removing a significant proportion of the enzyme. This initial precipitate did not form in the presence of myoglobin, and so would explain why this was the only protein present in the **bioMOF-2-2** samples.

2.2.2.3 Analysis of protein encapsulation/protection within bioMOF-2-1 and bioMOF-2-2

To conduct preliminary tests to determine whether enzyme encapsulation within **bioMOF-2** crystals was likely, confocal scanning laser microscopy (CLSM) was utilised. As noted previously, this assumes identical behaviour between the native and fluorescently tagged enzymes.

Initially FITC-tagged catalase (FCAT) and FITC-tagged myoglobin (FMb) were used in the synthesis of **bioMOF-2** to allow comparison of results for enzymes which did (catalase) or did not (myoglobin) form the initial amorphous material. While UV-Vis spectroscopy could not detect catalase within the **bioMOF-2** samples, CLSM allowed for secondary confirmation.

In the presence of FCAT, **bioMOF-2** did not precipitate out of solution within a 24-hour period, while **bioMOF-2** formed overnight in the presence of FMb. These precipitation times, or lack-there-of are significantly different than those observed for the native enzymes. To ensure that contamination of previously prepared FCAT and FMb solutions was not the cause, both stock solutions were re-purified by passing through an Illustra NAP-25 column. However, no change in precipitation was observed using these re-purified tagged enzymes. The significant inconsistencies between precipitation times for **bioMOF-2** in the presence of FCAT and FMb compared to the native enzymes suggested that the fluorescent tag changed key properties of the enzymes. As such, it appeared that FITC-tagged catalase and myoglobin interacted with the MOF differently to the native enzymes. As such, CLSM was not performed for **bioMOF-2** with FCAT or FMb as the confocal images were likely to not be indicative of the behaviour of native enzymes.

To determine if the use of a different fluorescence tag could impact the enzymatic behaviour to a lesser extent, RbITC-tagged catalase (RbCAT) and myoglobin (RbMb) were used in the synthesis of **bioMOF-2**. The precipitation of **bioMOF-2** in the presence of RbMb began after 3 hours, making it comparable to free enzyme, but subsequent precipitation occurred at an extremely slow rate. Further, **bioMOF-2** formed after 5-6 hours in the presence of RbCAT, with no initial amorphous precipitate produced. Despite the RbITC tag appearing to have a reduced impact compared to FITC, there were still discrepancies in the way the MOF formed. Thus, CLSM was not performed for **bioMOF-2** formed with RbMb and RbCAT as a result.

Due to these significant discrepancies between the tagged and free enzymes, FITC-tagged HRP (FHRP) and BSA (FBSA) were used instead. The addition of FHRP or FBSA to the synthesis of **bioMOF-2** both caused the immediate precipitation of an amorphous material, followed by a delayed overnight precipitation of crystalline zinc carnosine. Thus, suggesting that tagged and native HRP and BSA were interacting with the MOF in comparable ways.

The difference in biocomposite formation for tagged catalase and myoglobin compared to tagged BSA and HRP may be due to changes in pI upon addition of the FITC (or RbITC) tag. As **bioMOF-2** was formed in a neutral (pH 7) solution, any change in pI could have had a significant impact on the interaction with the MOF precursors.

Due to the apparent similarity between FITC tagged HRP and BSA and the native proteins, CLSM imaging was conducted on both the enzyme@**bioMOF-2-1** and enzyme@**bioMOF-2-2** composites (**Figure 35**, **Figure 36** and **Figure 37**).

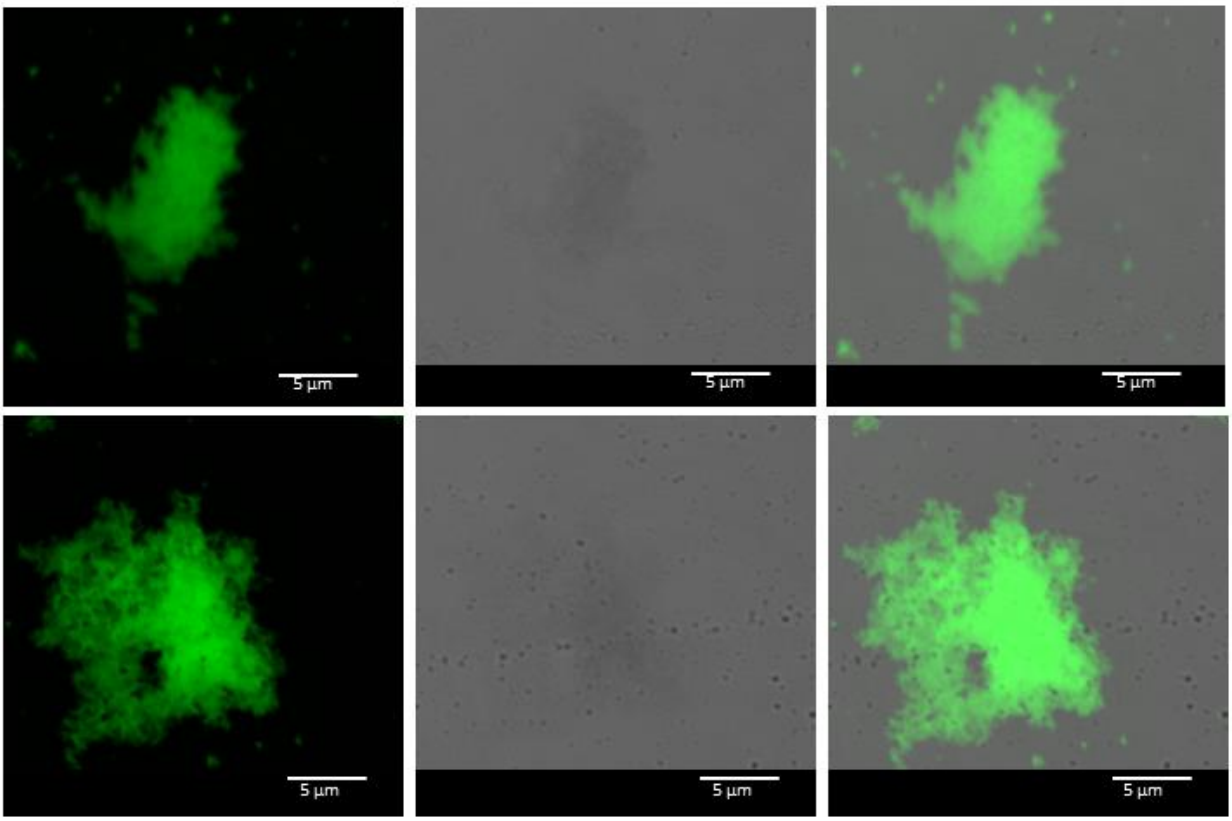

Figure 35: *CLSM images (fluorescence, bright field and overlay) of the initial amorphous precipitate FHRP@**bioMOF-2-1**. Tagged enzyme is shown in green.*

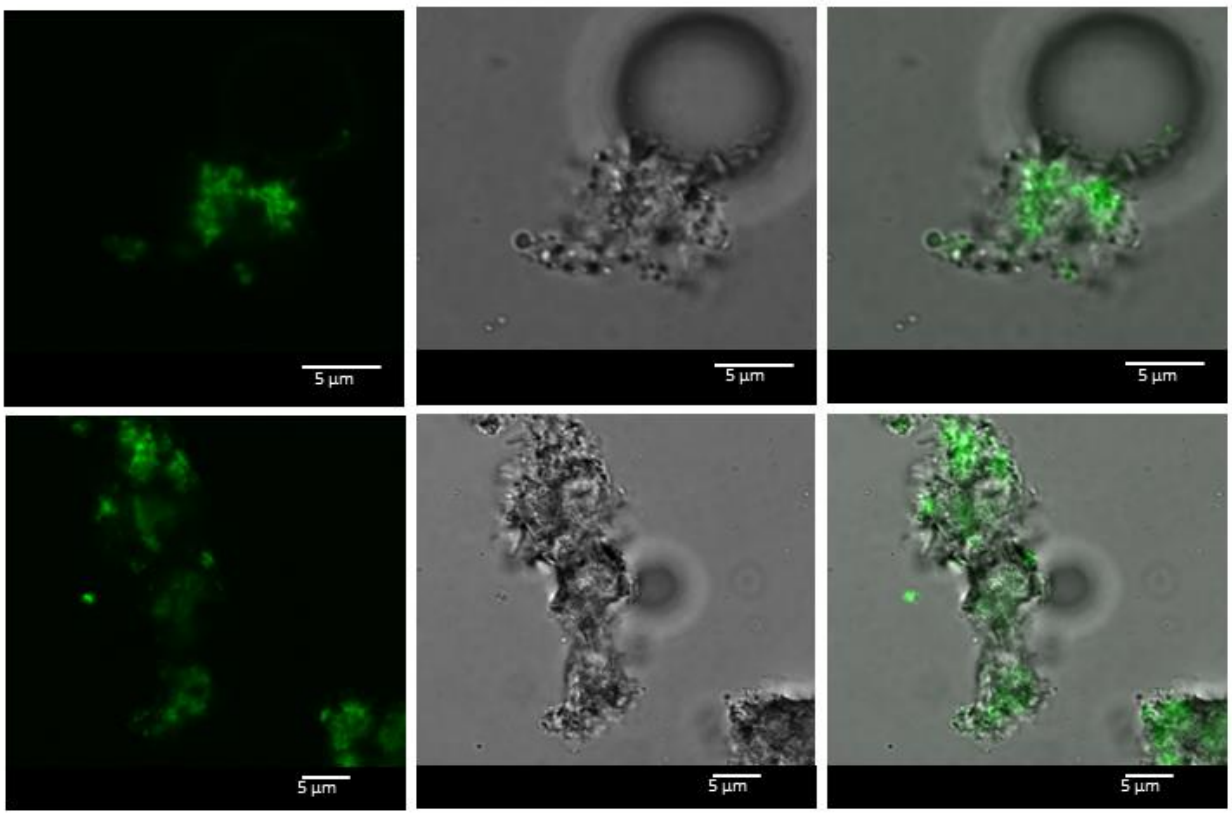

Figure 36: *CLSM images (fluorescence, bright field and overlay) of second precipitate FHRP@**bioMOF-2-2**. Tagged enzyme is shown in green.*

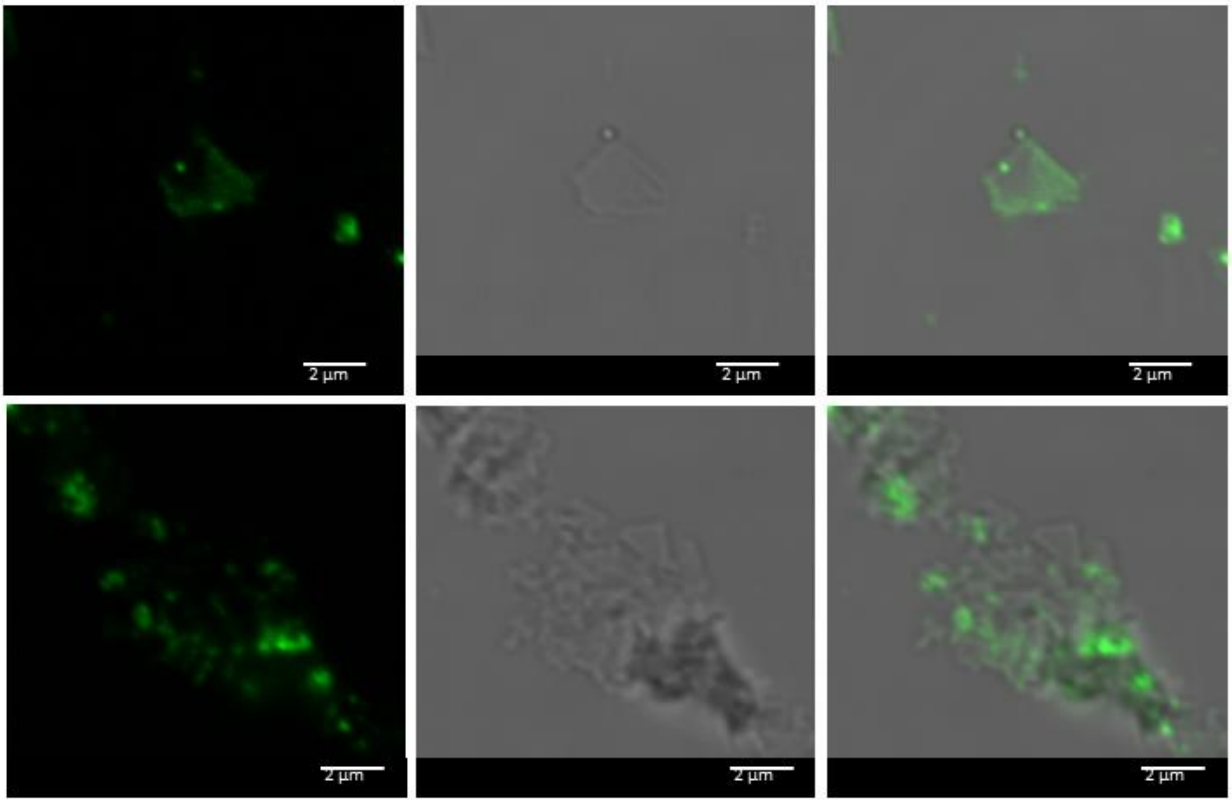

Figure 37: *CLSM images (fluorescence, bright field and overlay) of the second precipitate FBSA@**bioMOF-2-2**. Tagged enzyme is shown in green.*

The confocal images for the first precipitate (**Figure 35**) show that FHRP is present throughout the whole sample, as indicated by the homogenous distribution of intense fluorescence observed. No high-quality images of the first precipitate with FBSA were able to be produced due to small particle size. This CLSM data supported previous observations which indicated that the initial precipitate contained very high concentrations of protein. Further, the images for the second precipitate formed in the presence of either FHRP or FBSA (**Figure 36** and **Figure 37** respectively) both showed an inhomogeneous distribution of the fluorescence label across the crystals. While this data could confirm that the MOF and enzymes were co-located, it was difficult to determine whether the enzyme was encapsulated.

To more definitively determine whether encapsulation was occurring, aqueous assays were used to give measures of the activity of either catalase or peroxidase. These assays were initially performed on the overall enzyme@**bioMOF-2** composite prior to determining that the precipitation occurred in two steps. Following this realisation, the assays were also conducted on separate samples of **bioMOF-2-1** and **bioMOF-2-2**, as CLSM had confirmed the presence of enzyme in both. These methods produce quantitative data with fewer potential sources of error compared to the methods used for **bioMOF-1**. The reason for conducting more extensive

research into the encapsulation and protective ability of **bioMOF-2** compared to **bioMOF-1** was primarily due to the greater similarities between the zinc carnosine and ZIF materials.

To determine the enzymatic activity of catalase, a ferrous oxidation of xylenol orange (FOX) assay was conducted. This assay utilises the ability of catalase to promote the reduction of hydrogen peroxide by the following equation;[104]

$$H_2O_2 \rightarrow H_2O + O_2$$

Hydrogen peroxide is able to oxidise ferrous iron (+2) to ferric iron (+3), which can subsequently bind to the xylenol orange dye, while ferrous iron cannot.[105] Fe^{3+} bound to xylenol orange absorbs strongly at 560nm, while the unbound dye has minimal to no absorbance at this wavelength. This allows the use of UV-Vis spectroscopy to determine the amount of bound dye, and by extension the amount of hydrogen peroxide. A higher absorbance at 560 nm (purple colouration) is indicative of more bound Fe^{3+} xylenol orange, therefore a higher hydrogen peroxide concentration and so a lower catalase activity. A yellow colouration indicates the reverse.

Experimentally, FOX assays are performed by placing the sample in a solution of hydrogen peroxide (0.25 mM) and after specific time intervals (1, 5, 10 minutes for this work) a volume of this hydrogen peroxide mixture (50 µL) is reacted with FOX reagent (950 µL) for 30 minutes prior to analysis. These time intervals have been shown to be sufficient lengths of time for catalase@ZIF biocomposites.[106] Sampling over these time intervals also gave an indication of the rate at which any catalase present is able to decompose the hydrogen peroxide.

To measure the activity of peroxidases, such as HRP, pyrogallol assays were conducted wherein the peroxidase catalyses the conversion of pyrogallol to purpurogallin (**Scheme 3**). The initial pyrogallol solution is virtually colourless, while purpurogallin has a very strong yellow colour. UV-Vis spectroscopy can record the change in absorbance at 420 nm to determine the rate of purpurogallin production. A more rapid increase in absorbance at 420 nm indicates a higher purpurogallin production and, by extension, greater peroxidase activity.

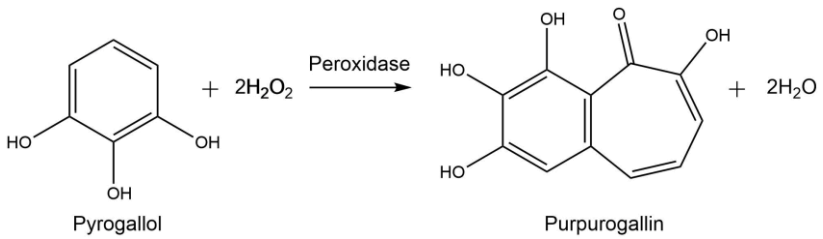

Pyrogallol Purpurogallin

Scheme 3: *Conversion of pyrogallol to purpurogallin in the presence of peroxide and H_2O_2.*

The activity of CAT@**bioMOF-2** was first analysed qualitatively using the FOX assays. This study was conducted for free catalase, bare **bioMOF-2** and CAT@**bioMOF-2** (**Figure 38**) to ensure that the catalase used was active and the bare MOF did not produce any false positives in the activity readings. These assays were performed on the combined precipitates as they were conducted prior to determining that precipitation occurred in two steps.

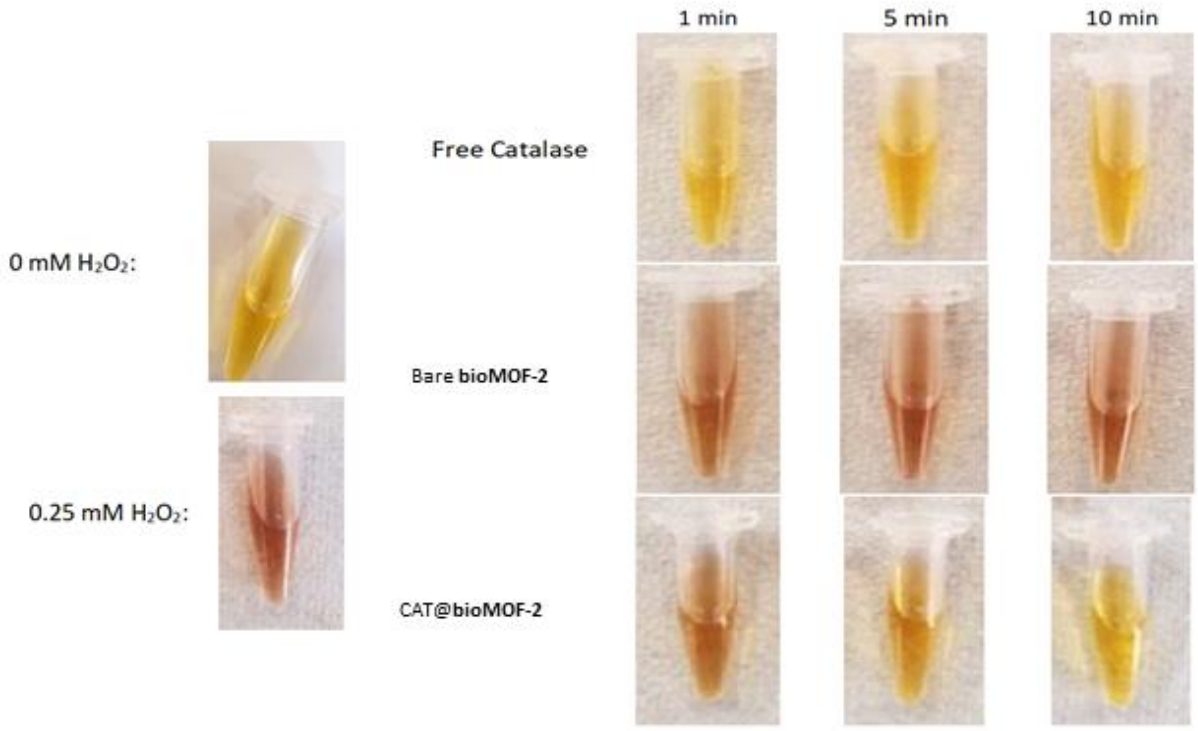

Figure 38: *Qualitative FOX assay results for free catalase, pure* ***bioMOF-2*** *and CAT@****bioMOF-2*** *compared to 0 mM and 0.25 mM H_2O_2. Assays were performed with [H_2O_2] of 0.25 mM, times refer to the length of time the test substances were left in H_2O_2 solution before adding to FOX reagent.*

The qualitative results for free catalase showed assay solutions possessing coloration that matched that of the standards with 0 mM hydrogen peroxide. This indicated that all peroxide present in the solution was decomposed in under one minute, confirming that the catalase was highly active. The results also confirmed that pure **bioMOF-2** sample was unable to decompose an observable quantity of peroxide. Finally, the CAT@**bioMOF-2** sample showed slight enzymatic activity, with a much more gradual decomposition of hydrogen peroxide compared to the free enzyme. However, these assays were not performed with equivalent catalase concentrations and so the absolute activities of the free enzyme and CAT@**bioMOF-2** samples could not be compared.

These qualitative assays were then repeated for free catalase and CAT@**bioMOF-2** after exposure to a range of harsh external conditions including base, acid, elevated temperatures, organic solvents and protease. If the enzymatic activity of catalase within the MOF samples decreased to a lesser extent than the free enzyme, this suggested that the MOF was offering protection to the biomolecule, potentially due to successful encapsulation. However, if the enzymatic activity decreased to the same or greater extent than the free enzyme, then encapsulation and protection of the biomolecule by **bioMOF-2** was deemed unsuccessful. The respective catalase activities for CAT@**bioMOF-2** following exposure to these conditions are shown qualitatively in **Figure 39**.

Controls confirmed that the presence of DMF, water, acid, base and protease had no effect on the assay (**Figure 84** in the appendix). The free enzyme experienced no observable loss in enzymatic activity upon exposure to acidic and basic solvents, and only slight activity losses upon exposure to DMF and protease. Only after exposure to elevated temperatures (120°C) did the free enzyme appear to lose most or all enzymatic activity, which agreed with literature data as 120°C falls far outside of the thermal stability region of catalase.[16] The significant reduction in activity upon exposure of the free enzyme to organic solvent and protease also agrees with previous results from literature.[65] The high stability of the free enzyme in basic conditions agrees with the literature data for pH stability as it is very close to the optimal pH of catalase, however, a pH of 3 is well below the accepted pH range in which catalase is stable, making this result unexpected.[16] It is possible that the concentration of enzyme was too high, such that high enough concentration of catalase were present to fully decompose the H_2O_2 present even after some decomposition had occurred.

The qualitative data indicated that, while the original CAT@**bioMOF-2** possessed observable enzymatic activity, this activity was removed upon exposure to protease, heating, DMF, acid and base. Therefore, the enzyme in the CAT@**bioMOF-2** biocomposites appeared to be less stable than the free enzyme, indicating that the MOF was unable to offer any protective capacity to the enzyme. This may have been because the enzyme was solely surface-bound, or it may be encapsulated but the MOF was unable to protect it from harsh external conditions. The former was supported by CLSM data in which the enzyme appeared to be predominantly located on the surface of the crystals.

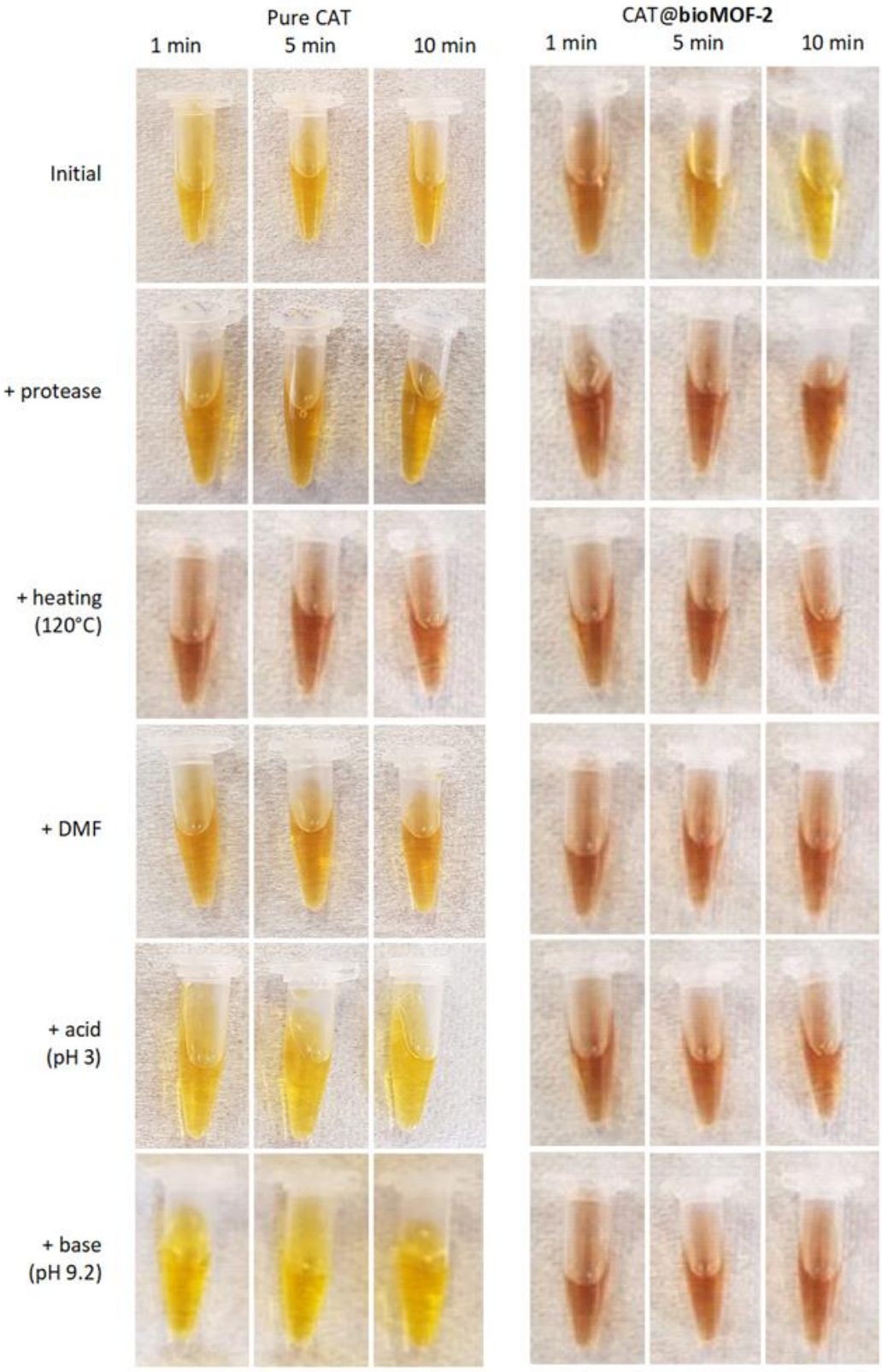

Figure 39: *Qualitative FOX assay results for free CAT (left) and CAT@**bioMOF-2** (right) after treatment with protease (2mg/mL in 0.05 M Tris-HCl pH 8 buffer, 2 hrs), heating (120°C in water, 1 hr), DMF (1 hr), acid (pH 3, dilute HCl, 1 hr) and base (pH 9.2 bicarbonate-carbonate buffer, 1 hr). Assays were performed with [H_2O_2] of 0.25 mM, times refer to the length of time samples were left in H_2O_2 solution before adding to FOX reagent.*

One alternate possibility is that the diffusion of assay reagents through the MOF to the enzymatic active site may have been significantly hindered, meaning the activity of encapsulated enzymes may not have been detected. **BioMOF-2** initially appeared very promising due to the 5 Å pore apertures, which are considerably larger than the 3.4 Å pore openings present in ZIF-8. However, the pore apertures in ZIF-8 open up into much larger pores 11.6 Å in diameter due to the sodalite topology, while in zinc carnosine the 5 Å openings continue as channels of the same width. Thus, while substrate diffusion through the initial pore apertures in ZIF-8 may be hindered, diffusion through the longer channels in **bioMOF-2** may be more restricted overall.

To test this theory, a method of decomposing the MOF without destroying any enzyme present was devised. This would allow the MOF to be dissolved, in turn releasing any encapsulated enzyme, making them freely accessible for subsequent assays. Thus, the activity of all enzyme present before and after exposure to harsh conditions could be compared without the potential issue of hindered substrate diffusion. Solutions of EDTA in pH 8 Tris-HCl buffer (0.05 M) were tested as EDTA has previously been shown to successfully decompose ZIF-8. However, EDTA interfered with the assays such that no conclusions could be made (**Table 18** in the appendix).[107] No alternate method of decomposing catalase@**bioMOF-2** could be identified.

To further investigate **bioMOF-2**, enzymatic activities for catalase@**bioMOF-2-1** (amorphous) and catalase@**bioMOF-2-2** (crystalline) composites was determined (**Figure 40**).

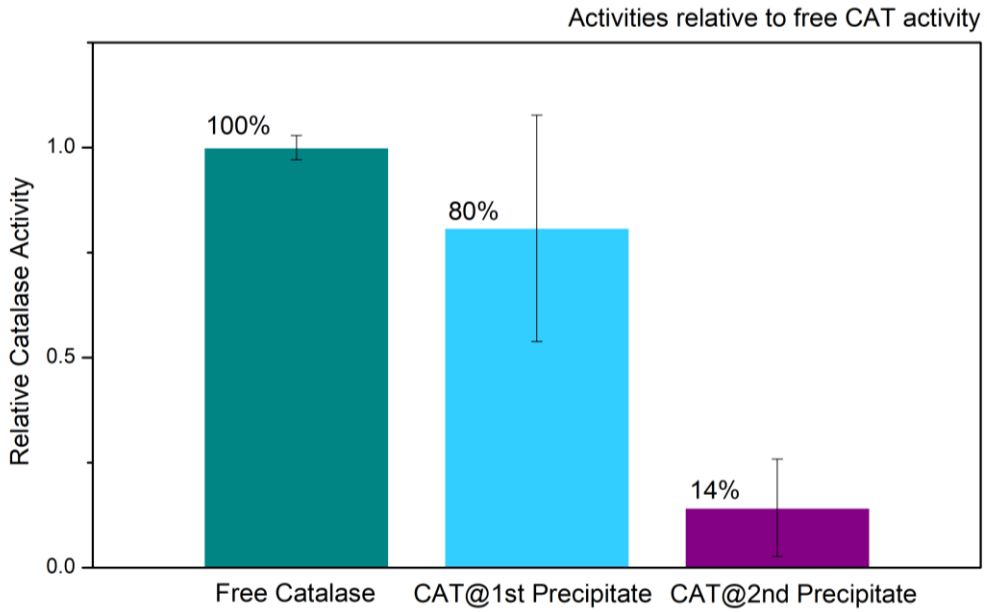

Figure 40: *Relative catalase activity for free catalase, CAT@**bioMOF-2**-1 (initial amorphous precipitate) and CAT@**bioMOF-2**-2 (second crystalline precipitate). Assays were performed with [H_2O_2] of 0.25 mM and a 10-minute exposure time to H_2O_2 solution before adding to FOX reagent. Assays were performed with equal masses of samples.*

The FOX assay data revealed that CAT@**bioMOF-2-1** possessed a significantly higher enzymatic activity compared to CAT@**bioMOF-2-2**, supporting previous theories that the initial precipitate was protein-rich. In turn, this reduced the amount of enzyme present in solution and available for the second precipitate, causing CAT@**bioMOF-2-2** to have a much lower catalase concentration and, thus, lower enzymatic activity. This low, and highly inhomogeneous, enzyme concentration is likely to be the key source of the large errors present in the CAT@**bioMOF-2-2** assay data.

To investigate the difference in ability of the first and second precipitates to protect catalase present in the biocomposites, activity testing was conducted before and after treatment with protease (**Figure 85** in the appendix). However, the uncertainties present in the assay results were too large to produce statistically significant conclusions. These high errors are likely a result of the inhomogeneous enzyme loading between samples, in addition to the low enzyme concentration in the CAT@**bioMOF-2-2-** biocomposites.

To determine whether the lack of protective ability of **bioMOF-2** for catalase was comparable to other enzymes, assays were then repeated for HRP@**bioMOF-2-2** using the aforementioned peroxidase assay. To ensure that pure **bioMOF-2-2** showed no detectable activity, preliminary tests were performed. Pure **bioMOF-2-2** showed minimal activity, and therefore this was excluded from subsequent results. Controls with acid (pH 3, dilute HCl), base (pH 9.2, bicarbonate-carbonate buffer), DMF and protease were all performed, causing minor conversion of pyrogallol (**Figure 86** in the appendix), which was subtracted from the calculated activity of the samples.

The relative change in peroxidase activity was then determined for free HRP and HRP@**bioMOF-2-2** upon exposure to DMF, acid (pH 3), base (pH 9.2) and protease solutions (**Figure 41**). For free HRP, noticeable reductions in enzymatic activity were observed following treatment in all harsh conditions tested, with the greatest loss of 30% occurring after exposure to protease. After exposure to acidic (pH 3) and basic (pH 9.2) solutions, the former caused a greater reduction in enzymatic activity of the free HRP. This agreed with literature data that indicated that HRP was stable between pHs of 5.0 and 9.0 for 16 hours.[108, 109] Yet, this may indicate that the activity loss following exposure to pH 3 should have been greater than 25%. However, the large errors, likely resulting from significant activity/stability variance for different HRP samples, indicates uncertainty in these measurements. Further, literature data states that HRP loses all enzymatic activity in pure DMF after 4 hours, indicating that the recorded activity loss was much lower than

expected.[110] Yet, the relatively small error in this data suggests high levels of certainty. The 30% loss of enzymatic activity upon proteolytic treatment for 2 hours seems reasonable when compared to a reported 50% reduction in activity of free HRP upon treatment with proteolytic enzymes for 24 hours.[111]

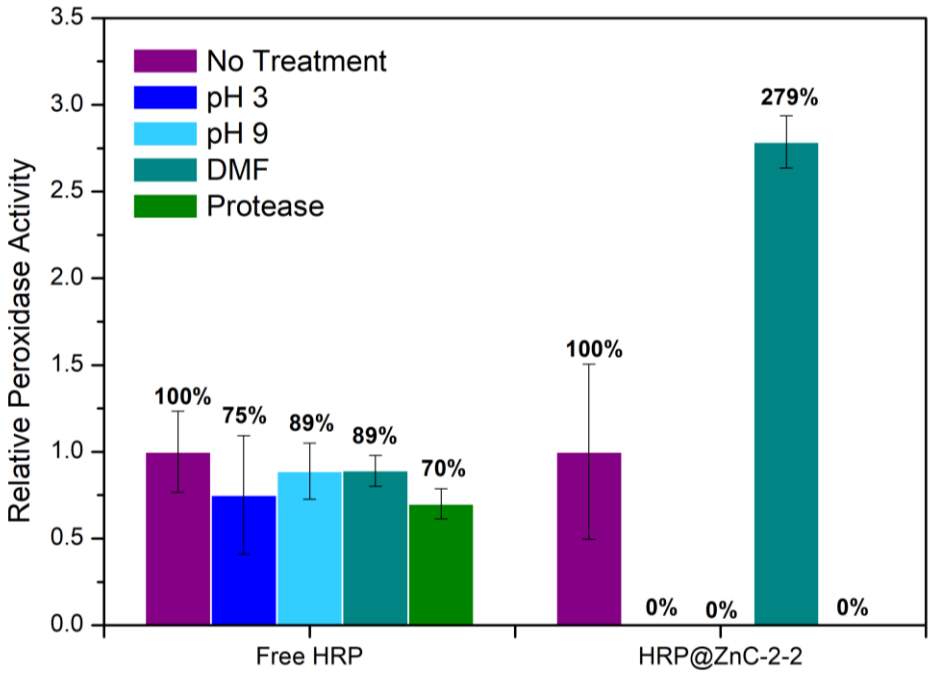

Figure 41: *Relative HRP activity for free HRP and HRP@**bioMOF-2-2** before (purple) and after exposure to pH 3 (dilute HCl, 1 hr) (dark blue), pH 9.2 (bicarbonate-carbonate buffer, 1 hr) (light blue), DMF (1 hr) (aqua) and protease (2 mg/mL in 0.05 M Tris-HCl pH 8 buffer, 2 hr) (green). Concentration of the sample used per assay was 1 mg/5 mL H_2O.*

Assay data for HRP@**bioMOF-2-2** revealed that treatment with DMF led to a significant increase in enzymatic activity, which was not consistent with the expected results. Since the activity of catalase did not increase upon DMF exposure, the DMF was potentially interacting with HRP or the peroxidase assay, which may also explain why the observed activity of free HRP in DMF was higher than expected. No experimental or literature data was able to support this hypothesis. Conversely, following exposure to pH 3, pH 9.2 and protease the enzymatic activity of HRP@**bioMOF-2-2** was completely removed. These results suggested a number of potential causes. Firstly, all HRP may have been present on the surface of the MOF, which would offer no protection. Secondly, enzyme may have been encapsulated within the MOF crystals, but this offered no protection against acidic, basic and proteolytic conditions. Thirdly, enzyme may have been encapsulated and protected but due to the large size of assay reagents and thus, an inability to diffuse through the framework, the activity of encapsulated enzyme may not have been detected. Regardless of the exact cause of these observations, the fact that the recorded

reduction in activity of HRP@**bioMOF-2-2** in pH 3, pH 9.2 and protease was greater than that of the free enzyme suggests that the encapsulation or surface-binding process led to a reduction in the stability of the enzyme.

To examine which theory is likely to be the case for HRP@**bioMOF-2-2**, the material before and after exposure to harsh conditions was subject to treatment with a 1% aqueous EDTA solution (**Figure 87** in the appendix). This decomposed the MOF, while not resulting in activity loss of the enzyme. As such, diffusion of substrate would no longer be hindered by the framework. However, due to the low and inhomogeneous enzyme concentration present in the HRP@**bioMOF-2-2** composites, the data was inconsistent and so no conclusions could be made with statistical confidence.

The exact reason for the inability of **bioMOF-2** to effectively protect HRP in these specific conditions was difficult to confirm. It was postulated that it could have been because the MOF was decomposing slightly in these harsher conditions, which may have allowed the external solvent to reach the enzyme within the MOF. Alternatively, if the MOF was decomposing this may have caused enzyme to leach into solution where it would be fully exposed to the external conditions. While stability testing of **bioMOF-2** was performed previously (**Table 8** and **Table 9**), the sole use of PXRD data to make these conclusions was potentially unable to detect slight framework decomposition.

2.3 Conclusions

After an extensive literature review, two zinc bioMOFs containing L-Glutamic acid or L-Carnosine (β-Ala-L-His) linkers were chosen to explore biomimetic mineralisation of proteins.

No changes to the synthesis of zinc glutamate (**bioMOF-1**) were required to ensure that it was compatible with biomolecule encapsulation. The rate of precipitation of **bioMOF-1** could be controlled by altering the concentration of base added during the synthesis, with high concentrations causing a faster precipitation. The addition of a suite of proteins did not result in changes to the crystalline structure of **bioMOF-1**, as confirmed by PXRD data. UV-Vis spectroscopic data for protein@**bioMOF-1** biocomposites indicated that proteins which were strongly attracted to the MOF caused delayed precipitation times, potentially due to protein complexing with the MOF components. Thus, the formation of protein@**bioMOF-1** was unlikely to be undergoing biomimetic mineralisation, wherein added enzyme accelerates MOF growth. Instead, it was likely that the precipitation of **bioMOF-1** was occurring either independently of

the enzyme, or as a co-precipitation event. UV-Vis, fluorescence and CLSM data for FITC-protein@**bioMOF-1** before and after treatment to remove all surface-bound enzyme, showed a significant reduction in the total quantity of protein present. Thus, it was concluded that the enzyme was predominantly surface bound in the enzyme@**bioMOF-1** biocomposites, and no further testing was performed.

For zinc carnosine (**bioMOF-2**), a new biomolecule-compatible synthetic procedure was devised using predominantly aqueous conditions at room temperature, wherein the rate of precipitation was controlled by the ethanol concentration. No changes in the crystalline structure of **bioMOF-2** were observed upon addition of protein, however, SEM images revealed that the presence of protein caused a change in the morphology of the MOF crystals. Further, the presence of proteins with pIs below approximately 6 caused the precipitation of an initial, amorphous solid prior to the formation of the MOF. This precipitate was deemed to be a protein-rich zinc salt. No such amorphous solid was produced when higher pI proteins were used, yet, due to lack of assays available for these proteins, no further analysis was performed. Future studies on these proteins in the enzyme@**bioMOF-2** composites could be of benefit, in addition to modifying the chemical functionalisation of catalase or HRP to increase the pI. Use of other chemical modulators such as polyvinylpyrrolidone (PVP) has also been attempted, with preliminary results showing that it prevents the formation of the amorphous material. Yet the PVP concentrations used prevented MOF formation, as such this needs to be tuned. Further analysis was performed solely on the crystalline precipitate of enzyme@**bioMOF-2**. Aqueous assays revealed that for catalase and HRP, only small quantities of enzyme were likely to be encapsulated within the MOF. However, the low and inhomogeneous enzyme loadings (CLSM data) prevented reliable quantitative data from being measured for the composites.

Thus, neither **bioMOF-1** nor **bioMOF-2** were shown to be able to encapsulate and protect enzyme by the approaches outlined. However, for **bioMOF-2**, this research indicates that further consideration of the synthetic approach (e.g. use of reagents such as PVP to stabilise the protein against initial precipitation), or chemical modification of the protein to achieve higher pIs could be used to develop stable protein@**bioMOF-2** composites. Further, this research shows that the presence of imidazole functionality within a MOF does not necessarily ensure that biomolecule encapsulation will occur via biomimetic mineralisation. Instead, it is likely that the nitrogen donor groups within the imidazole group must be the only binding site in the linker, as is seen in many of the frameworks that have been successfully used for this application such as ZIF-8, ZIF-90 and MAF-7.

2.4 Experimental

2.4.1: General Methods

All chemicals and solvents were purchased from commercial suppliers and used as received with no further purification.

Buffer Preparation:

0.05 M Tris-HCl: Trisaminomethane (Tris) (0.30 g, 2.5 mmol) was dissolved in water (40 mL), the pH adjusted with 32% hydrochloric acid and the solution was made up to a final volume of 50 mL with water.

Carbonate-bicarbonate (pH 9.2): Sodium carbonate (0.088 g, 0.83 mmol) was dissolved in water (4 mL). Sodium bicarbonate (0.74 g, 8.8 mmol) was dissolved in water (46 mL) and added to the sodium carbonate solution, followed by addition of water (150 mL).

Phosphate buffered saline (PBS): Sodium chloride (0.80 g, 13.7 mmol), potassium chloride (0.02 g, 0.27 mmol), $Na_2HPO_4{\cdot}2H_2O$ (0.144 g, 0.81 mmol) and KH_2PO_4 (0.024 g, 0.18 mmol) were dissolved in water (80 mL). The pH was adjusted using 32% hydrochloric acid and the solution was made up to a final volume of 100 mL with water.

Enzyme Modifications:

Amination: A 2 mL solution of EDTA (0.268 g, 4.01 mmol) dissolved in MQ water was prepared and the pH adjusted to 4.5 using 6 M hydrochloric acid. The protein (20 mg) was dissolved in the EDTA solution, followed by EDC.HCl (7.2 mg, 0.038 mmol). The solution was stirred on ice for 2 h before being washed by ultra-filtration once with phosphate buffer (100 mM, pH 7.4) and twice with MQ water to remove excess salts (Vivacell 100, Sartorius Stedim, 10 kDA at 4000 rpm/1699 g).

FITC-tagged protein: Catalase (CAT; Sigma-Aldrich, catalase from bovine liver, 2000-5000 units.mg^{-1} of protein, 20 mg) and fluorescein isothiocyanate (FITC) (1 mg, 0.0026 mmol) were dissolved in bicarbonate-carbonate aqueous buffer solution (0.1 M, pH 9.2, 2 mL) and stirred in darkness at room temperature for 2 h. The FITC-tagged protein was recovered by passing the reaction solution through an Illustra NAP-25 column (GE Healthcare Life Sciences, NSW, Australia). The obtained FCAT solution was stored in darkness at 4°C.

A similar method was used to prepare fluorescein-tagged peroxidase from horseradish (HRP; Sigma-Aldrich, Type VI-A, lyophilized powder, 950-2000 units.mg^{-1} of solid (using 2,2'-azino-bis(3-ethylbenzothiazoline-6-sulfonic acid)), ≥250 units.mg^{-1} (using pyrogallol)), fluorescein-tagged bovine serum albumin (BSA; Sigma-Aldrich, lyophilized powder, BioReagent, Suitable for cell culture, >96%) and fluorescein-tagged myoglobin (Mb; Sigma-Aldrich, myoglobin from equine skeletal muscle 95-10%, essentially salt-free, lyophilized powder).

RbITC-tagged protein: Catalase (CAT; Sigma-Aldrich, catalase from bovine liver, 2000-5000 units.mg^{-1} of protein, 20 mg) and Rhodamine b isothiocyanate (RbITC) (0.3 mg, 0.00056 mmol) were dissolved in bicarbonate-carbonate buffer solution (pH 9.2, 2.5 mL) and stirred at room temperature for 2 h. The RbITC-tagged protein was recovered by passing the reaction solution through an Illustra NAP-25 column (GE Healthcare Life Sciences, NSW, Australia). The obtained FCAT solution was stored in darkness at 4°C.

A similar method was used to prepare rhodamine b-tagged myoglobin (Mb; Sigma-Aldrich, myoglobin from equine skeletal muscle 95-10%, essentially salt-free, lyophilized powder).

2.4.2: Syntheses

L-Glutamic acid derived materials:

*Zn Glutamate (bioMOF-1) (general method – see **Table 15** in appendix for specific conditions):* L-Glutamic acid and base were dissolved in water (5 mL). The zinc salt was dissolved in water (5 mL) and the resultant solution was added dropwise to the glutamic acid solution with stirring to cause the precipitation of a white solid. The solid was isolated by filtration under reduced pressure, washed with water (x 3) and air dried to give a white solid. PXRD data is shown in **Figure 17** (literature synthesis), **Figure 18** (varying base concentration with $ZnSO_4 \cdot 7H_2O$) and **Figure 19** (varying base concentration with $ZnOAc \cdot 2H_2O$).

Enzyme@bioMOF-1: L-Glutamic acid (0.074 g 0.5 mmol), sodium bicarbonate (0.042 g, 0.625 mmol) and protein (2 mg) were dissolved in water (5 mL). $ZnSO_4 \cdot 7H_2O$ (0.14 g, 0.5 mmol) was dissolved in water (5 mL) and the resultant solution was added dropwise to the glutamic acid solution with stirring to cause the precipitation of a white solid. The solid was isolated by filtration under reduced pressure, washed with water (x 3) and air dried to give a white solid. PXRD data is shown in **Figure 20**, UV-Vis data is shown in **Figure 23** and CLSM images are shown in **Figure 24**. Precipitation times of the materials formed in the presence of a variety of enzymes are outlined in **Table 2**.

L-Carnosine derived materials:

*ZnC (bioMOF-2) – no alcohol (general method – see **Table 6** for specific conditions):* L-Carnosine and base were dissolved in water (5 mL). Zn salt was dissolved in H_2O (5 mL) and the resulting solution was added dropwise to the glutamate solution with stirring to cause precipitation. The precipitate was isolated via centrifugation (6000 rpm, 2656 x g, 2 min), washed with water (x 3) and dried to give a white solid.

*ZnC (bioMOF-2) – with alcohol (general method – see **Table 7** for specific conditions):* L-Carnosine and base were dissolved in ethanol and half of the total volume of water. $Zn(NO_3)_2{\cdot}6H_2O$ was dissolved in the remaining volume of water and the resulting solution was added dropwise to the carnosine solution, causing precipitation. The solid was isolated via centrifugation (6000 rpm, 2656 x g, 2 min), washed with water (x 3) ethanol (x 1) and dried to give a white solid. PXRD data is shown in **Figure 27** and SEM images are shown in **Figure 29**.

Enzyme@bioMOF-2: L-Carnosine (0.05 g, 0.22 mmol) and protein (0.002 g) were dissolved in water (4.5 mL) and ethanol (1 mL). $Zn(NO_3)_2{\cdot}6H_2O$ (0.13 g, 0.44 mmol) was dissolved in water (4.5 mL) and the resultant solution was added dropwise to the carnosine solution to cause precipitation. The solid was isolated by centrifugation (6000 rpm, 2656 x g, 2 min), washed with ethanol and dried to give the protein-bioMOF composite. PXRD data is shown in **Figure 30**, SEM images are shown in **Figure 31**, UV-Vis data is shown in **Figure 34** and CLSM images are shown in **Figure 36** and **Figure 37**. Precipitation times of enzyme@bioMOF-2 for a variety of enzymes are outlined in **Table 10**.

2.4.3: Characterisation

Confocal scanning laser microscopy (CLSM):

Images were taken on an Olympus FV3000 confocal laser scanning microscope, Olympus. The fluorescein-tagged proteins were excited at 488 nm and the fluorescence signal was collected between 495 and 545 nm.

UV-Vis Spectroscopy:

Solution absorption spectra was obtained using a Varian Cary 5000 UV-Vis spectrometer, using a 1 cm quartz cell. Turbidity measurements were conducted using the 'kinetics' program. Solid state UV-Vis data was collected using the same equipment with a Harrick Praying Mantis DRP

accessory. Samples were crushed and packed flat. 100% transmittance was set by zeroing against a flat sample of spectroscopic grade KBr.

Powder X-ray diffraction (PXRD):

PXRD patterns were collected on a Bruker D4 ENDEAVOR using a Co anode to produce K_α radiation (λ = 1.788965 Å). Flat plate diffraction data was collected across a range of 2θ = 5° to 40°. The PXRD data was converted to xy data using PowDLL converter (version 2.42.5186.29064). Simulated PXRD patterns were prepared in Mercury (version 3.9) and expressed as the cobalt-source irradiated patterns.

Scanning electron microscopy (SEM):

Samples were imaged on a Philips XL30 field-emission scanning electron microscope (FESEM). Prior to analysis, samples were dry loaded onto adhesive carbon tabs on 12 mm aluminium stubs and coated in carbon.

Fourier Transform Infrared (FTIR) Spectroscopy:

FTIR spectra were obtained on a PerkinElmer Spectrum 100 FTIR spectrometer using a small portion of dried, ground sample. Sixteen scans were recorded over the range of 40,000 to 650 cm^{-1}.

Fluorescence Spectrophotometry:

Fluorescence data was collected on a Varian Cary Eclipse fluorescence spectrophotometer using a 1 cm disposable cuvette.

NMR Spectroscopy:

All ^1H Nuclear Magnetic Resonance (NMR) spectra (499.818 MHz) were obtained using an Agilent DD2 NMR spectrophotometer at 26°C unless otherwise indicated. Spectra of samples were recorded in solutions in $CDCl_3$, using TMS as an internal standard, D_2O or d6-DMSO.

FOX Assay:

FOX Reagent: Sorbitol (3.6 g, 19.8 mmol), xylenol orange (0.0143 g, 0.02 mmol), water (50 mL) and concentrated sulfuric acid (281 µL) were combined, followed by the addition of

$(NH_4)_2FeSO_4.6H_2O$ (0.0196 g, 0.02 mmol). The resulting solution was made up to a final volume of 200 mL with water.

Calibration: Standard solutions of H_2O_2 (0.25, 0.125, 0.0625, 0.03125, 0.015625 mM) were prepared. 50 µL of sample was added to 950 µL of FOX reagent, followed by incubation at room temperature for 30 minutes, after which point the absorbance at 560 nm was recorded. From this data a calibration curve was produced.

Assay procedure: 2 mg of the sample to be analysed was added to 0.25 mM H_2O_2 (200 µL), and after 1, 5 and 10 minutes 50 µL of this solution was added to 950 µL FOX reagent and incubated at room temperature for 30 minutes after which time the absorbance at 560 nm was recorded.

Peroxidase Assay:

Blank: H_2O (2.1 mL), 0.05M Tris-HCl pH 6 buffer (0.32 mL), 0.5% H_2O_2 (0.16 mL) and 5% pyrogallol aq. solution (0.32 mL) were combined and left at rt for 10 minutes. H_2O (0.1 mL) was added and the change in absorbance at 420 nm was immediately recorded over 3 minutes.

Sample: H_2O (2.1 mL), 0.05M Tris-HCl pH 6 buffer (0.32 mL), 0.5% H_2O_2 (0.16 mL) and 5% pyrogallol aq. solution (0.32 mL) were combined and left at rt for 10 minutes. Sample solution (2 mg/10 mL H_2O, 0.1 mL) was added and the absorbance at 420 nm was immediately recorded over 3 minutes.

Calculations:

$$\text{units per mL enzyme} = \frac{\left(\frac{\Delta A_{420}}{20\ \text{sec}_{\text{test sample}}} - \frac{\Delta A_{420}}{20\ \text{sec}_{\text{blank}}}\right) \times 3 \times \text{df}}{12 \times 0.1}$$

$\frac{\Delta A_{420}}{20\ \text{sec}}$ = maximum rate of change of abs at 420 over 20 seconds

3 = volume (mL) of assay

df = dilution factor

12 = extinction coefficient of 1 mg/mL purpurogallin at 420 nm

0.1 = volume (mL) of enzyme used

$$\text{units per mg solid} = \frac{\text{units per mL enzyme}}{\text{mg solid per mL enzyme}}$$

CHAPTER 3: Zn MOFs with N-donor group-based linkers for biomolecule encapsulation

3.1: Introduction and scope of the chapter

As discussed in chapter 1, the process of biomimetic mineralisation using metal-organic frameworks (MOFs) is a relatively new field of research and, as such, there are still many aspects that require further investigation. One example of this is the lack of understanding around what chemical (metal node and linker donor groups, pore surface chemistry) and structural (pore size and shape) features of MOFs are needed to ensure the biomolecule is successfully encapsulated and protected within the MOF without significant loss of activity. Given that MOFs are prepared from a building block approach that confers significant control over the MOF structure, pore surface chemistry and pore network, these aspects can be readily explored.

The extensive use of zeolitic imidazolate frameworks (ZIFs) for biomimetic mineralisation has been mentioned previously. Within this family of materials, ZIF-8[6, 47, 57, 61] and, to a slightly lesser extent, ZIF-90[65] are arguably the most used and studied for biomolecule protection. This is likely a result of the high porosity, excellent chemical and thermal stability, and low cytotoxicity.[47] Metal-azolate frameworks (MAFs), such as MAF-7, have also been shown to be able to effectively protect encapsulated enzyme.[65] The ligands used in the synthesis of each of these MOFs are shown in **Figure 42**. These materials all have sodalite topology in their targeted form, noting that diamond[112] and layered[113] forms are also possible; the sodalite topology confers a relatively small limiting pore aperture size between 3.2 and 3.5 Å and thereby prohibits diffusion of molecules greater than *ca*. 5 Å. These limitations for the sodalite topology ZIF biocomposites could be addressed by identifying new MOFs with better structure metrics for reactant and product diffusion.

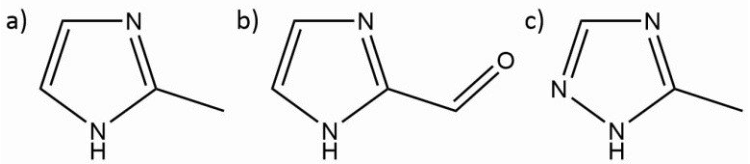

Figure 42: *Ligands used for the synthesis of a) ZIF-8, b) ZIF-90 and c) MAF-7.*

Each of these ligands contains basic N-donor binding sites (azine and azolate), and an absence of carboxylic acid groups that were present in the MOF linkers studied in Chapter 2. It is postulated that these MOFs are able to undergo biomimetic mineralisation due to a unique mechanism of

MOF growth initiated by Zn^{2+} ions aggregating around the biomolecule. Specifically, the mechanism for ZIF-8, and potentially other similar materials, involves the coordination of a metal node to the azine nitrogen, followed by deprotonation of the second nitrogen (azolate) which subsequently coordinates to a second metal centre (**Scheme 4**). This process repeats to form the ZIF-8 framework. This is the key reason why ZIF materials are believed to facilitate encapsulation via biomimetic mineralisation as growth is initiated by the high Zn^{2+} concentration at the biomolecule surface and propagated from the growing ZIF structure due to the facile deprotonation of coordinated imidazole.

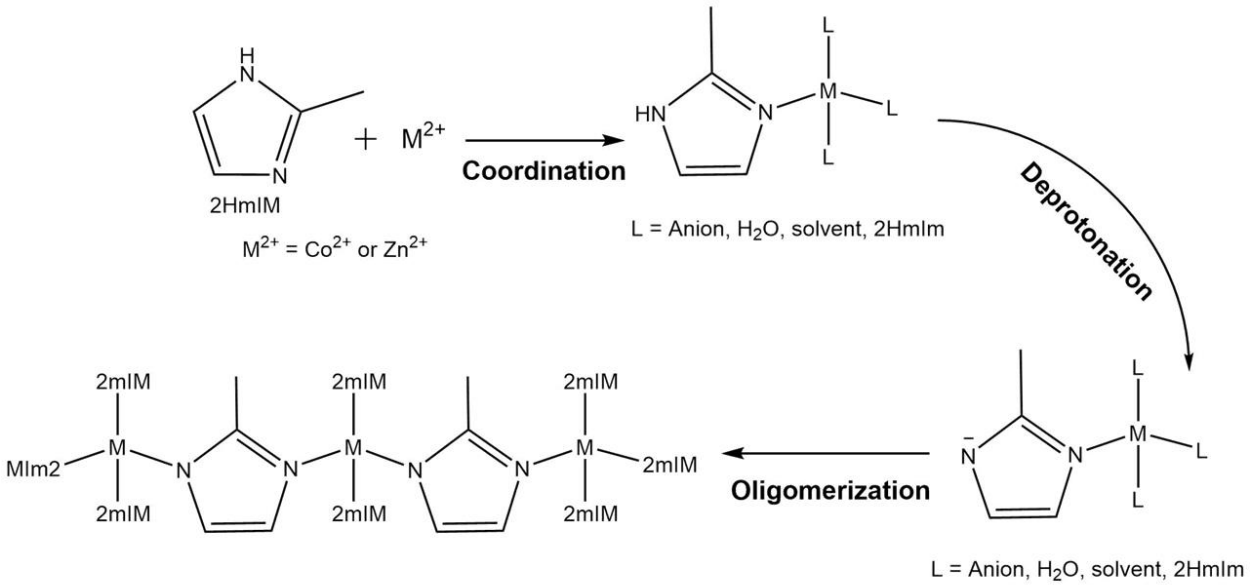

Scheme 4: *The proposed mechanism of ZIF-8 formation.*

In general, according to the HSAB principle wherein groups are defined as hard or soft Lewis acids or bases, azoles are typically classed as soft bases despite being deprotonated in order to coordinate to metal cations; this is the key reason for the less rapid metal-ligand coordination for azolate-based ligands.[114] It also must be noted that carboxylate MOF biocomposites are able to form, yet they are typically co-precipitated and so do not follow the biomimetic mineralisation mechanism seen for ZIF-8. One example of this is the immobilisation of soybean epoxide hydrolase with UiO-66-NH_2 via co-precipitation.[115] Nevertheless, studies have shown that biomolecules encapsulated within MOFs via biomimetic mineralisation are protected to a greater extent compared to those immobilised by co-precipitation.[6]

Thus, research presented in this chapter will utilise the observations obtained with ZIF materials to identify new MOFs with similar linkers that can undergo biomimetic mineralisation procedures rather than co-precipitation.

A large number of MOFs have been formed using a wide range of different N-donor binding sites. These typically require the use of sp^2 hybridised nitrogen atoms which bind to the metal nodes and can include groups such as azolates[116-120] (pyrazolate, imidazolate, triazolate, tetrazolate etc.) and pyridines,[121, 122] which refer to N-containing 5- and 6- membered rings respectively.

3.1.1: Review of metal azolate MOFs for biomolecule encapsulation

From the wide range of MOFs containing solely N-donor binding sites, a number were considered for their potential application to biomolecule encapsulation. To determine their suitability, the following criteria had to be met;

- A 2-D or 3-D connected structure with > 3.4 Å pore openings;
- Binary (or two component) MOFs;
- Chemically and thermally stable materials demonstrating permanent porosity;
- Commercially available or synthetically accessible linkers;
- Use of a zinc metal ion;
- Aqueous, room temperature MOF synthesis must be possible; and
- Solely N-donor binding sites

The majority of these criteria were also used in chapter 2 and are retained here for the same reasons. To add an element of consistency between all MOFs tested, only those with a zinc metal node will be studied. Further, while aqueous synthetic conditions at room temperature are desirable, it was noted in chapter 2 that MOF syntheses can be altered to meet this criterion.

One family of MOFs identified utilises a 3,3',5,5'-tetramethyl-4,4'-bipyrazole (H_2Me_4bpz) linker (**Figure 43**), and has been formed with zinc, but also cobalt, cadmium, copper and silver salts.[123, 124] As noted, to keep an element of consistency between these N-donor MOFs and the ZIF materials, only the zinc-based material will be considered. The zinc-based MOF has a cubic framework, with hourglass-shaped pores with a neck diameter of 3.3 Å and 10 Å pores.[123] Thus, the structure is comparable to the pore aperture and cavities of ZIF-8 (3.4 and 11.6 Å). Further, a key advantage of this MOF is the isoreticular analogues using 4,4'-bipyrazole (H_2bpz) and 1,4-(4-bispyrazolyl)benzene ligand (H_2bpb) linkers (**Figure 44**).[125, 126] Thus, further studies could be

extended to the isoreticular MOFs. This would allow for an excellent comparison of the biomineralisation ability of each of these frameworks, and an investigation of whether different functional groups present impact this ability. However, one issues with Zn(Me_4bpz) is that the reported synthesis requires extensive heating and the use of organic solvents, making it incompatible with biomolecule encapsulation. Thus, syntheses using aqueous conditions at room temperature would have to be designed to ensure compatibility with biomolecule encapsulation.

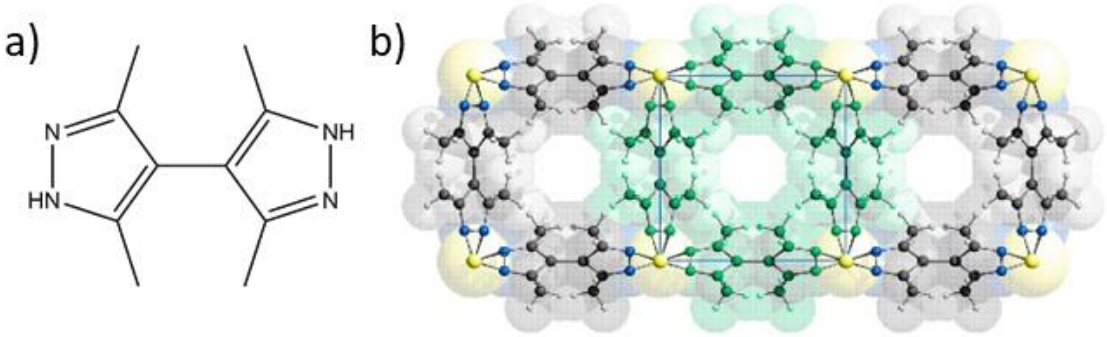

Figure 43: *a) H_2Me_4bpz ligand and b) Crystal structure of Zn(Me_4bpz) viewed along the c axis.*[123]

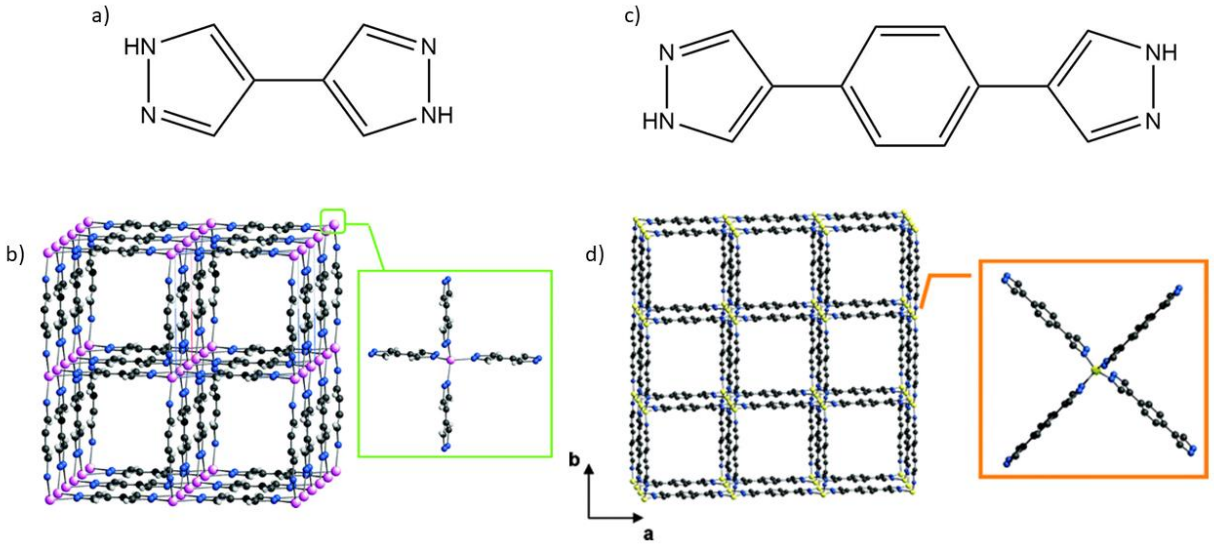

Figure 44: *Isoreticular analogues of Zn(Me_4bpz): a) H_2bpz ligand, b) Zn(bpz) MOF structure, c) H_2bpb ligand and d) Zn(bpb) MOF structure.*[125, 126]

A number of other zinc-based MOFs have also been reported that contain ditopic N-donor ligands. MFU-4, MFU-4l and CFA-1 are three MOFs within this family (**Figure 45**).[127-129] In DMF at 140°C, MFU-4 forms as an open, cubic framework with pore apertures and sizes of 2.52 Å and 3.87/11.94 Å respectively when van der Waals radii are considered.[127] However, when the synthetic conditions are changed to include DMA at 120°C, an extremely dense coordination polymer forms. MFU-4l utilises an extended version of the linker used in MFU-4, such that two

distinct pores sizes form (11.97 Å and 18.56 Å), which were both larger than the pores present in MFU-4.[128] CFA-1 is a chiral MOF, containing pore diameters in the range 9-12 Å.[129] However, the syntheses for these ligands involves multiple steps, meaning scalability may be challenging.

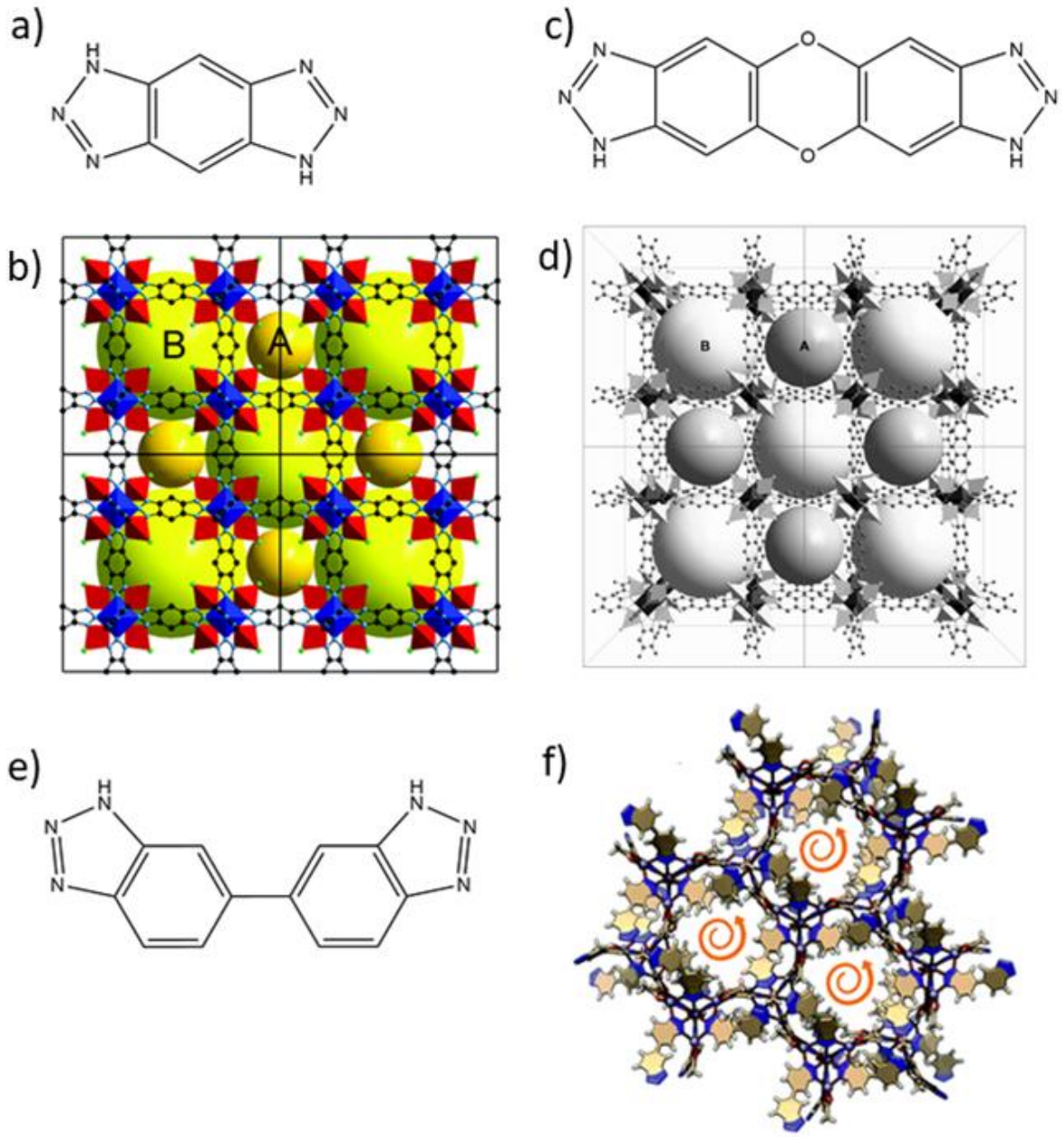

Figure 45: *a) Ligand used to form MFU-4, b) crystal structure of MFU-4 viewed along the a axis, yellow balls represent the size of imaginary spheres able to fit inside the framework pores,[127] c) ligand used to form MFU-4l, d) crystal structure of MFU-4l viewed along the a axis, grey balls represent in the size of imaginary spheres able to fit inside the framework pores,[128] e) ligand used to form CFA-1, f) crystal structure of CFA-1.[129]*

A further example of a zinc-based MOF comprised of N-donor containing ligands is Zn(TDT) (H_3TDT = 4,5-di(1H-tetrazol-5-yl)-2H-1,2,3-triazole) (**Figure 46**). Zn(TDT) formed in

dimethylacetamide (DMA) at 95°C has sodalite topology with pore apertures of 6.4 Å opening up into pores with a diameter of 12 Å.[40] Thus, the overall topology and pore size is comparable to that of ZIF-8, which has pores with a diameter of 11.6 Å.[62] However, the larger pore apertures in Zn(TDT) would likely allow better substrate diffusion. Further, this MOF has also been reported as a potential drug-delivery agent for the anticancer drug 5-Fluorouracil, suggesting that it is able to successfully encapsulate other moderately sized guests.[40]

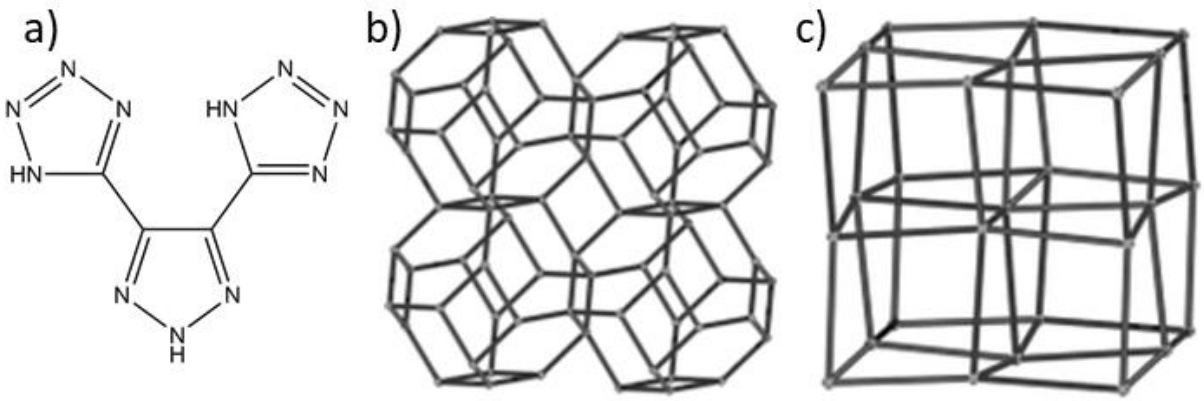

Figure 46: *a) H_3TDT ligand, b) sodalite topology of Zn(TDT) formed in DMA at 95°C and c) primitive cubic topology of Zn(TDT) formed in DMF at 120°C.*[130]

Yet upon increasing the temperature and changing the solvent (DMF), Zn(TDT) forms with primitive cubic (pcu) topology.[130] These observations show the MOF structure is heavily dependent on the synthesis conditions and thus, it is possible that different materials may form when attempting biomimetic mineralisation in predominantly aqueous solvents at room temperature. While forming a different MOF structure in the biocomposite may still provide protection, the sodalite topology form of Zn(TDT) could provide an ideal comparison to ZIF-8, ZIF-90 and MAF-7 biocomposites.

Zinc-based MOFs using a similar ligand (4, 5-bis(tetrazol-5-yl)imidazole (H_3IDT)) have also been studied (**Figure 47**).[131-135] Two examples have been reported, namely the formation of a 3-D MOF from an aqueous solution of zinc, linker and adenine at 160°C for 3 days, while a 2-D material was formed in identical conditions with the adenine replaced with 4,4'-bipyridine. Curiously, the syntheses required the use of adenine or 4,4'-bipyridine which, even though not part of the final structure, still add complexity to the synthesis. As such, these do not seem like prime candidates to asses for biomimetic mineralisation.

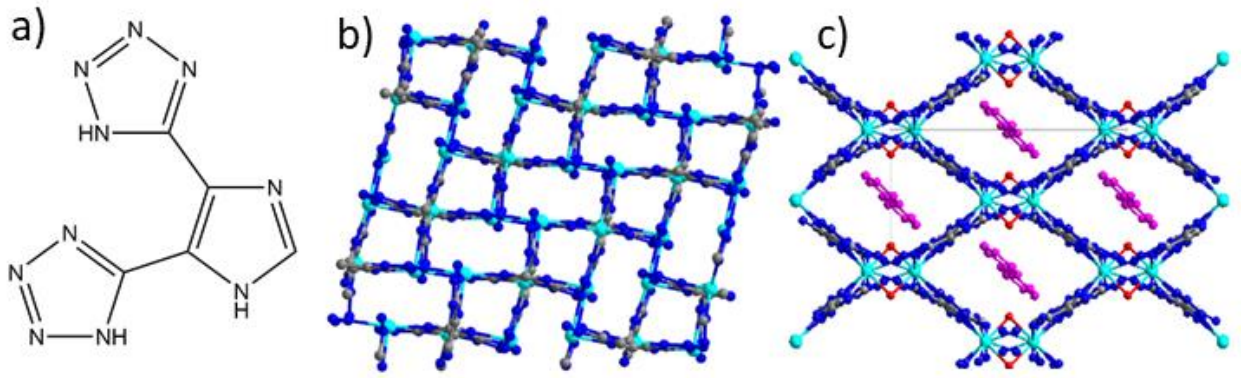

Figure 47: *a) H_3IDT ligand, b) crystal structure of Zn(IDT) formed in water in the presence of adenine at 160°C for 3 days and c) crystal structure of Zn(IDT) formed in water in the presence of 4,4'-bipyridine at 160°C for 3 days .*[135]

Several tritopic MOFs reported by the Long group contain solely N-donor binding sites.[136, 137] Two of these ligands are 1,3,5-tris(1H-pyrazol-4-yl)benzene (H_3BTP) and 1,3,5-benzenetristetrazolate (H_3BTP), which have been used to form 3-D MOFs with Ni/Cu/Zn/Co and Mn respectively (**Figure 48**). As only zinc-based MOFs are to be investigated, only this material will be discussed. The zinc-based MOF of BTP possesses relatively small 4 Å channels but was reported to have exceptional chemical and thermal stability, yet, both of these ligands required multistep syntheses (five synthetic steps) and so they were not considered for preliminary investigations.

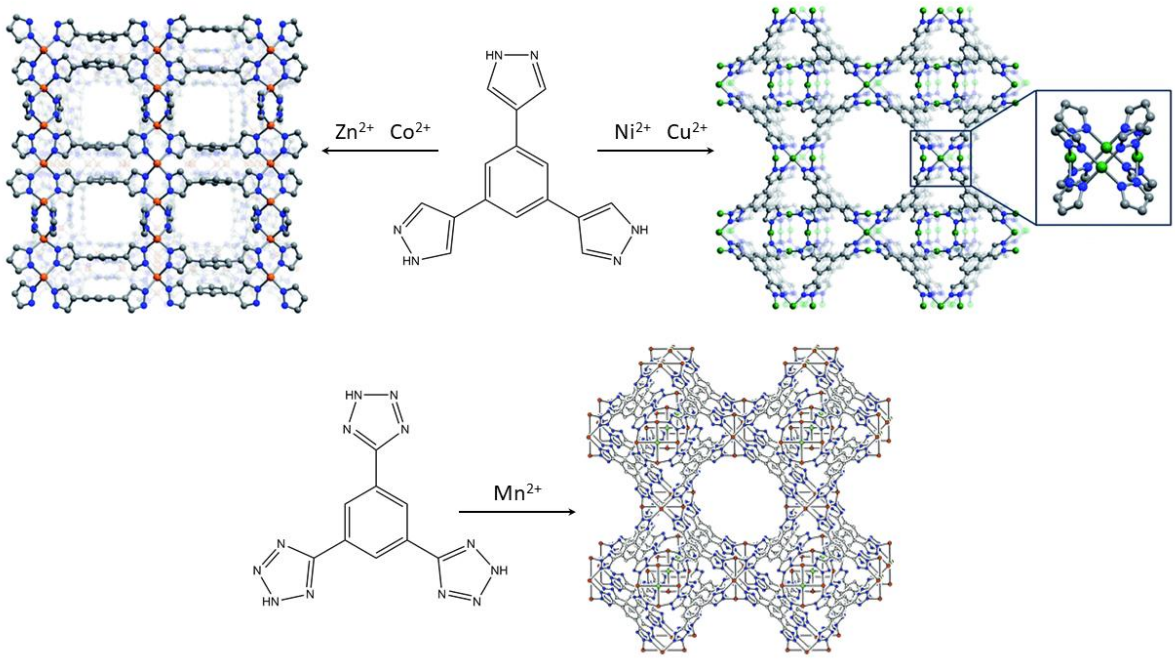

Figure 48: *Synthesis of Zn/Co or Ni/Cu MOFs with H_3BTP ligand (top) and synthesis of Mn MOF using H_3BTT ligand (bottom).*[136, 137]

Given the points raised above in relation to the criteria, Zn(Me_4bpz) and Zn(TDT) appear to be the most suitable due to the synthetic accessibility of the linkers. Zn(Me_4bpz) also has the key advantage of having a number of isoreticular analogues that could also be investigated. Further, the investigation of Zn(Me_4bpz) and Zn(TDT) allows the comparison of MOFs synthesised using ditopic and tritopic linkers, while retaining the same metal ion.

3.2: Results and Discussion

3.2.1: Zn(Me_4bpz)

3.2.1.1: Biocompatible synthesis and characterisation of Zn(Me_4bpz)

The literature synthesis of Zn(Me_4bpz) was performed by dissolving H_2Me_4bpz (50 mM) in DMF, followed by addition of $Zn(CF_3SO_3)_2$ (50 mM).[123] This solution was then stirred in a high-pressure glass tube at 130°C for 24 h. Due to the specific zinc salt and high-pressure equipment not being readily available, this literature synthesis was not attempted. Instead, attempts to form this zinc-based MOF in aqueous conditions at room temperature were undertaken directly. This involved using a 1:1 molar ratio of metal to Me_4bpz ligand as this is the ratio in the target structure, as well as the stoichiometry used in the literature synthesis. The MOF synthesised in aqueous conditions is hereafter referred to as **Zn(Me_4bpz)-aq.** The ligand was insoluble in water, and so a minimum volume of methanol was used to solubilise it. By increasing the methanol to water ratio, it was found that a 1:10 ratio resulted in the addition of the minimum quantity of methanol needed to fully solubilise the ligand. MOF synthesis was then attempted by dissolving the ligand in water and methanol with or without added base, followed by the dropwise addition of an aqueous solution of zinc nitrate. In the absence of base, no precipitate formed, and in the presence of ammonia an amorphous material was produced. Finally, it was established that the use of sodium bicarbonate as the base was required to induce precipitation of crystalline material (**Figure 49**). However, analysis of the PXRD data revealed that the X-ray diffraction data for the crystalline material does not entirely match the simulated powder patterns of other zinc-containing MOFs formed with the same or similar ligands.[123, 138, 139] However, the lowest angle peaks in both the experimental and synthesised PXRD patterns overlapped, suggesting that the overall structure is similar. Therefore, it is possible that the synthesised **Zn(Me_4bpz)-aq** material forms with a cubic arrangement, as is seen in the reported zinc MOFs containing an identical or similar ligand.

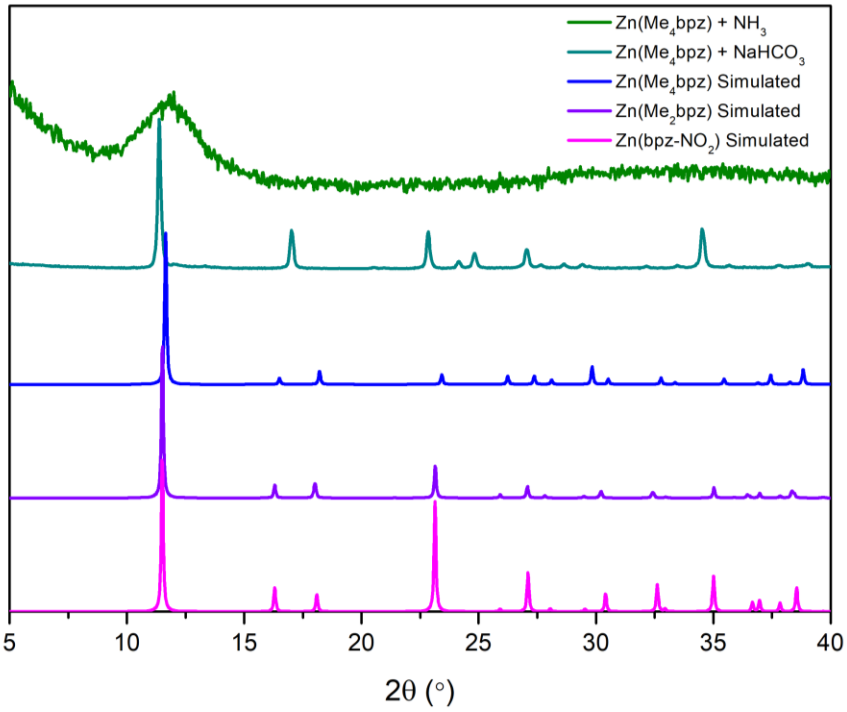

Figure 49: *Experimental PXRD patterns of synthesis attempts for* ***Zn(Me$_4$bpz)-aq*** *using NH_3 (red) and $NaHCO_3$ (blue) compared to patterns for Zn(Me$_4$bpz),[123] Zn(Me$_2$bpz)[138] and Zn(bpz-NO$_2$)[139] simulated from single crystal data.*

The key difference in the PXRD pattern of the experimentally synthesised **Zn(Me$_4$bpz)-aq** and the three reported N-donor containing Zn-MOFs are the peaks between 2θ = 16° and 18°. The single peak present within this range in the PXRD pattern of the synthesised MOF is approximately midway between the two peaks present in the simulated pattern, possibly suggesting some change in symmetry.

It was postulated that slight differences in the PXRD pattern may be due to the different solvents with which each sample is solvated. To examine this, samples of **Zn(Me$_4$bpz)-aq** were soaked in a variety of solvents for 1 hour, collected by centrifugation and analysed by ^{1}H NMR spectroscopy (solvate composition) and PXRD. The solvents of interest were dichloromethane (DCM), acetone and dimethylformamide (DMF) as these were the solvents used to wash the MOFs reported in the literature. Stepwise soaking of acetone followed by DCM, each for 1 hour, was also trialled to reduce the polarity change compared to if the water-solvated sample was solely treated with DCM. The ^{1}H NMR spectra for **Zn(Me$_4$bpz)-aq** samples soaked in acetone, DMF or DCM each showed peaks corresponding to these solvents, in addition to water. Thus, as water was still present in the sample, soaking the samples for 1 hour was unable to fully exchange the MOF solvates. Nevertheless, PXRD data was collected to determine if changes to the solvation may have caused changes in the MOF structure. However, PXRD data revealed no observable changes

in peak positioning after soaking the as-synthesised material in each of these solvents (**Figure 50**). This lack of change indicated that solvation was not the main cause of the differences in the PXRD patterns.

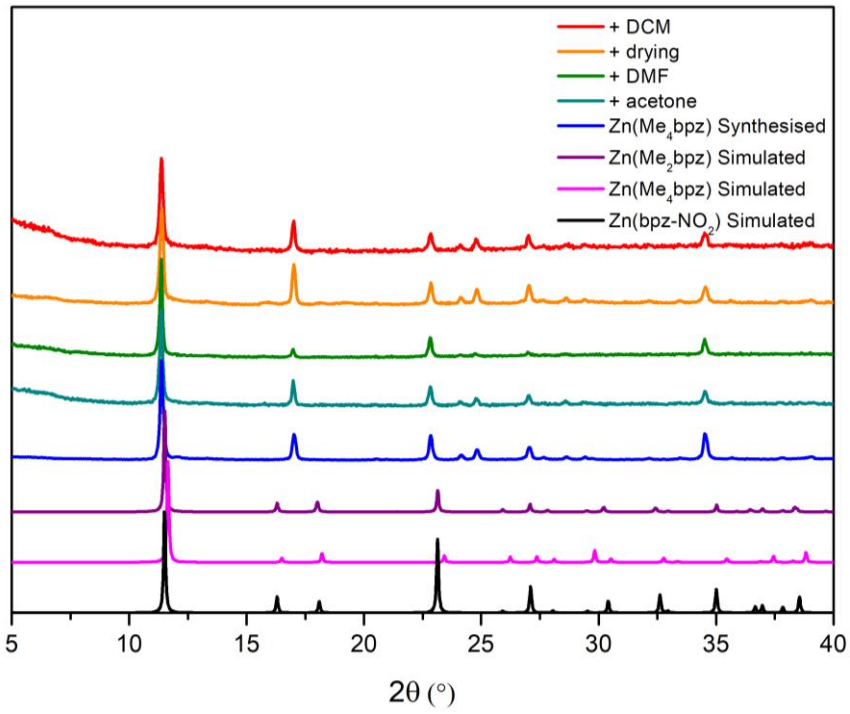

Figure 50: *PXRD of* ***Zn(Me$_4$bpz)-aq*** *exposed to DCM, DMF and acetone, as well as a dried sample compared to* ***Zn(Me$_4$bpz)-aq*** *synthesised and Zn(Me$_2$bpz),[138] Zn(Me$_4$bpz)[123] and Zn(bpz.NO$_2$)[139] simulated from single crystal data.*

Further, to confirm the presence of zinc in the original **Zn(Me$_4$bpz)-aq** material synthesised using the 1:1 metal to ligand ratio, scanning electron microscopy (SEM) and energy dispersive X-ray spectroscopy (EDX) was performed (raw data shown in **Table 21** and **Figure 94** in appendix). EDX data confirmed the presence of zinc, with an average Zn:N ratio of 1:3.5 across the sample, corresponding to a metal to ligand ratio of 1:0.9.

Thus, the EDX data supports the composition of **Zn(Me$_4$bpz)-aq** being very similar to the composition of material synthesised via the literature solvothermal methods, which has a 1:1 metal to ligand ratio, despite small discrepancies in the PXRD data. However, there have also been a number of other reported Zn MOFs containing the Me$_4$bpz ligand with a 1:1 metal to ligand ratio. One example is Zn(Me$_4$bpz)(SO$_4$); a 2-D MOF with Zn(Me$_4$bpz) sheets held together via SO$_4$ molecules.[140] This highlights that a 1:1 Zn to Me$_4$bpz ratio (N:Zn = 4:1) is not necessarily indicative only of the cubic structure of Zn(Me$_4$bpz) MOF.[123]

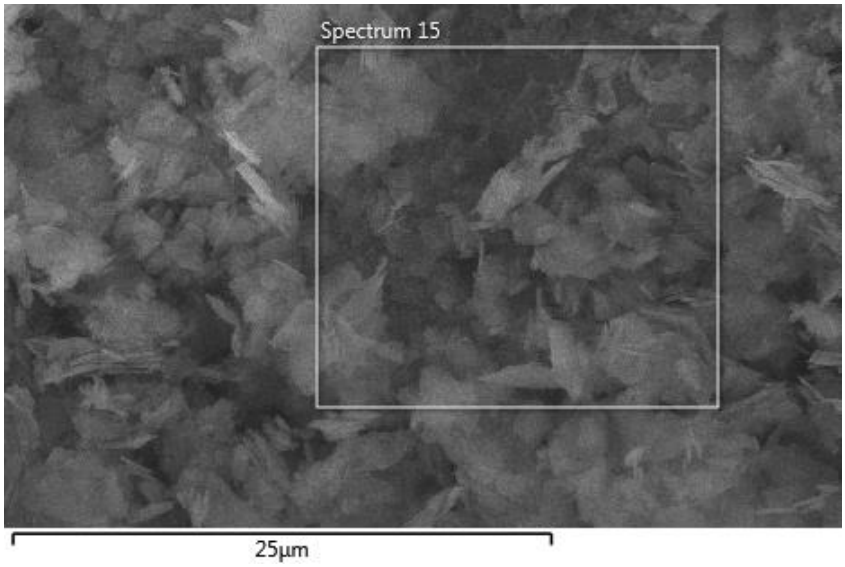

Figure 51: *SEM image of* ***Zn(Me$_4$bpz)-aq****, the outlined region is spectrum 15 which had a 6 At% zinc concentration as determined by EDX, with the top-left corner of the outlined region containing material that appears distinct from the bulk material.*

As the exact structure of the synthesised **Zn(Me$_4$bpz)-aq** was not known, gas adsorption was used to determine whether the material had similar porosity to the reported **Zn(Me$_4$bpz)** MOF. To ensure that the gas adsorption data for the synthesised MOF could be compared to the reported MOF, identical conditions were used for the activation and gas adsorption experiment.[123] Activation was performed at 110°C overnight, after which the uptake of N_2 at 77K was recorded (**Figure 52**). PXRD analysis confirmed that no decomposition of the MOF had occurred under the activation conditions used (**Figure 89** in appendix).

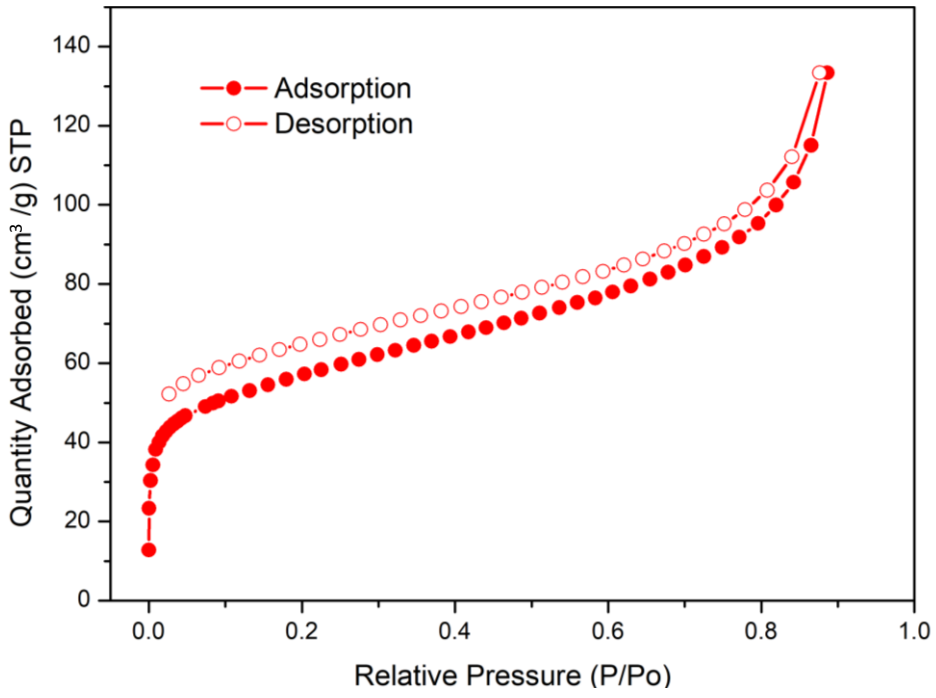

Figure 52: *Gas adsorption isotherm for* ***Zn(Me$_4$bpz)-aq*** *under N_2 at 77K.*

77 K N_2 adsorption data shows an initial uptake of N_2 at low pressures, indicating the presence of micropores, while an additional uptake at higher pressures suggests that mesopores are also present. These observations were also made for the literature MOF with the same Me_4bpz ligand. Slight hysteresis is observed, further supporting the presence of mesopores.

Using this data, a calculated BET surface area of 203 m^2/g was obtained, which is notably lower than the BET surface area of 396 m^2/g reported in the literature for **Zn(Me_4bpz)**.[123] The resulting pore size distribution data derived from the gas adsorption data (**Figure 53**) indicated a pore width of approximately 16 Å, which is significantly different to the *ca.* 10 Å pore width reported for the literature MOF.[123] Other peaks in the pore size distribution data were likely due to large mesopores present with pore widths of 25 Å and 40-60 Å, which vary slightly from the 25-50 Å mesopores reported for the literature **Zn(Me_4bpz)** material. For the literature material, these 'mesopores' were deemed to be interparticle voids, which may also be the case for the **Zn(Me_4bpz)-aq** material given the crystal morphology seen via SEM.

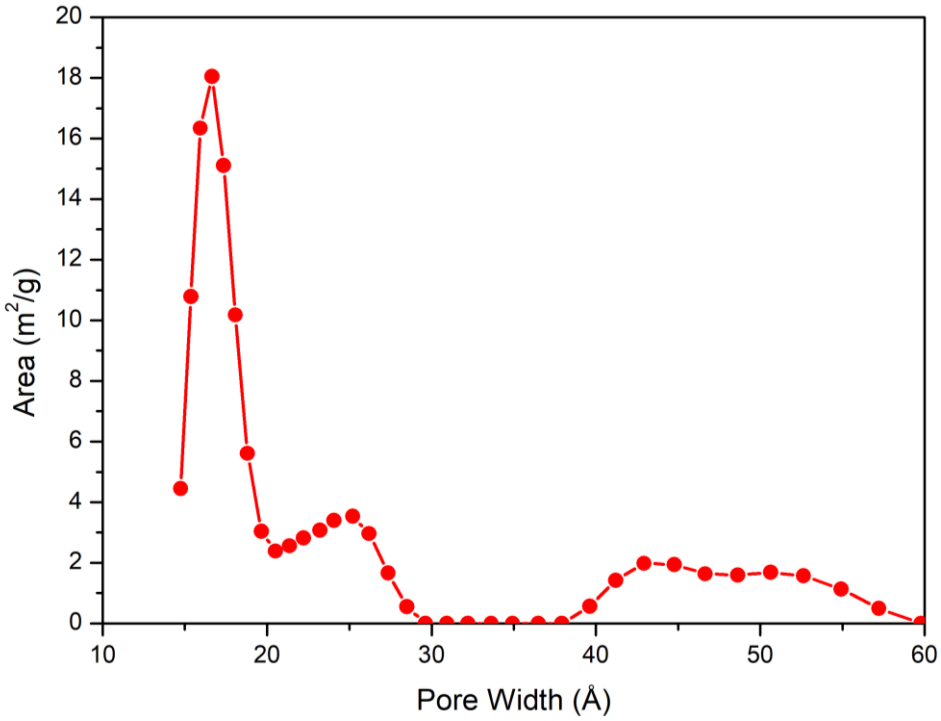

Figure 53: *Pore size distribution of* ***Zn(Me_4bpz)-aq*** *determined by applying the NLDFT to the N_2 isotherms.*

The notable deviations in both the pore size distribution and surface area calculations, coupled with differences in the PXRD patterns, for the synthesised **Zn(Me_4bpz)-aq** material compared to the reported MOF strongly suggested that the structure of the two materials are different. This may be due to missing linker defects or slight deviations in the structure.

To better understand the structure of **Zn(Me$_4$bpz)-aq**, attempts were made to grow single crystals of the material (**Table 22** in the appendix). A number of conditions were trialled, some of which were reflective of the original aqueous conditions outlined above but with variations such as the use of a different base, slow mixing or evaporation to try and reduce the rate of precipitation. Numerous attempts were also trialled with excess ligand added as it has been shown for other MOFs such as ZIF-8 that altering the metal to ligand ratio can alter the particle size produced, with excess ligand promoting the formation of larger crystals.[141] The use of solvothermal methods, with DMF as the solvent, was also attempted as this was reflective of the original synthesis conditions reported in the literature for **Zn(Me$_4$bpz)**.[123]

The results show that slow evaporation was the only method that was able to grow single crystals, yet, this was also only the case when an excess molar concentration of ligand was used. Metal to ligand ratios of 1:2, 1:4 and 1:16 were used, with and without base. For the attempts with added base, the initial precipitate that formed was isolated by centrifugation, and the supernatant was collected and allowed to undergo slow evaporation. This was performed with and without added enzyme (BSA) to determine whether the presence of enzyme could promote crystal formation. Attempts with no added base were also conducted to prevent the initial precipitation event, and, therefore, ensuring that sufficient concentrations of ligand and metal remained in solution to allow crystal growth.

All attempts with no added base successfully formed single crystals. The 1:16 metal to ligand ratio produced large, needle-like crystals overnight, while the 1:4 and 1:2 ratios formed smaller, cubic or tetragonal crystals after two and ten days respectively (**Figure 54a-c**). For the attempts with added base, only the supernatant from the synthesis using the 1:4 metal to ligand ratio in the presence of BSA was successful, forming large crystals after seven days (**Figure 54d**).

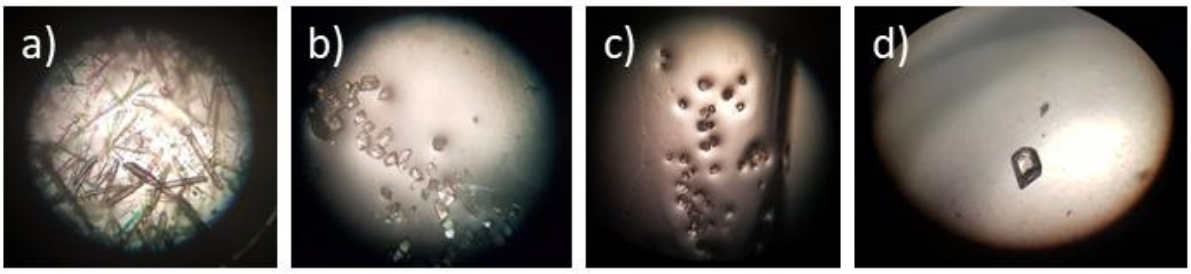

Figure 54: *Microscope images of single crystals formed for a) 1:16, b) 1:4 and c) 1:2 metal to ligand ratio with no base and no BSA and d) 1:4 metal to ligand ratio with base and BSA.*

To determine whether the structure of each of the single crystals synthesised matched that of the original **Zn(Me$_4$bpz)-aq** material synthesised, PXRD data was collected for crushed samples of each single crystal (**Figure 55**). In particular, this was performed to ensure that changing the metal to ligand ratio did not impact the structure of the material formed.

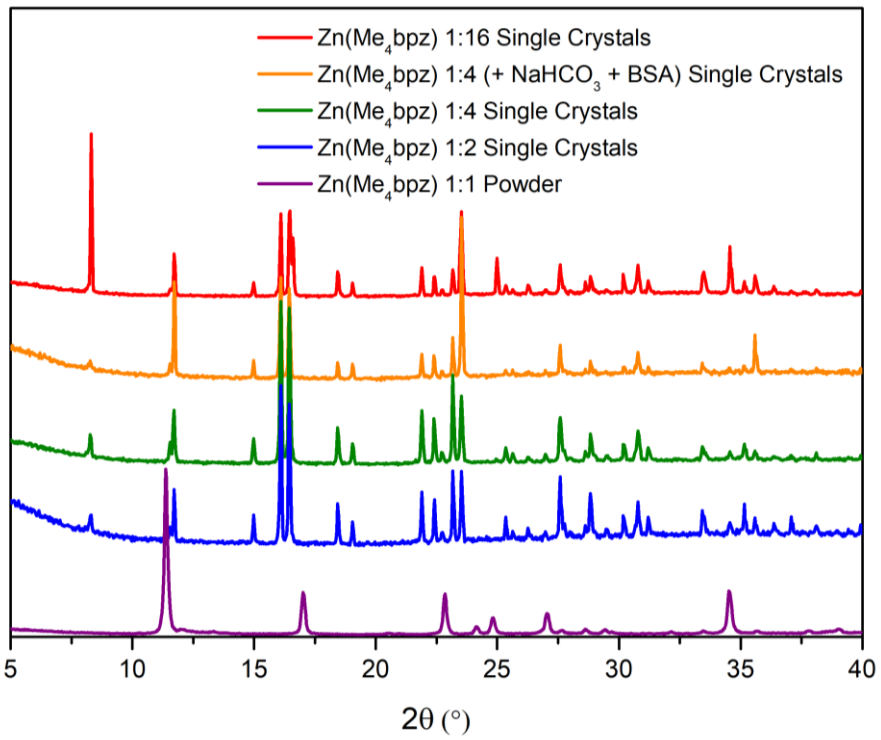

Figure 55: *PXRD data for crushed single crystals of* ***Zn(Me$_4$bpz)-aq*** *produced using 1:16 (red), 1:4 (orange), 1:2 (blue) metal to ligand ratio (no base, no BSA) and 1:4 metal to ligand ratio (with base and BSA, green) compared to the* ***Zn(Me$_4$bpz)-aq*** *precipitate (1:1 metal to ligand ratio, purple).*

The PXRD data for the single crystals were significantly different to that of **Zn(Me$_4$bpz)-aq** synthesised with a 1:1 metal to ligand ratio. While there appeared to be slight overlap of peaks around 2θ = 11.5°, the remainder of the powder pattern indicated that the two materials were distinct. Yet, PXRD results revealed that all four single crystal samples had matching powder patterns, with the only significant discrepancies being changes in relative peak intensities, likely due to different preferred orientations during crystal growth as a result of the varying crystallisation times.

To investigate the new structure, a portion of one of the crystals formed in the 1:16 metal to ligand ratio sample was used to obtain a single crystal structure. No zinc could be identified in the structure, and so the material was deemed to be a hydrogen-bonded organic framework, hereafter referred to as **Me$_4$bpz-HOF**. The material crystallised with a tetragonal crystal system

and in the $I4_1/acd$ space group with the structure shown in **Figure 56**, (unit cell parameters a = 24.7504(4) Å, b = 24.7504(4) Å and c = 14.8658(4) Å). The asymmetric group contains a single ligand and a singly deprotonated water molecule (**Figure 57**).The methyl groups present in the Me_4bpz linker point into the otherwise square-shaped channels along the c axis. Water molecules are shown to occupy the x-shaped pores when viewed along the c axis.

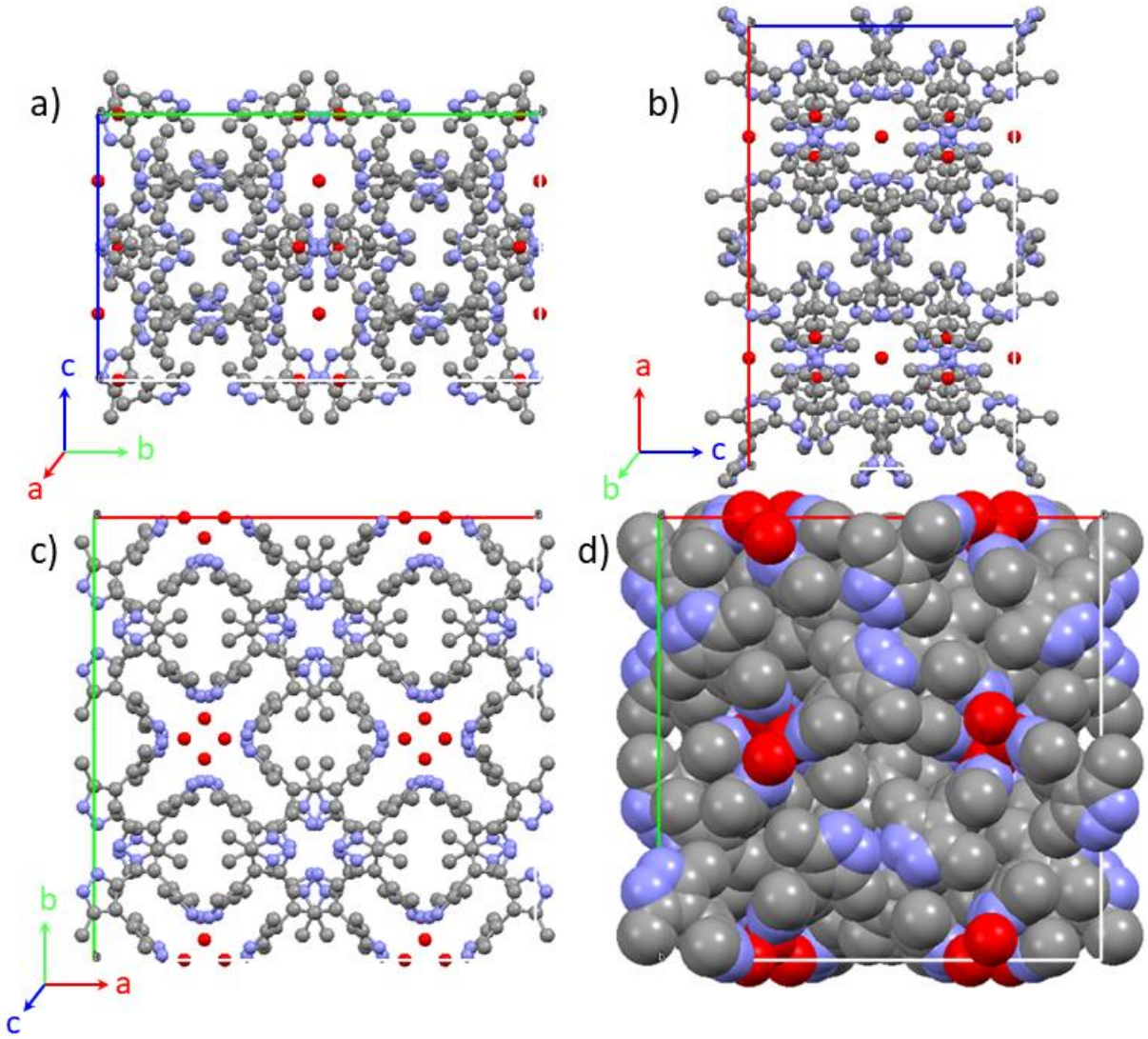

Figure 56: *a-c) Unit cell for* ***Zn(Me$_4$bpz)-aq*** *formed with a 1:16 metal to ligand ratio viewed along the a, b and c axes and d) space-filling data for* ***Zn(Me$_4$bpz)-aq*** *viewed along the c axis. H atoms omitted for clarity (C = grey, N = purple, O = red).*

The lack of zinc, in addition to the extensive hydrogen-bonding occurring throughout the structure revealed that the material formed from solutions containing excess ligand was a densely packed hydrogen-bonded organic framework. Thus, it is likely that by increasing the ratio of ligand to metal, there was no longer sufficient concentration of zinc present in solution to form the desired MOF. The presence of the methyl groups and structurally important water molecules

block any channels and render the material non-porous. Thus, this material is still referred to the **Me$_4$bpz-HOF** for simplicity sake despite HOFs typically possessing porosity. This close-packed, non-porous structure is not desirable for enzyme encapsulation as it would significant hinder substrate diffusion through the framework to reach the enzymatic site within.

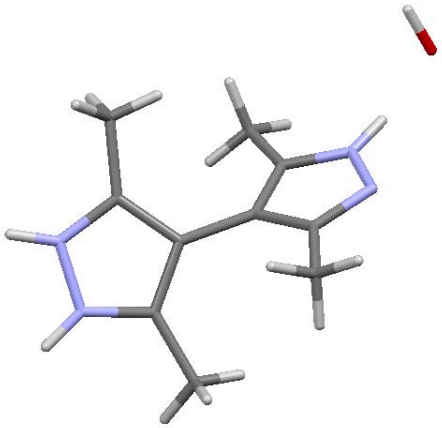

Figure 57: *Asymmetric unit of* ***Me$_4$bpz-HOF****. (C = grey, N = purple, O = red, H = light grey). The hydrogen atom of the pyrazole ring that hydrogen bonds with a symmetry generated pyrazole is disordered over both nitrogen atoms, whereas pyrazole NH hydrogen bonded to the water molecule was localised. These hydrogen positions could be located in the electron density difference map.*

As mentioned above, extensive hydrogen-bonding was observed within the crystal structure, including hydrogen bonding between the bis-pyrazole compound and water molecules present in the pores in a tetrahedral arrangement (**Figure 58**).

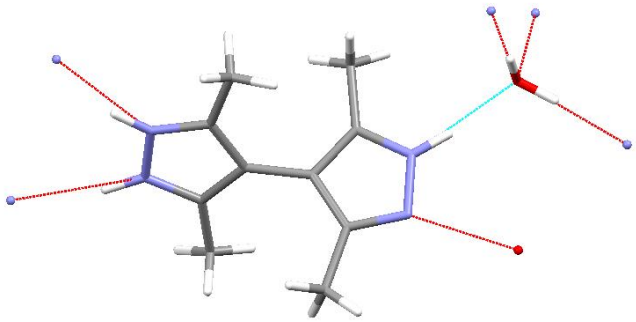

Figure 58: *Single crystal data for the* ***Me$_4$bpz-HOF*** *showing the tetrahedral hydrogen bonding formed between the water molecules and ligand. (C = grey, N = purple, O = red, H = white, dashed lines = H-bonding contacts).*

Given that the synthetic conditions used to obtain **Me_4bpz-HOF** contained Zn^{2+} ions, the synthesis was further investigated. Curiously, no precipitation immediately occurred upon dissolving only the ligand and base; instead the HOF formed immediately upon addition of zinc. Yet, when a solution of ligand and base was allowed to undergo slow evaporation, clear and colourless needle-like crystals of **Me_4bpz-HOF** formed overnight. This suggested that the zinc acted as a catalyst to promote the instantaneous formation of the hydrogen-bonded framework.

To confirm that the single crystal data was representative of the bulk samples obtained under all slow evaporation conditions, a PXRD pattern was simulated from the single crystal data and compared to the experimental pattern of the synthesised **Me_4bpz-HOF** crystals (**Figure 59**). The identical peak positions in both PXRD patterns indicated that the crystal structure was representative of the bulk with no additional crystalline phases present.

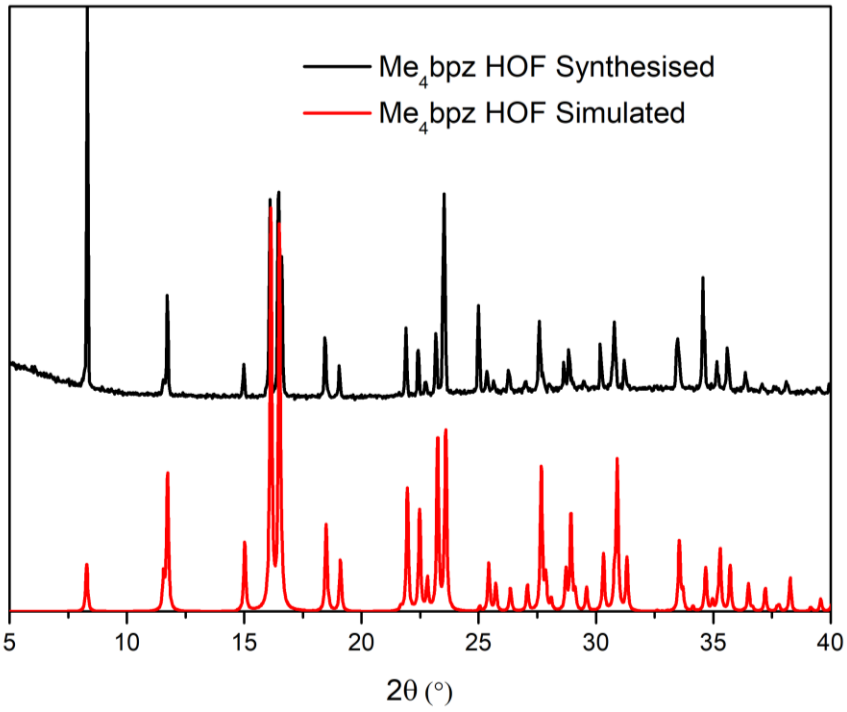

Figure 59: *PXRD data for experimentally synthesised* ***Me_4bpz-HOF*** *(black) compared to the PXRD pattern simulated from single crystal data.*

Analysis by SEM-EDX was used to further confirm the absence of zinc in the **Me_4bpz-HOF** samples. EDX data calculated zinc percentages between 0.0 and 0.2%, strongly supporting the conclusions that this material was a hydrogen-bonded organic material. Any trace quantities of zinc present in the sample are likely to be left-over from the synthetic procedure.

3.2.1.2: Synthesis of protein@Zn(Me$_4$bpz)-aq and protein@Me$_4$bpz-HOF biocomposites

While permanently porous materials are desirable for biocatalysis applications, both **Zn(Me$_4$bpz)-aq** and the **Me$_4$bpz-HOF** were used for enzyme encapsulation attempts, despite the close-packed nature of the latter. Such hydrogen-bonded organic frameworks lacking in permanent porosity may still be applicable to biomolecule therapeutic delivery and thus biocomposites of this dense phase were investigated. To form the **Me$_4$bpz-HOF**, a 1:16 metal to ligand ratio was used as this was the only ratio that was able to form as a microcrystalline precipitate upon combining the metal and ligand/base solutions. While it was found that the presence of zinc was not required to form crystals of the **Me$_4$bpz-HOF**, the addition of zinc allowed for precipitation of the microcrystalline powder which is easier to characterise.

To examine whether protein would alter the structure of the frameworks formed, syntheses were conducted with a sample of enzymes. For the **Zn(Me$_4$bpz)-aq** MOF and **Me$_4$bpz-HOF**, FITC-tagged catalase (FCAT) was used, predominantly due to the FOX assay allowing for rapid determination of enzymatic activity. Catalase was tagged with FITC to remove any inconsistencies between results from CLSM and other techniques that would have otherwise been performed with native enzymes. For both materials, the protein encapsulation procedure involved the addition of enzyme to the ligand solution followed by subsequent addition of the zinc solution. PXRD analysis confirmed that the addition of FCAT did not change the structure of the **Zn(Me$_4$bpz)-aq** or **Me$_4$bpz-HOF** materials that formed (**Figure 60**).

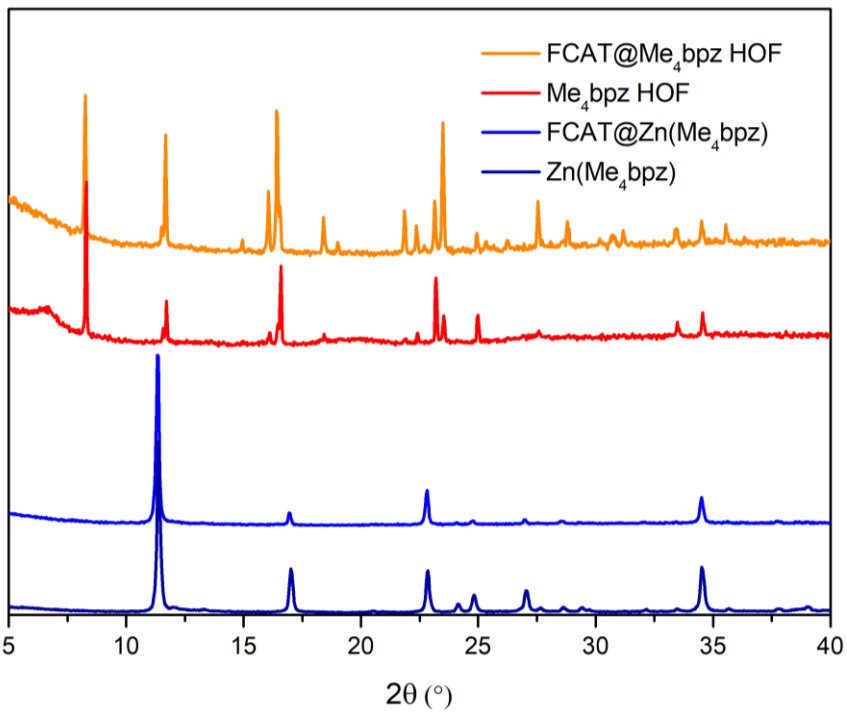

Figure 60: *PXRD for **Zn(Me$_4$bpz)-aq** and **Me$_4$bpz-HOF** synthesised with and without added FCAT.*

To determine whether the addition of enzyme influenced the rate of growth for either of the frameworks, turbidity data was collected (**Figure 61**). By extension, this was used to provide insight into whether enzyme encapsulation might occur via biomimetic mineralisation, through biomolecules accelerating framework growth.

As outlined in chapter 2, turbidity analysis is performed by measuring the change in absorbance of a wavelength not absorbed by the material forming. Thus, increases in absorbance are due to the formation of a solid that scatters incident light. More rapid increases in absorbance are indicative of more rapid precipitation.

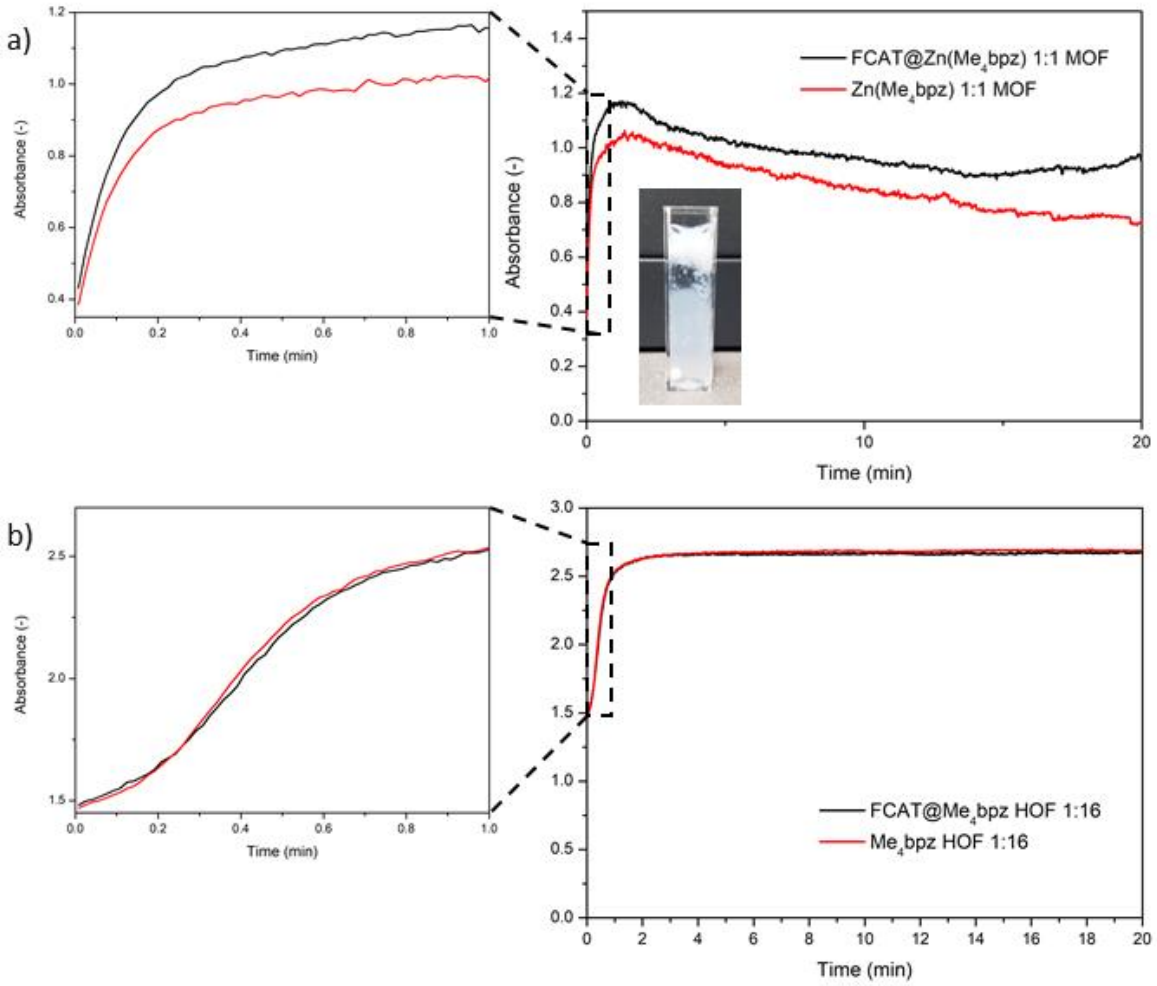

Figure 61: *Turbidity graphs for a) the* ***Zn(Me$_4$bpz)-aq*** *MOF (inserted image is the sample immediately after turbidity testing) and b)* ***Me$_4$bpz-HOF*** *with (black) and without (red) the FCAT added initially.*

Turbidity data reveals that the **Zn(Me$_4$bpz)-aq** MOF forms very rapidly, both with and without added enzyme, upon addition of zinc to the ligand solution, as seen by the immediate sharp increase in absorbance, agreeing with experimental observations. After this initial precipitation

event, the absorbance reaches a maximum, followed by a subsequent reduction in absorbance, likely due to aggregation of the precipitate on the surface of the solution (**Figure 61a** insert). While rapid stirring was used throughout the entire duration of turbidity analysis, this was not sufficient to ensure thorough mixing of the entire contents of the cuvette. Nevertheless, comparison of the initial precipitation rates of **Zn(Me$_4$bpz)-aq** with and without added enzyme reveals that the presence of enzyme resulted in a small but observable increase in the precipitation rate, suggesting that biomimetic mineralisation may be occurring.

The turbidity results for the **Me$_4$bpz-HOF** material showed a similar trend to that of **Zn(Me$_4$bpz)-aq**, wherein an initial rapid precipitation was seen within the first minute, both with and without added enzyme, agreeing with experimental observations. However, no decrease in absorbance was seen over the course of the analysis, likely because the material was denser and did not float. Comparison of turbidity data for the HOF material with and without added FCAT showed no significant difference in the rate or precipitation, making biomimetic mineralisation unlikely.

To confirm the presence of FCAT in all samples formed, solid state UV-Vis analysis was conducted. Free FCAT absorbs strongly at 500 nm due to the fluorescein isothiocyanate tag (**Figure 62**).

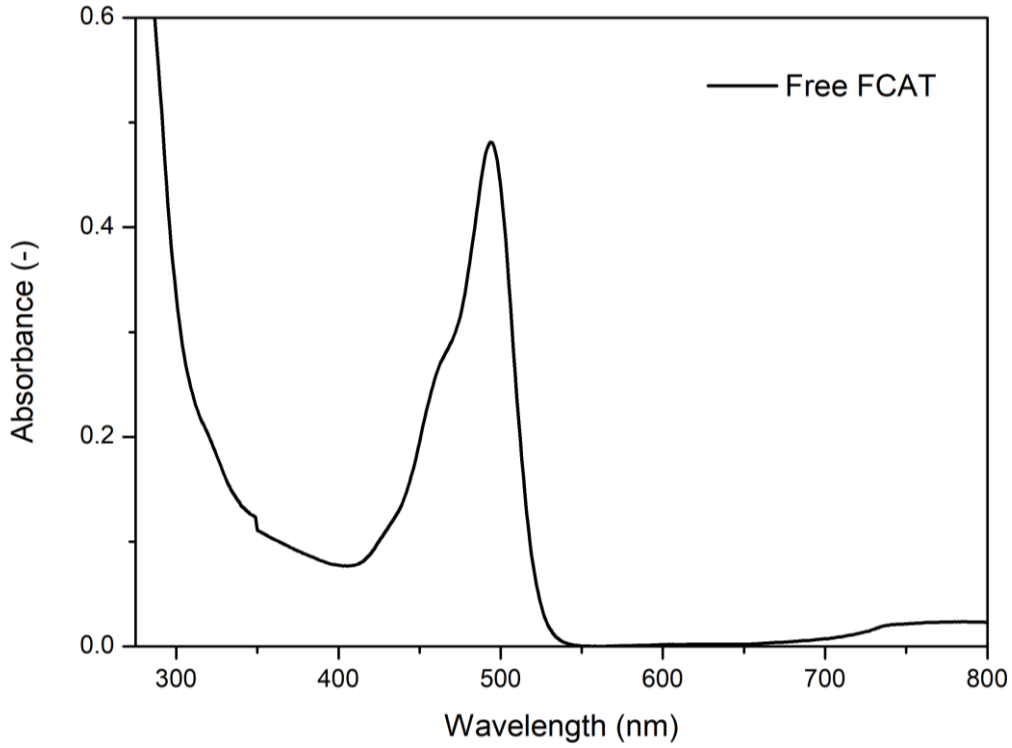

Figure 62: *Solution-state UV-Vis absorbance for free FCAT.*

Solid-state UV-Vis data for both pure **Zn(Me$_4$bpz)-aq** and pure **Me$_4$bpz-HOF** showed that neither of these materials absorbs strongly around 500 nm, and so any absorbance at this wavelength for the FITC-enzyme@**Zn(Me$_4$bpz)-aq** and FITC-enzyme@**Me$_4$bpz-HOF** samples was assumed to

be due to the presence of FITC-tagged enzyme. Solid-state UV-Vis analysis of FCAT@**Zn(Me$_4$bpz)-aq** and FCAT@**Me$_4$bpz-HOF** strongly indicated the presence of FCAT within these samples (**Figure 63**); however, the technique does not provide spatial information demonstrating whether the enzyme is present within the crystals or purely surface bound.

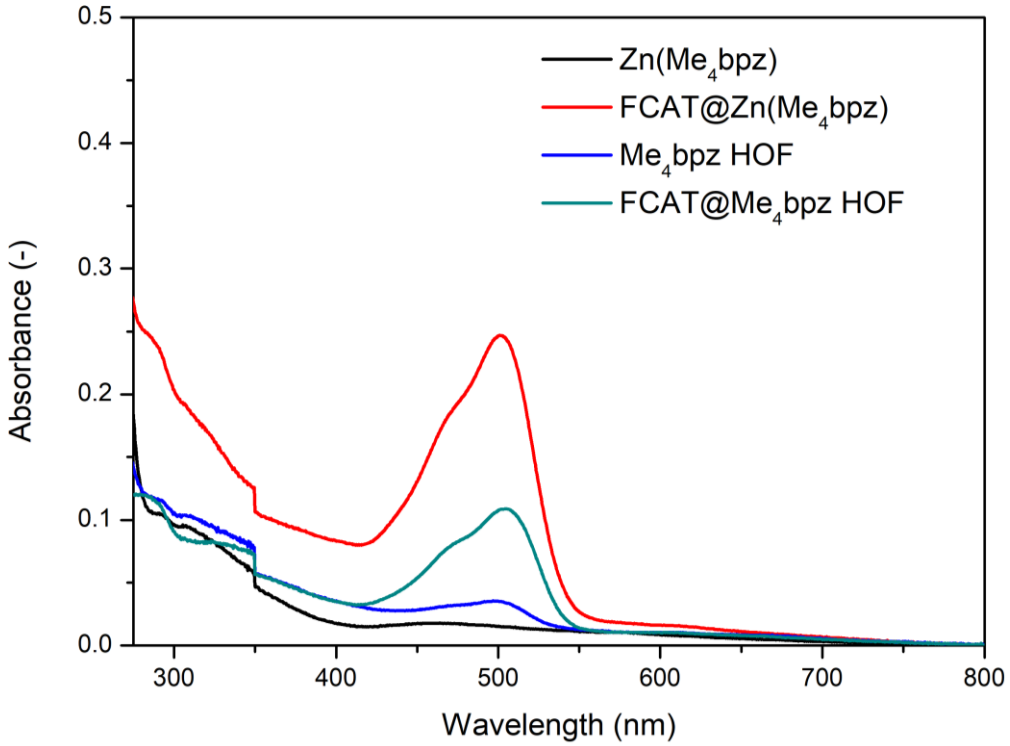

Figure 63: Solid-state UV-Vis absorbance for **Zn(Me$_4$bpz)** and **Me$_4$bpz-HOF** formed with and without added FCAT.

To ensure future testing of enzymatic activity within the FCAT@**Zn(Me$_4$bpz)-aq** and FCAT@**Me$_4$bpz-HOF** materials could be performed with equal enzyme concentrations, the percentage FCAT loading within each of the frameworks was calculated. A limitation of the assay data presented in chapter 2 for the zinc carnosine MOF was that the enzyme concentrations in each sample were not consistent, meaning that only the relative changes in activity could be compared. Thus, by calculating the enzyme loading within each sample, all future tests can be performed with consistent enzyme concentrations to allow for comparison of absolute activities.

To determine the FCAT loading in the **Me$_4$bpz-HOF**, a known mass of the FCAT@HOF sample was dissolved in citrate buffer (pH 5, 0.1 M), and the fluorescence of the resultant solution was measured. Calibration data was then used to convert this fluorescence reading into a concentration of FCAT and, by extension, a %w/w loading of FCAT within the HOF. This method was not compatible with the FCAT@**Zn(Me$_4$bpz)-aq** sample as the MOF was unable to be dissolved in any solvents that would not impact the fluorescent tag. Instead, inductively coupled plasma mass spectrometry (ICP-MS) was used to determine the sulfur concentration of free FCAT

and FCAT@**Zn(Me$_4$bpz)-aq** after digestion in a mixture of concentrated nitric and hydrochloric acids. The calculated FCAT loadings are outlined in **Table 13**, with raw data and calculations shown in appendix (**Table 19** (ICP-MS) and **Figure 90** & **Figure 91** & **Table 20** (fluorescence)). This data is consistent with loadings achieved for other enzyme@ZIF materials.[142]

Table 13: *Calculated %w/w FCAT loading within* ***Me$_4$bpz HOF*** *and* ***Zn(Me$_4$bpz)*** *MOF samples.*

	%w/w FCAT Loading
Zn(Me$_4$bpz)-aq (ICP-MS)	1.7 ± 0.8%
Me$_4$bpz-HOF (Fluorescence)	1.6 ± 0.5%

3.2.1.3: Analysis of protein encapsulation/protection within Zn(Me$_4$bpz)-aq and Me$_4$bpz-HOF

To provide preliminary insight into the spatial distribution of the FITC-tagged enzyme relative to the MOF and HOF crystals, CLSM was used (**Figure 64**). As noted, this tool provides overlayed optical and fluorescence microscopy images which can indicate whether the enzyme is co-located with the crystals. If the particles are sufficiently large, these images can also suggest whether the enzyme is likely to be predominantly surface-bound or encapsulated.

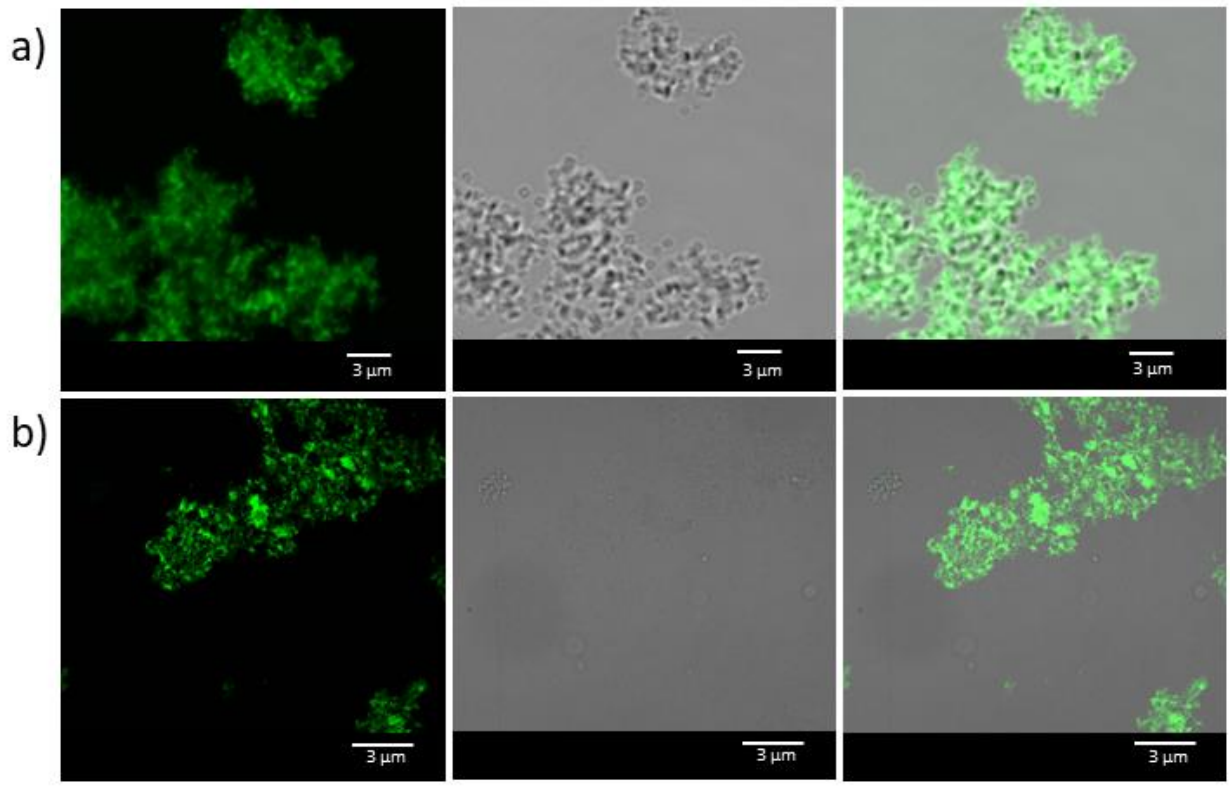

Figure 64: *Confocal images (fluorescence, bright field and overlay) for a) 1:1 FCAT@* ***Zn(Me$_4$bpz)-aq*** *MOF and b) FCAT@* ***Me$_4$bpz-HOF.*** *Tagged enzyme is shown in green.*

CLSM data revealed that the crystals for both the **Zn(Me$_4$bpz)-aq** MOF and the **Me$_4$bpz-HOF** were extremely small, and beyond the resolution of the microscope. As such, it was impossible to determine whether the enzyme was predominantly located on the surface of the crystals or encapsulated within. While there were a small number of slightly larger crystals in the **Zn(Me$_4$bpz)-aq** sample which appeared to potentially have encapsulated enzyme, it was unknown whether these were representative of the bulk sample.

To expand on the preliminary CLSM data, quantitative assays were used to determine whether the enzyme was encapsulated within and protected by the MOF and HOF crystals. Specifically, ferrous oxidation of xylenol orange (FOX) assays, which have been explained in chapter 2, will be used to determine the presence and stability of the FCAT present.

General MOF stability testing

To determine the test conditions to which the FCAT@**Zn(Me$_4$bpz)-aq** and FCAT@**Me$_4$bpz-HOF** samples would be exposed, the chemical and thermal stability of the frameworks needed to be ascertained. This ensured that no framework decomposition would occur during the FOX assays. Specifically, both frameworks were exposed to elevated temperatures, organic solvents and pHs from 5 to 10f for three minutes, followed by PXRD analysis (**Figure 65**). Both **Me$_4$bpz-HOF** and FCAT@**Me$_4$bpz-HOF** dissolved in DMF and so no PXRD data was obtained.

The PXRD data for **Zn(Me$_4$bpz)-aq** revealed that the MOF was stable in all conditions tested, with the exception of the pH 5 buffer for which a slight reduction in crystallinity was observed, as indicated by the lower signal-to-noise ratio. However, the PXRD data for all conditions tested also contained a low intensity peak at $2\theta = 7°$, which was not present in the pattern for the original material. This suggested that a new phase may be beginning to form, or the framework is beginning to slowly decompose. Nevertheless, the retention of all key peaks following exposure to each of the conditions tested suggested that the frameworks would remain intact.

Conversely, the PXRD data for **Me$_4$bpz-HOF** revealed that it had much lower stability compared to **Zn(Me$_4$bpz)-aq**, likely as a result of the weaker hydrogen bonding interactions. In all conditions tested, with the exception of pH 10, the HOF material either completely or partially decomposed during the three-minute exposure time. Curiously, when identical stability testing was performed for FCAT@**Me$_4$bpz-HOF** samples, the PXRD results indicated that the enzyme had a stabilising effect on the framework, as no observable decomposition occurred following exposure to pH 5 and 80°C. However, the presence of FCAT was unable to stabilise the HOF in organic solvents.

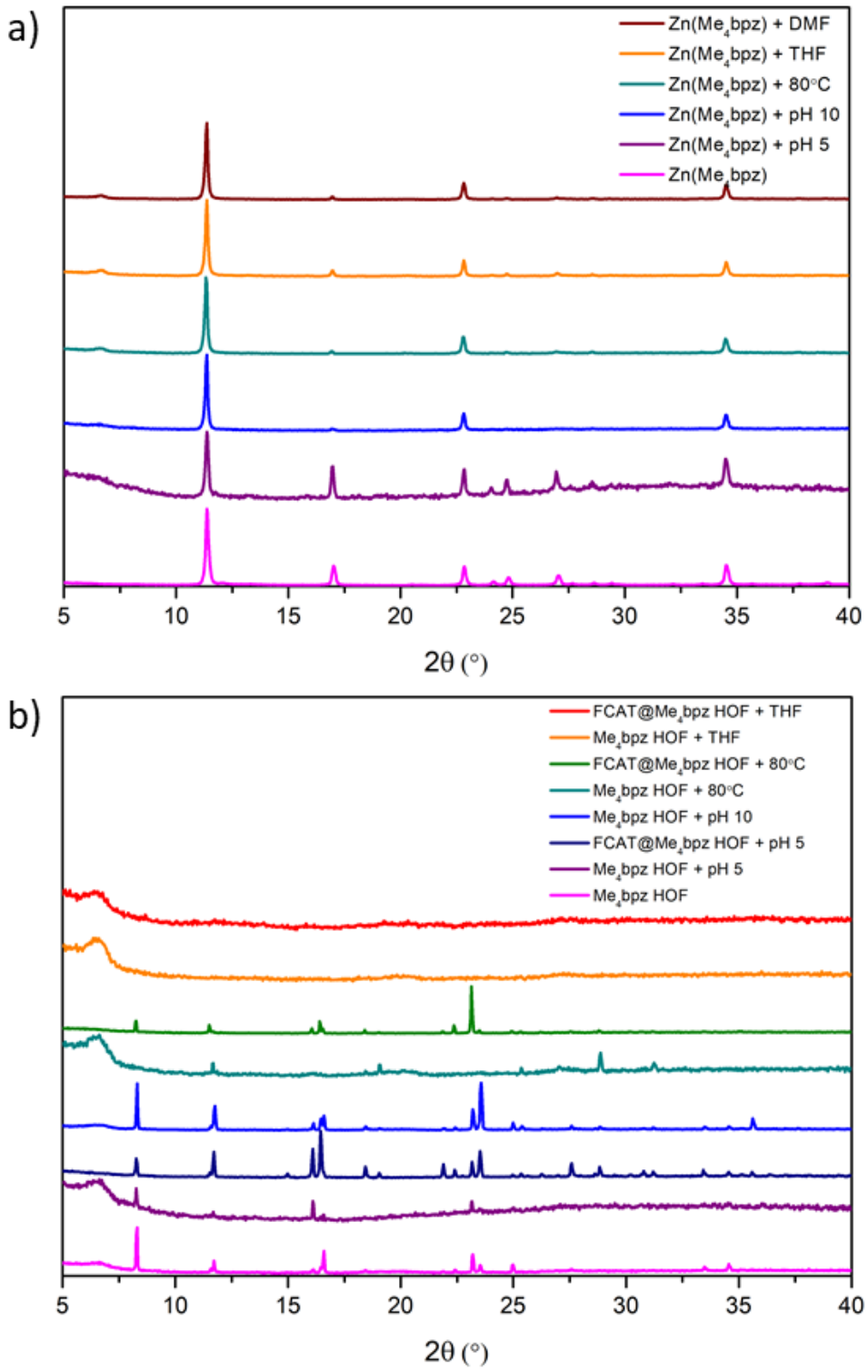

Figure 65: *PXRD patterns for a)* ***Zn(Me$_4$bpz)-aq*** *(1:1) and b)* ***Me$_4$bpz-HOF*** *before and after exposure to DMF, THF, pH 5 (0.1M citric-trisodium citrate buffer), pH 10 (0.1 M glycine buffer) and 80°C for 3 minutes.*

The exact cause of this stabilising effect had by the enzyme is not known, however, there were two possibilities considered. The first was that the formation of an enzyme surface-coating around the MOF which limited exposure to the harsh external conditions. Another explanation was that encapsulated enzyme within the HOF prevented it from collapsing and/or dissolving.

The inability of the enzyme to stabilise the framework in THF and DMF was noted too. The PXRD of the **Me$_4$bpz-HOF** after exposure to these solvents, without added enzyme, showed it was amorphous. Hydrogen-bonded organic frameworks rarely show stability in polar organic solvents,[143] due to the ability of such solvents to disrupt the hydrogen-bonding within the material, which could have caused the rapid loss of crystallinity.

Therefore, the **Zn(Me$_4$bpz)-aq** MOF was deemed to be sufficiently stable for activity testing under all of the conditions tested, while the **Me$_4$bpz-HOF** was only considered to be stable for activity testing at elevated temperatures and pH 5 to 10.

To ascertain that **Zn(Me$_4$bpz)-aq** and **Me$_4$bpz-HOF** do not decompose hydrogen peroxide and, by extension, create false positive enzymatic activity readings in the FOX assays, assays were carried out for these materials (**Figure 66**). This was performed by exposing either material to 0.25 mM hydrogen peroxide, with aliquots of the hydrogen peroxide/sample suspension taken at specific time intervals which were then reacted with FOX reagent. This assay data revealed minimal hydrogen peroxide decomposition compared to the initial concentration of 0.25 mM, indicating that both materials were inactive.

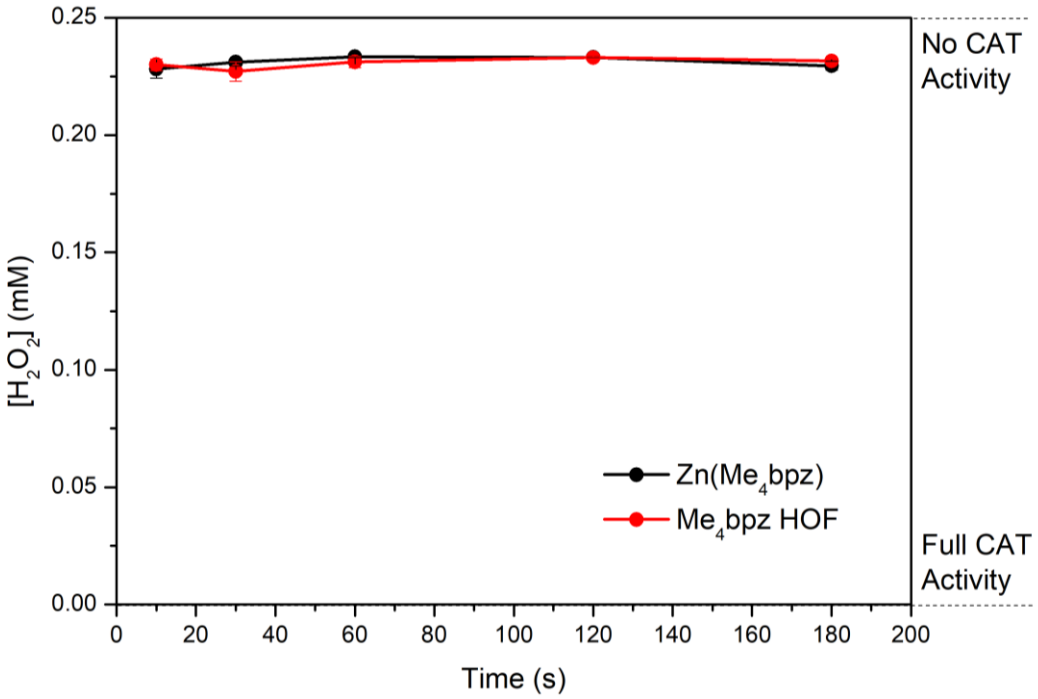

Figure 66: *Hydrogen peroxide decomposition by **Zn(Me$_4$bpz)-aq** and **Me$_4$bpz-HOF** determined via FOX assay. Initial [H_2O_2] was 0.25 mM. Time refers to the period of time the samples were exposed to the 0.25 mM H_2O_2 solution before reacting with the FOX reagent. Error bars show the standard error of three independent measurements.*

Protective capacity toward elevated temperatures

To determine the protective capacity of both **Zn(Me$_4$bpz)-aq** and **Me$_4$bpz-HOF** for encapsulated FCAT at elevated temperatures, the reduction in enzymatic activity for the FCAT@MOF/HOF samples upon heating was determined and compared to that of the free enzyme. The heating procedure involved exposure of aqueous stock solutions of FCAT@**Zn(Me$_4$bpz)-aq**, FCAT@**Me$_4$bpz-HOF** and free FCAT to elevated temperatures. To depict the rate of change of enzymatic activity, aliquots of the sample stock solutions were taken at specific time intervals up until 3 minutes and immediately cooled on ice to prevent further decomposition due to residual heat. Each aliquot was then reacted with 0.25 mM hydrogen peroxide for 10 minutes before transferring 50 µL of the hydrogen peroxide solution into 950 µL of FOX reagent. After 30 minutes, the absorbance at 560 nm of the FOX reagent was measured and converted to a hydrogen peroxide concentration using a calibration curve.

Raw data showing the change in enzymatic activity of each sample, including free FCAT, after exposure to elevated temperatures for 3 minutes are shown in **Figure 67**. High hydrogen peroxide concentrations, close to 0.25 mM, indicate minimal hydrogen peroxide decomposition and, thus, low catalase activity, while low hydrogen peroxide concentrations indicate the reverse.

The information provided by the raw data was two-fold; first it indicates the relative activities of each sample and secondly, it shows the rates of activity loss upon heating. The raw data revealed that the free FCAT had a much higher overall enzymatic activity up to 70°C compared to the FCAT within either of the frameworks. Several scenarios can explain this reduction in activity. If no encapsulation occurred (i.e. surface bound or a conglomerate), then the presence of the framework may decrease the enzymatic activity of the catalase (surface adsorption can inactivate enzymes[65]). Alternatively, if encapsulation was successful (the CLSM analysis was equivocal to this point), it caused a reduction in the activity of the enzyme, possibly due to reduced accessibility of the active sites. For the assay, reagents must reach the FCAT encapsulated within either of the frameworks; to do so they must diffuse through the pores, a process that is more hindered than when the enzyme is free in solution. As such, more hindered diffusion would lead to less enzymatic activity being utilised in a given period of time, causing a reduction in the recorded activity. This is commonly observed that encapsulated enzymes are not as active as the free enzyme under optimal conditions.[65, 98] This latter hypothesis was supported by the observation that the enzymatic activity for FCAT in **Me$_4$bpz-HOF** was negligible due to the lack of pores present in this material. Any activity present for this sample would have been due to surface-bound enzyme of crystal defects that allow for substrate diffusion.

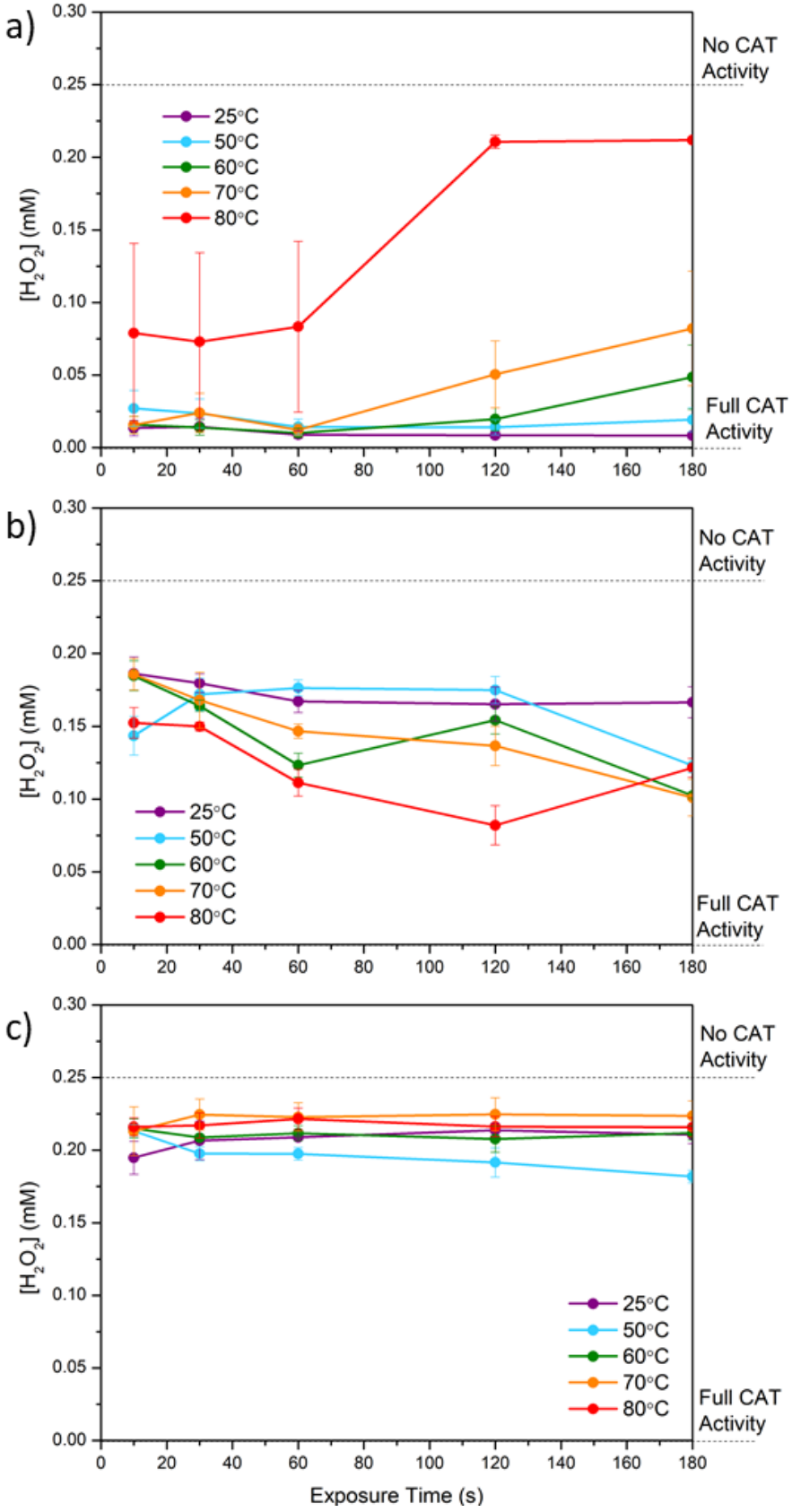

Figure 67: *Catalytic activity of FCAT in a) free FCAT, b) FCAT@**Zn(Me₄bpz)-aq** and c) FCAT@**Me₄bpz-HOF** after exposure to 25, 50, 60, 70 and 80°C for 3 minutes. The assay was performed with [FCAT] = 30 nM and initial [H_2O_2] = 0.25 mM with a H_2O_2 exposure time of 10 minutes. Exposure time refers to the time over which the sample was exposed to elevated temperatures. Error bars show the standard error for three independent measurements.*

The raw data was then used to determine the overall relative activity losses after exposure to the elevated temperatures for both the free enzyme and the FCAT@framework samples (**Figure 68**).

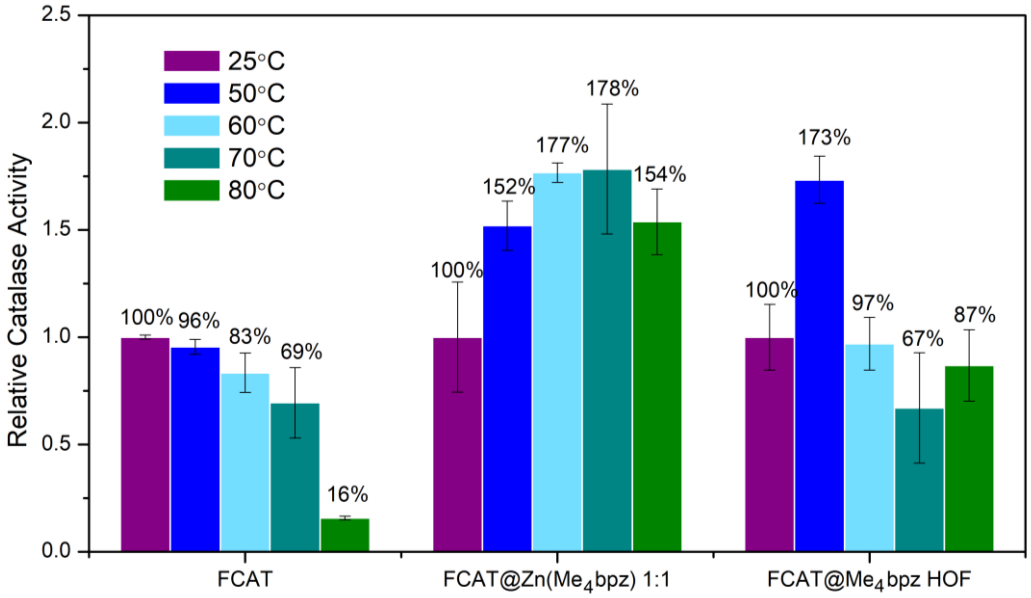

Figure 68: *Relative FCAT activity (relative to 25°C for each sample) in free FCAT, FCAT@**Zn(Me₄bpz)-aq** and FCAT@**Me₄bpz-HOF** after exposure to 25, 50, 60, 70 and 80°C for 3 minutes. The assay was performed with an FCAT concentration of 30 nM and initial H_2O_2 mM. Error bars show the standard error for three independent measurements.*

This assay data depicted the expected trend for the free enzyme wherein the activity gradually decreased as the temperature in increased, with an 84% reduction in enzymatic activity upon heating to 80°C. Catalase is reported to be stable up to temperatures of 60°C, and so the significant loss of enzymatic activity observed after 80°C treatment agrees with literature data.[16]

For both the FCAT@**Zn(Me₄bpz)-aq** and FCAT@**Me₄bpz-HOF** samples the enzymatic activity appeared to increase initially as the exposure temperature was increased to 70°C and 50°C, respectively, before the activity decreased. However, an increase in activity was not expected; it is likely that this was due to enzyme leaching from the composites. If this occurred, the enzyme would be more freely accessible, and not limited by substrate diffusion through the pores or defect pathways of the HOF and MOF coatings, likely leading to an increase in the observed activity. Further, it is noted that the subsequent decreases in enzymatic activity occur at temperatures at which the MOF and HOF respectively were unable to offer protection to any enzyme that may have been encapsulated. As catalase is significantly larger than the pore apertures in either of the frameworks (the HOF is non-porous), this indicates that some decomposition must be occurring upon heating the MOF to these elevated temperatures to allow enzymes to be released into solution. The enzyme must be protected by the material but

displaced during the heating/icing step before the assay. As such, the observation that the temperature at which the enzymatic activity reduces for the FCAT@**Me_4bpz-HOF** biocomposite is lower than that of the FCAT@**Zn(Me_4bpz)-aq** agrees with previous data showing that the HOF material was less stable than the MOF. Thus, decomposition of the framework to the point at which it is unable to protect encapsulated enzyme would be likely to occur at lower temperatures for the less stable HOF material. Further, if the MOF was decomposing, it is likely that zinc was leached into solution as well, which may also affect the assay. This is due to the ability of zinc to bind to the xylenol orange dye, such that the zinc-bound dye absorbs strongly at 570 nm. Thus, significant absorption at 560 nm is also observed, leading to a false enzymatic activity reading.[144]

To determine the proportion of enzyme activity due to leaching, FOX assays were performed separately on the supernatant and isolated solid materials after exposure to elevated temperatures. Any enzymatic activity in the supernatant was assumed to be due to leached enzyme or zinc (the latter for MOF only). ICP-MS was used to determine the concentration of zinc in the supernatant after exposing the MOF to elevated temperatures. This concentration was then converted to an effective enzymatic activity using a calibration curve shown in appendix (**Figure 92**). The total observed activity of the samples was broken down into proportions reflecting the activity due to encapsulated enzyme, leached zinc and leached enzyme (**Figure 69**).

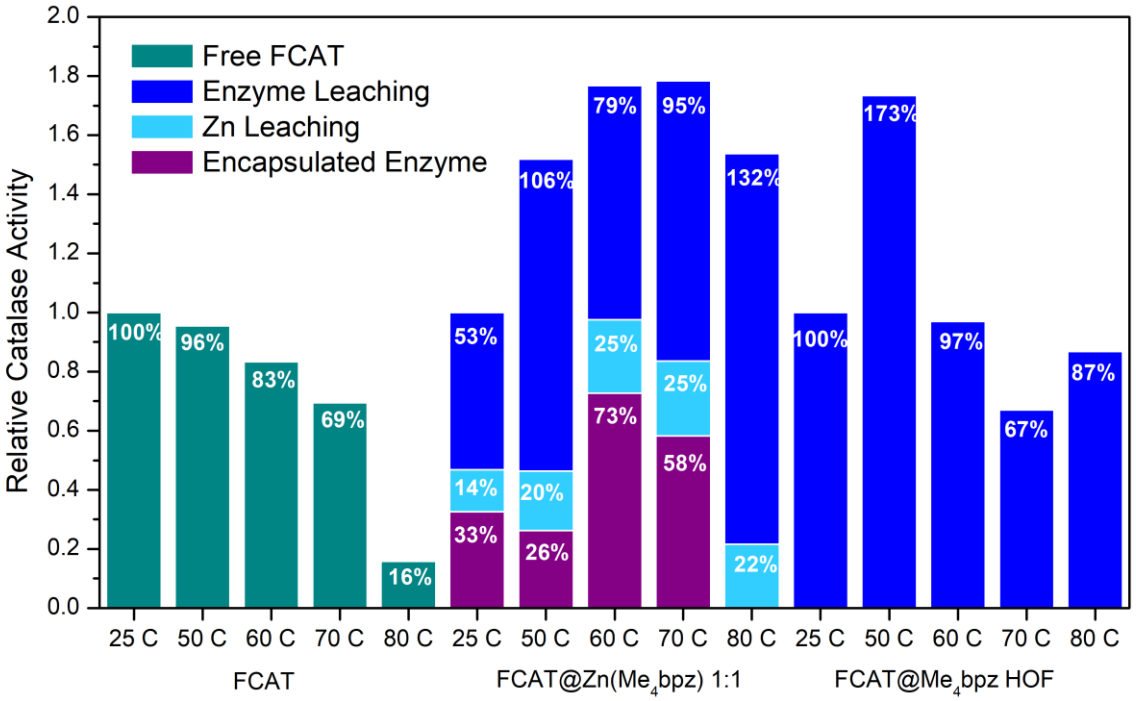

Figure 69: *Relative activity for free FCAT, FCAT@**Zn(Me_4bpz)-aq** and FCAT@**Me_4bpz-HOF** caused by encapsulated enzyme (purple), leached zinc (light blue) and leached enzyme (dark blue). Activities relative to the activity for each sample at 25°C. The assay was performed with an FCAT concentration of 30 nM and initial H_2O_2 concentration of 0.25 mM.*

The assay data revealed that for **Zn(Me$_4$bpz)-aq** a significant proportion of the activity observed was due to the supernatant. ICP-MS data showed that high zinc concentrations were present in all of the FCAT@**Zn(Me$_4$bpz)-aq** supernatants after heating samples to elevated temperatures, indicating that MOF decomposition was occurring. While stability testing had been done previously, PXRD analysis may not have been sufficient to detect this decomposition.

After removing the activity in the supernatant due to zinc, the remaining activity was assumed to be due to leached enzyme. Importantly, there was also high proportions of activity due to leached zinc and enzyme for the FCAT@**Zn(Me$_6$bpz)-aq** biocomposite in water at room temperature (25°C). This indicated that significant proportions of the enzyme present in the biocomposite were loosely bound to the MOF or co-precipitated such that any treatment dislodges it. This observation was further confirmed by washing the FCAT@**Zn(Me$_4$bpz)-aq** biocomposite with water several times before performing fluorescence analysis of these washes (**Figure 93b**). All four water washes performed had observable fluorescence readings, corresponding to FCAT concentrations between 7 and 9 nM indicating a high proportion of FCAT present in the biocomposite was loosely bound. Further, the leached zinc in water at room temperature also indicates that the stability of **Zn(Me$_4$bpz)-aq** is very low, such that some decomposition occurs at room temperature.

The assay data for FCAT@**Zn(Me$_4$bpz)-aq** also revealed that at 80°C, the leached zinc and enzyme accounted for 100% of all activity observed. This supported the previous hypotheses that at this temperature the MOF decomposed to the point at which it is no longer able to offer protection and so there is no remaining active encapsulated enzyme. The significant increase in the activity due to leached enzyme upon increasing the temperature from 70°C to 80°C also supports significant MOF decomposition. The residual enzyme@MOF activity, solely due to the solid MOF sample after the activity due to leached enzyme and zinc had been subtracted, still showed an increase upon heating to 60°C and 70°C relative to the activity at room temperature. This may be due to defects (e.g. cracks) forming in the MOF composite that allowed for less hindered diffusion of assay reagents to the enzymatic site which would in turn make the enzyme appear more active as it could be more readily detected.

For the **Me$_4$bpz-HOF** it was assumed that any zinc present from the synthesis would have been removed during the washing procedures and, thus, no ICP-MS analysis was performed on the supernatant. Assay results from the separated solid sample and the supernatant after exposure to the elevated temperatures showed that, at all temperatures, 100% of the activity observed

was due to leached enzyme. One possible explanation for this was the reduced stability of the HOF compared to **Zn(Me$_4$bpz)-aq**, which either allowed the complete destruction or leaching of encapsulated enzyme (likely only at the higher temperature treatments) or encapsulated enzyme was unable to be detected by the assay. Given the very high-density and lack of porosity in the hydrogen-bonded framework, the latter is reasonable; the assay reagents and products may not have been able to diffuse through to the enzymatic site. Thus, while active enzyme may have been present within the composite, its activity was unable to be observed. As a result, this data provided no insight into the encapsulation ability nor the protective capacity of the HOF.

Protective capacity of frameworks across pH 5 - 10

To determine the protective capacity of both **Zn(Me$_4$bpz)-aq** and the **Me$_4$bpz-HOF** for encapsulated FCAT across a range of pHs, the reduction in enzymatic activity for the FCAT@MOF/HOF samples upon exposure to various buffers of known pH was determined and compared to that of the free enzyme. The procedure involved exposure of FCAT@**Zn(Me$_4$bpz)-aq**, FCAT@**Me$_4$bpz-HOF** and free FCAT to buffers with pH 5 to 10 for 3 minutes. Each sample was then worked up via the method reported for the thermal stability testing.

Raw data showing the change in enzymatic activity of free FCAT, FCAT@**Zn(Me$_4$bpz)-aq** and FCAT@**Me$_4$bpz-HOF** across the pHs 5 to 10 are shown in **Figure 70**. Hydrogen peroxide concentrations close to 0.25 mM indicate a low catalase activity as minimal hydrogen peroxide decomposition has occurred, while low hydrogen peroxide concentrations indicate the reverse.

The raw data reveals a similar trend in the relative activities of each sample as was seen for the thermal stability testing wherein the free enzyme generally has the greatest enzymatic activity, followed by FCAT@**Zn(Me$_4$bpz)-aq** and then FCAT@**Me$_4$bpz-HOF**. The activity data for FCAT@**Me$_4$bpz-HOF** indicates that it is essentially inactive which, as has been discussed previously, is likely due to the extremely dense packing of this material, leading to hindered or impossible diffusion of assay reagents through to the enzymatic site.

Overall the free FCAT appears to be active over the pH range of 5 to 10, agreeing with literature data.[16] The free FCAT showed the highest activity in the pH 9.2 buffer, which is in agreement with literature studies showing that pH 9 is the optimal pH for catalase.[16] Further, the free FCAT appeared to be least stable in the pH 5 buffer, which seems plausible as this is the lowest pH at which catalase is deemed to be active.[16] A reduction in activity upon exposure to pH 7 and pH 8 compared to pH 6 and pH 9.2 was also observed, despite expecting this trend to only have one

local point of minimum activity. Yet, due to the relatively large uncertainties present in this data set, there is no statistical basis to this observation. The exact cause of the relatively large errors present in the free FCAT data is difficult to understand, however, it is noted that two of the three measurements were performed at a separate instance to the initial run. While new calibration data was produced for each run, removing potential errors due to variations in absolute hydrogen peroxide concentration or the FOX reagent, there may have been slight variations in the activity of the FCAT stock solution used.

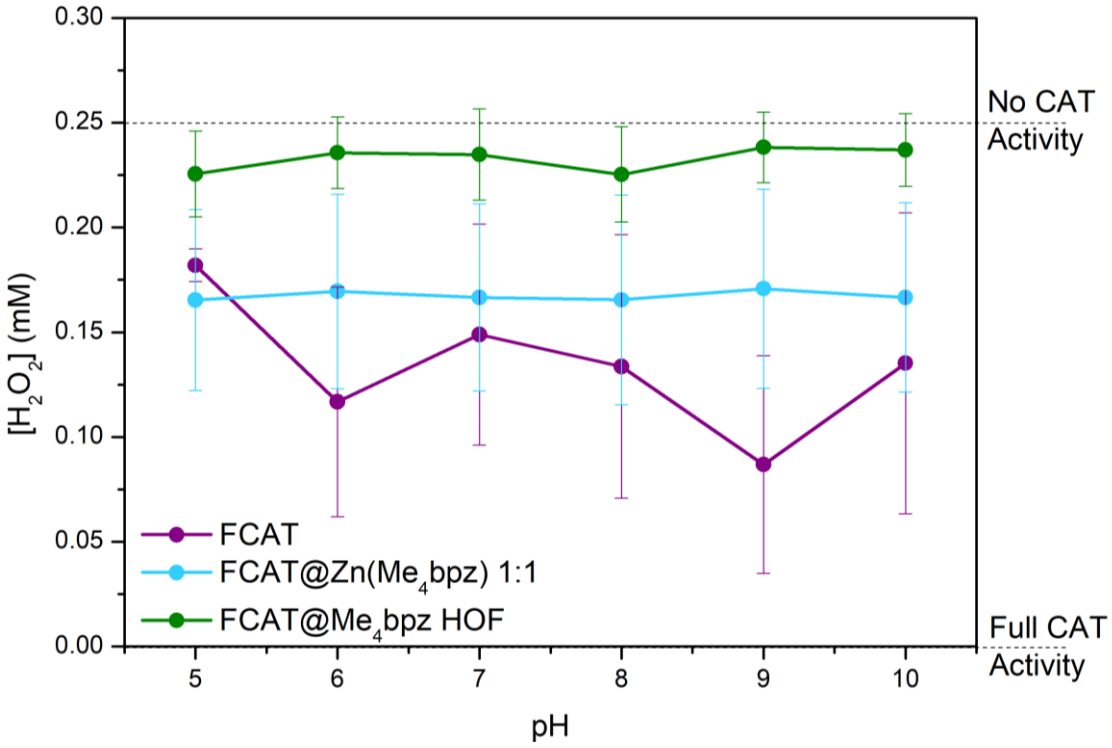

Figure 70: *Catalytic activity of free FCAT (purple), FCAT@**Zn(Me$_4$bpz)-aq** (blue) and FCAT@**Me$_4$bpz-HOF** (green) after exposure to pH 5-10 for 3 minutes. pH 5 buffer – 0.1 M Citric-tri-sodium citrate buffer solution, pH 6-8 buffers – 0.1 M phosphate buffered solution and pH 9.2-10 buffers – 0.1 M glycine buffer. The assay was performed with an FCAT concentration of 30 nM and initial H_2O_2 concentration of 0.25 mM, with an exposure time of 10 minutes. . Exposure time refers to the time over which the sample was exposed to elevated temperatures. Error bars show the standard error for three independent measurements.*

The pH stability testing data was then extrapolated to give the overall percentage of activity change in all samples after three minutes in buffers ranging from pH 5 to 10 compared to the samples in pure water. However, the resultant data had extremely high errors, and so was not able to provide meaningful conclusions. This was most likely a result of inhomogeneous

distribution of the solid samples throughout the stock solutions, leading to inconsistencies in the masses of solid present in each aliquot used for assay analysis.

Nevertheless, studies were conducted to determine whether MOF decomposition and enzyme leaching had occurred using the same methods outlined above for thermal testing. Similar to the thermal data, these results showed that significant proportions of the total calculated enzymatic activity were due to leached enzyme and zinc. For FCAT@**Zn(Me$_4$bpz)-aq**, no activity was observed in the solid biocomposite sample at pHs of 7 and below, indicating a significant decomposition of the MOF in these neutral to acidic conditions, likely as a result of protonation of the N-donor sites in the ligand. Yet, for pHs of 8 and above, the solid biocomposite retained activity, suggesting that the MOF was less susceptible to decomposition in basic conditions. A reverse trend was observed for FCAT@**Me$_4$bpz-HOF** wherein no enzymatic activity was observed in the solid biocomposite following exposure to pHs of 9 and 10, while activity was retained by the biocomposite for pHs 5 to 8, suggesting that this material was more susceptible to decomposition due to deprotonation in basic environments. This is expected as deprotonation would destroy the hydrogen-bonding interactions holding the material together.

Thus, due to the uncertainty in some of the original measurements, no conclusions can be made confidently in regard to the overall protective capacity of **Zn(Me$_4$bpz)-aq** and **Me$_4$bpz-HOF** across this pH range. Yet, the results still suggest that a large proportion of the enzyme was loosely bound to the surface of the material and readily leached into solution.

Protective capacity of frameworks in organic solvents

To determine the protective capacity of **Zn(Me$_4$bpz)-aq** for encapsulated FCAT in organic solvents, the reduction in enzymatic activity for the FCAT@MOF samples upon exposure to THF and DMF for 3 minutes was determined and compared to that of the free enzyme. Each sample was then worked up via the same method reported for the thermal and pH stability testing. No organic stability testing was conducted for FCAT@**Me$_4$bpz-HOF** due to instability of the material in these solvents. Raw data showing the change in enzymatic activity of free FCAT and FCAT@**Zn(Me$_4$bpz)-aq** in THF and DMF are shown in **Figure 71**. Hydrogen peroxide concentrations close to 0.25 mM indicate a low catalase activity as minimal hydrogen peroxide decomposition has occurred, while low hydrogen peroxide concentrations indicate the reverse.

The raw data shows trends that agree with the pH and thermal stability testing, wherein the free enzyme is consistently more active than FCAT in the **Zn(Me$_4$bpz)-aq** sample, once again attributed to hindered substrate diffusion.

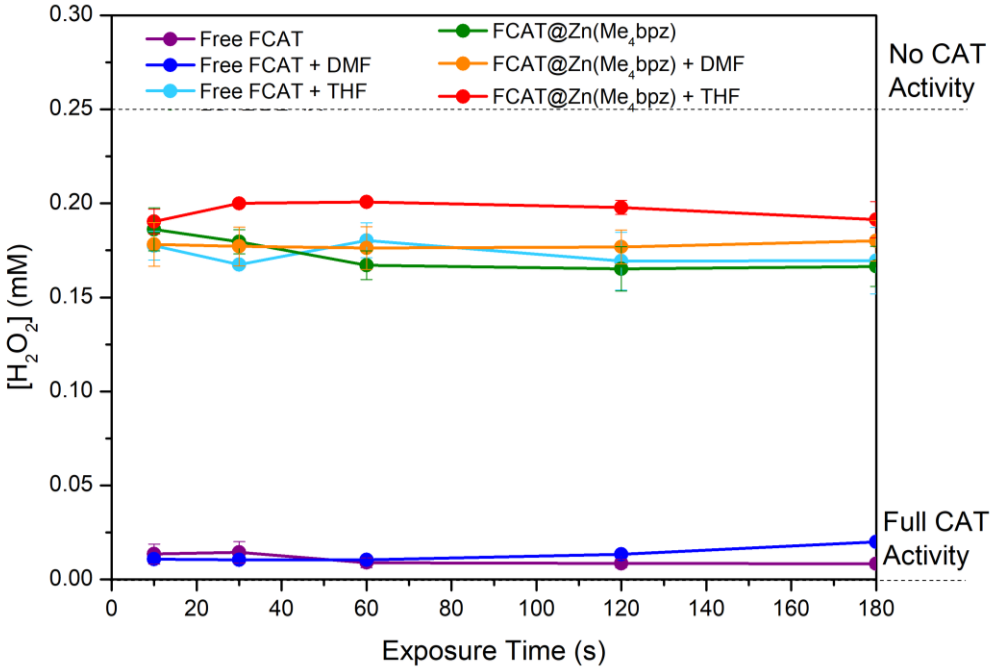

Figure 71: *Catalytic activity of FCAT in free FCAT and FCAT@**Zn(Me$_4$bpz)-aq** after exposure to a) DMF and b) THF for 3 minutes. The assay was performed with [FCAT] = 30 nM and initial [H_2O_2] = 0.25 mM, with a H_2O_2 exposure time of 10 minutes. Exposure time refers to the time over which the sample was exposed to elevated temperatures. Error bars show the standard error for three independent measurements.*

This data was then extrapolated to give the overall percentage of activity loss in all samples after three minutes in organic solvents (**Figure 72**).

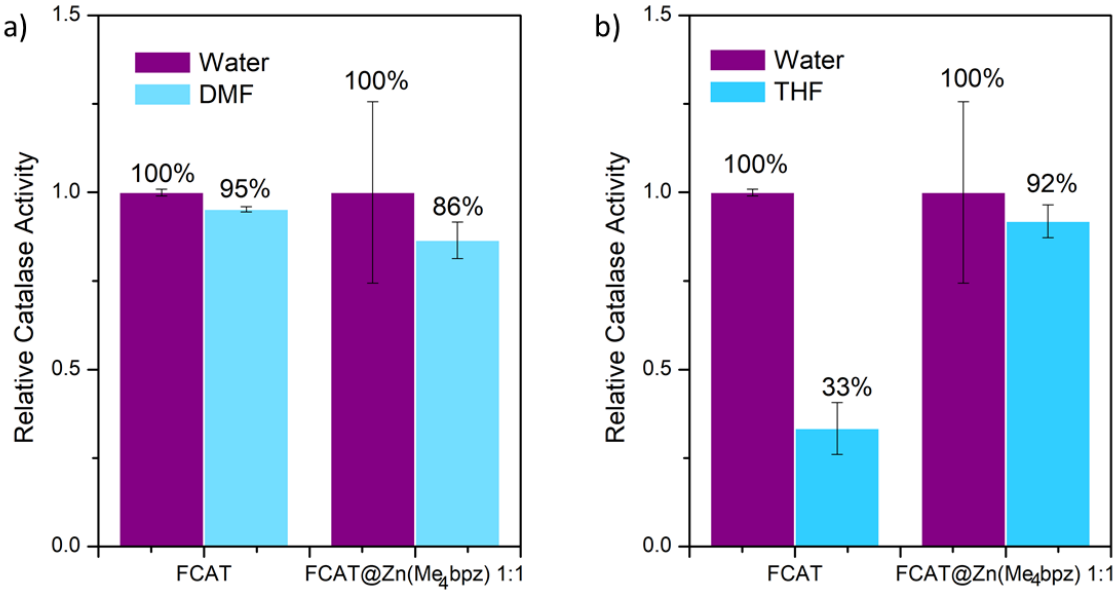

Figure 72: *Relative FCAT activity in FCAT and FCAT@**Zn(Me$_4$bpz)-aq** after exposure to a) DMF and b) THF for 3 minutes. The assay was performed with an FCAT concentration of 30 nM and initial H_2O_2 concentration of 0.25 mM, with an exposure time of 10 minutes. Error bars show the standard error for three independent measurements.*

This data revealed that the free enzyme was more stable in DMF, with an activity loss of only 5%, compared to 67% after exposure to THF. Literature data reported an 85% reduction in activity of free FCAT after exposure to THF for 2 hours, and so a 67% activity loss after 1 hour seems reasonable.[65] However, quantitative data could not be found in the literature for the expected activity loss upon exposure to DMF. Nevertheless, the very small errors observed after performing the assays in triplicate suggests that data is reliable.

For FCAT@**Zn(Me$_4$bpz)-aq**, the assay data showed no change in activity, within error, upon exposure to DMF and THF. As the data for free FCAT showed that minimal activity loss occurred upon DMF exposure it is difficult to ascertain whether the MOF is offering protection against this solvent. However, free FCAT experienced significant activity loss upon exposure to THF, suggesting that **Zn(Me$_4$bpz)-aq** may be able to protect encapsulated FCAT in this organic solvent.

To remain consistent with the thermal and pH activity testing, the activity due to zinc and enzyme leaching was determined. The concentration of zinc in the organic solvent supernatant was not able to be determined via ICP-MS as the organic solvents were not compatible with this method.

The total observed enzymatic activity was then broken down into proportions corresponding to the activities due to encapsulated enzyme and leached zinc and enzyme (**Figure 73**).

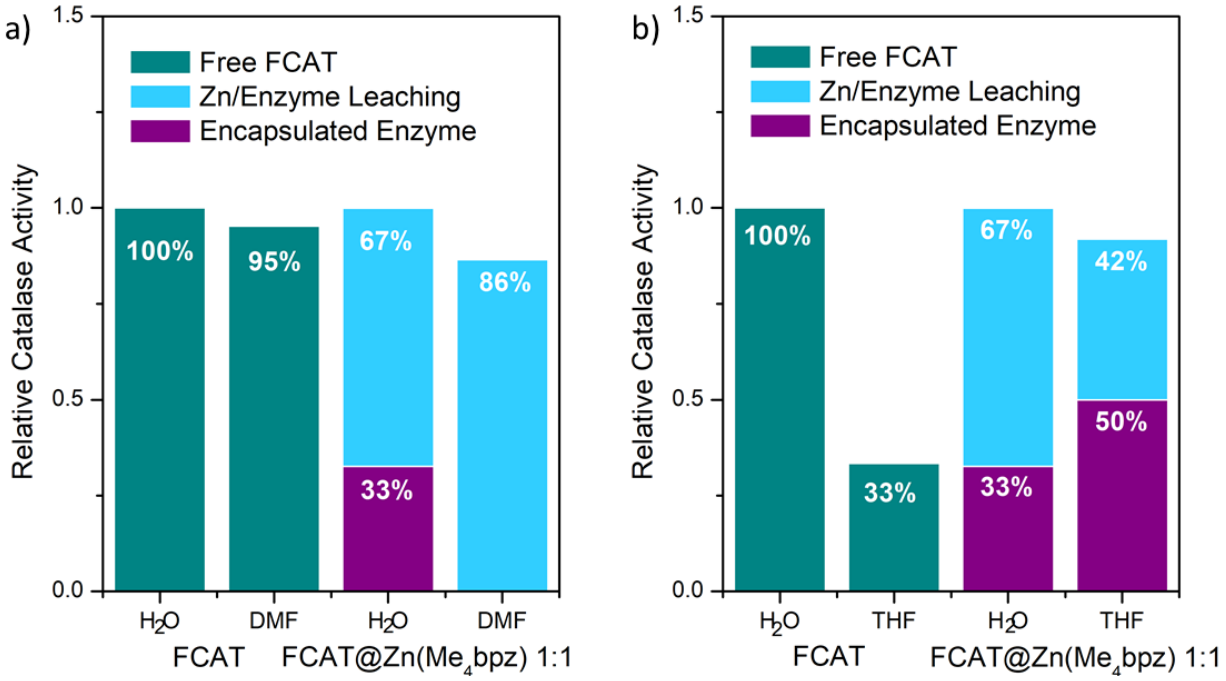

Figure 73: *Relative activity for free FCAT and FCAT@**Zn(Me$_4$bpz)-aq** caused by encapsulated enzyme (purple) and leached zinc/enzyme (blue). Activities relative to the activity for each sample in water. Assays were performed with an [FCAT] = 30 nM and initial [H_2O_2] = 0.25 mM.*

The activity data for FCAT@**Zn(Me$_4$bpz)-aq** revealed that 100% of the activity observed after exposure to DMF was due to leached zinc and enzyme. Conversely, the activity data for FCAT@**Zn(Me$_4$bpz)-aq** following exposure to THF showed that less than 50% of the recorded activity was due to leaching. Upon removing the activity due to leaching, the FCAT@**Zn(Me$_4$bpz)-aq** sample appeared to have slightly increased enzymatic activity following THF exposure. This was again attributed to defect formation in the MOF composite, causing any encapsulated enzyme to appear more active.

Thus, the assay data for all test conditions indicated that a significant proportion of the enzyme present in both the FCAT@**Zn(Me$_4$bpz)-aq** and FCAT@**Me$_4$bpz-HOF** biocomposites was loosely bound to the surface of the material or located in the subsurface region of the crystals. This allowed it to be easily removed upon washing with or suspending in water, buffers or organic solvents. Further, the results from ICP-MS analysis showed that significant concentrations of zinc were being leached into solution, indicating that suspending the MOF in water, buffers or organic solvents led to partial MOF decomposition.

Due to the enzyme and zinc leaching, in combination with the MOF decomposition occurring, the data was unable to conclusively determine whether enzyme was able to be encapsulated and protected by either **Zn(Me$_4$bpz)-aq** or **Me$_4$bpz-HOF**. Yet, the results do highlight that the low

stability of both materials make them unsuitable for biomolecule encapsulation and protection in comparison to other materials such as the aforementioned ZIFs and MAFs which exhibit much higher thermal and chemical stability.[1, 3, 145]

3.2.2: Zn(TDT)

3.2.2.1: Biocompatible synthesis and characterisation of Zn(TDT)

Due to the inability of **Zn(Me$_4$bpz)-aq** to encapsulate and protect enzymes, likely as a result of low stability and significant surface-binding or co-precipitation occurring, another N-donor MOF, **Zn(TDT)**, was investigated in hopes more ZIF-like performance would be encountered. This MOF was primarily chosen because of its sodalite topology and large pore apertures (6.4 Å), which would allow for excellent comparison between this and other sodalite materials such as ZIF-8, with less hindered substrate diffusion.

To initially ensure the repeatability of the **Zn(TDT)** synthesis, the literature MOF synthesis was performed (**Figure 74**).[40] PXRD data confirmed that **Zn(TDT)** with sodalite topology was prepared.

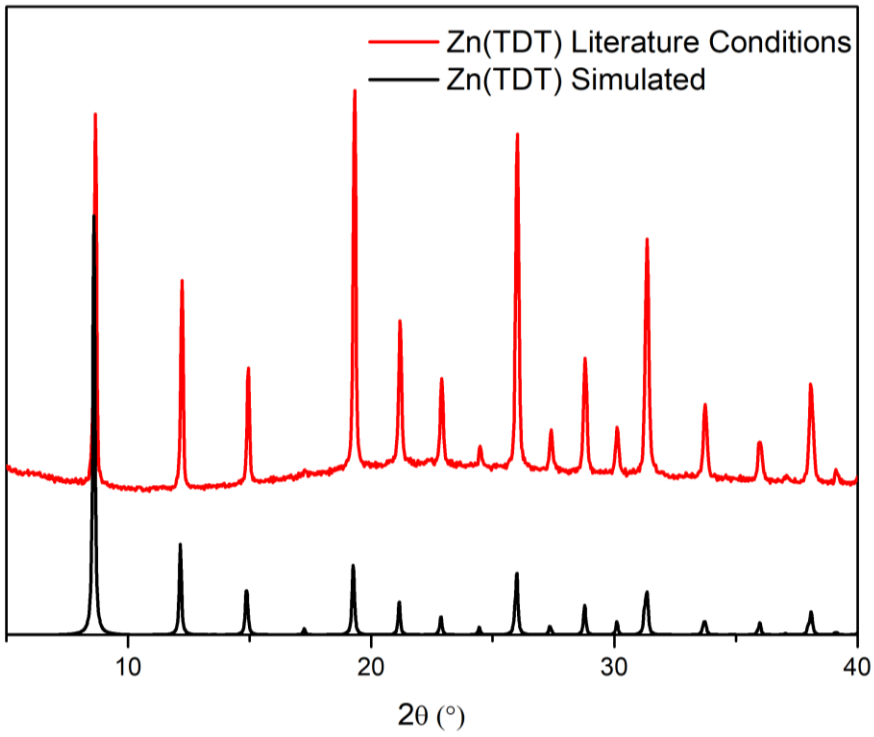

Figure 74: *PXRD data for* ***Zn(TDT)*** *synthesised via the solvothermal literature conditions (red) compared to the simulated data for sodalite* ***Zn(TDT)*** *constructed from single crystal data (black).*[40]

To ensure that synthesis of **Zn(TDT)** was compatible with biomolecule encapsulation, organic solvents and elevated temperatures needed to be replaced with predominantly aqueous conditions at room temperature. However, solubility issues were encountered as the ligand was unable to be dissolved in water, methanol, ethanol and various buffers.

In an attempt to overcome solubility issues, the water-soluble sodium salt of the H_3TDT ligand was synthesised by mixing a 1:2 molar ratio of H_3TDT and sodium hydroxide in water, before isolating the solid by filtration and drying. ^{1}H NMR data for the sodium salt showed a complete removal of peaks corresponding to NH groups, indicating that all had been deprotonated to form a trisodium salt, while IR showed key stretches associated with the ligand. Numerous methods for the synthesis of **Zn(TDT)** were attempted in aqueous conditions at room temperature (**Figure 75** and **Table 23**). Alcohols were used as these had been shown to promote the formation of crystalline Zn Carnosine and ZIF-8.[100] The **Zn(TDT)** material synthesised using the sodium salt of the H_3TDT ligand is hereafter referred to as **Zn(TDT)-Na**.

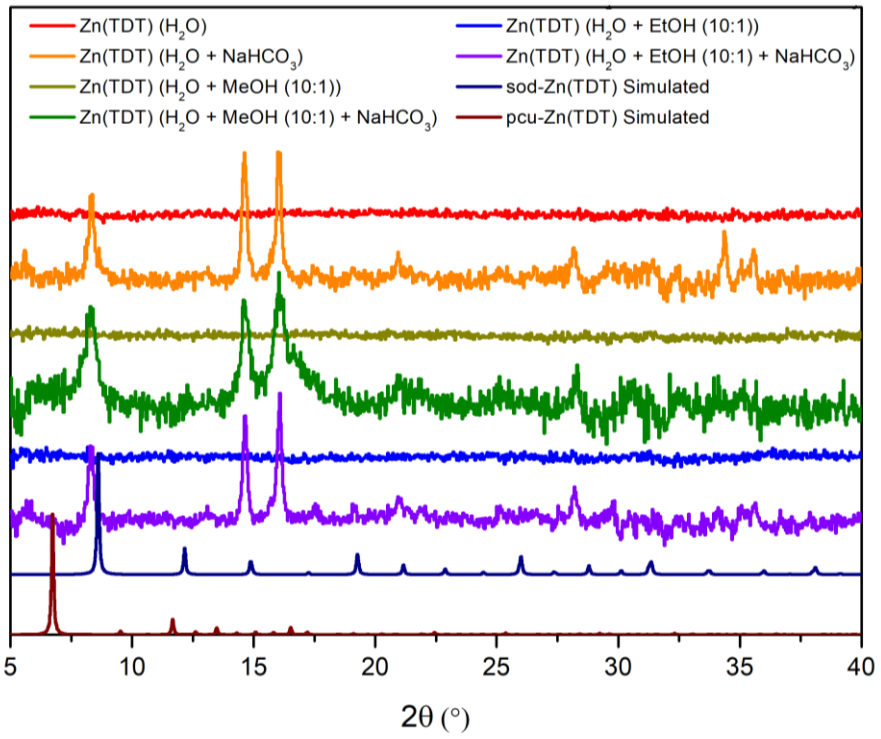

Figure 75: *Baseline corrected PXRD patterns for* ***Zn(TDT)*** *synthesised using the sodium salt of the H_3TDT ligand at room temperature compared to the simulated pattern for the sodalite* ***Zn(TDT)*** *MOF constructed from single crystal data.*

PXRD data revealed that the materials synthesised in aqueous, or predominantly aqueous, conditions with added base were crystalline, however it did not match **Zn(TDT)** synthesised solvothermally. Washing solvothermally synthesised **Zn(TDT)** with methanol and ethanol

confirmed that solvent effects were not the cause of the variations in PXRD data (**Figure 95** in the appendix).

To further investigate the nature of the crystalline material formed via the biomimetic conditions, PXRD data for the experimentally synthesised material was collected on wet (solvated) samples (**Figure 76**). Given the anticipated high chemical stability of Zn(TDT), all previous PXRD data for this material had been collected from dried samples. PXRD data revealed that the wet sample possessed greater crystallininity than the dried sample, indicating that crystallinity had been lost upon drying. Thus, this suggested that the stability of the material synthesised in water was much lower than the **Zn(TDT)** MOF synthesised via solvothermal conditions, as the latter showed no loss of crystallinity upon drying.

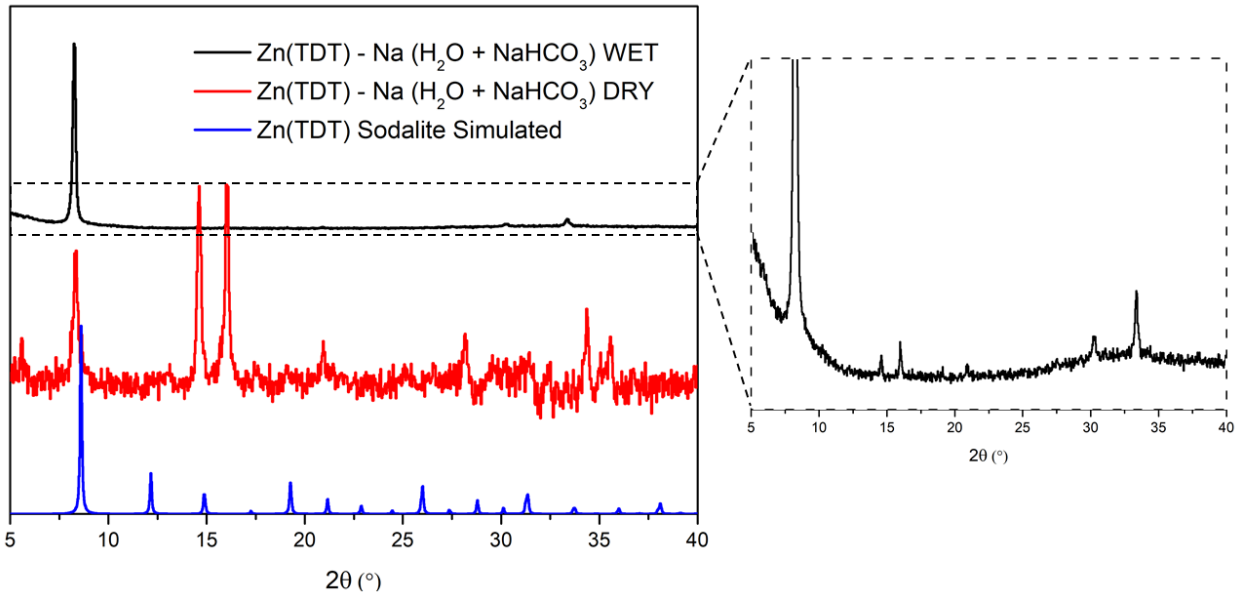

Figure 76: *PXRD of wet loaded and dry loaded* ***Zn(TDT)*** *formed using the sodium H_3TDT ligand in water with added $NaHCO_3$ compared to the simulated pattern of sodalite* ***Zn(TDT)*** *constructed from single crystal data. Figure on right shows enlarged PXRD pattern for the wet* ***Zn(TDT)*** *sample.*

This low stability suggested **Zn(TDT)-aq** may be an organic salt or hydrogen-bonded material. To test this theory, SEM-EDX was used to determine zinc concentration. SEM images showed that **Zn(TDT)-Na** formed as a very irregular material containing a large variation in particle size and morphology.

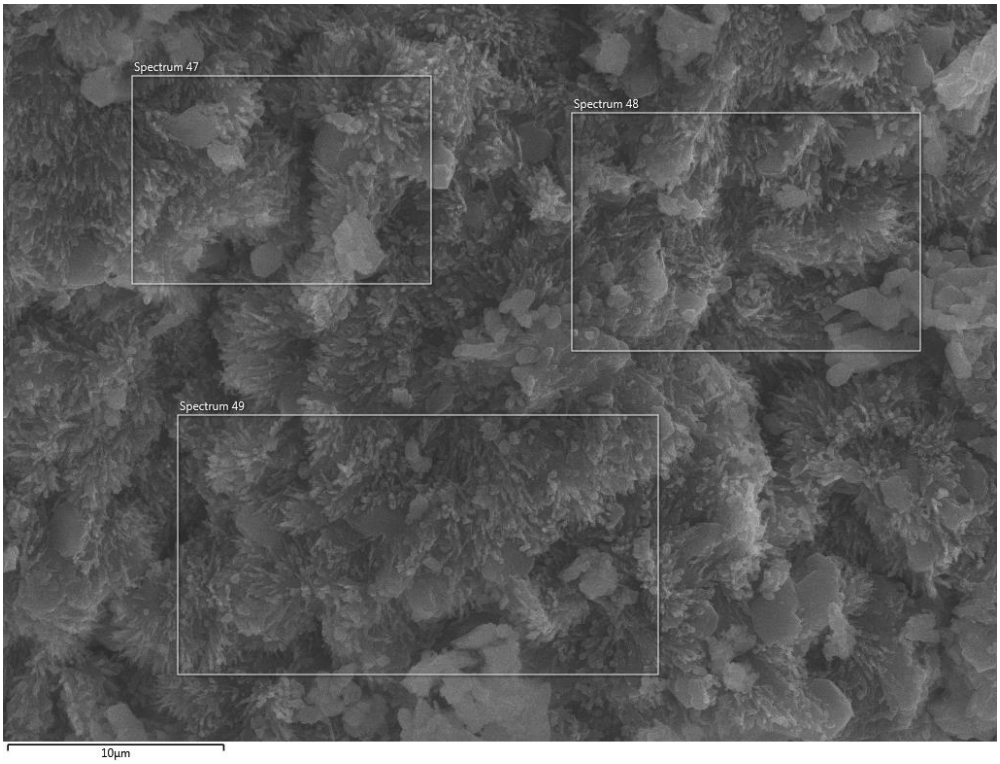

Figure 77: *SEM image of* ***Zn(TDT)-Na****. Outlined rectangles show the sites selected for EDX analysis.*

The EDX results (**Table 24** and **Figure 102** in appendix) revealed an average Zn:N ratio of 2:12, which is close to the expected 2:11 ratio based on the 2:1 zinc to ligand ratio present in solvothermally prepared **Zn(TDT)**. There were also consistently high proportions of sodium present throughout the sample, up to 23%, yet it is not known whether the sodium is present in the structure or left over from the MOF synthesis.

While attempts were made to synthesise single crystals of the **Zn(TDT)-Na** material, no success was had. Thus, the focus was shifted to synthesising a more stable phase of **Zn(TDT)-Na**, such that it could be further investigated for use in biomolecule encapsulation. A number of synthetic factors were investigated including the base concentration, ethanol concentration, zinc source and reduced temperature (**Figure 96, 97** and **98** respectively in the appendix), however none of these resulted in a more stable material. The addition of 3% w/v 2-methylimidazole was trialled to investigate whether this could form ZIF-8 crystals to seed the growth of sodalite **Zn(TDT)**. However, PXRD data (**Figure 99** in the appendix) and ^{1}H NMR data showed that only ZIF-8 was formed under these conditions. To prevent this preferential ZIF-8 formation, ZIF-8 seed crystals were synthesised separately and added during the **Zn(TDT)-Na** synthesis, however, this resulted in the formation of a precipitate that did not match any known material and so no further analysis was performed (**Figure 100** in the appendix).

In further attempts to form stable **Zn(TDT)**, the tetrabutylammonium salt of the TDT linker was synthesised by combining a solution of potassium carbonate and H_3TDT in acetone with a solution of tetrabutylammonium (TBA) bromide in DCM (1:1 molar ratio of TBA and H_3TDT). NMR analysis confirmed the presence of both TBA and TDT and showed that a bis(TBA) salt had formed. Attempts to synthesise **Zn(TDT)** using this TBA salt, were performed in pure water and a 10:1 water to ethanol mixture with added base. This formed a crystalline material, referred to as **Zn(TDT)-TBA**, which showed no loss of crystallinity upon drying (**Figure 78**). However, the lack of low angle peaks in the PXRD patterns suggested it was a crystalline salt with a relatively small unit cell.

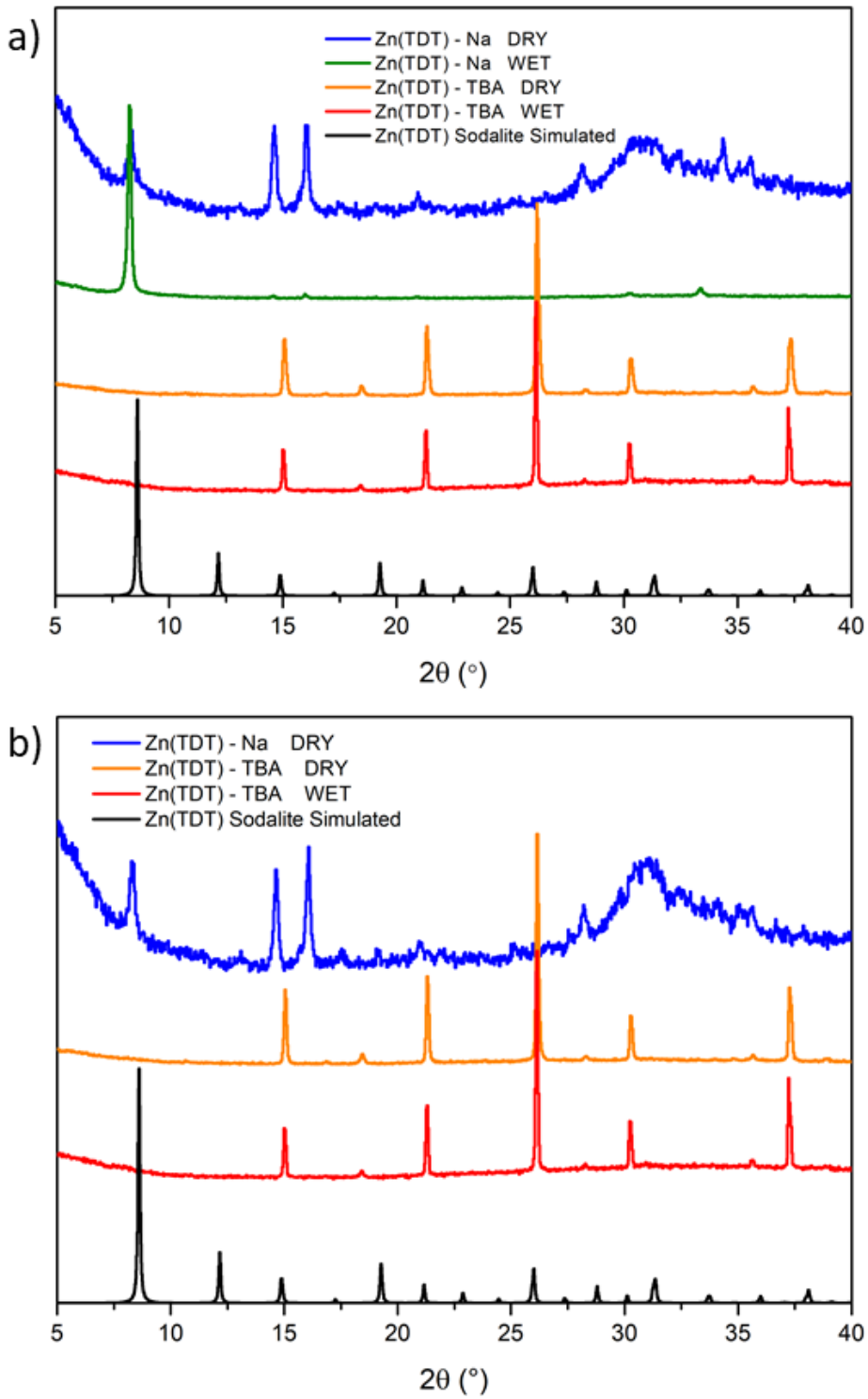

Figure 78: *PXRD data for attempted syntheses of* ***Zn(TDT)*** *using the sodium salt (blue and green) and tetrabutylammonium salt (orange and red) of the H_3TDT ligand in a) pure water and b) a 10:1 mixture of water and ethanol and a 1:1:4.75 molar ratio of metal to ligand to base compared to the patterns of* ***Zn(TDT)*** *(black) constructed from single crystal data.*

N_2 gas adsorption was performed on an activated sample of **Zn(TDT)-TBA** to investigate the porosity of the material. The absence of low angle peaks below 2θ = 15° in the PXRD pattern suggested that this material might be close-packed. This was supported by N_2 gas adsorption data (**Figure 79**), which showed minimal evidence of porosity and a low BET surface area of 49.8 m^2/g.

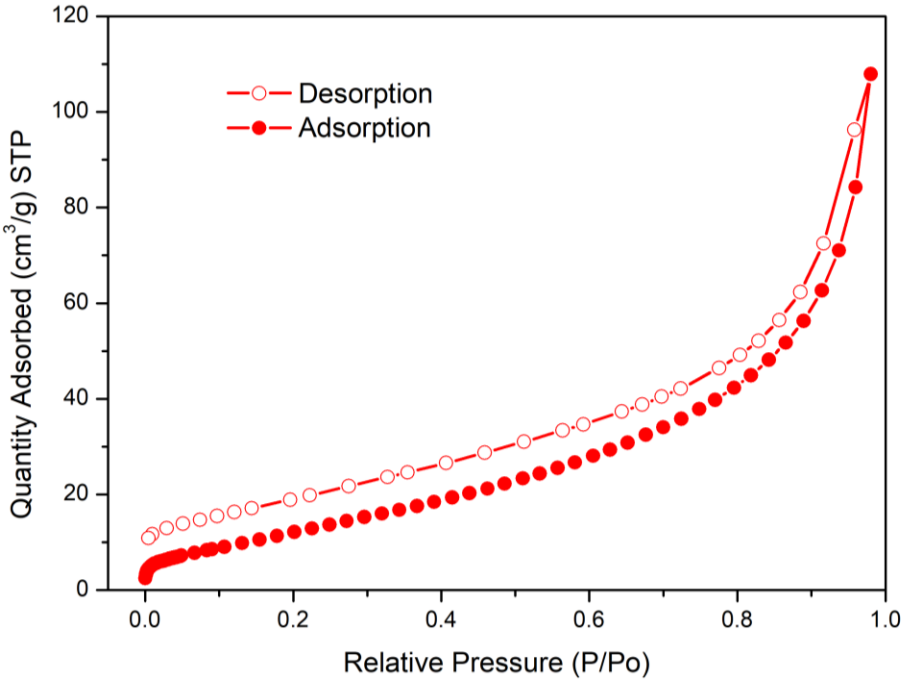

Figure 79: *N_2 gas adsorption isotherm for **Zn(TDT)-TBA** at 77 K. The sample was activated by washing with DCM and then drying under high vacuum overnight.*

SEM-EDX was also performed on **Zn(TDT)-TBA** for further characterisation of the material (raw data in **Table 25** and **Figure 103** in appendix). **Zn(TDT)-TBA** formed as regular cubic particles approximately 4 µm in size (**Figure 80**), with a consistent Zn:N ratio of 2:1. Yet, this Zn:N ratio is significantly different to the expected 2:1 metal to ligand ratio (2:11 Zn:N), suggesting that the synthesised **Zn(TDT)-TBA** material had a very high zinc concentration, whether this be from a higher quantity of zinc present in the framework, or zinc remaining in the sample from the MOF synthesis.

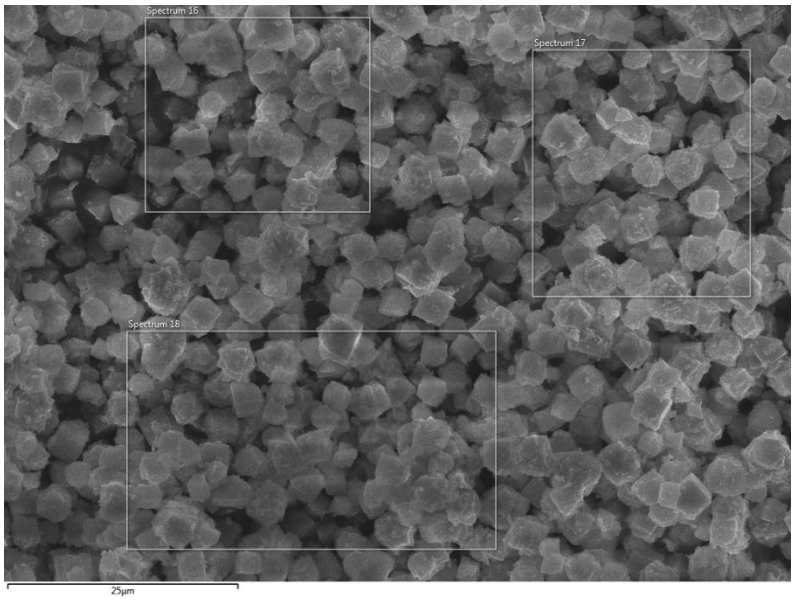

Figure 80: *a) SEM image of Zn(TDT)-TBA, with high magnification images of b) cubic crystals and c) spherical crystals. Outlined rectangles show the sites selected for EDX analysis.*

Thus, no method was found to synthesise sod- or pcu-**Zn(TDT)** in aqueous conditions at room temperature. Further, the stability of **Zn(TDT)-Na** was unable to be improved, nor could the TBA salt of the H_3TDT linker promote MOF formation in aqueous conditions at room temperature.

3.2.2.2: Synthesis of protein@Zn(TDT) biocomposites

Despite the inability to successfully form sodalite **Zn(TDT)** in aqueous conditions, the ability of **Zn(TDT)-Na** to encapsulate enzymes was still investigated. The main reason for conducting these experiments was to determine whether the presence of enzyme could stabilise the material. As the experiments above provided no evidence to suggest that the use of ethanol in the solvent system was advantageous in regard to the stability or crystallinity of **Zn(TDT)-Na**, only pure water was used in the enzyme encapsulation experiments to increase the biocompatibility. FITC-tagged catalase (FCAT), bovine serum albumin (FBSA) and myoglobin (FMb) were added during syntheses of **Zn(TDT)-Na** to represent enzymes with a range of pIs and molecular weights. The biomolecule encapsulation procedure involved the dropwise addition of an aqueous zinc solution to an aqueous solution of the sodium salt of the H_3TDT linker, sodium bicarbonate and enzyme. In the presence of each of the three enzymes, precipitation occurred immediately upon addition of the zinc solution. PXRD data revealed that the presence of FBSA and FMb resulted in the precipitation of amorphous material, regardless of whether it was wet or dry, while the presence of FCAT formed a crystalline material which lost significant crystallinity upon drying (**Figure 81**).

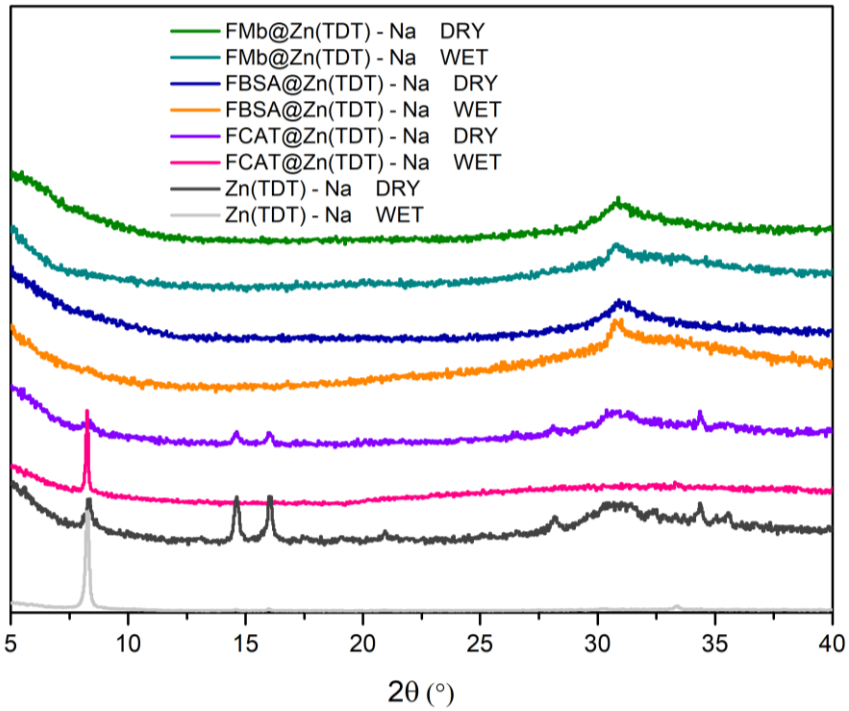

Figure 81: *PXRDs for Zn(TDT) formed in the presence of a) FCAT, b) FBSA and c) FMb analysed wet or dry, before and after suspending in ethanol.*

Thus, the addition of enzyme was unable to stabilise **Zn(TDT)-Na**, and select enzymes also prevented the formation of crystalline material. As such, the stability of the material was considered to be too low and so further investigation of this MOF was deemed impractical.

3.3: Conclusions

Given that MOFs which reliably encapsulate biomolecules (ZIF-8, ZIF-90, MAF-7) are comprised of azolate ligands (e.g. imidazoles and triazoles), it was hypothesised that chemically similar, albeit structurally distinct materials could be used for biomimetic mineralisation. Thus, a literature review was conducted to identify azolate-based (N-donors) MOFs with differing structure metrics to the sodalite materials (ZIF-8, ZIF-90, MAF-7) routinely used for biomolecule protection. From the suite of N-donor containing MOFs surveyed, two materials were identified; **Zn(Me$_4$bpz)** and **Zn(TDT)**. The two ligands needed to prepare these MOFs were synthesised with the intention of using these to synthesise the target zinc-based MOFs under aqueous conditions at room temperature. However, the materials formed via biocompatible syntheses did not match the expected structures of the target MOFs synthesised solvothermally.

Me$_4$bpz was used to form a MOF, **Zn(Me$_4$bpz)-aq** and a hydrogen-bonded organic framework, **Me$_4$bpz-HOF**, both in aqueous conditions at room temperature. **Zn(Me$_4$bpz)-aq** gave a PXRD pattern similar to that of the **Zn(Me$_4$bpz)** MOF synthesised under solvothermal conditions. EDX data confirmed that the **Zn(Me$_4$bpz)-aq** MOF possessed the same 1:1 metal to ligand ratio as the literature material. Gas adsorption data revealed that **Zn(Me$_4$bpz)-aq** was permanently porous, with pores of 16 Å compared to 10 Å pores seen in the solvothermally synthesised MOF. Thus, the characterisation data suggested that the Zn(Me$_4$bpz) MOF synthesised in aqueous and solvothermal conditions were similar. However, due to the synthetic approach, single crystals of **Zn(Me$_4$bpz)-aq** could not be obtained and so the definitive structure of this MOF remained unknown. Gas adsorption data showed that **Me$_4$bpz-HOF** was close-packed and significantly less stable than the MOF.

The addition of enzyme caused no structural changes that were observable by PXRD in either of the materials, and the enzyme loading for FCAT was determined to be 1.7 ± 0.8% and 1.6 ± 0.5% for the MOF and HOF respectively. Turbidity data showed that the presence of enzyme increased the rate at which the **Zn(Me$_4$bpz)-aq** MOF formed, while not appearing to impact the rate of **Me$_4$bpz-HOF** formation, suggesting that biomimetic mineralisation could be the formation mechanism of the former. However, CLSM data for both biocomposites were inconclusive as the bulk of the material was too small and beyond the resolution of the microscope.

The stability tests conducted for **Zn(Me$_4$bpz)-aq** and **Me$_4$bpz-HOF** in DMF, THF, pH range 5 to 10 and elevated temperatures up to 80°C showed that the former was stable in all test conditions, while the latter showed evidence of decomposition in all conditions except pH 10. Interestingly, the presence of enzyme had a stabilising effect as FCAT@**Me$_4$bpz-HOF** biocomposites showed no such reduction in crystallinity following exposure to pH 5 and elevated temperatures. Enzyme was unable to stabilise the HOF in organic solvents.

Assays were then conducted to quantify the activity of enzyme in the FCAT@**Zn(Me$_4$bpz)-aq** and FCAT@**Me$_4$bpz-HOF** biocomposites. The assays were performed before and after each sample was exposed to test conditions to ascertain the protective ability of both materials towards the encapsulated enzyme. For FCAT@**Zn(Me$_4$bpz)-aq**, a significant portion of the observed enzymatic activities was due to leached zinc and enzyme. Enzyme leaching occurred even at room temperature in water, indicating a high proportion of loosely-bound enzyme. Further, the leached zinc indicated that MOF decomposition was occurring in the conditions tested, which could form defects in the protective shell to facilitate enzyme leaching. Similar observations were made for the FCAT@**Me$_4$bpz-HOF** biocomposite in that significant enzymatic activity was due to enzyme in solution, suggesting that the enzyme was loosely bound to the HOF and/or the HOF was unstable. The closely packed nature of this material would also significantly hinder substrate diffusion. These observations deemed **Zn(Me$_4$bpz)-aq** and **Me$_4$bpz-HOF** unsuitable for enzyme encapsulation and protection.

While further characterisation with different biomolecules could be of interest, the low stability of both the **Zn(Me$_4$bpz)-aq** and **Me$_4$bpz-HOF** materials would be consistent, regardless of the enzyme used and so no further investigation was deemed necessary. Despite neither of the Me$_4$bpz derived materials being able to successfully encapsulate or protect biomolecules, these results still provide useful information. Notably, the sole presence of azole N-donor groups in the MOF does not guarantee the ability to form a biocomposite able to encapsulate and protect protein. Further, the stability of frameworks must be more rigorously tested to ensure that no decomposition occurs in the conditions where it is being used to protect the encapsulated biomolecules. This particularly applies to cases where the MOF has been induced to form rapidly, under aqueous conditions, and will likely not form the desired defect-free materials that produced via solvothermal conditions. Understanding the thermal and chemical stability of the rapidly precipitated form of the framework would provide confidence that the observed activity for the biocomposites is unlikely to be due to enzyme leaching.

Zn(TDT) was synthesised from the ligand, H_3TDT (4,5-di(1H-tetrazol-5-yl)-2H-1,2,3-triazole. A significant challenge with this material was the insolubility of the ligand, which required the formation of the sodium or organic salts to ensure its solubility in aqueous, or predominantly aqueous, conditions. Attempts to synthesise **Zn(TDT)** using the sodium ligand salt (designated **Zn(TDT)-Na**) resulted in the formation of a crystalline material that was distinct from Zn(TDT) synthesised solvothermally. SEM-EDX analysis confirmed it had a 2:1 metal to ligand ratio, in agreement with that of the solvothermally synthesised **Zn(TDT)**. However, the stability of **Zn(TDT)-Na** was significantly less stable than the solvothermally synthesised MOF. No conditions trialled, including the addition of enzyme, were able to increase the stability. Further, the use of the bis(tetrabutylammonium) ligand salt resulted in the formation of a crystalline material (**Zn(TDT)-TBA**) with low porosity, low surface area (49.8 m^2/g) and a high zinc concentration.

3.4: Experimental

3.4.1: General Methods

All chemicals and solvents were purchased from commercial suppliers and used as received with no further purification.

Buffer syntheses and enzyme-tagging methods are outlined in the experimental section of chapter 2.

3.4.2: Syntheses

Me_4bpz derived materials:

Ligand Synthesis:

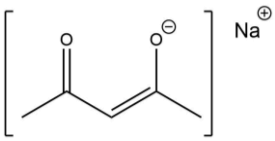

Sodium Acetylacetone: Using a procedure modified from that of Charles,[146] sodium hydroxide (10.0 g, 0.25 mol) was dissolved in water (12.5 mL), followed by the addition of methanol (50 mL). The solution was added to acetylacetone (25.5 mL, 0.25 mol) slowly, with stirring. The solution was cooled on ice for 2 hours, filtered, washed with cold methanol (x 2) and dried to give sodium acetylacetone as a pale orange crystalline solid (22.86 g, 74%). ^{1}H NMR (DMSO-d6, 500 MHz): 1.93 (3H, s, C**H$_3$**-C=O), 1.98 (3H, s, C**H$_3$**-C=CH), 5.41 (1H, s, CH) ppm. This matches the literature ^{1}H NMR data exactly.

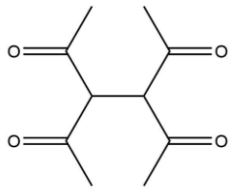

3,4 Diacetyl-hexane-2,5-dione: Using a procedure modified from that of Charles,[146] sodium acetylacetone (14.45 g, 0.10 mol) was ground to a fine powder, followed by the addition of diethyl ether (150 mL). Iodine (12.70 g, 0.05 mol) was dissolved in diethyl ether (150 mL) and added to the sodium acetylacetone solution dropwise via dropping funnel over approximately 3 hours. The suspension was left to evaporate overnight. Water (250 mL) was added and the suspension was stood at room temperature for 2 hours. The solid was collected by filtration, washed with water, dried and recrystallised (methanol) to give 3,4-diacetyl-hexane-2,5-dione as an off-white solid (9.91 g, 14%), ^{1}H NMR (DMSO-d6, 500 MHz): 1.98 (12H, s, C**H$_3$**), ^{13}C NMR(DMSO-d6, 500 MHz): 195.9, 110.83, 26.5 ppm. This is mostly in agreement with literature data, with some slight deviations in chemical shift.

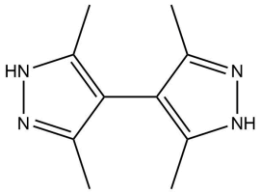

3,3',5,5'-Tetramethyl-4,4'-bipyrazole (H_2Me_4bpz): Using a procedure modified from that of Boldog *et al.*,[147] 3,4 diacetyl-hexane-2,5-dione (1.34 g, 6.75 mmol) was dissolved in water (1.4 mL). The solution was added portion wise to hydrazine hydrate (1.6 mL, 33.8 mmol) and cooled on ice. The suspension was stirred at room temperature for 2 hours, filtered, washed with ice water and recrystallised (water) to give H_2Me_4bpz as an off-white crystalline solid (0.81 g, 63 %). ^{1}H NMR (DMSO-d6, 500 MHz): 1.95 (12H, s, CH_3), 12.14 (2H, s, br, NH) ppm, ^{13}C NMR (DMSO-d6, 500 MHz): 111.43 ppm. This in agreement with literature data.

Zn(Me_4bpz): Me_4bpz (9.5 mg, 0.05 mmol) and sodium bicarbonate (52.5 mg, 0.625 mmol) were dissolved in methanol (1 mL) and water (5 mL). $Zn(NO_3)_2{\cdot}6H_2O$ (14.9 mg, 0.05 mmol) was dissolved in water (5 mL) and added dropwise to the Me_4bpz solution with stirring which resulted in precipitation of a white solid. The suspension was stirred for 30 minutes at room temperature and the solid was collected by centrifugation (7000 rpm, 3615 x g, 2 min). PXRD data shown in **Figure 50**, N_2 gas adsorption data shown in **Figure 52** and pore size distribution data shown in **Figure 53**.

Enzyme@Zn(Me_4bpz): Me_4bpz (9.5 mg, 0.05 mmol) and sodium bicarbonate (52.5 mg, 0.625 mmol) were dissolved in methanol (1 mL) and water (4 mL). Enzyme (2 mg) was dissolved in water (1 ml) and added to Me_4bpz solution. $Zn(NO_3)_2{\cdot}6H_2O$ (14.9 mg, 0.05 mmol) was dissolved in water (5 mL) and added dropwise to the Me_4bpz solution with stirring resulting in precipitation of a white solid. The suspension was stirred for 30 minutes at room temperature and the solid was collected by centrifugation (7000 rpm, 3615 x g, 2 min). PXRD data shown in **Figure 60**, solid-state

UV-Vis data shown in **Figure 63**, CLSM images shown in **Figure 64** and enzyme (catalase) loadings listed in **Table 13**.

Me_4bpz HOF microcrystalline powder (added zinc): Me_4bpz (152 mg, 0.8 mmol) and sodium bicarbonate (52.5 mg, 0.625 mmol) were dissolved in methanol (3 mL) and water (4 mL). $Zn(NO_3)_2 \cdot 6H_2O$ (14.9 mg, 0.05 mmol) was dissolved in water (5 mL) and added dropwise to the Me_4bpz solution with stirring resulting in precipitation of a white solid. The suspension was stirred for 30 minutes at room temperature, and the solid was collected by centrifugation (7000 rpm, 3615 x g, 2 min).

Enzyme@Me_4bpz HOF: Me_4bpz (152 mg, 0.8 mmol) and sodium bicarbonate (52.5 mg, 0.625 mmol) were dissolved in methanol (3 mL) and water (3 mL). Enzyme (2 mg) was dissolved in water (1 mL) and added to Me_4bpz solution with stirring. $Zn(NO_3)_2 \cdot 6H_2O$ (14.9 mg, 0.05 mmol) was dissolved in water (5 mL) and added dropwise to the Me_4bpz solution with stirring resulting in precipitation of a white solid. The suspension was stirred for 30 minutes at room temperature, and the solid was collected by centrifugation (7000 rpm, 3615 x g, 2 min). PXRD data shown in **Figure 60**, solid-state UV-Vis data shown in **Figure 63,** CLSM images shown in **Figure 64** and enzyme (catalase) loadings listed in **Table 13**.

Preparation of single crystals:

1:4 (with zinc, base and BSA): The Zn(Me_4bpz) synthesis were performed as outlined above, the precipitate was isolated by centrifugation (7000 rpm, 3615 x g, 2 min), and the supernatant was left to sit at room temperature, exposed to air to allow slow evaporation. Clear, slightly cubic crystals formed after 1 week.

1:2, 1:4 and 1:16 (with zinc, no base): The Zn(Me_4bpz) synthesis was performed as outlined above, omitting the base, such that no immediate precipitation occurred. The solution was left to sit open at room temperature for slow evaporation. 1:16 formed clear, needle-like crystals overnight, 1:4 and 1:2 formed clear, irregular crystals after 2 and 10 days respectively.

Me_4bpz single crystals (no zinc): Me_4bpz (76 mg, 0.4 mmol) and sodium bicarbonate (26.3 mg, 0.3125 mmol) were dissolved in methanol (1.5 mL) and water (1.5 mL). The solution was left exposed to air and allowed to evaporate. Clear and colourless crystals of the Me_4bpz HOF formed overnight.

PXRD data for single crystals is shown in **Figure 55** and single crystal data is shown in **Figure 56** (unit cell), **Figure 57** (asymmetric unit) and **Figure 58** (hydrogen-bonding).

H_3TDT derived materials:

Ligand Synthesis:

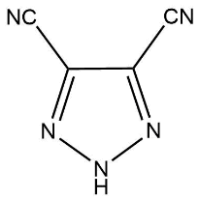

4,5 Dicyano-1H-(1,2,3)-triazole: Using a modified procedure from that of Crawford,[148] a slurry of diaminomaleonitrile (2.70 g, 25 mmol) in water (31 mL) was acidified with hydrochloric acid (1 M, 25 mL). The solution was cooled to 0°C and sodium nitrite (1.72 g, 25 mmol) was added portion wise. The suspension was then warmed to room temperature and stirred for 1 hr. The solution was extracted with diethyl ether (5 x 20 mL) and the combined ether extracts were evaporated to dryness under reduced pressure to yield 4,5-dicyano-1H-(1,2,3)-triazole as an orange solid (2.81 g, 94%). ^{1}H NMR (DMSO-d6, 500 MHz): 9.39 (1H, s, br, NH) ppm. IR (cm^{-1}): 3256.1 (NH, m, br), 2262.8 (C=N, m), 1478.5 (CH, w), 1381.6 (CH, m). This data is in agreement with literature results.

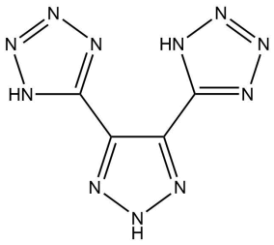

4,5 Bis(1H-tetrazol-5-yl)-2H-1,2,3-triazole (H_3TDT): Using a modified procedure from that of Dinca,[136] a mixture of 4,5-dicyano-1H-(1,2,3)-triazole (0.47 g, 4.0 mmol), sodium azide (1.56 g, 24 mmol) and triethylamine hydrochloride (3.30 g, 24 mmol) were suspended in a mixture of toluene (30 mL) and methanol (6 mL), and the suspension was heated at reflux for 3 days. The suspension was cooled to room temperature and aq. sodium hydroxide (1 M, 20 mL) was added. The solution was stirred at room temperature for 30 minutes. The aqueous layer was treated with aq. hydrochloric acid (1 M, 20 mL) and the precipitate was collected via filtration, dried, and dissolved in aq. sodium hydroxide (1 M, 30 mL). Aq. hydrochloric acid (1 M, 25 mL) was added until a pH of 4-5 was obtained. The precipitate was collected by filtration, washed with water (x 3), methanol (x 2) and acetone (x 1) to yield 4,5-di(1H-tetrazol-5-yl)-2H-1,2,3-triazole as a pale orange solid (0.77 g, 94%). ^{1}H NMR (DMSO-d6, 500 MHz): 6.84 (3H, s, br, NH) ppm. ^{13}C NMR (DMSO-d6, 500 MHz): 134.27, 151.68 ppm. IR (cm^{-1}): 3497.3 (NH, m, br), 3372.7 (NH, m, br), 3238.2 (NH, m, br), 3024.3 (NH, w), 2470.3 (OH, br, m), 1848.7 (CH, m), 1687.0 (C=N, w), 1654.6 (C=C, m), 1586.3 (C=C, s). This is in moderate agreement with the literature data.

CAUTION: Metal azides are water sensitive and potentially explosive and should be handled with care. Although no incidents were encountered while handling H_3TDT or Zn(TDT) MOFs under the

conditions of these experiments, previous reports have suggested that handling H_3TDT at temperatures exceeding 160°C is potentially hazardous and the melting with decomposition (explosion) may occur at 280°C.[149]

4,5 Bis(1H-tetrazol-5-yl)-2H-1,2,3-triazole trisodium salt: Using a modified procedure from that of Tanaka,[150] a 48% aqueous sodium hydroxide solution (0.275 mL, 5 mmol) was added to a suspension of 4,5-di(1H-tetrazol-5-yl)-2H-1,2,3-triazole (0.52 g, 2.5 mmol) in water (25 mL). The solution was stirred at room temperature for 1 hour, followed by filtration. The filtrate was evaporated to dryness under reduced pressure to give the sodium salt of 4,5-di(1H-tetrazol-5-yl)-2H-1,2,3-triazole as a pale orange solid (0.60 g, 96%). ^{1}H NMR (D_2O): no peaks, IR (cm^{-1}): 3600.0 (NH, w), 3207.5 (NH, br, s), 1644.2 (NH, br, m), 1537.0 (C=C, m), 1409.1 (CH, s).

4,5 Bis(1H-tetrazol-5-yl)-2H-1,2,3-triazole bis(tetrabutylammonium) salt: Using a modified procedure from that reported by Katritzky,[151] a suspension of anhydrous potassium carbonate (0.70 g, 5 mmol) and 4,5-di(1H-tetrazol-5-yl)-2H-1,2,3-triazole (0.62 g, 3 mmol) in acetone (30 mL) was stirred at room temperature for 10 minutes. A solution of tetrabutylammonium bromide (0.97 g, 3 mmol) in dichloromethane (30 mL) was added to the reaction suspension and stirred at room temperature for 3 hours. The reaction suspension was filtered, and the filtrate was concentrated under reduced pressure. The residue was extracted with acetone, the extract was filtered, and the solvent was removed under reduced pressure to give the tetrabutylammonium salt as a pale yellow solid (0.91 g, 57%). ^{1}H NMR (DMSO-d6, 500 MHz): 0.93 (3H, t, J = 3 MHz, C**H$_3$**-CH_2), 1.30 (2H, sx, J = 7 MHz, CH_3-C**H$_2$**-CH_2), 1.56 (2H, p, J = 7.5 Hz, CH_2-C**H$_2$**-CH_2), 3.16 (2H, t, J = 10 MHz, CH_2-C**H$_2$**-N), 3.49 (1H, s, br, NH) ppm. IR (cm^{-1}): 2958.9 (NH, s), 2873.8 (NH, m), 2734.1 (CH, w), 1698.3 (C=N, w), 1606.1 (C=C, w), 1473.7 (CH, s).

*Zn(TDT)-Na (general procedure – see conditions and results in **Table 23***): HTDT·2Na (31.1 mg, 0.125 mmol), base and any additional chemicals excluding zinc were dissolved in water (half of the total volume used) and any additional solvents used. Zinc source (0.125 mmol) was dissolved in the remaining water and then added dropwise to the ligand solution with stirring. The reaction solution was stirred at room temperature for 30 minutes after which the solid was isolated by centrifugation (7000 rpm, 3615 x g, 2 minutes). Samples to be dried were washed with ethanol (x 1) and then dried in a vacuum desiccator. PXRD data is shown in **Figure 75**, **Figure 76** (wet vs dried samples), **Figure 99** (3% HmIM added), **Figure 96** (varying base concentration), **Figure 97** (varying ethanol concentration) and **Figure 98** (zinc acetate metal source).

ZIF-8/Zn(TDT)-Na: ZIF-8 crystals were synthesised via the reported synthesis in Liang, W *et al.*,[65] zinc acetate dihydrate (22.0 mg, 0.12 mmol) was dissolved in water (1.5 mL) and added to a solution of 2-methylimiazole (HmIM) in water (1.5 mL). The solution was left static at room temperature for 24 h. The precipitate was isolated by centrifugation (10,000 rpm, 7378 x g, 5 min) to give a white solid. The ZIF-8 material was then re-suspended in a solution of H_3TDT.2Na (31.1 mg, 0.125 mmol) and sodium bicarbonate (50.0 mg, 0.595 mmol) in water (1.25 mL). $Zn(NO_3)_2.6H_2O$ (37.5 mg, 0.125 mmol) was dissolved in water (1.25 mL) and this solution was added to the ZIF-8 suspension. The suspension was left static at room temperature for 1 h. The precipitate was isolated by centrifugation (10,000 rpm, 7378 x g, 5 min) to give a white solid. PXRD data is shown in **Figure 100.**

Zn(TDT)-TBA (water only): HTDT·bis(TBA) (26.3 mg, 0.0625 mmol) and $NaHCO_3$ (25 mg, 0.30 mmol) were dissolved in water (0.625 mL). $Zn(NO_3)_2·6H_2O$ (18.8 mg, 0.0625 mmol) was dissolved in water (0.625 mL) and then added dropwise to the ligand solution with stirring. The reaction solution was stirred at room temperature for 30 minutes after which the solid was isolated by centrifugation (7000 rpm, 3615 x g, 2 minutes). Samples to be dried were washed with ethanol (x 1) and then dried in a vacuum desiccator. PXRD data is shown in **Figure 78**.

Zn(TDT)-TBA (10:1 water and ethanol): HTDT·bis(TBA) (26.3 mg, 0.0625 mmol) and $NaHCO_3$ (25 mg, 0.30 mmol) were dissolved in water (0.625 mL) and ethanol (0.125 mL). $Zn(NO_3)_2·6H_2O$ (18.8 mg, 0.0625 mmol) was dissolved in water (0.625 mL) and then added dropwise to the ligand solution with stirring. The reaction solution was stirred at room temperature for 30 minutes after which the solid was isolated by centrifugation (7000 rpm, 3615 x g, 2 minutes). Samples to be dried were washed with ethanol (x 1) and then dried in a vacuum desiccator. PXRD data is shown in **Figure 78**.

Protein@Zn(TDT)-Na: H_3TDT·2Na (31.1 mg, 0.125 mmol), $NaHCO_3$ (50.0 mg, 0.595 mmol) and protein (2 mg) were dissolved in water (1.25 mL). $Zn(NO_3)_2·6H_2O$ (37.5 mg, 0.125 mmol) was dissolved in water (1.25 mL) and then added dropwise to the ligand solution with stirring. The reaction solution was stirred at room temperature for 30 minutes after which the solid was isolated by centrifugation (7000 rpm, 3615 x g, 2 minutes). Samples to be dried were washed with ethanol (x 1) and then dried in a vacuum desiccator. PXRD data is shown in **Figure 81**.

3.4.3 Characterisation

For methods used for **CLSM**, **PXRD**, **NMR**, **FTIR** and **fluorescence spectroscopy** see experimental section in chapter 2.

Scanning electron microscopy (SEM):

Samples were imaged on a Philips XL30 field-emission scanning electron microscope (FESEM). Prior to analysis, samples were dry loaded onto adhesive carbon tabs on 12 mm aluminium stubs and coated in platinum.

Gas Adsorption

Zn(Me$_4$bpz): Gas adsorption isotherm measurements were collected on a Micromeritics 3-Flex Analyser. Pure samples of Zn(Me$_4$bpz) were activated by washing methanol (x 1) and dried under high vacuum at 110°C overnight prior to gas sorption measurements. Gas adsorption measurements were performed in N_2 at 77K. The BET surface areas were determined using proprietary software.

Zn(TDT)-TBA: Gas adsorption isotherm measurements were collected on a Micromeritics 3-Flex Analyser. Pure samples of Zn(TDT)-TBA were activated by washing methanol (x 1) and dichloromethane (x 1) and dried under high vacuum at room temperature overnight prior to gas sorption measurements. Gas adsorption measurements were performed in N_2 at 77K. The BET surface areas were determined using proprietary software.

Single Crystal X-ray Data:

A single crystal of Zn(Me$_4$bpz) was mounted in paratone-N oil on a nylon loop and X-ray diffraction data were collected at 150(2) K on an Oxford X-calibur single crystal diffractometer using Mo Kα radiation. The data set was corrected for absorption using a multi-scan method, and the structures solved by direct methods using SHELXS-2008 and refined by full-matrix least squares on F^2 by SHELXL-2014,[152-154] interfaced through the programs X-Seed[155] and Olex[152] (Tables).[156] Unless otherwise stated, non-hydrogen atoms were refined anisotropically and hydrogen atoms were included as invariants at geometrically estimated positions. The hydrogen atoms involved in hydrogen bonding (pyrazole-NH and water-OH) were located in the difference map and refined with U(iso) parameters of 1.2 and 1.5 times the pyrazole-N and water-O atoms, respectively. DFIX restraints (-0.95) were used to ensure the pyrazole-NH and water-OH bond lengths were chemically sensible but allowed to refine. The pyrazole-NH involved in hydrogen

bonding the pyrazole nitrogen is disordered over two positions and was refined over both positions with 50% occupancy of each site. The table below provides the crystal data and structure refinement details for Zn(Me_4bpz).

Table 14: *Crystal data and structure refinement for* ***Me_4bpz-HOF*** *(TP-ZnP1-16).*

Identification code	TP-ZnP1-16
Empirical formula	$C_{20}H_{30}N_8O$
Formula weight	398.52
Temperature/K	150(2)
Crystal system	Tetragonal
Space group	$I4_1/acd$
a/Å	24.7504(4)
b/Å	24.7504(4)
c/Å	14.8658(4)
α/°	90
β/°	90
γ/°	90
Volume/$Å^3$	9106.5(4)
Z	16
$P_{calc}/g/cm^3$	1.163
μ/mm^1	0.077
F(000)	3424.0
Crystal size/mm^3	0.45 x 0.33 x 0.2
Radiation	MoKα (λ = 0.71073)
2θ range for data collection/°	7.32 to 57.376
Index ranges	-19 ≤ h ≤ 31, -28 ≤ k ≤ 30, -18 ≤ l ≤ 20
Reflections collected	18995
Independent reflections	2631 [Rint = 0.0371, Rsigma = 0.0250]
Data/restraints/parameters	2631/4/148
Goodness-of-fit on F^2	1.032
Final R indexes [I>2σ (I)]	R_1 = 0.0467, wR_2 = 0.1237
Final R indexes [all data]	R_1 = 0.0628, wR_2 = 0.1351
Largest diff. peak/hole / e $Å^{-3}$	0.30/-0.23

FOX Assays:

FOX Reagent: Sorbitol (3.6 g, 19.8 mmol), xylenol orange (0.0143 g, 0.02 mmol), water (50 mL) and concentrated sulfuric acid (281 µL) were combined, followed by the addition of $(NH_4)_2FeSO_4.6H_2O$ (0.0196 g, 0.02 mmol). The resulting solution was made up to a final volume of 200 mL with water.

Calibration: Standard solutions of H_2O_2 (0.25, 0.125, 0.0625, 0.03125, 0.015625 mM) were prepared. 50 µL of standard was added to 950 µL of FOX reagent, followed by incubation at room temperature for 30 minutes, after which point the absorbance at 560 nm was recorded. From this data a calibration curve was produced.

Assay procedure (thermal testing): For free FCAT, 20 µL of FCAT stock solution (3.77 mg/mL) was added to 180 µL of water. This solution was heated to the desired temperature. After 10, 30, 60, 120 and 180 second, 30 µL aliquots were removed and placed on ice immediately. To these aliquots, H_2O_2 (0.25 mM, 1500 µL) was added. After 10 minutes, 50 µL of this aliquot/H_2O_2 solution was added to 950 µL of FOX reagent. After 30 minutes the absorbance at 560 nm was recorded and converted to a [H_2O_2] using the aforementioned calibration curve.

For FCAT@Zn(Me_4bpz) and FCAT@Me_4bpz HOF, stock solutions to be tested were made up of 4.2 mg (FCAT loading = 1.7%) and 4.7 mg (FCAT loading = 1.6%) respectively in 200 µL water. All remaining analysis was performed as above for the free FCAT.

Assay procedure (organic solvent testing): For free FCAT, 20 µL of FCAT stock solution (3.77 m/mL) was added to 180 µL of the desired organic solvent. The remainder of the assay was performed as outlined above for the free FCAT thermal analysis.

For FCAT@Zn(Me_4bpz) and FCAT@Me_4bpz HOF, stock solutions to be tested were made up of 4.2 mg (FCAT loading = 1.7%) and 4.7 mg (FCAT loading = 1.6%) respectively in 200 µL organic solvent. All remaining analysis was performed as above for the free FCAT.

Assay procedure (pH testing): For free FCAT, 3 µL of FCAT stock solution (3.77 m/mL) was added to 27 µL of the buffer of desired pH. After 3 minutes, H_2O_2 (0.25 mM, 1500 µL) was added. The remainder of the assay was performed as outlined above for the free FCAT thermal analysis.

For FCAT@Zn(Me_4bpz) and FCAT@Me_4bpz HOF, stock solutions to be tested were made up of 4.2 mg (FCAT loading = 1.7%) and 4.7 mg (FCAT loading = 1.6%) respectively in 30 µL buffer. All remaining analysis was performed as above for the free FCAT.

Inductively Coupled Plasma Mass Spectrometry (ICP-MS)

ICP-MS was performed on a Solution 7500cs ICP-MS spectrophotometer. All ICP-MS experiments were completed in triplicate.

Calibration: Stock solutions of element to be measured were made in 3% ICP-MS grade HNO_3 (concentrations used were 1000, 500, 200, 100, 50, 20, 10 and 0 ppb).

Process blank: 150 µL conc. HCl and 250 µL conc. ICP-MS grade HNO_3 were combined at left at room temperature overnight. The solution was vented and centrifuged to remove any solid impurities. 0.3429 mL of supernatant was made up to 5 mL using MQ water.

Sample preparation: A precisely measured quantity of sample (free enzyme ≈ 1 mg, enzyme@Zn(Me_4bpz) ≈ 1 mg and enzyme@Me_4bpz HOF ≈ 0.5 mg) was dissolved in conc. HCl (150 µL) and conc. ICP-MS grade HNO_3 (250 µL) and left at room temperature overnight. The solution was vented and centrifuged to remove any solid impurities. 0.3429 mL of supernatant was made up to 5 mL using MQ water.

Chapter 4: Conclusions and Future Directions

In chapter 2 two bioMOFs were synthesized; zinc glutamate (**bioMOF-1**) and zinc carnosine (**bioMOF-2**) (L-carnosine = β-alanine-L-histidine). The use of both MOFs for biomolecule encapsulation and protection was attempted, targeting the formation of biocomposites via biomimetic mineralisation. PXRD data revealed that the structure of neither MOF changed upon the inclusion of protein. However, changes in the morphology of **bioMOF-2** crystals were noticed, where pure **bioMOF-2** and enzyme@**bioMOF-2** formed as sheet-like and block-shaped crystals respectively. For **bioMOF-2**, addition of proteins with pI less than 6 led to the formation of an amorphous precipitate, likely a protein-rich zinc salt, prior to the precipitation of **bioMOF-2**, potentially due to pH effects. This led to a reduction in the concentration of protein available to be encapsulated within **bioMOF-2**. No amorphous precipitate was formed upon addition of proteins with higher pIs.

UV-Vis spectroscopy data for the protein@**bioMOF-1** composites revealed that those that contained protein experienced a longer precipitation time compared to pure **bioMOF-1**. This suggested that interactions between protein and the MOF components hindered MOF formation, potentially due to the formation of complexes between the protein and MOF component. Thus, the formation of protein@**bioMOF-1** composites was different to biomimetic mineralisation wherein the presence of protein accelerates MOF growth. Further, CLSM/fluorescence data for FITC-tagged protein@**bioMOF-1** samples, before and after removing surface-bound enzyme showed significant reduction in the total quantity of protein present. This data suggested that the protein was predominantly surface-bound and therefore minimal quantities of protein were encapsulated within the MOF crystals.

For the protein@**bioMOF-2** composites, aqueous assays were used to determine the change in enzymatic activity upon exposing the biocomposites to harsh conditions. These results confirmed that the initial amorphous precipitate had a higher enzymatic activity than the protein@**bioMOF-2** samples. Further, the assay data showed that for CAT@**bioMOF-2** and HRP@**bioMOF-2**, the MOF was unable to offer protection to the catalase present upon exposure to elevated temperatures, organic solvents and acidic and basic conditions. Instead, it appeared that the MOF made the enzymes more susceptible to decomposition.

Thus, despite the inability of either bioMOF to successfully encapsulate and protect enzymes, these results still produced useful information. Specifically, increasing the complementarity between the MOF and biomolecule does not necessarily lead to greater chances of successful

biomolecule encapsulation. For the two bioMOFs investigated, this increased compatibility may have instead caused undesirable observations such as the formation of the amorphous precipitate during **bioMOF-2** syntheses, or the delayed precipitation of **bioMOF-1** when protein was attracted to the MOF components, potentially due to pH effects. Further, the imidazole side chain of carnosine does not ensure that the MOF will undergo successful biomimetic mineralisation. Instead, it is more likely that the N-donor groups must be the sole binding sites in the ligands such that no hard donor groups such as carboxylates can promote much more rapid MOF growth.

Chapter 3 was concerned with the synthesis and investigation of frameworks containing purely azolate linkers. Two different N-donor ligands were synthesized and used for the formation of zinc-based MOFs; Me_4bpz and H_3TDT (4,5-di(1H-tetrazol-5-yl)-2H-1,2,3-triazole). The former was used to form **Zn(Me_4bpz)-aq** and **Me_4bpz-HOF**.

The PXRD data of **Zn(Me_4bpz)-aq** did not match that of the solvothermally synthesised material, and the inability to synthesise single crystals meant that the structure was unable to be determined. By comparing PXRD and gas adsorption data for **Zn(Me_4bpz)-aq** and the solvothermally synthesised material, it was postulated that the two materials were only slightly different, potentially as a result of missing linker defects.

Me_4bpz-HOF was discovered during attempts to grow single crystals of **Zn(Me_4bpz)-aq**. Single crystal data for **Me_4bpz-HOF** revealed it to be a closely-packed material comprising only organic building blocks. The structure also contained hydrogen-bonded water molecules that were integral to the structure.

As expected, **Zn(Me_4bpz)-aq** was found to be significantly more stable than **Me_4bpz-HOF**, however, the presence of protein was able to stabilize the latter in acidic solutions and at elevated temperatures. Turbidity testing revealed that **Zn(Me_4bpz)-aq** experienced accelerated growth in the presence of protein, while the **Me_4bpz-HOF** grew identically with and without added enzyme, suggesting that only the former was potentially undergoing biomimetic mineralisation. Aqueous assays were then conducted on both FCAT@**Zn(Me_4bpz)** and FCAT@**Me_4bpz-HOF** samples which revealed that significant proportions of the enzymatic activity observed was due to leached zinc or enzyme. This leaching was also observed in water at room temperature, indicating that a large proportion of the enzyme present was loosely-bound to the surface of the material. Upon accounting for this leaching, the remaining enzymatic activity present in the solid samples still increased following exposure to harsh environments including

THF and elevated temperatures. This suggested that defects were forming in the crystals which allowed for less hindered diffusion of assay reagents through the framework or further, more significant enzyme leaching. As a result of the low stability of both **Zn(Me_4bpz)** and **Me_4bpz-HOF**, in addition to the close-packed nature of the latter, and the high prevalence of loosely bound enzyme, these two materials were deemed to be unsuitable for enzyme encapsulation.

The second N-donor containing ligand (H_3TDT) was used to synthesise **Zn(TDT)**. However, despite attempting this with both the sodium and tetrabutylammonium (TBA) ligand salts to ensure solubility in aqueous conditions, the reported sodalite **Zn(TDT)** MOF was unable to be synthesised. The material formed using the sodium salt (**Zn(TDT)-Na**) was extremely unstable, with no conditions, including the addition of enzyme, being able to increase the stability of the material. Further, PXRD data and N_2 adsorption analysis for the material formed with the TBA salt (**Zn(TDT)-TBA**) revealed that it was a non-porous structure.

Thus, despite the similar coordination chemistry of these linkers and those used in the ZIF-8 and related materials, the low stability of the materials and the observed decomposition that occurred following exposure to test conditions makes **Zn(Me_4bpz)** and **Zn(TDT)** unsuitable for biomolecule encapsulation.

Despite the inability to successfully encapsulate and protect biomolecules within either of the Me_4bpz derived materials, key pieces of information were still ascertained. The sole presence of azolate groups does not guarantee that the MOF will be able to undergo biomimetic mineralisation to result in successful enzyme protection. Further, rigorous stability testing must be performed on materials used for biomolecule encapsulation to ensure that they do not decompose, whether partially or fully, upon exposure to the conditions in which they are being used to protect the biomolecule. This would ensure that significant enzymatic activity is not due to leached metal or enzyme.

One of the areas of future research activity with regard to using MOFs to encapsulate and protect biomolecules includes investigation of a greater range of frameworks. This will provide a wider understanding of key features necessary to facilitate biomimetic mineralisation and form stable biocomposites. Additional bioMOFs could be investigated, for example those comprised of histidine- or proline-containing peptides to further investigate the effect of imidazole functionality or rigidity respectively. BioMOFs using alternate biological linkers such as cyclodextrins and porphyrins could also be investigated for their ability to encapsulate and

protect biomolecules; the former gives access to the co-called ‘edible MOFs’ when combined with sodium or potassium ions.

Further, a more targeted area of future work is to prevent the formation of the initial amorphous precipitate during the enzyme@**bioMOF-2** syntheses with lower pI enzymes. This would ensure ample protein concentrations are available to precipitate with the crystalline material. Proteins with high pIs could be investigated if suitable assays are available. Alternatively, surface modification of low pI enzymes by processes such as amination could be performed to increase the pI, meaning that previously used assays were still viable. Modulators such as polyvinylpyrrolidone (PVP) could also be added as these have been shown to aid encapsulation via co-precipitation.

The isoreticular structures of **Zn(Me$_4$bpz)** could be studied to investigate the effect the changing the ligand (e.g. functionality, steric bulk) has on the ability to encapsulate and protect enzymes, without changing the structure of the MOF. Changing the ligand functionality could modify the solubility of the linker and allow stable biocomposite formation in aqueous conditions. Additional steric bulk would only be feasible if the linker length was increased to ensure no reduction in pore size. A wider variety of N-donor containing frameworks should also be investigated, such as the MFU-4, MFU-4*l* and CFA-1 MOFs mentioned in the introduction of chapter 3. The use of these three MOFs would investigate the effect of ligand length and MOF chirality on the ability of a framework to successfully undergo biomimetic mineralisation.

Appendix 1: Supplementary Information for Chapter 2

Table 15: *Conditions for synthesis of* ***bioMOF-1****. All tests were conducted in water (10 mL). Shaded sections highlight sets of trials that appeared to be most promising.*

Factor Being Investigated	L-Glutamic Acid (mmol)	Base (mmol)	Zn Salt (mmol)	Time for Initial Precipitation	PXRD
Concentration	2 mmol	NaOH (5 mmol)	$ZnSO_4·7H2O$ (2 mmol)	immediate	ZnGlut
	1 mmol	NaOH (2.5 mmol)	$ZnSO_4·7H_2O$ (1 mmol)	immediate	amorphous
	0.5 mmol	NaOH (1.25 mmol)	$ZnSO_4·7H_2O$ (0.5 mmol)	immediate	ZnGlut
Type and amount of base for $ZnSO_4.7H_2O$	0.5 mmol	KOH (1.25 mmol)	$ZnSO_4·7H_2O$ (0.5 mmol)	immediate	amorphous
	0.5 mmol	K_2CO_3 (1.25 mmol)	$ZnSO_4·7H_2O$ (0.5 mmol)	immediate	amorphous
	0.5 mmol	$NaHCO_3$ (1.25 mmol)	$ZnSO_4·7H_2O$ (0.5 mmol)	30-60 seconds	ZnGlut
	0.5 mmol	$NaHCO_3$ (0.625 mmol)	$ZnSO_4·7H_2O$ (0.5 mmol)	5 min	ZnGlut
	0.5 mmol	$NaHCO_3$ (0.55 mmol)	$ZnSO_4·7H_2O$ (0.5 mmol)	10-30 min	ZnGlut
	0.5 mmol	$NaHCO_3$ (0.5 mmol)	$ZnSO_4·7H_2O$ (0.5 mmol)	overnight	ZnGlut
	0.5 mmol	$NaHCO_3$ (0.417 mmol)	$ZnSO_4·7H_2O$ (0.5 mmol)	No precipitate after 3 days	N/A
	0.5 mmol	$NaHCO_3$ (0.3125 mmol)	$ZnSO_4·7H_2O$ (0.5 mmol)	No precipitate after 3 days	N/A
	0.5 mmol	No base	$ZnSO_4·7H_2O$ (0.5 mmol)	No precipitate after 3 days	N/A
Type and amount of base for $(ZnOAc)_2.2H_2O$	0.5 mmol	NaOH (1.25 mmol)	$ZnAcetate·2H_2O$ (0.5 mmol)	5 seconds	amorphous
	0.5 mmol	KOH (1.25 mmol)	$ZnAcetate·2H_2O$ (0.5 mmol)	5 seconds	amorphous
	0.5 mmol	No base	$ZnAcetate·2H_2O$ (0.5 mmol)	No precipitate overnight	N/A
	0.5 mmol	$NaHCO_3$ (1.25 mmol)	$ZnAcetate·2H_2O$ (0.5 mmol)	30-60 seconds	ZnGlut
	0.5 mmol	$NaHCO_3$ (1 mmol)	$ZnAcetate·2H_2O$ (0.5 mmol)	60 seconds	ZnGlut
	0.5 mmol	$NaHCO_3$ (0.5 mmol)	$ZnAcetate·2H_2O$ (0.5 mmol)	6 min	ZnGlut
	0.5 mmol	$NaHCO_3$ (0.4 mmol)	$ZnAcetate·2H_2O$ (0.5 mmol)	40 min	ZnGlut
Other metal salts	0.5 mmol	NaOH (1.25 mmol)	$ZnNO_3·6H_2O$ (0.5 mmol)	immediate	amorphous
	0.5 mmol	NaOH (1.25 mmol)	$ZnCl_2$ (0.5 mmol)	immediate	amorphous

Table 16: *Washing procedures used to remove surface bound FCAT and FMb from* ***bioMOF-1*** *(% concentrations are in w/v, all solutions are made up in water). Tagged enzyme shown in green.*

Wash	No. of Washes	CLSM Results	
		FCAT-on-bioMOF-1	**FMb-on-bioMOF-1**
No Wash	-	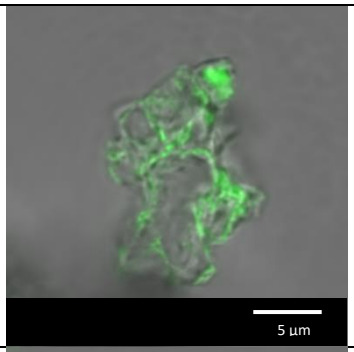	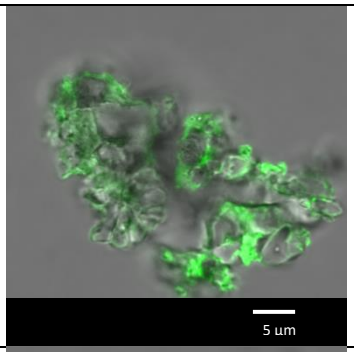
10% SDS	4		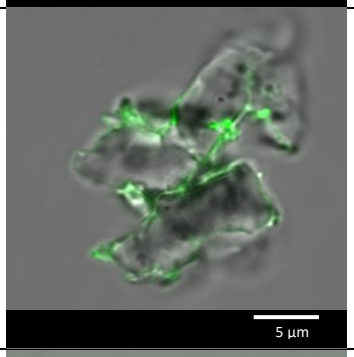
1% EDTA	3	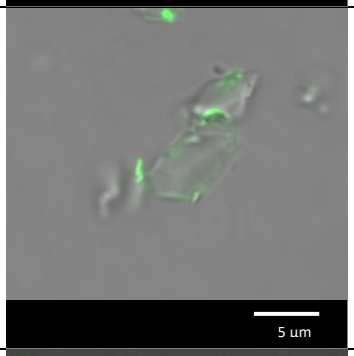	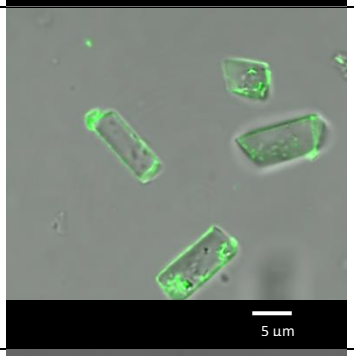
10% SDS + 10% EDTA (1:1)	4	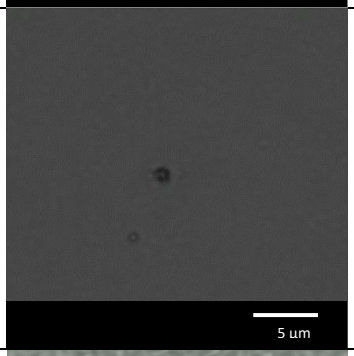	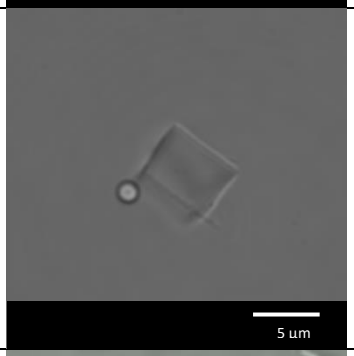
10% SDS + 1% EDTA (1:1)	3	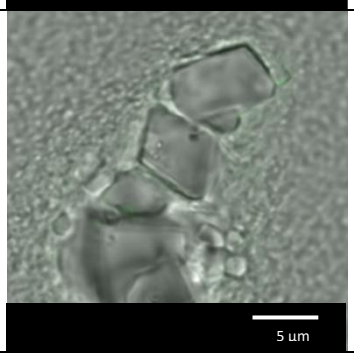	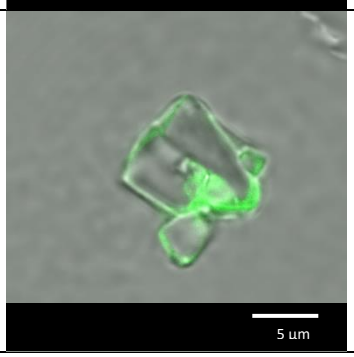

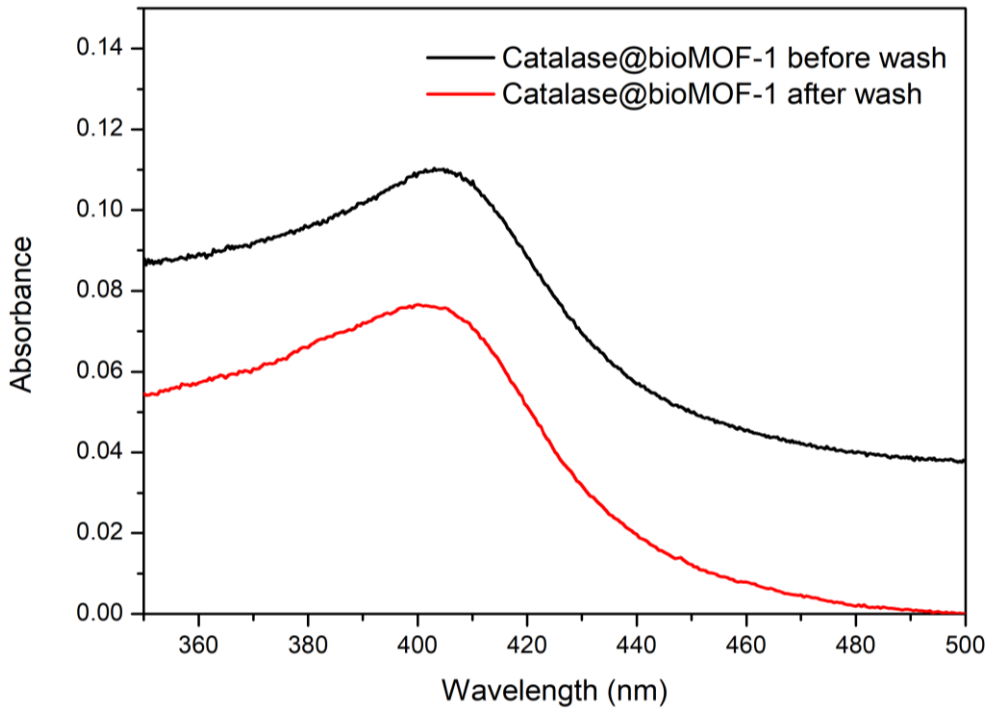

Figure 82: *Solid-state UV-Vis data for CAT@**bioMOF-1** before and after washing with a 1:1 mixture of 10% SDS and 1% EDTA.*

Table 17: *Acidic and basic stability tests for **bioMOF-2.***

pH	Acid or base used	After 1 hour	PXRD	Conclusion
0	Conc. HCl	Dissolved (immediate)	N/A	Unstable
3	Acetic acid	Dissolved (30 min)	N/A	Unstable
3	Diluted HCl	No observable decomposition	Correct	Stable
5	Diluted HCl	No observable decomposition	Correct	Stable
9	Bicarbonate-carbonate buffer	No observable decomposition	Correct	Stable
11	NaOH	Slightly dissolved	Amorphous	Unstable
14	NaOH	Dissolved (immediate)	N/A	Unstable

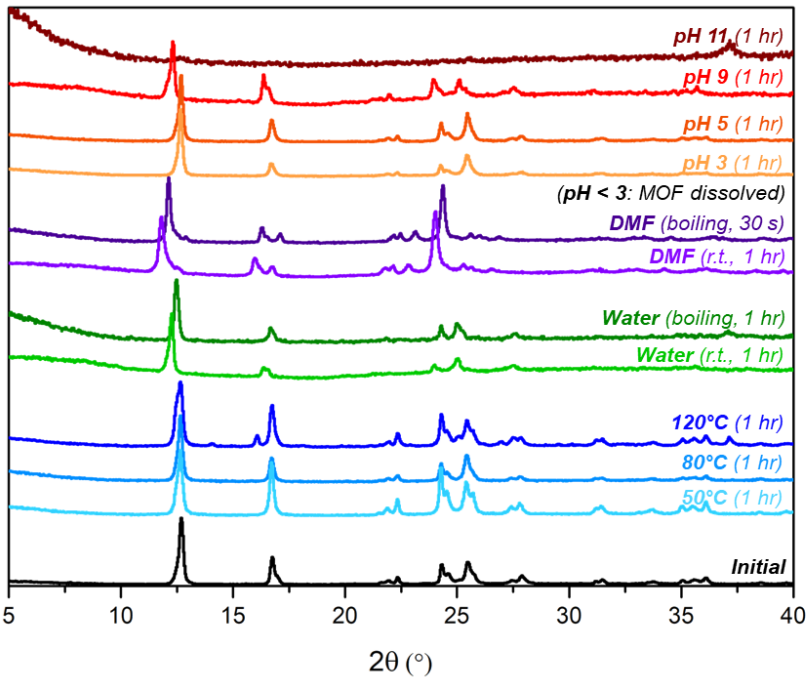

Figure 83: *PXRD data for* ***bioMOF-2*** *samples following exposure to various pHs, DMF, water and elevated temperatures to determine the stability of the material.*

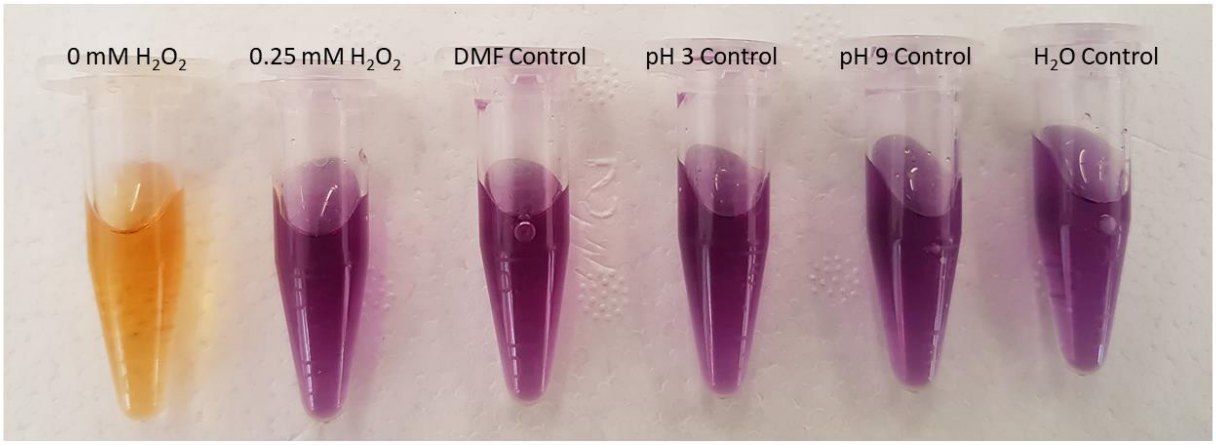

Figure 84: *Qualitative controls for DMF, pH 3 (dilute HCl), pH 9.2 (bicarbonate-carbonate buffer) and water in the FOX Assay compared to 0 mM and 0.25 mM H_2O_2 standards. Each control was performed by reacting 50 µL of solvent with 1 mL of 0.25 mM H_2O_2 for 10 minutes before adding 50 µL of this reaction solution to 950 µL of FOX reagent. Photo was taken after reacting FOX plus H_2O_2 solutions for 30 minutes at room temperature.*

Table 18: *Analysis of success for solutions of EDTA in Tris-HCl buffer (pH 8, 0.05 M) of varying concentrations for the decomposition of* ***bioMOF-2,*** *plus qualitative FOX assays for free catalase after exposure to the EDTA solutions. All samples were exposed to the EDTA solutions for 10 minutes. Percentage concentrations are m/V. 1-, 5- and 10-minute times refer to length of time samples were exposed to 0.25 mM H_2O_2 prior to addition to FOX reagent.*

	Did MOF dissolve	**PXRD after 10 min**	**FOX assay EDTA controls**		
			1 min	**5 min**	**10 min**
0% EDTA	Did not dissolve	ZnCarn	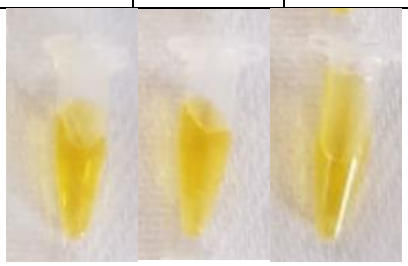		
0.1% EDTA	Did not dissolve	Amorphous	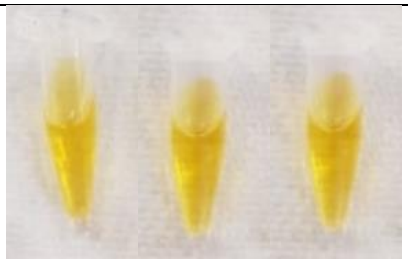		
1% EDTA	Dissolved	N/A	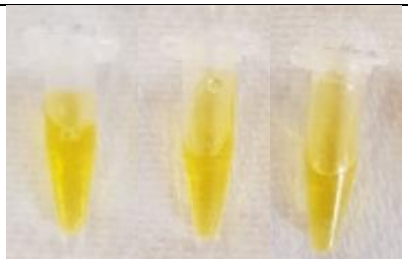		
10% EDTA	Dissolved	N/A	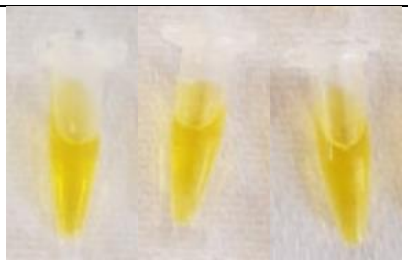		

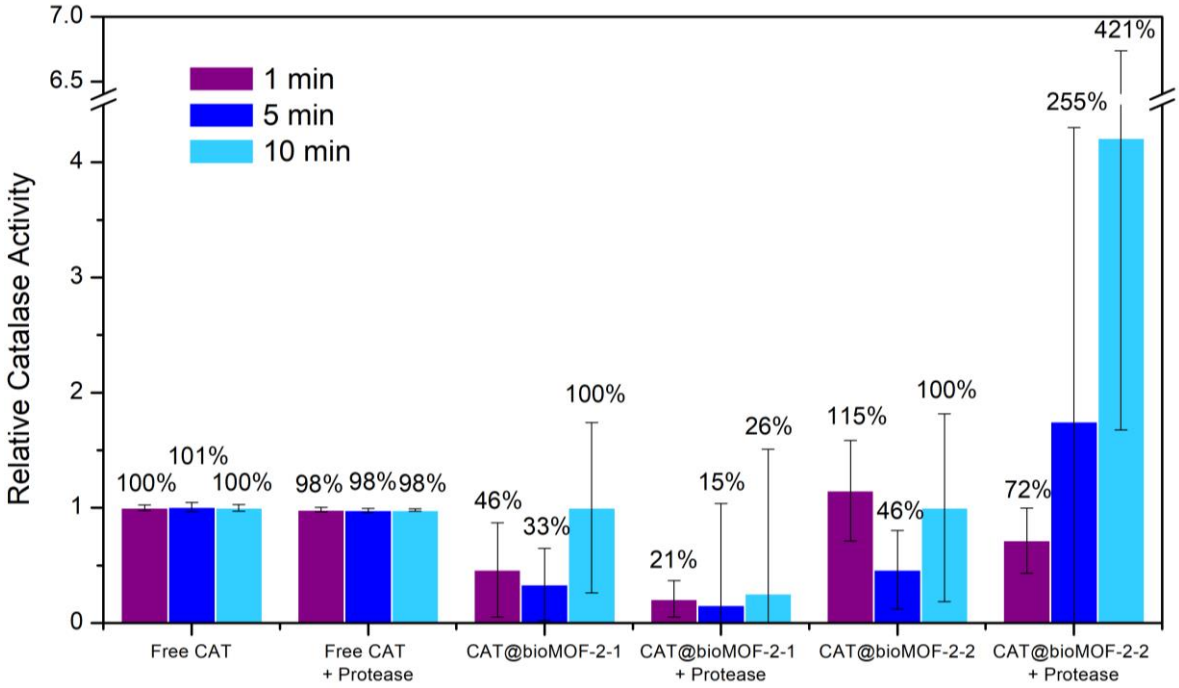

Figure 85: *Relative (activity relative to the original activity of each sample prior to protease exposure (after 10 min exposure to 0.25 mM H_2O_2)) catalase activity for CAT@**bioMOF-2**-1 (initial amorphous precipitate) and CAT@**bioMOF-2**-2 (second crystalline precipitate) before and after exposure to protease (2 mg/mL in 0.05 M Tris-HCl pH 8 buffer, 2 hr). Assays were performed with [H_2O_2] of 0.25 mM, times refer to the length of time samples were left in H_2O_2 solution before adding to FOX reagent. Activity values are relative to the activity of each sample prior to protease treatment with 10 min H_2O_2 treatment time.*

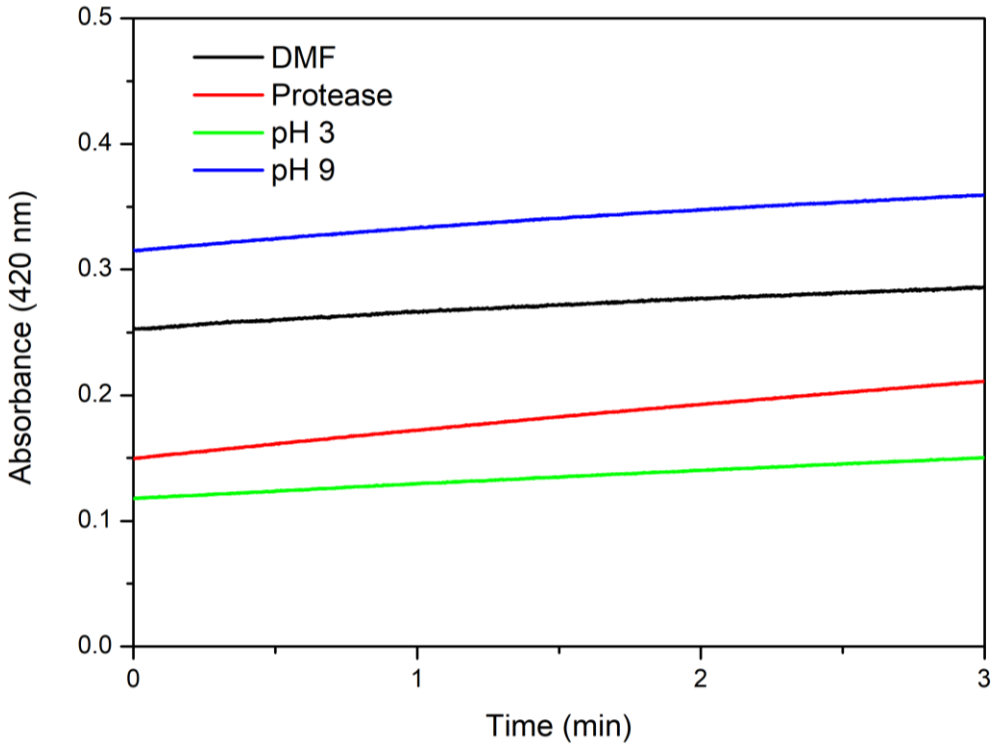

Figure 86: *Raw data from the solvent controls run for the peroxidase assay with DMF, protease (2mg/mL in Tris buffer (0.05 M, pH 8)), acid (pH 3, dilute HCl) and base (bicarbonate-carbonate buffer, pH 9.2). Change in absorbance at 420 nm indicates the rate of conversion of pyrogallol to purpurogallin.*

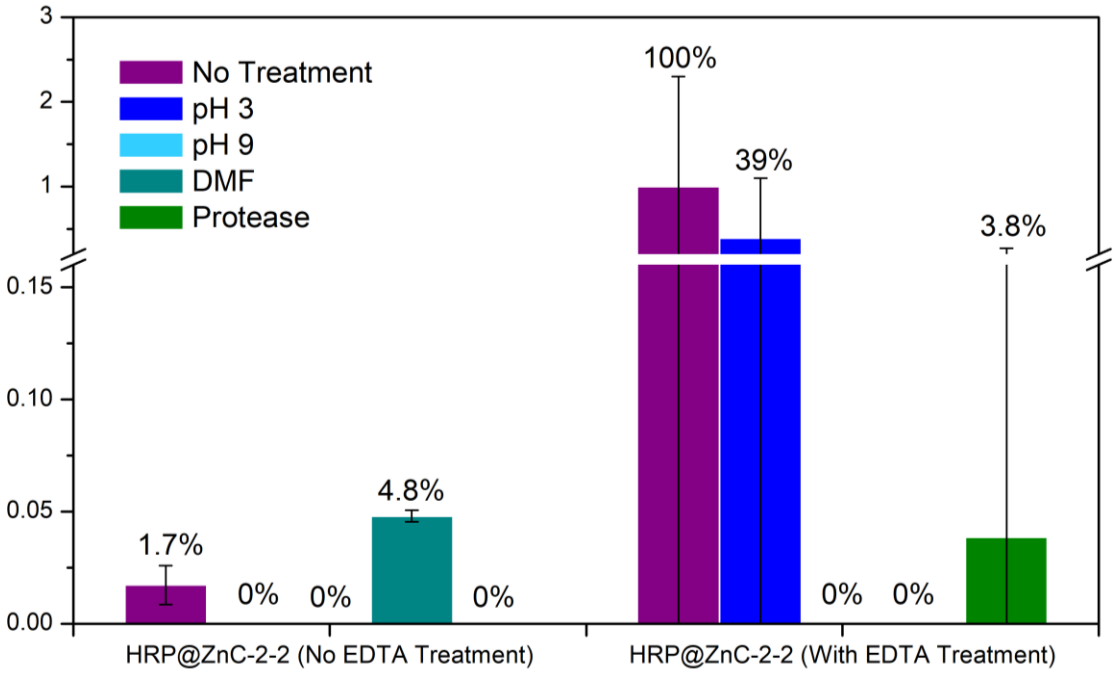

Figure 87: *Relative HRP activity for HRP@**bioMOF-2** before (purple) and after exposure to pH 3 (dilute HCl, 1 hr) (dark blue), pH 9.2 (bicarbonate-carbonate buffer, 1 hr) (light blue), DMF (1 hr) (aqua) and protease (2 mg/mL in 0.05 M Tris-HCl pH 8 buffer, 2 hr) (green) with and without subsequent treatment with EDTA (1% w/v EDTA in 0.05 M Tris-HCl pH 8 buffer).*

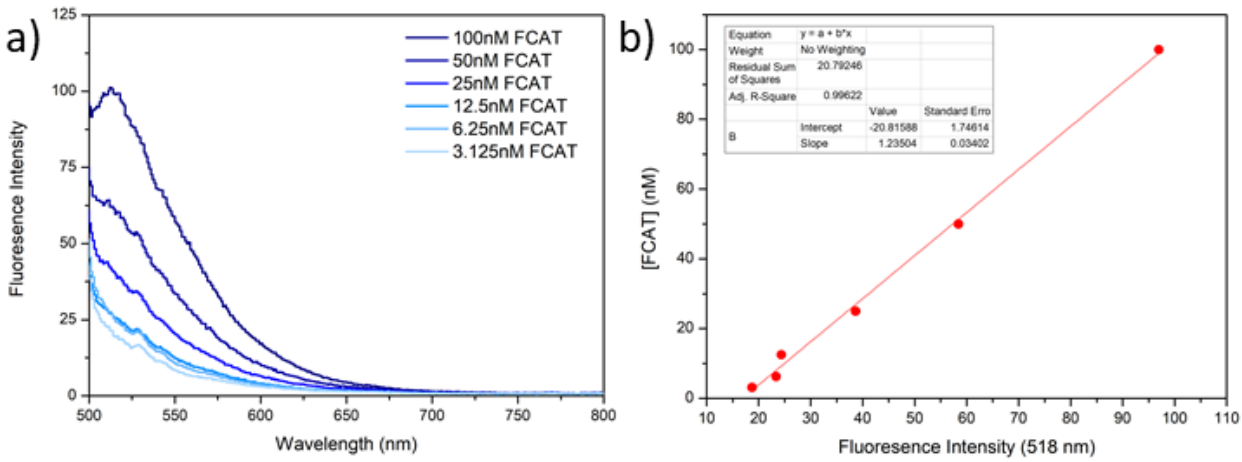

Figure 88: *a) Raw fluorescence data for calibration of FCAT in 5% EDTA with excitation at 488 nm and b) calibration curve for FCAT concentration (in 0.1M pH 5 citric-trisodium citrate buffer) against fluorescence intensity at 518 nm.*

Appendix 2: Supplementary Information for Chapter 3

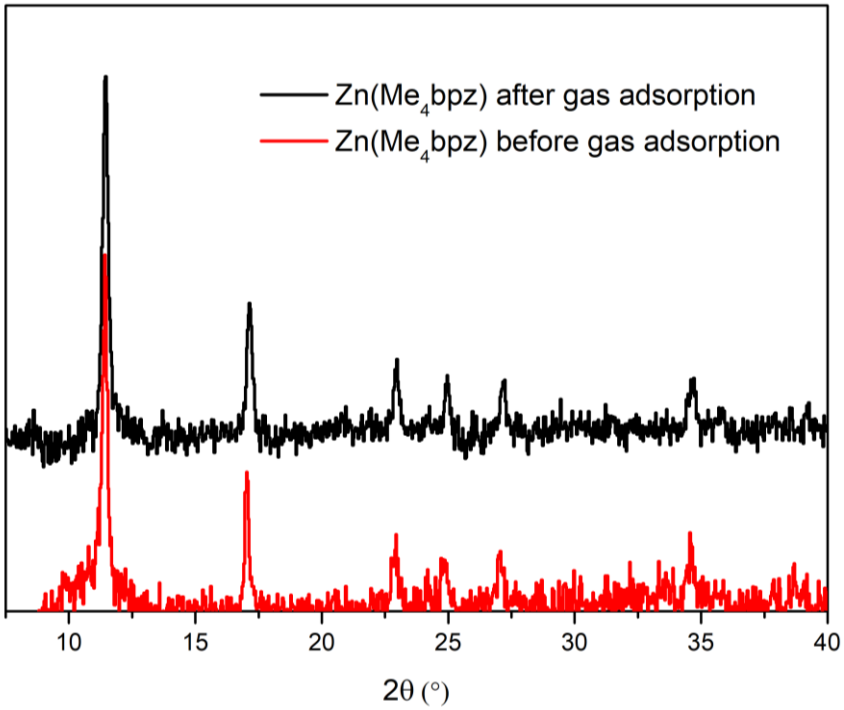

Figure 89: *PXRD of Zn(Me4bpz) before (red) and after (black) N_2 gas adsorption following activation at 110°C overnight.*

Table 19: *ICP-MS data and FCAT loading calculations for FCAT@1:1 and 1:16 Zn(Me4bpz) – 52.209 mg of FCAT per mg of S recorded (based off of free FCAT ICP-MS data).*

	[S] (ppb)	m_{FCAT}	m_{sample} (mg)	FCAT Loading (%)	**Average ± error (std. dev.) (%)**
FCAT@1:1 Zn(Me4bpz)	81.496	0.021274	1	2.127435	**1.685223 ± 0.791023**
	<23.658	< 0.006176	0.8	< 0.771981	
	115.640	0.030188	1.4	2.156254	
FCAT@1:16 Zn(Me4bpz)	<23.658	< 0.006176	0.5	< 1.235169	**1.509651 ± 0.475417**
	<23.658	< 0.006176	0.3	< 2.058615	
	<23.658	< 0.006176	0.5	< 1.235169	

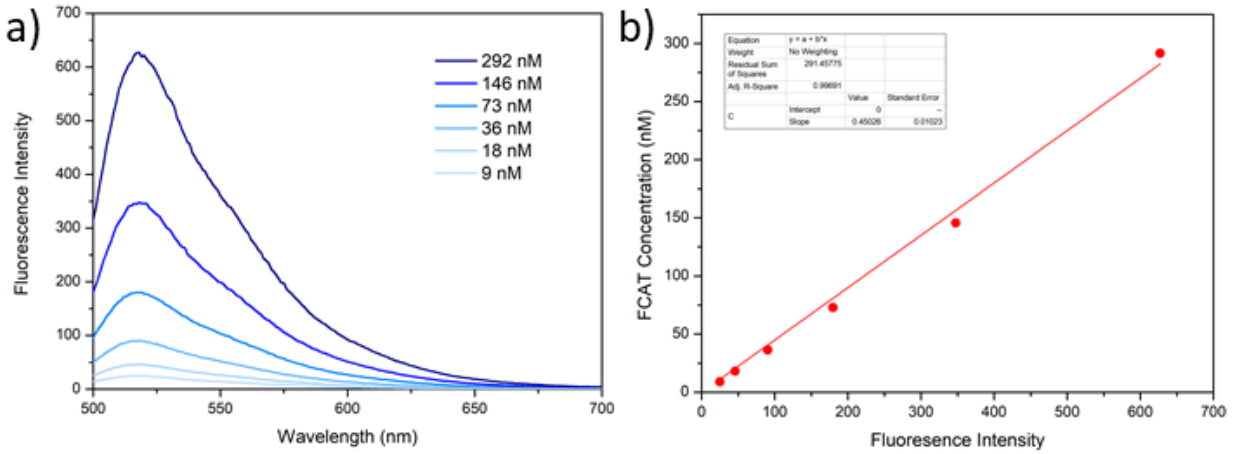

Figure 90: *a) Raw fluorescence data for calibration of FCAT in 0.1 M pH 5 citric-trisodium citrate buffer with excitation at 488 nm (sample 1 only). b) calibration curve for FCAT concentration (in 0.1M pH 5 citric-trisodium citrate buffer) against fluorescence intensity at 518 nm.*

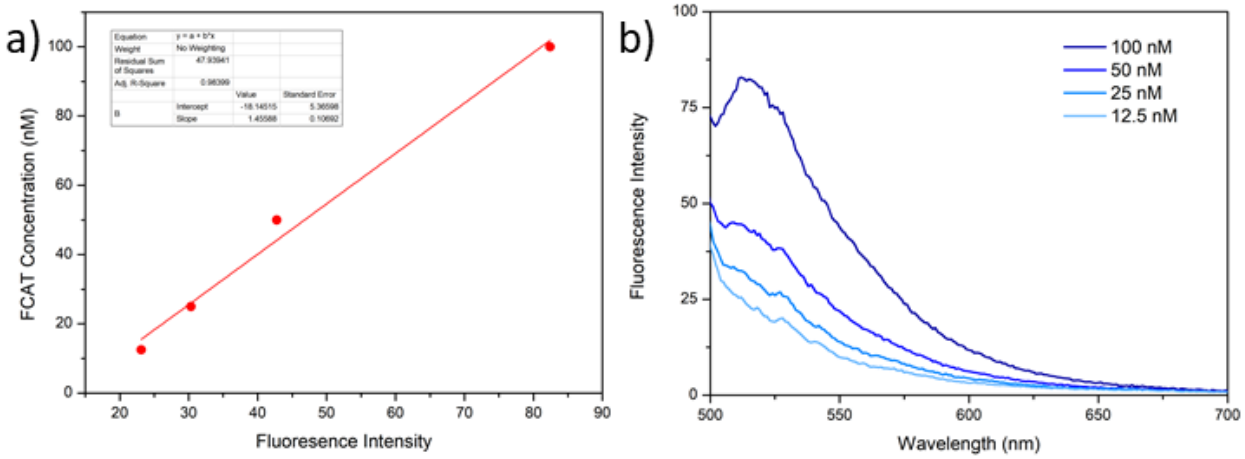

Figure 91: *a) Raw fluorescence data for calibration of FCAT in 0.1 M pH 5 citric-trisodium citrate buffer with excitation at 488 nm (samples 2 and 3 only). b) calibration curve for FCAT concentration (in 0.1M pH 5 citric-trisodium citrate buffer) against fluorescence intensity at 518 nm.*

Table 20: *Fluorescence data and FCAT loading calculations for FCAT@1:16 Zn(Me$_4$bpz) in 0.1 M pH 5 citric-trisodium citrate buffer.*

	Sample	Fluorescence Intensity (518 nm)	Calculated FCAT Concentration (nM)	Volume (mL)	FCAT present (mg)	Mass Sample (mg)	**Loading (%)**	**Average ± error (std. dev.) (%)**
1:16 Zn(Me$_4$bpz)	1	446.66	201.13	4.0	0.19	9.2	**2.10 %**	**1.6 ± 0.5 %**
	2	60.27	69.60	1.5	0.025	2.0	**1.25 %**	
	3	52.88	58.84	1.5	0.021	1.6	**1.32 %**	

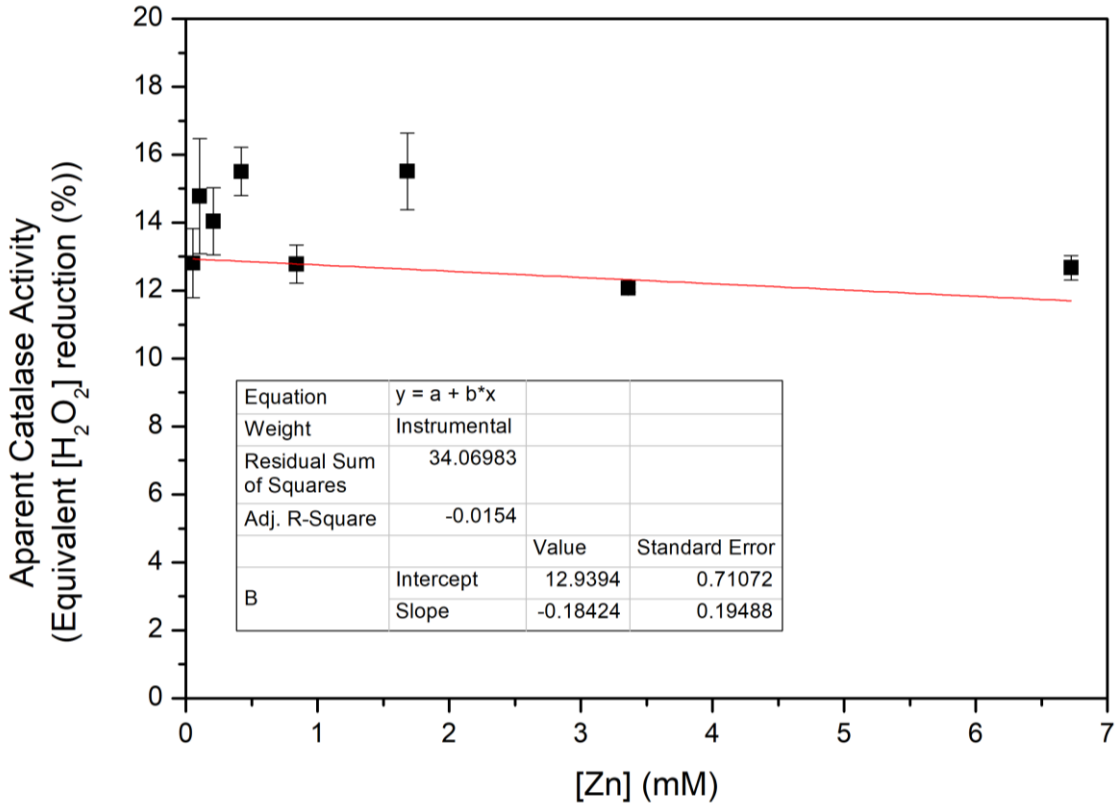

Figure 92: *Decomposition of H_2O_2 by aq. zinc solutions in the FOX assay. Results were obtained by adding 30 µL of $Zn(NO_3)_2{\cdot}6H_2O$ stock solution in water to H_2O_2 (0.25 mM, 1500 µL) and leaving to react for 10 minutes before adding 50 µL of the stock/H_2O_2 solution to FOX reagent (950 µL). After standing at room temperature for 30 minutes, the absorbance at 560 nm was recorded. These absorbances were converted to [H_2O_2] concentrations using a calibration curve, and % H_2O_2 decomposition is relative to the 0.25 mM starting concentration. Errors at the standard error of three independent measurements.*

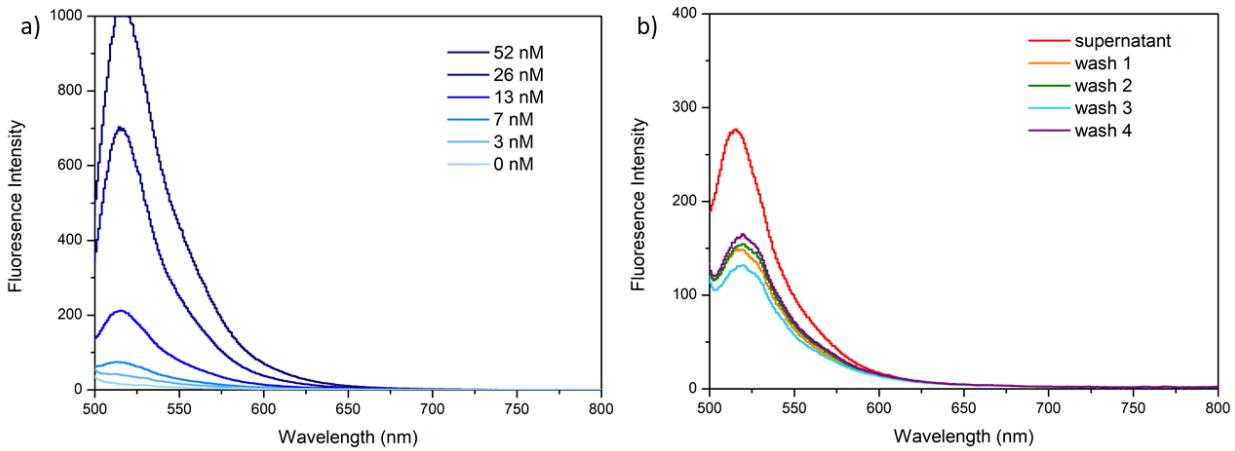

Figure 93: *a) Calibration data for FCAT fluorescence in water and b) raw data showing fluorescence intensity of supernatant from the FCAT@**Zn(Me$_4$bpz)-aq** synthesis and water washes of the synthesised material to remove loosely bound FCAT.*

Table 21: Raw EDX data for atomic percentages in various sites within a sample of Zn(Me_4bpz).

	Atomic Percent (%)										
Site	**C**	**O**	**N**	**Zn**	**Na**	**Pt**	**S**	**Si**	**Zr**	**Ti**	**Mo**
1	73.1	14.2	8.7	2.0	1.6	0.3	0.2	-	-	-	-
2	76.0	15.1	4.7	2.1	1.6	0.2	0.2	-	-	-	-
3	72.5	13.2	7.8	3.9	2.1	0.4	-	-	-	-	-
4	70.5	11.8	9.8	4.1	3.1	0.3	-	0.3	0.1	-	-
5	62.9	19.3	11.7	3.0	2.4	0.2	0.2	0.2	-	-	-
6	72.5	13.2	7.8	3.9	2.1	0.4	-	-	-	-	-
7	76.6	12.9	5.9	2.5	2.0	0.2	-	-	-	-	-
8	83.1	11.8	-	2.9	1.8	0.3	0.2	-	-	-	-
9	83.9	11.0	-	2.5	2.0	0.4	-	-	-	0.1	-
10	67.6	12.9	14.8	2.5	1.7	0.3	0.1	-	-	-	-
11	65.9	12.2	18.5	1.8	1.0	0.3	0.1	0.1	-	-	-
12	87.8	9.6	-	2.1	-	0.3	-	-	-	-	0.2
13	59.4	13.0	19.6	3.7	3.7	0.2	-	0.3	-	-	-
14	59.4	14.3	19.3	4.3	2.4	0.2	-	-	-	-	-
15	62.7	12.1	15.6	5.9	3.4	0.3	-	-	-	-	-

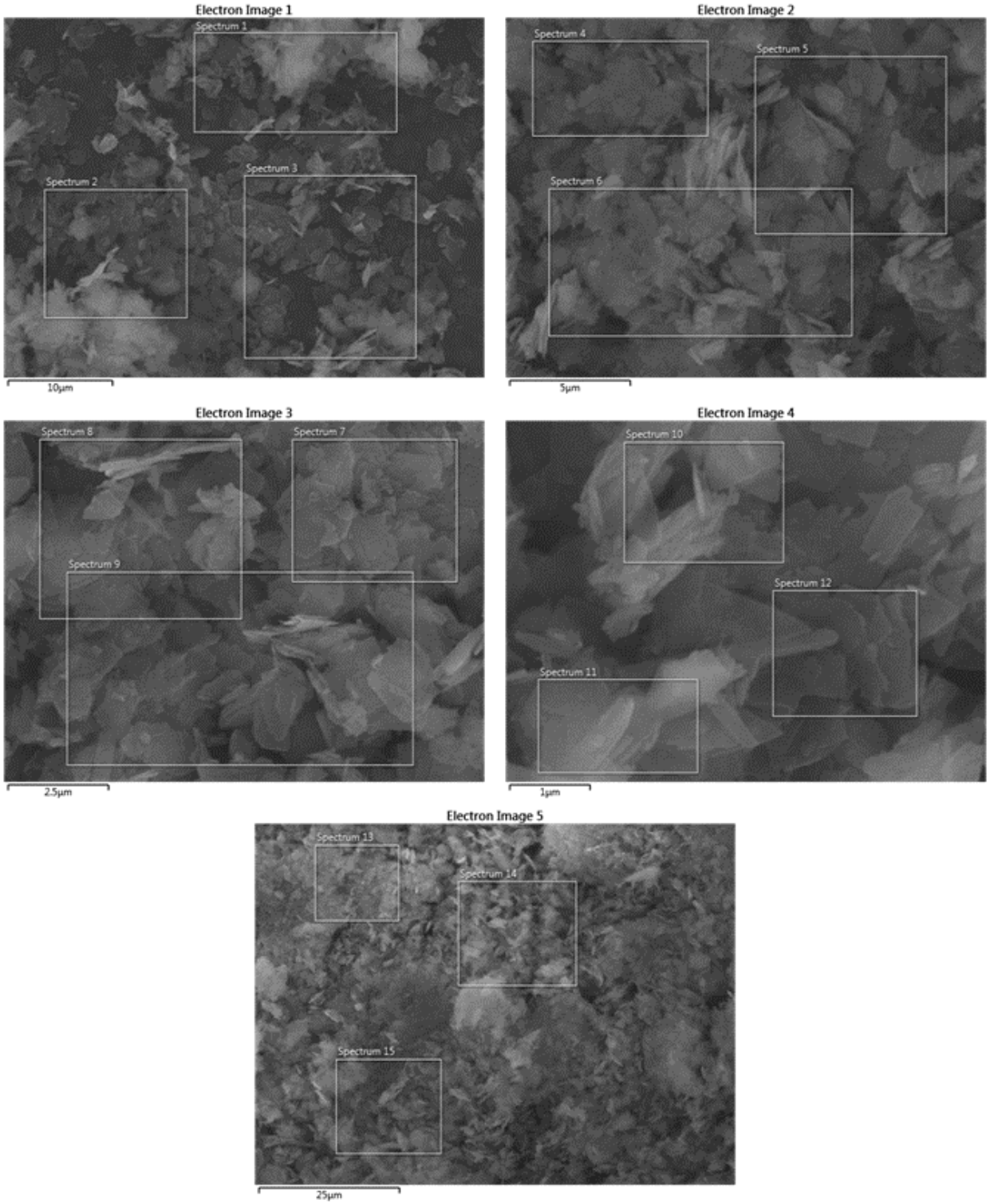

Figure 94: *SEM images of Zn(Me$_4$bpz) showing regions used to produce EDX spectra 1-15.*

Table 22: *Crystallisation attempts for* ***Zn(Me$_4$bpz)-aq***

Crystallisation Method	Top Layer	Bottom Layer	Results
Slow diffusion *via* layering	Me_4bpz in EtOH (1 mL, 20 mM)	$Zn(NO_3)_2$ in 28% aq. NH_3 (1 mL, 20 mM)	No crystals
	Me_4bpz in MeOH (1 mL, 20 mM)	$Zn(NO_3)_2$ in H_2O (1 mL, 20 mM)	No crystals

Crystallisation Method	Vial 1	Vial 2	Method	Results
Slow mixing	$Zn(NO_3)_2$ in H_2O (2 mL, 20 mM)	Me_4bpz (20mM) and $NaHCO_3$ (0.24 M) in MeOH (2 mL)	Place vial 1 in vial 2, the slowly add water to vial 2 until solutions in both vials combine	White powder formed around rim of vial 1 (1-2 days). No single crystals

Crystallisation Method	m ($Zn(NO_3)_2·6H_2O$) (mg)	m (Me_4bpz) (mg)	Solvent system	Conditions	Results
Solvothermal	14.9 (0.05 mmol)	9.5 (0.05 mmol)	DMF (5 mL) HNO_3 (1 drop)	85°C overnight	No single crystals
	7.5 (0.025 mmol)	9.5 (0.05 mmol)	DMF (5 mL)	85°C overnight	No single crystals
	14.9 (0.05 mmol)	9.5 (0.05 mmol)	DMF (5 mL)	120°C overnight	No single crystals

Crystallisation Method	m ($Zn(NO_3)_2$) (mg)	m (Me_4bpz) (mg)	m ($NaHCO_3$) (mg)	m (BSA) (mg)	Solvent system	Results
Slow evaporation	7.5 (0.025 mmol)	9.5 (0.05 mmol)	26.3 (0.3125 mmol)	-	H_2O (5 mL) MeOH (0.5 mL)	No single crystals
	7.5 (0.025 mmol)	19 (0.1 mmol)	26.3 (0.3125 mmol)	-	H_2O (5 mL) MeOH (0.5 mL)	No single crystals
	7.5 (0.025 mmol)	76 (0.4 mmol)	26.3 (0.3125 mmol)	-	H_2O (5 mL) MeOH (1.5 mL)	No single crystals
	7.5 (0.025 mmol)	9.5 (0.05 mmol)	26.3 (0.3125 mmol)	2	H_2O (5 mL) MeOH (0.5 mL)	No single crystals
	7.5 (0.025 mmol)	19 (0.1 mmol)	26.3 (0.3125 mmol)	2	H_2O (5 mL) MeOH (0.5 mL)	Clear, cubic crystals after 7 days
	7.5 (0.025 mmol)	76 (0.4 mmol)	26.3 (0.3125 mmol)	2	H_2O (5 mL) MeOH (1.5 mL)	No single crystals
	7.5 (0.025 mmol)	9.5 (0.05 mmol)	-	-	H_2O (5 mL) MeOH (0.5 mL)	Clear, cubic crystals after 10 days
	7.5 (0.025 mmol)	19 (0.1 mmol)	-	-	H_2O (5 mL) MeOH (0.5 mL)	Clear, cubic crystals after 2 days
	7.5 (0.025 mmol)	76 (0.4 mmol)	-	-	H_2O (5 mL) MeOH (1.5 mL)	Clear, needle-like crystals overnight

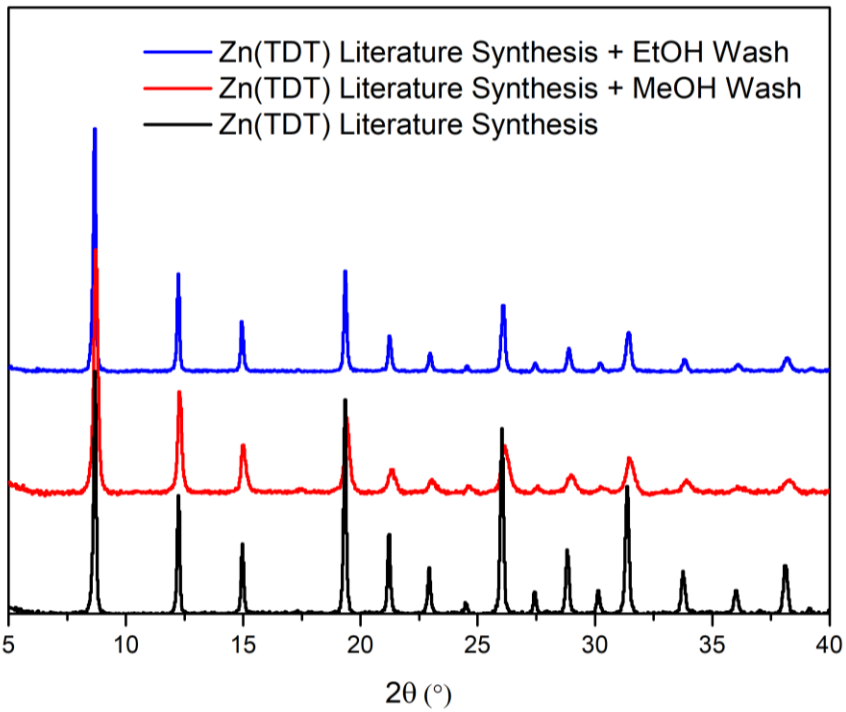

Figure 95: *PXRD patterns for* ***Zn(TDT)*** *synthesised via the literature method with subsequent MeOH (red) and EtOH (blue) washes.*

Table 23: *Synthesis attempts for* ***Zn(TDT)*** *at room temperature using the sodium H_3TDT ligand. All tests were performed with HTDT·2Na (31.1 mg, 0.125 mmol) and $Zn(NO_3)_2 \cdot 6H_2O$ (37.5 mg, 0.125 mmol). $NaHCO_3$ (50 mg, 0.595 mmol) was used as the base.*

	Base added (mg)	**Solvents (mL)**	**Precipitation Time**	**PXRD**
A	No	H_2O (2.5 mL)	Immediate	Amorphous
B	Yes	H_2O (2.5 mL)	10 s	Crystalline
C	No	H_2O (2.5 mL) MeOH (0.25 mL)	Immediate	Amorphous
D	Yes	H_2O (2.5 mL) MeOH (0.25 mL)	Immediate	Crystalline
E	No	H_2O (2.5 mL) EtOH (0.25 mL)	Immediate	Amorphous
F	Yes	H_2O (2.5 mL) EtOH (0.25 mL)	Immediate	Crystalline

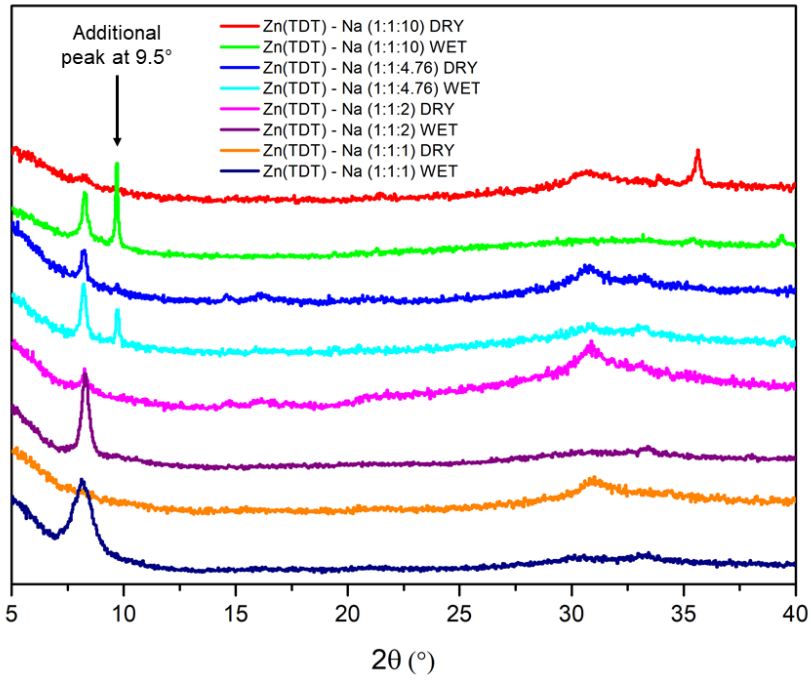

Figure 96: *PXRD patterns for* ***Zn(TDT)*** *formed in a 10:1 water/ethanol mixture. Ratio in parentheses refers to the molar ratio of metal to ligand to base.*

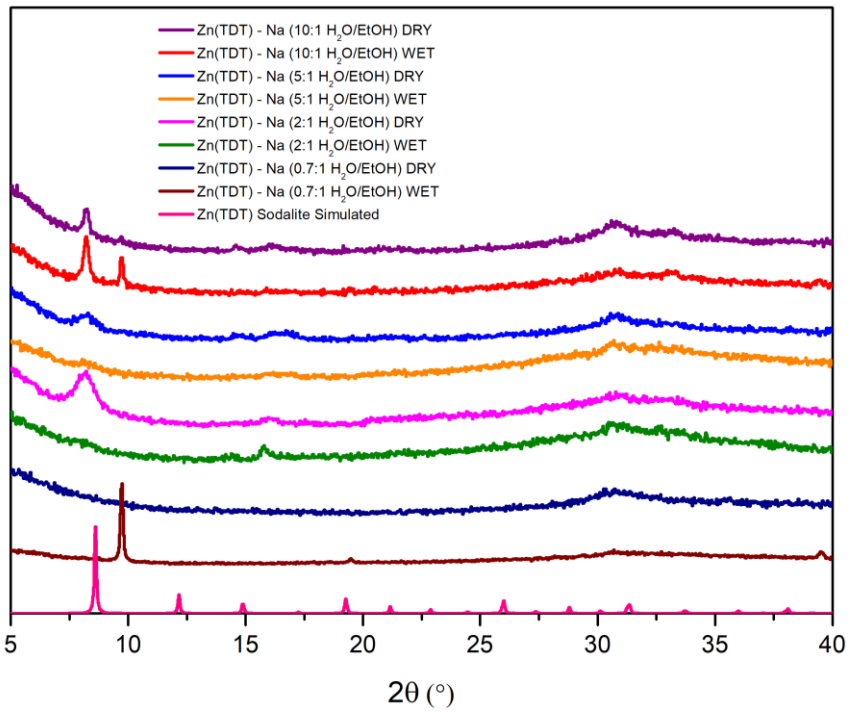

Figure 97: *PXRD patterns for* ***Zn(TDT)*** *formed in various ratios of water to ethanol (ratio in parentheses), compared to the simulated pattern for sodalite* ***Zn(TDT)*** *constructed from single crystal data.*

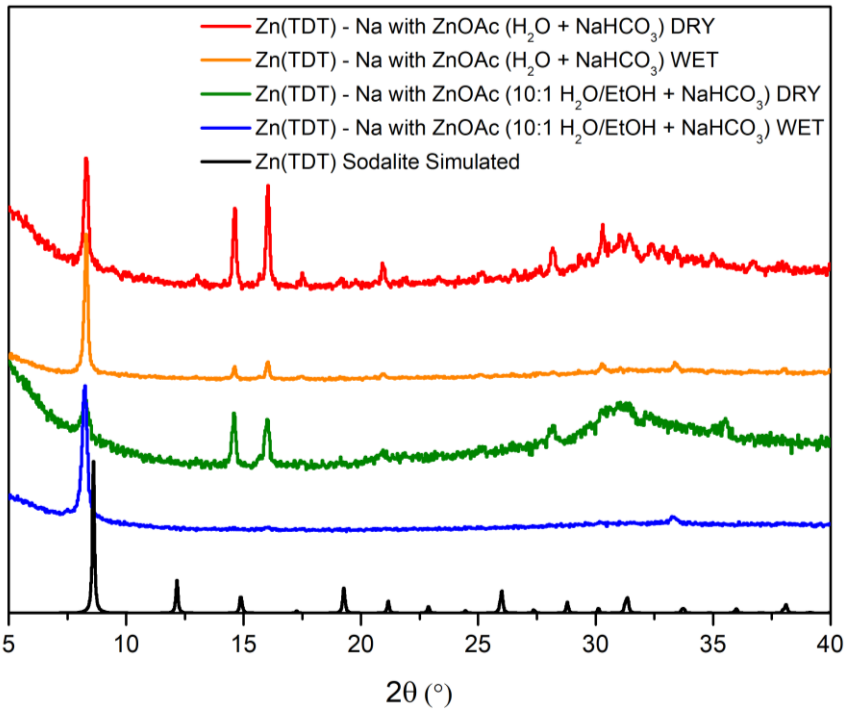

Figure 98: *PXRD patterns for* ***Zn(TDT)*** *formed with zinc acetate in pure water (red (dry sample)/orange (wet sample)) or a 10:1 mixture of water and ethanol (green (dry sample)/blue (wet sample)) compared to the simulated pattern for* ***Zn(TDT)*** *constructed from single crystal data.*

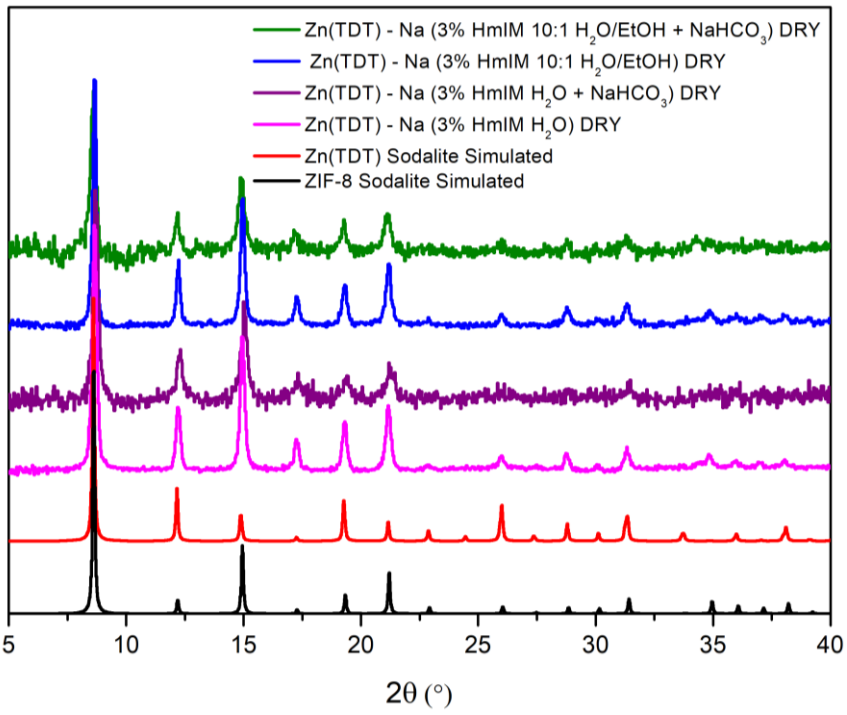

Figure 99: *Baseline corrected PXRD patterns for* ***Zn(TDT)*** *formed in the presence of 3% w/v 2-methylimidazole (HmIM) compared to simulated patterns for ZIF-8 and* ***Zn(TDT)*** *constructed from single crystal date.*

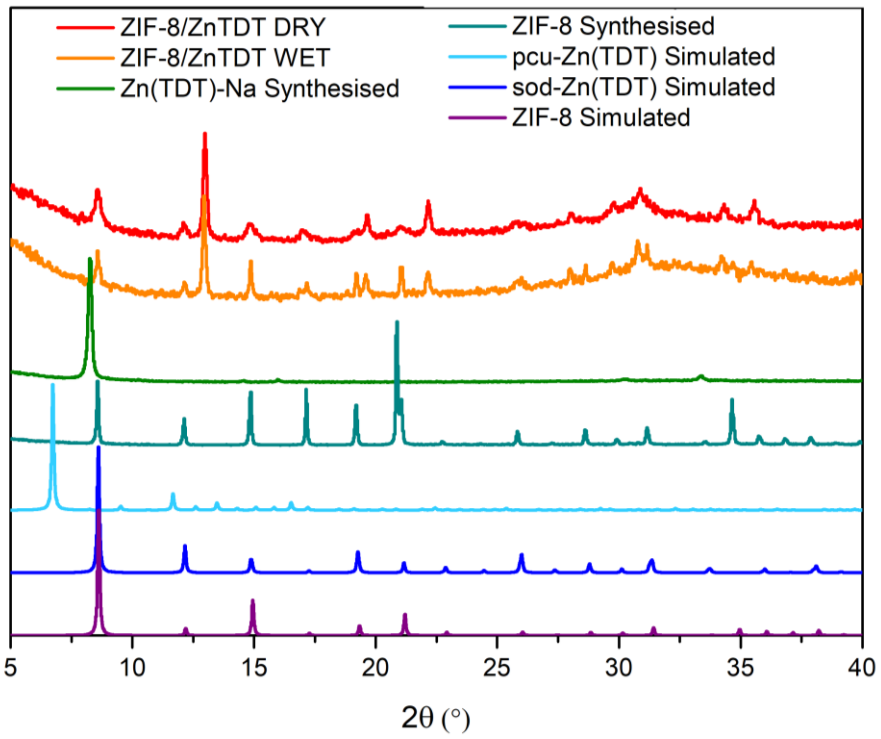

Figure 100: *PXRD patterns for the attempted formation of Zn(TDT) around sod-ZIF-8 for wet (orange) and dry (red) samples compared to the data for synthesised Zn(TDT)-Na (green) and ZIF-8 (aqua) as well as simulated patterns for sod-ZIF-8 (purple), sod-Zn(TDT) (dark blue) and pcu-Zn(TDT) (light blue).*

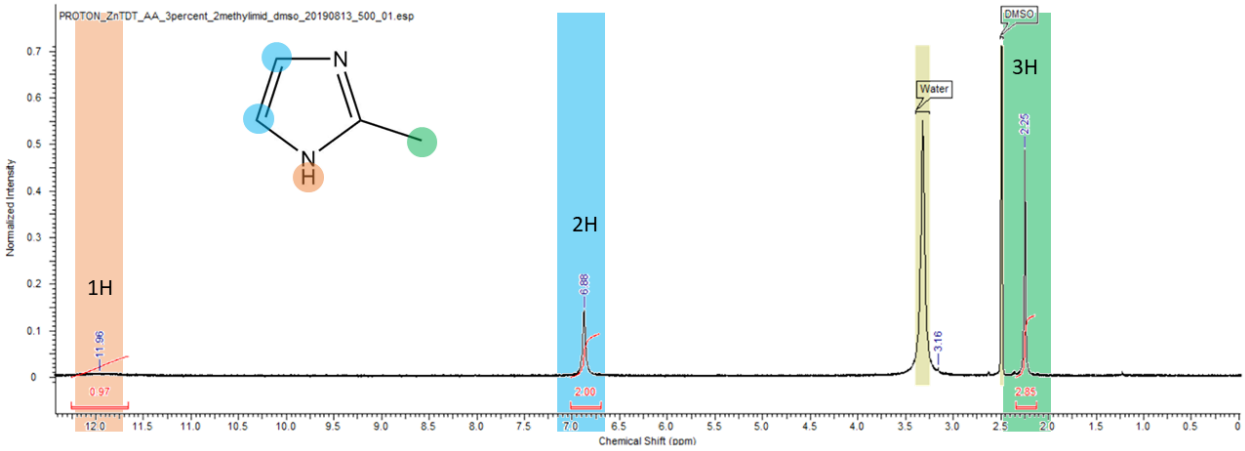

Figure 101: ^{1}H NMR spectrum for a sample of Zn(TDT)-Na formed in the presence of 3% 2-methylimidazole in an attempt to seed growth of sod-Zn(TDT)-Na. Only peaks corresponding to H atoms present in the 2-methylimidazole ligand can be observed, as highlighted in green, blue and orange, with no peaks corresponding to NH group in the H_3TDT linker.

Table 24: *Raw EDX data for atomic percentages in various sites within a sample of Zn(TDT)-Na.*

	Atomic Percentage (%)							
SITE	**C**	**O**	**N**	**Na**	**Zn**	**Pt**	**Cl**	**Zr**
41	33.9	29.8	20.2	12.6	3.2	0.3	-	-
42	23.9	22.5	32.8	14.1	6.3	0.3	-	-
43	47.6	15.2	20.0	9.7	6.0	0.3	0.3	-
44	15.7	34.3	29.2	16.8	3.8	0.3	-	-
45	23.0	34.8	25.0	13.5	3.4	0.3	-	-
46	24.5	28.0	32.1	11.0	4.1	0.4	-	-
47	21.6	43.1	8.6	21.4	3.0	0.6	1.7	-
48	10.8	50.5	11.5	23.2	2.3	0.3	1.1	0.3
49	13.3	45.3	11.8	22.7	4.5	0.8	1.5	-
50	15.8	35.7	29.4	14.7	4.1	0.3	-	-
51	17.9	29.1	31.6	14.8	6.2	0.5	-	-
52	16.4	34.1	30.2	13.9	4.9	0.4	-	-
53	37.4	31.1	19.2	9.1	3.0	0.3	-	-
54	-	39.7	31.1	22.0	6.7	0.6	-	-
55	35.8	25.1	26.1	9.0	3.6	0.2	-	0.1
56	13.1	36.1	29.7	15.1	5.5	0.3	-	-
57	9.5	42.7	27.1	16.4	4.1	0.3	-	-
58	12.7	39.5	29.0	14.4	3.9	0.1	-	0.4

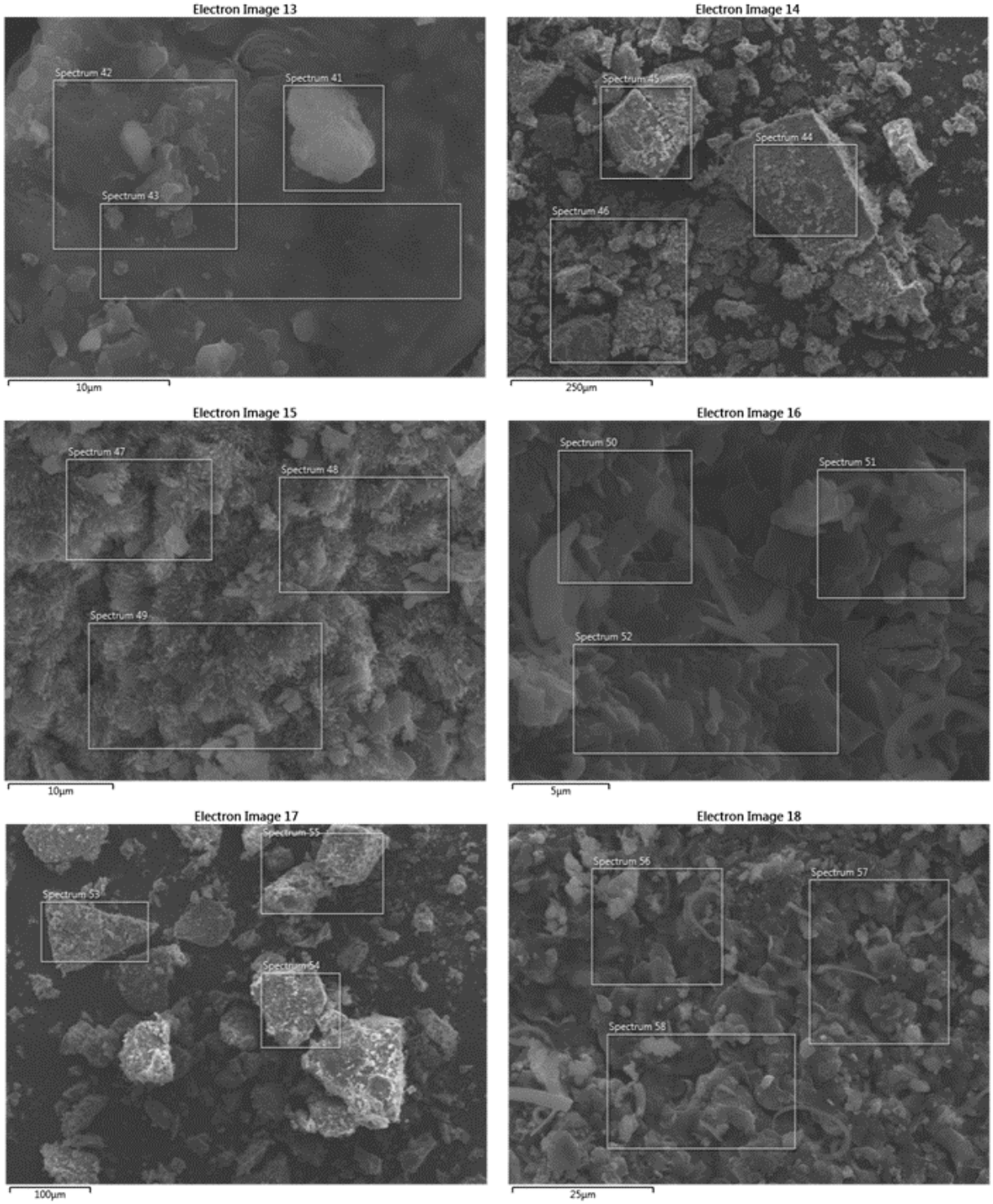

Figure 102: *SEM images of Zn(TDT)-Na showing regions used to produce EDX spectra 41-58.*

Table 25: *Raw EDX data for atomic percentages in various sites within a sample of Zn(TDT)-TBA.*

	Atomic Percentage (%)						
SITE	**C**	**O**	**N**	**Na**	**Zn**	**Pt**	**Zr**
16	25.5	45.2	7.4	11.0	10.5	0.2	-
17	26.2	44.0	7.3	10.4	11.9	0.2	-
18	25.1	46.5	6.7	11.3	10.2	0.2	0.0
19	26.8	45.7	5.1	10.6	11.5	0.3	0.1
20	-	56.9	9.9	14.0	18.9	0.4	-
21	24.1	45.2	6.9	10.8	12.7	0.3	-
22	24.6	45.5	6.8	10.9	11.8	0.2	0.2
23	26.2	46.2	7.7	9.4	10.4	0.2	-
24	21.1	46.0	6.6	13.4	12.7	0.2	-
25	23.2	47.2	6.9	11.4	11.1	0.2	-
26	27.1	48.1	4.9	10.3	9.3	0.3	-
27	23.9	48.2	6.4	10.9	10.4	0.2	-
34	22.8	47.0	6.2	11.6	11.7	0.0	0.8
35	25.9	44.6	3.3	9.4	16.4	0.4	-
36	29.6	42.0	6.2	9.2	12.7	0.4	-
37	25.5	43.6	5.5	12.1	13.1	0.2	-
38	21.7	52.5	4.8	11.9	8.8	0.3	-
39	23.6	43.8	9.2	8.4	14.9	0.2	-

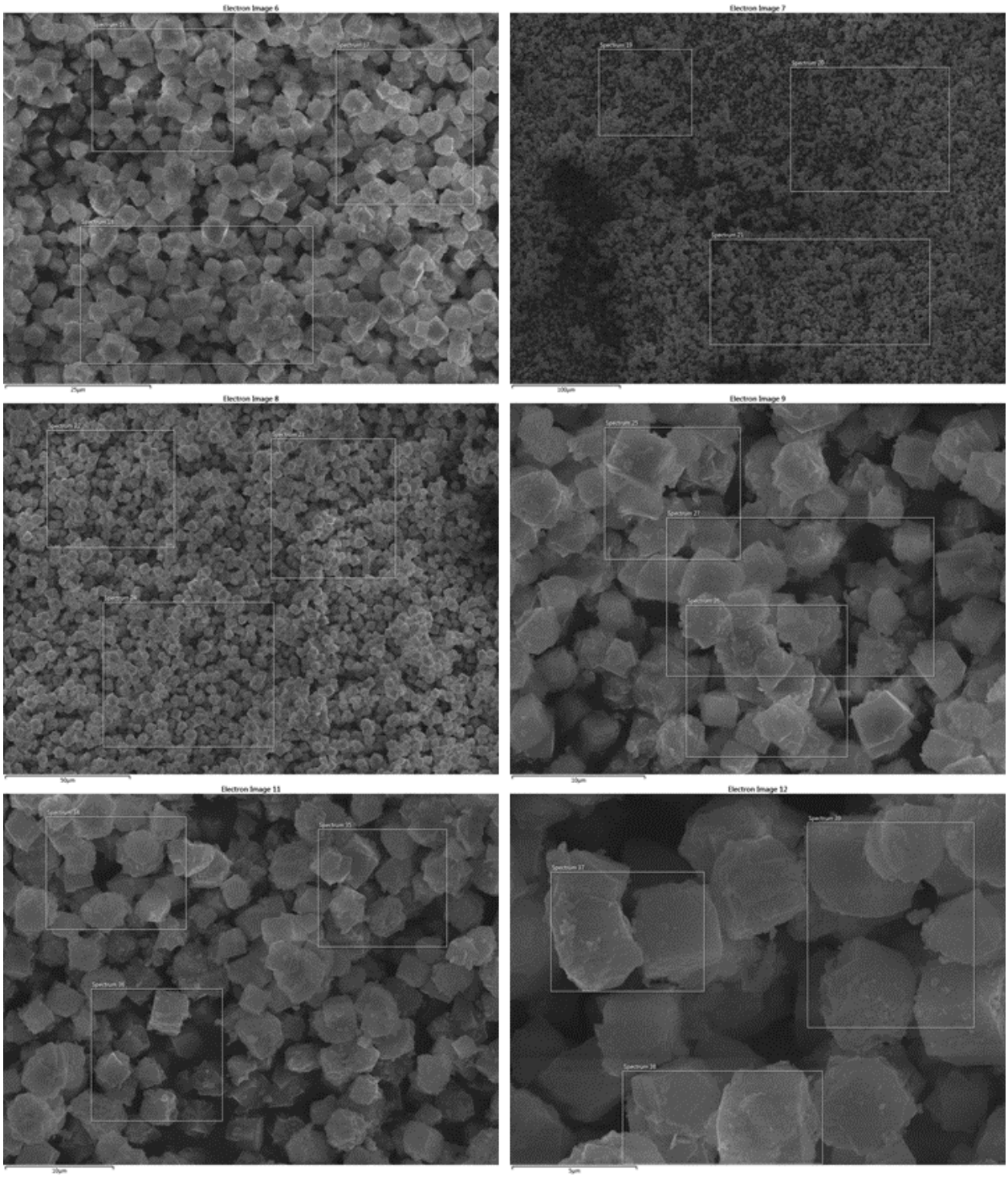

Figure 103: *SEM images of Zn(TDT)-TBA showing regions used to produce EDX spectra 16-27, 34-39.*

References

1. Zhang, J.-P.; Zhu, A.-X.; Lin, R.-B.; Qi, X.-L.; Chen, X.-M., *Adv. Mat.* **2011,** *23*, 1268-1271.
2. Huang, X.-C.; Lin, Y.-Y.; Zhang, J.-P.; Chen, X.-M., *Angew. Chem. Ind. Ed.* **2006,** *45*, 1557-1559.
3. Morris, W.; Doonan, C. J.; Furukawa, H.; Banerjee, R.; Yaghi, O. M., *J. Am. Chem. Soc.* **2008,** *130*, 12626-12627.
4. Katsoulidis, A. P.; Park, K. S.; Antypov, D.; Martí-Gastaldo, C.; Miller, G. J.; Warren, J. E.; Robertson, C. M.; Blanc, F.; Darling, G. R.; Berry, N. G.; Purton, J. A.; Adams, D. J.; Rosseinsky, M. J., *Angew. Chem. Int. Ed.* **2014,** *53*, 193-198.
5. Kathalikkattil, A. C.; Roshan, R.; Tharun, J.; Babu, R.; Jeong, G.-S.; Kim, D.-W.; Cho, S. J.; Park, D.-W., *Chem. Comm.* **2016,** *52*, 280-283.
6. Liang, K.; Coghlan, C. J.; Bell, S. G.; Doonan, C.; Falcaro, P., *Chem. Comm.* **2016,** *52*, 473-476.
7. Kirk, O.; Borchert, T. V.; Fuglsang, C. C., *Curr. Opin. Biotechnol.* **2002,** *13*, 345-351.
8. Wells, A. S.; Finch, G. L.; Michels, P. C.; Wong, J. W., *Org. Process Res. Dev.* **2012,** *16*, 1986-1993.
9. Patel, R. N., *Biomolecules* **2013,** *3*, 741-777.
10. Maurer, S. C.; Schulze, H.; Schmid, R. D.; Urlacher, V., *Adv. Synth. Catal.* **2003,** *345*, 802-810.
11. Fuganti, C.; Lemiere, G.; Simon, H.; Gunther, H.; Thanos, J.; Winterfeldt, E.; Roberts, S. M.; Godtfredsen, S.; Ingvorsen, K.; Yde, B.; Andresen, O.; Gais, H.-J.; Ohno, M.; Kobayashi, S.; Adachi, K.; Brooks, D. W.; Sinay, P.; Hoppe, D.; Wong, C.-H.; Pugh, S., YR; Ghisalba, O.; Schar, H.-P.; Tombo, G. M. R.; Young, D. W.; Wandrey, C.; Reimerdes, E. H.; Hilvert, D.; Kaiser, E.; Leatherbarrow, R. J.; Wells, T. N. C.; Fersht, A. R.; Nambiar, K. P.; Stackhouse, J.; Presnell, S. R.; Benner, S. A., *Enzymes as catalysts in organic synthesis*. Springer: Dordrecht, 1986.
12. Huang, Y.; Locy, R.; Weete, J. D., *Lipids* **2004,** *39*, 251-258.
13. Yang, L.-q.; Wang, S.-h.; Tian, Y.-p., *App. Biochem. Biotechnol.* **2010,** *160*, 303-313.
14. Jellouli, K.; Bougatef, A.; Daâssi, D.; Balti, R.; Barkia, A.; Nasri, M., *Food Chem.* **2009,** *116*, 644-650.
15. Klomklao, S.; Kishimura, H.; Yabe, M.; Benjakul, S., *Comp. Biochem. Physiol., Part B: Biochem. Mol. Biol.* **2007,** *147*, 682-689.
16. Calandrelli, V.; Gambacorta, A.; Romano, I.; Carratore, V.; Lama, L., *World J. Microbiol. Biotechnol.* **2008,** *24*, 2269.
17. Habibi, A. E.; Khajeh, K.; Naderi-Manesh, H.; Ranjbar, B.; Nemat-Gorgani, M., *J. Biotechnol.* **2006,** *123*, 434-442.
18. Wu, Z.; Zhen, Z.; Jiang, J.-H.; Shen, G.-L.; Yu, R.-Q., *J. Am. Chem. Soc.* **2009,** *131*, 12325-12332.
19. Zhang, P.; Sun, F.; Tsao, C.; Liu, S.; Jain, P.; Sinclair, A.; Hung, H.-C.; Bai, T.; Wu, K.; Jiang, S., *Proc. Natl. Acad. Sci.* **2015,** *112*, 12046.
20. Matsuura, S.-i.; El-Safty, S. A.; Chiba, M.; Tomon, E.; Tsunoda, T.; Hanaoka, T.-a., *Mater. Lett.* **2012,** *89*, 184-187.
21. Wang, Y.; Caruso, F., *Chem. Mater.* **2005,** *17*, 953-961.
22. Adhikari, C.; Mishra, A.; Nayak, D.; Chakraborty, A., *J Drug Deliv Sci Technol* **2018,** *47*, 1-11.
23. Furukawa, H.; Cordova, K. E.; O'Keeffe, M.; Yaghi, O. M., *Science* **2013,** *341*, 1230444.
24. Chui, S. S. Y.; Lo, S. M. F.; Charmant, J. P. H.; Orpen, A. G.; Williams, I. D., *Science* **1999,** *283*, 1148.
25. Li, H.; Eddaoudi, M.; O'Keeffe, M.; Yaghi, O. M., *Nature* **1999,** *402*, 276-279.
26. Eddaoudi, M.; Kim, J.; Rosi, N.; Vodak, D.; Wachter, J.; Keeffe, M.; Yaghi, O. M., *Science* **2002,** *295*, 469.

27. Cavka, J. H.; Jakobsen, S.; Olsbye, U.; Guillou, N.; Lamberti, C.; Bordiga, S.; Lillerud, K. P., *J. Am. Chem. Soc.* **2008,** *130*, 13850-13851.
28. Chae, H. K.; Siberio-Pérez, D. Y.; Kim, J.; Go, Y.; Eddaoudi, M.; Matzger, A. J.; O'Keeffe, M.; Yaghi, O. M.; Materials Design and Discovery, G., *Nature* **2004,** *427*, 523-527.
29. Marshall, R. J.; Forgan, R. S., *Eur. J. Inorg. Chem.* **2016,** *2016*, 4310-4331.
30. Fast, C. D.; Woods, J.; Lentchner, J.; Makal, T. A., *Dalton Trans.* **2019,** *48*, 14696-14704.
31. Devic, T.; Serre, C., *Chem. Soc. Rev.* **2014,** *43*, 6097-6115.
32. Yuan, S.; Qin, J.-S.; Lollar, C. T.; Zhou, H.-C., *ACS Central Science* **2018,** *4*, 440-450.
33. Kim, S.-N.; Kim, J.; Kim, H.-Y.; Cho, H.-Y.; Ahn, W.-S., *Catal. Today* **2013,** *204*, 85-93.
34. Luz, I.; Llabrés i Xamena, F. X.; Corma, A., *J. Catal.* **2010,** *276*, 134-140.
35. Luz, I.; Llabrés i Xamena, F. X.; Corma, A., *J. Catal.* **2012,** *285*, 285-291.
36. Dhakshinamoorthy, A.; Alvaro, M.; Garcia, H., *Adv. Synth. Catal.* **2009,** *351*, 2271-2276.
37. Wei, N.; Zuo, R.-X.; Zhang, Y.-Y.; Han, Z.-B.; Gu, X.-J., *Chem. Comm.* **2017,** *53*, 3224-3227.
38. Min Wang, Q.; Shen, D.; Bülow, M.; Ling Lau, M.; Deng, S.; Fitch, F. R.; Lemcoff, N. O.; Semanscin, J., *Microporous Mesoporous Mat.* **2002,** *55*, 217-230.
39. Li, B.; Wen, H.-M.; Zhou, W.; Chen, B., *J. Phys. Chem. Lett.* **2014,** *5*, 3468-3479.
40. Qin, J.-S.; Du, D.-Y.; Li, W.-L.; Zhang, J.-P.; Li, S.-L.; Su, Z.-M.; Wang, X.-L.; Xu, Q.; Shao, K.-Z.; Lan, Y.-Q., *Chem. Sci.* **2012,** *3*, 2114-2118.
41. Rowsell, J. L. C.; Yaghi, O. M., *Microporous Mesoporous Mat.* **2004,** *73*, 3-14.
42. Sumida, K.; Rogow, D. L.; Mason, J. A.; McDonald, T. M.; Bloch, E. D.; Herm, Z. R.; Bae, T.-H.; Long, J. R., *Chem. Rev.* **2012,** *112*, 724-781.
43. Cui, Y.; Yue, Y.; Qian, G.; Chen, B., *Chem. Rev.* **2012,** *112*, 1126-1162.
44. Yu, J.; Cui, Y.; Xu, H.; Yang, Y.; Wang, Z.; Chen, B.; Qian, G., *Nat. Comm.* **2013,** *4*, 2719.
45. Horcajada, P.; Gref, R.; Baati, T.; Allan, P. K.; Maurin, G.; Couvreur, P.; Férey, G.; Morris, R. E.; Serre, C., *Chem. Rev.* **2012,** *112*, 1232-1268.
46. Wang, C.; Zhang, T.; Lin, W., *Chem. Rev.* **2012,** *112*, 1084-1104.
47. Liang, K.; Ricco, R.; Doherty, C. M.; Styles, M. J.; Bell, S.; Kirby, N.; Mudie, S.; Haylock, D.; Hill, A. J.; Doonan, C. J.; Falcaro, P., *Nat. Comm.* **2015,** *6*, 7240.
48. Feng, D.; Liu, T.-F.; Su, J.; Bosch, M.; Wei, Z.; Wan, W.; Yuan, D.; Chen, Y.-P.; Wang, X.; Wang, K.; Lian, X.; Gu, Z.-Y.; Park, J.; Zou, X.; Zhou, H.-C., *Nat. Comm.* **2015,** *6*, 5979.
49. Lykourinou, V.; Chen, Y.; Wang, X.-S.; Meng, L.; Hoang, T.; Ming, L.-J.; Musselman, R. L.; Ma, S., *J. Am. Chem. Soc.* **2011,** *133*, 10382-10385.
50. Shieh, F.-K.; Wang, S.-C.; Yen, C.-I.; Wu, C.-C.; Dutta, S.; Chou, L.-Y.; Morabito, J. V.; Hu, P.; Hsu, M.-H.; Wu, K. C. W.; Tsung, C.-K., *J. Am. Chem. Soc.* **2015,** *137*, 4276-4279.
51. Hou, M.; Ge, J., Chapter Three - Armoring Enzymes by Metal–Organic Frameworks by the Coprecipitation Method. In *Methods in Enzymology*, Kumar, C. V., Ed. Academic Press: 2017; Vol. 590, pp 59-75.
52. Wu, X.; Yang, C.; Ge, J., *Bioresources and Bioprocessing* **2017,** *4*, 24.
53. Patil Pravin, D.; Yadav Ganapati, D., *ChemistrySelect* **2018,** *3*, 4669-4675.
54. Abdelhamid, H. N.; Huang, Z.; El-Zohry, A. M.; Zheng, H.; Zou, X., *Inorg. Chem.* **2017,** *56*, 9139-9146.
55. Kumar, P.; Bansal, V.; Paul, A. K.; Bharadwaj, L. M.; Deep, A.; Kim, K.-H., *Appl Nanosci* **2016,** *6*, 951-957.
56. Li, W.; Zhang, Y.; Xu, Z.; Meng, Q.; Fan, Z.; Ye, S. Z., Guoliang, *Angew. Chem. Int. Ed.* **2016,** *55*, 5.
57. Liang, K.; Richardson Joseph, J.; Cui, J.; Caruso, F.; Doonan Christian, J.; Falcaro, P., *Adv Mat.* **2016,** *28*, 7910-7914.
58. Astria, E.; Thonhofer, M.; Ricco, R.; Liang, W.; Chemelli, A.; Tarzia, A.; Alt, K.; Hagemeyer, C. E.; Rattenberger, J.; Schroettner, H.; Wrodnigg, T.; Amenitsch, H.; Huang, D. M.; Doonan, C. J.; Falcaro, P., *Mater. Horizons* **2019,** *6*, 969-977.

59. Fan, X.; Wang, W.; Li, W.; Zhou, J.; Wang, B.; Zheng, J.; Li, X., *ACS Appl. Mater. Interfaces* **2014,** *6*, 14994-14999.
60. Watanabe, S.; Ohsaki, S.; Fukuta, A.; Hanafusa, T.; Takada, K.; Tanaka, H.; Maki, T.; Mae, K.; T. Miyahara, M., *Characterization of mixing performance in a microreactor and its application to the synthesis of porous coordination polymer particles*. 2017; Vol. 28.
61. Maddigan, N. K.; Tarzia, A.; Huang, D. M.; Sumby, C. J.; Bell, S. G.; Falcaro, P.; Doonan, C. J., *Chem. Sci.* **2018,** *9*, 4217-4223.
62. Fairen-Jimenez, D.; Moggach, S. A.; Wharmby, M. T.; Wright, P. A.; Parsons, S.; Düren, T., *J. Am. Chem. Soc.* **2011,** *133*, 8900-8902.
63. Eum, K.; Jayachandrababu, K. C.; Rashidi, F.; Zhang, K.; Leisen, J.; Graham, S.; Lively, R. P.; Chance, R. R.; Sholl, D. S.; Jones, C. W.; Nair, S., *J. Am. Chem. Soc.* **2015,** *137*, 4191-4197.
64. Davis, J. W.; Phillips, P. E., *Blood* **1971,** *38*, 417.
65. Liang, W.; Xu, H.; Carraro, F.; Maddigan, N. K.; Li, Q.; Bell, S. G.; Huang, D. M.; Tarzia, A.; Solomon, M. B.; Amenitsch, H.; Vaccari, L.; Sumby, C. J.; Falcaro, P.; Doonan, C. J., *J. Am. Chem. Soc.* **2019,** *141*, 2348-2355.
66. Cai, H.; Huang, Y.-L.; Li, D., *Coord Chem Rev.* **2017**.
67. McKinlay, A. C.; Morris, R. E.; Horcajada, P.; Férey, G.; Gref, R.; Couvreur, P.; Serre, C., *Angew. Chem. Int. Ed.* **2010,** *49*, 6260-6266.
68. Anderson, S. L.; Stylianou, K. C., *Coord. Chem. Rev.* **2017,** *349*, 102-128.
69. Jeong, G. S.; Kathalikkattil, A. C.; Babu, R.; Chung, Y. G.; Won Park, D., *Chin. J. Catal.* **2018,** *39*, 63-70.
70. Kathalikkattil, A. C.; Babu, R.; Roshan, R. K.; Lee, H.; Kim, H.; Tharun, J.; Suresh, E.; Park, D.-W., *J. Mat. Chem. A* **2015,** *3*, 22636-22647.
71. Rabone, Y.; Yue, Y.-F.; Chong, S. Y.; Stylianou, K. C.; Basca, J.; Bradshaw, D.; Darling, G. R.; Berry, N. G.; Khimyak, Y. Z.; Ganin, A. Y.; Wiper, P.; Claridge, J. B.; Rosseinsky, M. J., *Science* **2010,** *329*, 5.
72. Mantion, A.; Massüger, L.; Rabu, P.; Palivan, C.; McCusker, L. B.; Taubert, A., *J. Am. Chem. Soc.* **2008,** *130*, 2517-2526.
73. Rajkumar, T.; Kukkar, D.; Kim, K.-H.; Sohn, J. R.; Deep, A., *J. Ind. Eng. Chem.* **2019,** *72*, 50-66.
74. Li, X.; Guo, T.; Lachmanski, L.; Manoli, F.; Menendez-Miranda, M.; Manet, I.; Guo, Z.; Wu, L.; Zhang, J.; Gref, R., *Int. J. Pharm.* **2017,** *531*, 424-432.
75. Liu, J.; Bao, T.-Y.; Yang, X.-Y.; Zhu, P.-P.; Wu, L.-H.; Sha, J.-Q.; Zhang, L.; Dong, L.-Z.; Cao, X.-L.; Lan, Y.-Q., *Chem. Comm.* **2017,** *53*, 7804-7807.
76. Sha, J.-Q.; Zhong, X.-H.; Wu, L.-H.; Liu, G.-D.; Sheng, N., *RSC Adv.* **2016,** *6*, 82977-82983.
77. Liu, G.; Li, L.; Xu, D.; Huang, X.; Xu, X.; Zheng, S.; Zhang, Y.; Lin, H., *Carbohydr. Polym.* **2017,** *175*, 584-591.
78. Yu, F.; Han, X.; Chen, L., *Chem. Comm.* **2014,** *50*, 12234-12249.
79. Moussa, Z.; Hmadeh, M.; Abiad, M. G.; Dib, O. H.; Patra, D., *Food Chem.* **2016,** *212*, 485-494.
80. Han, S.; Warren, S. C.; Yoon, S. M.; Malliakas, C. D.; Hou, X.; Wei, Y.; Kanatzidis, M. G.; Grzybowski, B. A., *J. Am. Chem. Soc.* **2015,** *137*, 8169-8175.
81. Han, S.; Wei, Y.; Grzybowski, B. A., *Chem. Eur. J.* **2013,** *19*, 11194-11198.
82. Yang, J.; Trickett, C. A.; Alahmadi, S. B.; Alshammari, A. S.; Yaghi, O. M., *J. Am. Chem. Soc.* **2017,** *139*, 8118-8121.
83. Lin, W.; Hu, Q.; Jiang, K.; Yang, Y.; Yang, Y.; Cui, Y.; Qian, G., *J. Solid State Chem.* **2016,** *237*, 307-312.
84. Li, T.; Kozlowski, M. T.; Doud, E. A.; Blakely, M. N.; Rosi, N. L., *J. Am. Chem. Soc.* **2013,** *135*, 11688-11691.
85. Rojas, S.; Devic, T.; Horcajada, P., *J. Mat. Chem. B* **2017,** *5*, 2560-2573.

86. Wang, S.; Wahiduzzaman, M.; Davis, L.; Tissot, A.; Shepard, W.; Marrot, J.; Martineau-Corcos, C.; Hamdane, D.; Maurin, G.; Devautour-Vinot, S.; Serre, C., *Nat. Comm.* **2018,** *9*, 4937.
87. Navarro-Sánchez, J.; Argente-García, A. I.; Moliner-Martínez, Y.; Roca-Sanjuán, D.; Antypov, D.; Campíns-Falcó, P.; Rosseinsky, M. J.; Martí-Gastaldo, C., *J. Am. Chem. Soc.* **2017,** *139*, 4294-4297.
88. Canivet, J.; Aguado, S.; Bergeret, G.; Farrusseng, D., *Chem. Comm.* **2011,** *47*, 11650-11652.
89. An, J.; Shade, C. M.; Chengelis-Czegan, D. A.; Petoud, S.; Rosi, N. L., *J. Am. Chem. Soc* **2011,** *133*, 1220-1223.
90. Marti-Gastaldo, C.; Warren, J.; Briggs, M.; Armstrong, J.; Thomas, M.; Rosseinsky, M., *Chem. Eur. J.* **2015,** *21*, 8.
91. Marti-Gastaldo, C.; Warren, J.; Stylianou, K.; Flack, N.; Rosseinsky, M., *Angew. Chem. Int. Ed.* **2012,** *51*, 5.
92. (TGA), T. G. A., Compositional guideline: Polaprezinc. Health, D. o., Ed. Australian Government: Australia, 2015.
93. Matsukura T ; ., T. H., *Biochem. (Mosc)* **2000,** *65*, 817-823.
94. Itagaki, M.; Saruta, M.; Saijo, H.; Mitobe, J.; Arihiro, S.; Matsuoka, M.; Kato, T.; Ikegami, M.; Tajiri, H., *Scand. J. Gastroenterol.* **2014,** *49*, 164-172.
95. Davison, G.; Marchbank, T.; March, D. S.; Thatcher, R.; Playford, R. J., *AM. J. Clin. Nutr.* **2016,** *104*, 526-536.
96. Mahmood, A.; FitzGerald, A. J.; Marchbank, T.; Ntatsaki, E.; Murray, D.; Ghosh, S.; Playford, R. J., *Gut* **2007,** *56*, 168-175.
97. Kawahara, M.; Tanaka, K.-i.; Kato-Negishi, M., *Nutrients* **2018,** *10*.
98. Liang, W.; Carraro, F.; Solomon, M. B.; Bell, S. G.; Amenitsch, H.; Sumby, C. J.; White, N. G.; Falcaro, P.; Doonan, C. J., *J. Am. Chem. Soc.* **2019,** *141*, 14298-14305.
99. Li, Z.; Xia, H.; Li, S.; Pang, J.; Zhu, W.; Jiang, Y., *Nanoscale* **2017,** *9*, 15298-15302.
100. Liang, W.; Ricco, R.; Maddigan, N. K.; Dickinson, R. P.; Xu, H.; Li, Q.; Sumby, C. J.; Bell, S. G.; Falcaro, P.; Doonan, C. J., *Chem. Mater.* **2018,** *30*, 1069-1077.
101. Wu, C.-s.; Xiong, Z.-h.; Li, C.; Zhang, J.-m., *RSC Adv.* **2015,** *5*, 82127-82137.
102. Zhang, F.-M.; Dong, H.; Zhang, X.; Sun, X.-J.; Liu, M.; Yang, D.-D.; Liu, X.; Wei, J.-Z., *ACS Appl. Mater. Interfaces* **2017,** *9*, 27332-27337.
103. Howarth, A. J.; Liu, Y.; Li, P.; Li, Z.; Wang, T. C.; Hupp, J. T.; Farha, O. K., *Nat. Rev. Mat.* **2016,** *1*, 15018.
104. Ou, P.; Wolff, S. P., *J. Biochem. Biophys. Method* **1996,** *31*, 59-67.
105. Gay, C.; Collins, J.; Gebicki, J. M., *Anal. Biochem.* **1999,** *273*, 143-148.
106. Cai, H.; Huang, Y.-L.; Li, D., *Coord. Chem. Rev.* **2019,** *378*, 207-221.
107. Wang, X.; Shi, J.; Zhang, S.; Wu, H.; Jiang, Z.; Yang, C.; Wang, Y.; Tang, L.; Yan, A., *J. Mat. Chem. B* **2015,** *3*, 6587-6598.
108. Schomberg, D.; Salzmann, M.; Stephan, D., *Enzyme Handbook 7, EC 1.11.1.7:1-6*. 1993.
109. Shinmen, Y.; Asami, S.; Amachi, T.; Shimizu, S.; Yamada, H., *Agric. Biol. Chem.***1986,** *50*, 247-249.
110. Akita, M.; Tsutsumi, D.; Kobayashi, M.; Kise, H., *Biosci., Biotechnol. Biochem.* **2001,** *65*, 1581-1588.
111. Zhao, Z.; Fu, J.; Dhakal, S.; Johnson-Buck, A.; Liu, M.; Zhang, T.; Woodbury, N. W.; Liu, Y.; Walter, N. G.; Yan, H., *Nat. Comm.* **2016,** *7*, 10619.
112. Shi, Q.; Chen, Z.; Song, Z.; Li, J.; Dong, J., *Angew. Chem., Int. Ed.* **2011,** *50*, 672-675.
113. Ding, B.; Wang, X.; Xu, Y.; Feng, S.; Ding, Y.; Pan, Y.; Xu, W.; Wang, H., *J. Colloid Interface Sci.* **2018,** *519*, 38-43.
114. Yuan, S.; Feng, L.; Wang, K.; Pang, J.; Bosch, M.; Lollar, C.; Sun, Y.; Qin, J.; Yang, X.; Zhang, P.; Wang, Q.; Zou, L.; Zhang, Y.; Zhang, L.; Fang, Y.; Li, J.; Zhou, H.-C., *Adv. Mat.* **2018,** *30*, 1704303.

115. Cao, S.-L.; Yue, D.-M.; Li, X.-H.; Smith, T. J.; Li, N.; Zong, M.-H.; Wu, H.; Ma, Y.-Z.; Lou, W.-Y., *ACS Sustainable Chem. Engin.* **2016,** *4*, 3586-3595.
116. Yin, X.; Chen, H.; Song, Y.; Wang, Y.; Li, Q.; Zhang, L., *J. Colloid Interface Sci.* **2014,** *413*, 175-182.
117. Yin, X.; Song, Y.; Wang, Y.; Zhang, L.; Li, Q., *Science China Chemistry* **2014,** *57*, 135-140.
118. Dincă, M.; Yu, A. F.; Long, J. R., *J. Am. Chem. Soc.* **2006,** *128*, 8904-8913.
119. Sumida, K.; Foo, M. L.; Horike, S.; Long, J. R., *Eur. J. Inorg. Chem.* **2010,** *2010*, 3739-3744.
120. Demessence, A.; Long, J. R., *Chem. Eur. J.* **2010,** *16*, 5902-5908.
121. Caputo, C. B.; Vukotic, V. N.; Sirizzotti, N. M.; Loeb, S. J., *Chem. Comm.* **2011,** *47*, 8545-8547.
122. Kumar, S.; Doctorovich, F., *Inorg. Chem. Comm.* **2012,** *15*, 33-36.
123. Tăbăcaru, A.; Pettinari, C.; Timokhin, I.; Marchetti, F.; Carrasco-Marín, F.; Maldonado-Hódar, F. J.; Galli, S.; Masciocchi, N., *Cryst. Growth Des.* **2013,** *13*, 3087-3097.
124. Young, R. J.; Begg, S. L.; Coghlan, C. J.; McDevitt, C. A.; Sumby, C. J., *Eur. J. Inorg. Chem.* **2018,** *2018*, 3512-3518.
125. Galli, S.; Masciocchi, N.; Colombo, V.; Maspero, A.; Palmisano, G.; López-Garzón, F. J.; Domingo-García, M.; Fernández-Morales, I.; Barea, E.; Navarro, J. A. R., *Chem. Mater.* **2010,** *22*, 1664-1672.
126. Pettinari, C.; Tăbăcaru, A.; Boldog, I.; Domasevitch, K. V.; Galli, S.; Masciocchi, N., *Inorg. Chem.* **2012,** *51*, 5235-5245.
127. Biswas, S.; Grzywa, M.; Nayek, H. P.; Dehnen, S.; Senkovska, I.; Kaskel, S.; Volkmer, D., *Dalton Trans.* **2009**, 6487-6495.
128. Denysenko, D.; Grzywa, M.; Tonigold, M.; Streppel, B.; Krkljus, I.; Hirscher, M.; Mugnaioli, E.; Kolb, U.; Hanss, J.; Volkmer, D., *Chem.: Eur. J.* **2011,** *17*, 1837-1848.
129. Schmieder, P.; Denysenko, D.; Grzywa, M.; Baumgärtner, B.; Senkovska, I.; Kaskel, S.; Sastre, G.; van Wüllen, L.; Volkmer, D., *Dalton Trans.* **2013,** *42*, 10786-10797.
130. Qin, J.-S.; Zhang, S.-R.; Du, D.-Y.; Shen, P.; Bao, S.-J.; Lan, Y.-Q.; Su, Z.-M., *Chem. Eur. J.* **2014,** *20*, 5625-5630.
131. Dang, Q.; Ji, F.; Zhang, X., *Chinese J. Chem.* **2012,** *30*, 2232-2236.
132. He, H.; Sun, F.; Zhao, N.; Yuan, R.; Zhu, G., *RSC Adv.* **2014,** *4*, 21535-21540.
133. Wang, J.; Huang, C.; Gao, K.; Wang, X.; Liu, M.; Ma, H.; Wu, J.; Hou, H., *Chem. Asian J.* **2016,** *11*, 1856-1862.
134. Xu, J.-G.; Wang, S.-H.; Zhang, M.-J.; Sun, C.; Xiao, Y.; Li, R.; Zheng, F.-K.; Guo, G.-C.; Huang, J.-S., *ACS Omega* **2017,** *2*, 346-352.
135. Mu, X.; Liu, C.; Zhao, N.; Liu, J.; Sun, F., *Inorg. Chem. Comm.* **2019,** *102*, 256-261.
136. Dincă, M.; Dailly, A.; Liu, Y.; Brown, C. M.; Neumann, D. A.; Long, J. R., *J. Am. Chem. Soc.* **2006,** *128*, 16876-16883.
137. Colombo, V.; Galli, S.; Choi, H. J.; Han, G. D.; Maspero, A.; Palmisano, G.; Masciocchi, N.; Long, J. R., *Chem. Sci.* **2011,** *2*, 1311-1319.
138. Mosca, N.; Vismara, R.; Fernandes, J. A.; Casassa, S.; Domasevitch, K. V.; Bailón-García, E.; Maldonado-Hódar, F. J.; Pettinari, C.; Galli, S., *Cryst. Growth Des.* **2017,** *17*, 3854-3867.
139. Mosca, N.; Vismara, R.; Fernandes, J. A.; Tuci, G.; Di Nicola, C.; Domasevitch, K. V.; Giacobbe, C.; Giambastiani, G.; Pettinari, C.; Aragones-Anglada, M.; Moghadam, P. Z.; Fairen-Jimenez, D.; Rossin, A.; Galli, S., *Chem. Eur. J.* **2018,** *24*, 13170-13180.
140. Zhang, E.; Jia, Q.; Zhang, J.; Ji, Z., *Chin. J. Chem.* **2016,** *34*, 191-195.
141. Linder-Patton, O. M.; de Prinse, T. J.; Furukawa, S.; Bell, S. G.; Sumida, K.; Doonan, C. J.; Sumby, C. J., *CrystEngComm* **2018,** *20*, 4926-4934.
142. Liang, W.; Xu, H.; Carraro, F.; Maddigan, N. K.; Li, Q.; Bell, S. G.; Huang, D. M.; Tarzia, A.; Solomon, M. B.; Amenitsch, H.; Vaccari, L.; Sumby, C. J.; Falcaro, P.; Doonan, C. J., *J. Am. Chem. Soc.* **2019,** *141*, 2348-2355.

143. Lin, R.-B.; He, Y.; Li, P.; Wang, H.; Zhou, W.; Chen, B., *Chem. Soc. Rev.* **2019,** *48*, 1362-1389.
144. Studlar, K.; Janousek, I., *Talanta* **1960,** *8*, 203-208.
145. Park, K. S.; Ni, Z.; Côté, A. P.; Choi, J. Y.; Huang, R.; Uribe-Romo, F. J.; Chae, H. K.; O'Keeffe, M.; Yaghi, O. M., *PNAS* **2006,** *103*, 10186.
146. Charles, R. G., *Org. Synth.* **1959,** *39*.
147. Boldog, I.; Rusanov, E. B.; Chernega, A. N.; Sieler, J.; Domasevitch, K. V., *Polyhedron* **2001,** *20*, 887-897.
148. Crawford, M.-J.; Karaghiosoff, K.; Klapötke, T. M.; Martin, F. A., *Inorg. Chem.* **2009,** *48*, 1731-1743.
149. Xiao, D. J.; Gonzalez, M. I.; Darago, L. E.; Vogiatzis, K. D.; Haldoupis, E.; Gagliardi, L.; Long, J. R., *J. Am. Chem. Soc.* **2016,** *138*, 7161-7170.
150. Tanaka, H.; Toda, T. Process for the prepar ation of 4, 5- di (5- tetrazolyl) - [1, 2, 3] triazole compounds from 4, 5- dicyano [1, 2, 3] triazole. 2007.
151. Katritzky, A. R.; Singh, S.; Kirichenko, K.; Smiglak, M.; Holbrey, J. D.; Reichert, W. M.; Spear, S. K.; Rogers, R. D., *Chem. Eur. J.* **2006,** *12*, 4630-4641.
152. Sheldrick, G., *Acta Crystallogr., Sect A: Found. Crystallogr.* **2008,** *64*.
153. Sheldrick, G. *SHELXS-2014 and SHELXL-2014. Program for X-ray Crystal Structure Determination*, Göttingen University: Göttingen, Germany, 2014.
154. Sheldrick, G., *Acta Crystallogr., Sect. C: Struct. Chem.* **2015,** *71*.
155. Barbour, L., *J. Supramolecular Chem.* **2001,** *1*, 189-191.
156. Dolomanov, O. V.; Bourhis, L. J.; Gildea, R. J.; Howard, J. A.; Puschmann, H., *J. Appl. Crystal.* **2009,** *42*, 339.